IMAGING SYNAPSE STRUCTURE AND FUNCTION

EDITED BY: George J. Augustine and Marc Fivaz
PUBLISHED IN: Frontiers in Synaptic Neuroscience

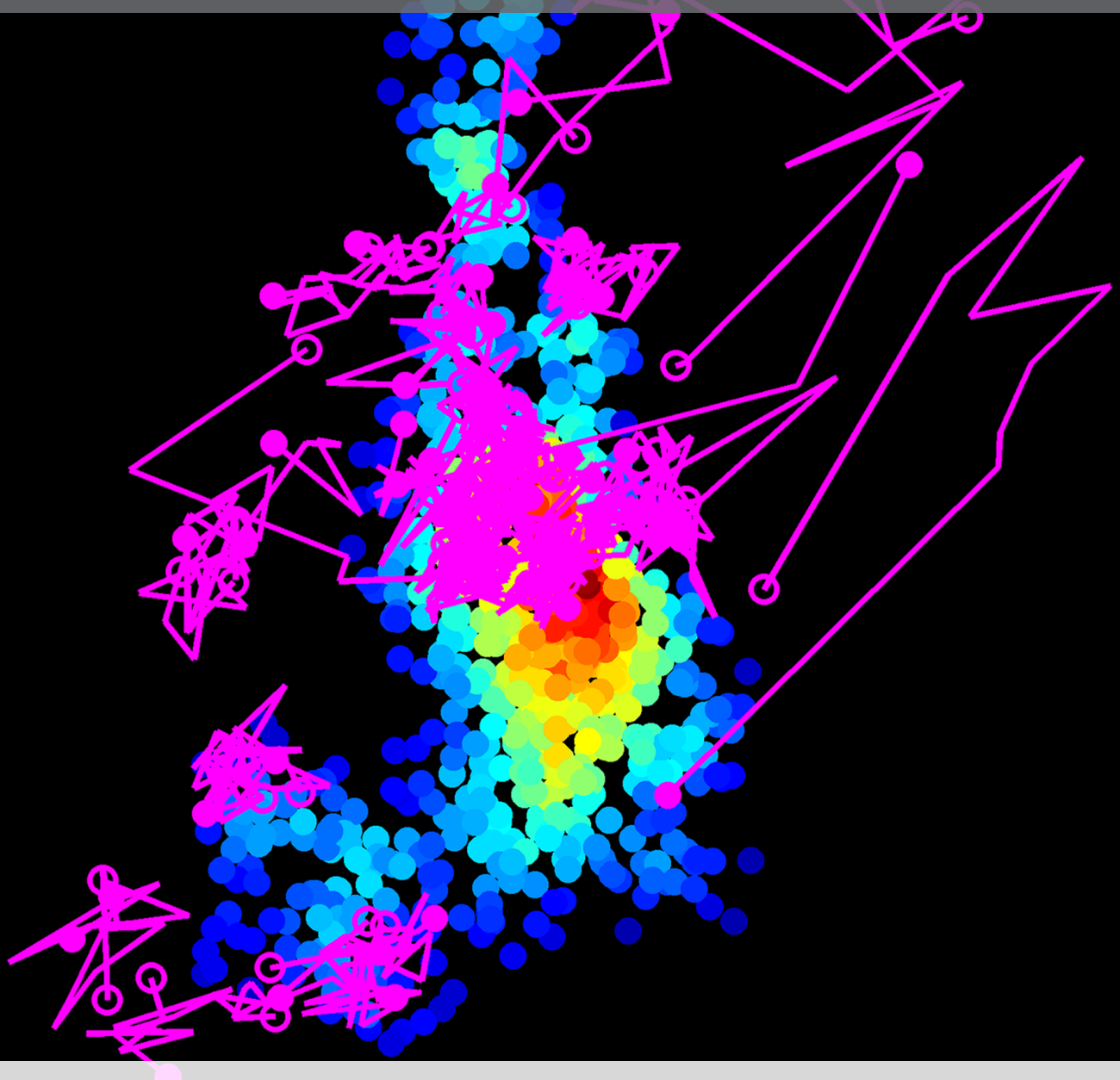

frontiers Research Topics

ISSN 1664-8714
ISBN 978-2-88945-175-3
DOI 10.3389/978-2-88945-175-3

About Frontiers

Frontiers is more than just an open-access publisher of scholarly articles: it is a pioneering approach to the world of academia, radically improving the way scholarly research is managed. The grand vision of Frontiers is a world where all people have an equal opportunity to seek, share and generate knowledge. Frontiers provides immediate and permanent online open access to all its publications, but this alone is not enough to realize our grand goals.

Frontiers Journal Series

The Frontiers Journal Series is a multi-tier and interdisciplinary set of open-access, online journals, promising a paradigm shift from the current review, selection and dissemination processes in academic publishing. All Frontiers journals are driven by researchers for researchers; therefore, they constitute a service to the scholarly community. At the same time, the Frontiers Journal Series operates on a revolutionary invention, the tiered publishing system, initially addressing specific communities of scholars, and gradually climbing up to broader public understanding, thus serving the interests of the lay society, too.

Dedication to Quality

Each Frontiers article is a landmark of the highest quality, thanks to genuinely collaborative interactions between authors and review editors, who include some of the world's best academicians. Research must be certified by peers before entering a stream of knowledge that may eventually reach the public - and shape society; therefore, Frontiers only applies the most rigorous and unbiased reviews.
Frontiers revolutionizes research publishing by freely delivering the most outstanding research, evaluated with no bias from both the academic and social point of view.
By applying the most advanced information technologies, Frontiers is catapulting scholarly publishing into a new generation.

What are Frontiers Research Topics?

Frontiers Research Topics are very popular trademarks of the Frontiers Journals Series: they are collections of at least ten articles, all centered on a particular subject. With their unique mix of varied contributions from Original Research to Review Articles, Frontiers Research Topics unify the most influential researchers, the latest key findings and historical advances in a hot research area! Find out more on how to host your own Frontiers Research Topic or contribute to one as an author by contacting the Frontiers Editorial Office: **researchtopics@frontiersin.org**

IMAGING SYNAPSE STRUCTURE AND FUNCTION

Topic Editors:
George J. Augustine, Lee Kong Chian School of Medicine, Nanyang Technological University, Singapore
Marc Fivaz, Duke-NUS Medical School, Singapore

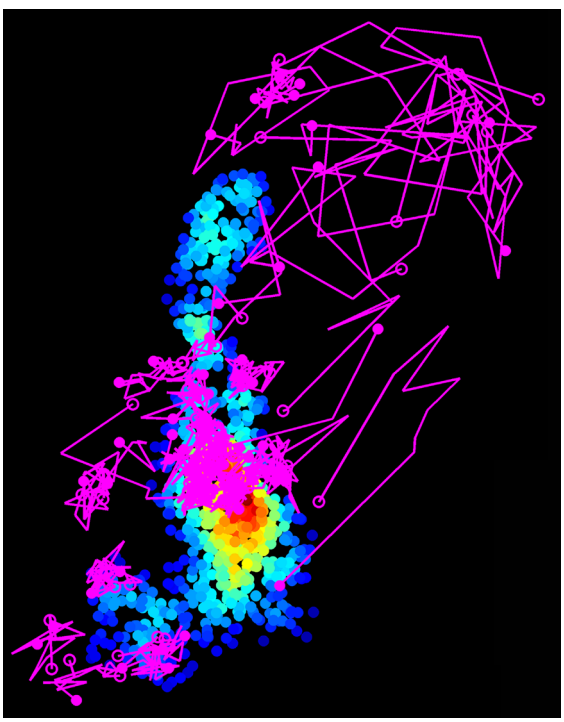

Two complementary super-resolution imaging techniques reveal interactions of single protein molecules with an individual synapse. The scaffold molecule PSD-95 was mapped using live-cell PALM, and the positions of those molecules are plotted color-coded by the density of their neighbors. Trajectories of a probe transmembrane protein were simultaneously measured, using UPAINT technology, and are shown in pink.
Image by Tuo Peter Li and Thomas Blanpied; see article by these authors in this eBook

Development of new imaging technologies in recent years has transformed neuroscience in profound ways. Following on the heels of the revolution based on the Green Fluorescent Protein, refined genetically-encoded fluorescent reporters and genetic targeting strategies now enable optical recording of synaptic transmission in defined neuronal populations at speeds approaching the enviable temporal resolution of electrophysiology. Super-resolution light microscopy

permits observation of synapses and their molecular machinery at sub-diffraction resolution. At the ultrastructural level, automated forms of electron microscopy, improvements in specimen fixation methods, and recent efforts to correlate data from light and electron micrographs now make the reconstruction of functional neural circuits a reality. Finally, the use of optogenetic actuators, such as channelrhodopsins, allows precise temporal and spatial manipulation of neuronal activity and is revealing profound insights into the organization of neural circuits and their roles in behavior.

This research topic highlights recent advances in both light and electron microscopy, with a specific focus on approaches that combine innovations from several different fields to obtain novel information about synapse structure and function. We are confident that this collection of articles - three original research papers, six reviews, one methods paper and one perspective article - will enable neuroscientists to achieve the next generation of experiments aimed at cracking the neural code.

Citation: Augustine, G. J., Fivaz, M., eds. (2017). Imaging Synapse Structure and Function. Lausanne: Frontiers Media. doi: 10.3389/978-2-88945-175-3

Table of Contents

frontiers in Synaptic Neuroscience

EDITORIAL
published: 15 December 2016
doi: 10.3389/fnsyn.2016.00036

Editorial: Imaging Synapse Structure and Function

George J. Augustine[1] *and Marc Fivaz*[2]*

[1] *Lee Kong Chiang School of Medicine, Nanyang Technological University, Singapore, Singapore,* [2] *Program in Neuroscience and Behavioral Disorders, Duke-NUS Medical School, Singapore, Singapore*

Keywords: synapse, optical microscopy, electron microscopy, circuits, genetically-encoded biosensors, optogenetics

Editorial on the Research Topic

Imaging Synapse Structure and Function

These are the glory days for imaging synapse structure and function. Thanks to recent advances in both optical and electron microscopy, it is now possible to image individual synapses with unprecedented spatial and temporal resolution. The parallel development of a wide range of genetically-encoded synaptic reporters enables all-optical recording of synaptic activity in genetically-defined neuronal populations. These engineering breakthroughs allow neuroscientists to interrogate the brain in ways that were inconceivable just a few years ago. The ability to image synaptic structure and activity in large functional circuits is beginning to yield key insights into how the brain stores, processes, and computes information. This research topic consists of eleven articles (methods, primary research papers, and reviews) that provide an overview of the latest developments in synapse imaging. Rather than attempting an exhaustive list of synaptic reporters and microscopy techniques, our collection emphasizes approaches that merge technical advances from diverse areas to extract a rich palette of novel information from individual synapses.

Watanabe presents a method that combines optogenetics and rapid freezing (Flash-and-Freeze) to visualize the synaptic vesicle (SV) cycle at the ultrastructural level with millisecond resolution Watanabe. This revolutionary approach revealed ultra-fast endocytosis of SVs at central synapses and neuromuscular junctions (Watanabe et al., 2013a,b) and promises to uncover many new kinetic aspects of synapse dynamics. Begemann and Galic review recent efforts to image neuronal preparations with both light and electron microscopy, with a series of hybrid techniques referred to as Correlative Light Electron Microscopy (CLEM). Jackson and Burrone describe the first genetically-encoded fluorescent reporter (sypHy-RGECO) that enables concurrent monitoring of calcium dynamics and SV fusion. sypHy-RGECO will undoubtedly be a powerful means of examining calcium triggering of SV exocytosis at the level of individual presynaptic boutons. Using similar probes, Tang et al. show that the mental disease gene DISC1 (Disrupted-In-Schizophrenia-1) accelerates SV exocytosis by facilitating calcium influx through N-type voltage-gated Ca^{2+} channels. Calcium transients at synapses are also shaped by both mobilization and sequestration of calcium by intracellular stores. Kwon et al. report on the latest advances in organelle-specific calcium sensors and review the contribution of the endoplasmic reticulum and mitochondria to calcium dynamics and synaptic transmission/plasticity.

Until recently, one major impediment to imaging of synaptic activity has been our inability to directly measure membrane potential with adequate signal/noise ratio. This is rapidly changing with the recent improvement of a wide range of genetically-encoded voltage indicators (GEVIs) that now are capable of monitoring both single action potentials and even subthreshold synaptic potentials, both *in vitro* and *in vivo* Nakajima et al. Three papers describe recent

OPEN ACCESS

Edited and reviewed by:
Per Jesper Sjöström, McGill University, Canada

***Correspondence:**
Marc Fivaz
marc.fivaz@duke-nus.edu.sg

Received: *19 October 2016*
Accepted: *22 November 2016*
Published: *15 December 2016*

Citation:
Augustine GJ and Fivaz M (2016) Editorial: Imaging Synapse Structure and Function. Front. Synaptic Neurosci. 8:36. doi: 10.3389/fnsyn.2016.00036

advances on the localization, dynamics and function of postsynaptic receptors and scaffolds. Using a combination of single-molecule tracking (uPAINT) and photoactivated localization microscopy (PALM), Li and Blanpied assess the diffusion properties of membrane proteins within the postsynaptic density (PSD). The same authors recently used localization microscopy to demonstrate the existence of transsynaptic nanocolumns that align the neurotransmitter release machinery to postsynaptic receptors (Tang et al., 2016a). Dosemeci et al. review a series of EM studies that reveal the presence of a dense lamina—the "pallium"—just beneath the core layer of the PSD, and discuss how translocation of signaling proteins and scaffolds in and out of the pallium may shape activity-induced changes in dendritic spines. In keeping with the theme of postsynaptic signaling, Dore et al. discuss evidence for metabotropic functions of NMDARs, based on time-resolved FRET and other imaging approaches. Finally, at the level of synaptic circuits, two reviews describe the use of genetically-encoded synaptic labels to trace neural circuits in a variety of different model systems, ranging from *C. elegans* to mammals (Hong and Park; Lee et al.).

Overall, we hope that the fine collection of papers contained within this research topic highlights a useful synapse imaging toolkit for the neuroscience community. The next big challenge in brain imaging will be to scale up these synaptic measurements to large ensembles of neurons to comprehend how circuits compute. This will require synaptic reporters that operate in a synaptically-relevant time scale (milliseconds), along with improved genetic targeting strategies, further advances in automated high-speed microscopy, and refined bioinformatics tools for analysis of the resulting large datasets.

AUTHOR CONTRIBUTIONS

All authors listed, have made substantial, direct and intellectual contribution to the work, and approved it for publication.

FUNDING

This work was supported by Singapore Ministry of Education grants MOE2015-T1-001-069 and MOE2015-T2-2-095 to GA and grant MOE2013-T2-1-053 to MF.

REFERENCES

Tang, A. H., Chen, H., Li, T. P., Metzbower, S. R., Macgillavry, H. D., and Blanpied, T. A. (2016a). A trans-synaptic nanocolumn aligns neurotransmitter release to receptors. *Nature* 536, 210–214. doi: 10.1038/nature19058

Watanabe, S., Liu, Q., Davis, M. W., Hollopeter, G., Thomas, N., Jorgensen, N. B., et al. (2013a). Ultrafast endocytosis at *Caenorhabditis elegans* neuromuscular junctions. *Elife* 2:e00723. doi: 10.7554/eLife.00723

Watanabe, S., Rost, B. R., Camacho-Perez, M., Davis, M. W., Söhl-Kielczynski, B., Rosenmund, C., et al. (2013b). Ultrafast endocytosis at mouse hippocampal synapses. *Nature* 504, 242–247. doi: 10.1038/nature12809

Conflict of Interest Statement: The authors declare that the research was conducted in the absence of any commercial or financial relationships that could be construed as a potential conflict of interest.

frontiers in Synaptic Neuroscience

ORIGINAL RESEARCH
published: 14 June 2016
doi: 10.3389/fnsyn.2016.00015

Stimulation of Synaptic Vesicle Exocytosis by the Mental Disease Gene *DISC1* is Mediated by N-Type Voltage-Gated Calcium Channels

*Willcyn Tang[1†], Jervis Vermal Thevathasan[1†], Qingshu Lin[2], Kim Buay Lim[1], Keisuke Kuroda[3], Kozo Kaibuchi[3], Marcel Bilger[4], Tuck Wah Soong[2] and Marc Fivaz[1,2]**

[1] DUKE-NUS Medical School, Program in Neuroscience and Behavioral Disorders, Singapore, Singapore, [2] Department of Physiology, Yong Loo Lin School of Medicine, National University of Singapore, Singapore, Singapore, [3] Department of Cell Pharmacology, Nagoya University Graduate School of Medicine, Nagoya, Japan , [4] DUKE-NUS Medical School, Program in Health Services and Systems Research, Singapore, Singapore

Lesions and mutations of the DISC1 (Disrupted-in-schizophrenia-1) gene have been linked to major depression, schizophrenia, bipolar disorder and autism, but the influence of DISC1 on synaptic transmission remains poorly understood. Using two independent genetic approaches—RNAi and a DISC1 KO mouse—we examined the impact of DISC1 on the synaptic vesicle (SV) cycle by population imaging of the synaptic tracer vGpH in hippocampal neurons. DISC1 loss-of-function resulted in a marked decrease in SV exocytic rates during neuronal stimulation and was associated with reduced Ca^{2+} transients at nerve terminals. Impaired SV release was efficiently rescued by elevation of extracellular Ca^{2+}, hinting at a link between DISC1 and voltage-gated Ca^{2+} channels. Accordingly, blockade of N-type Cav2.2 channels mimics and occludes the effect of DISC1 inactivation on SV exocytosis, and overexpression of DISC1 in a heterologous system increases Cav2.2 currents. Collectively, these results show that DISC1-dependent enhancement of SV exocytosis is mediated by Cav2.2 and point to aberrant glutamate release as a probable endophenotype of major psychiatric disorders.

Keywords: DISC1, hippocampus, glutamate, psychiatric disorders, schizophrenia, neurotransmitter, synaptic vesicle release

OPEN ACCESS

Edited by:
Stéphane Martin, IPMC CNRS UMR7275 - University of Nice Sophia antipolis, France

Reviewed by:
Timothy A. Ryan, Weill Medical College of Cornell University, USA
Yann Humeau, Centre National de la Recherche Scientifique (CNRS), France

***Correspondence:**
Marc Fivaz
marc.fivaz@duke-nus.edu.sg

†These authors have contributed equally to this work.

***Received:** 01 February 2016*
***Accepted:** 31 May 2016*
***Published:** 14 June 2016*

Citation:
Tang W, Thevathasan JV, Lin Q, Lim KB, Kuroda K, Kaibuchi K, Bilger M, Soong TW and Fivaz M (2016) Stimulation of Synaptic Vesicle Exocytosis by the Mental Disease Gene DISC1 is Mediated by N-Type Voltage-Gated Calcium Channels. Front. Synaptic Neurosci. 8:15. doi: 10.3389/fnsyn.2016.00015

INTRODUCTION

Genome-wide association studies and exome sequencing efforts have led to the identification of hundreds of variants associated with psychiatric disorders (International Schizophrenia et al., 2009; Moskvina et al., 2009; Glessner et al., 2010; Fromer et al., 2014; Schizophrenia Working Group of the Psychiatric Genomics, 2014), confirming the complex polygenic nature of these diseases. These genomic data also revealed a significant overlap in genes or gene networks associated with distinct mental illnesses (Cross-Disorder Group of the Psychiatric Genomics et al., 2013), suggesting a common genetic and perhaps circuitry basis for major psychiatric disorders. However, the synaptic and circuitry defects underlying these disorders remain poorly defined, hindering the development of therapeutic solutions.

DISC1 is the prototypical example of a gene associated with several major psychiatric disorders. It was discovered in a Scottish family at the site of a balanced chromosomal translocation that strongly segregates with major depression, schizophrenia and bipolar disorder (St Clair et al., 1990; Millar et al., 2000, 2001). The high penetrance (∼70%) of this translocation for mental illness supports a causal link between this genetic lesion and major psychiatric conditions (Chubb et al., 2008). DISC1 variants (haplotypes, single nucleotide polymorphisms and copy number variations) have since been independently associated with depression, schizophrenia, bipolar disorders and autism spectrum disorders (Ekelund et al., 2001, 2004; Sachs et al., 2005; Kilpinen et al., 2008). Thus, DISC1 is a major susceptibility factor for mental illness and a relevant genetic entry point to identify core endophenotypes implicated in neuropsychiatric disorders.

The translocation breakpoint in this Scottish family is located in the C-terminal portion of DISC1 and results in overall reduced expression of the full-length transcript and protein (Millar et al., 2005), suggesting that haploinsufficiency is the main mechanism by which this chromosomal alteration confers risk to disease. Alternatively, it has been proposed that a C-terminal truncated form of DISC1 is expressed from the translocated allele and may be pathogenic (Hikida et al., 2007; Pletnikov et al., 2008), although expression of the truncated DISC1 protein in translocation carriers remains to be demonstrated. Consistent with a disease mechanism based on DISC1 loss-of-function, DISC1 expression is also attenuated in human induced pluripotent stem (iPS) cells derived from members of a family with a DISC1 frame-shift mutation that co-segregates with major psychiatric disorders (Wen et al., 2014).

The identification of a large DISC1 interactome consisting of proteins belonging to different ontologic families suggests broad functions of DISC1 in nerve cells. Accordingly, DISC1 has been implicated in multiple aspects of neuronal and brain development, including neurogenesis (Clapcote et al., 2007; Shen et al., 2008; Mao et al., 2009; Singh et al., 2010; Lee et al., 2011), neuronal migration (Kamiya et al., 2005; Duan et al., 2007; Kubo et al., 2010; Steinecke et al., 2012) and maturation (Duan et al., 2007; Shinoda et al., 2007; Niwa et al., 2010). Even though DISC1 interacts with several signaling proteins known to regulate synaptic functions, relatively little is known about functions of DISC1 at the synapse. In particular, the impact of DISC1 on neurotransmitter release remains largely unexplored, despite the fact that aberrant dopamine and glutamate neurotransmission is a probable cause of schizophrenia and other mood disorders (Howes et al., 2015).

Given the preferential expression of DISC1 in the hippocampus and the involvement of this brain structure in cognition and psychiatric disorders (Chubb et al., 2008), we set out to determine the impact of DISC1 on synaptic vesicle (SV) cycling in hippocampal neurons. We used two independent genetic strategies to alter DISC1 expression—RNAi and a DISC1 KO mouse—and imaged SV cycling and Ca^{2+} dynamics in large synapse populations. We show that DISC1 elevates synaptic Ca^{2+} signals and boosts SV exocytosis at glutamatergic terminals. Our results further indicate that N-type voltage-gated Ca^{2+} channels (VGCCs) mediate the stimulatory effect of DISC1 on SV release. These findings identify a central role of DISC1 in neurotransmitter release and provide new insights on the biological basis of synaptic dysfunction in major psychiatric disorders.

MATERIALS AND METHODS

DNA, shRNA Constructs, Lentiviruses and Antibodies

The pCAGGs vGlut1-pHluorin (vGpH) and pCAGGs Synaptophysin-GCaMP3 (SyGC3) constructs were gifts from R. Edwards (UCSF; Voglmaier et al., 2006) and S. Voglmaier (UCSF; Li et al., 2011). The pFUGW (Addgene #14883) shRNA-expressing lentiviral vector was modified to express mCherry (pFUmChW). The shRNA targeting sequences are as follows: (1) Scramble 5′GGAGCAGACGCTGAATTAC3′ (Kamiya et al., 2005); (2) DISC1-E 5′GGCTACATGAGAAGCACAG3′ (exon 2; Duan et al., 2007); and (3) DISC1-A 5′GGAAGG GCTAGAGATGTTC3′ (exon 9) designed with Block-it shRNA from Invitrogen. pFUGW scramble shRNA was a gift from A. Sawa (Johns Hopkins). The DISC1 shRNAs constructs were cloned by introducing double-stranded DNA oligos into lentiviral vector pll3.7 (Addgene #11795) using the HpaI and XhoI sites. DNA fragments containing the U6 promoter and shRNAs were then PCR amplified and cloned into pFUmChW using the PacI site. The human DISC1 gene L variant (NCBI Refseq NM018662.2) was PCR amplified from pCMV6-XL5 DISC1-tGFP (Origene) and cloned into pIRES2-DsRed-Express (Clontech) using NheI and SmaI sites. All constructs were sequenced before use. Lentiviral particles expressing pFUmChW shRNAs were prepared as described in Tiscornia et al. (2006). The DNA constructs used for whole-cell patch clamp recording are as follows: Cav2.1 (generated in T. W. Soong's lab), Cav2.2 (Addgene #26568), GFP-β_{2a} and $\alpha_2\delta_1$ (kindly provided by T. Snutch, UBC). The rabbit polyclonal Abs against Cav2.1 (#ACC-001) and Cav2.2 (#ACC-002) were from Alomone Labs. The polyclonal Ab against the C-terminus of mouse DISC1 was previously described (Kuroda et al., 2011). The polyclonal Ab against human DISC1 (ab59017) and monoclonal Ab against bassoon were from Abcam (ab82958).

Mouse Lines, Primary Neuron Cultures and Transfection Protocols

DISC1 (Δ2–3) mice (C57BL/6JJmsSlc) have been described before Kuroda et al. (2011). Heterozygous $DISC1^{wt/\Delta 2-3}$ mice were crossed to each other to obtain $DISC1^{wt/wt}$ and $DISC1^{\Delta 2-3/\Delta 2-3}$ lines from which hippocampal neurons were prepared from E17/E18 embryos, according to published procedures using papain (Worthington) digestion (Huettner and Baughman, 1986). Primary rat hippocampal neurons were prepared from E18 embryos according to Kaech and

Banker (2006) and as previously described in Garcia-Alvarez et al. (2015). For live-cell imaging and immunocytochemistry experiments, neurons were grown on poly-L-Lysine coated glass coverslips, on top of a glial feeder according to the Banker Protocol (Kaech and Banker, 2006). For biochemical analysis, cells were seeded on poly-L-Lysine coated 6-well culture dishes. Unless otherwise stated, neurons were cultured for 14–16 days. The vGpH and SyGC3 constructs were electroporated in freshly-dissociated neurons using the Nucleofector kit (Amaxa Biosystems, Lonza). Lentiviral particles expressing shRNAs were added on DIV2, at a MOI (multiplicity of infection) of 1–3. All animal procedures were approved by the SingHealth Institutional Animal Care and Use Committee (IACUC) of Singapore.

Live-Cell Confocal Imaging and Immunofluorescence

Time-lapse confocal imaging was performed on an inverted Eclipse TE2000-E microscope (Nikon, USA), mounted with a spinning-disk confocal scan head (CSU-10; Yokogawa, Japan), and equipped with a temperature controlled (36.5°C) stage and an autofocusing system (PFS; Nikon). Images were acquired with an Orca-Flash 4.0 CCD camera (Hamamatsu Photonics, Japan) controlled by MetaMorph 7.8.6 (Molecular Devices, CA, USA) at 0.5 Hz or 20 Hz. Samples were imaged using a 60× (NA 1.4) objective in Tyrode's buffer (150 mM NaCl, 2.5 mM KCl, 1 mM $CaCl_2$, 1 mM $MgCl_2$, 6 mM glucose, 25 mM HEPES, pH 7.4) supplemented with 25 μM 6-cyano-7-nitroquinoxaline-2,3-dione/CNQX (Tocris Bioscience) and 50 μM D,L-2-amino-5-phosphonovaleric acid/AP5 (Tocris Bioscience). Coverslips were mounted in an RC-21BRFS chamber (Warner Instruments, USA) equipped with platinum wire electrodes. Field stimulation was induced by a square pulse stimulator (Grass Technologies, USA) and monitored by an oscilloscope (TDS210, Tektronix, USA). Trains of action potentials (APs) were generated by applying 20 V pulses (1 ms duration) at 10 or 20 Hz. Our typical stimulation paradigm for vGpH measurements involved two consecutive trains of 300 APs at 10 Hz, separated by ∼5 min to allow synapses to recover. vGpH responses between the first and second stimulation were highly reproducible (data not shown). For measuring SV exocytic rates, the second stimulation was preceded (30 s earlier) by the addition of Bafilomycin A1 (Baf; AG scientific, USA) 0.5 μM. To normalize for total expression of vGpH in each individual bouton, 50 mM NH_4Cl was added at the end of the time series. For SyGC3 measurements, Ca^{2+} signals were normalized by adding 10 μM or 50 μM (for **Figure 4G**) ionomycin (Sigma-Aldrich) at the end of the stimulation protocol. ω-agatoxin TK125 nM (Tocris Bioscience) and ω-conotoxin GVIA 125 nM (Alomone Labs) were used for experiment involving inhibition of P/Q-type Ca^{2+} channels and N-type Ca^{2+} channels activity, respectively. For immunofluorescence studies, neurons grown on glass coverslips were fixed in 4% paraformaldehyde with 4% sucrose in PBS and permeabilized with 100 ng/ml Digitonin (Sigma-Aldrich). Cells were then incubated with 5% goat serum to block non-specific binding sites and stained with the primary and Alexa Fluor-conjugated secondary antibodies (Life Technologies). Coverslips were then mounted on glass slides and imaged with an inverted laser scanning confocal microscope (LSM710, Zeiss) with a Plan-Apochromat 63× (NA = 1.40) objective.

Image Analysis

For automated analysis of vGpH responses, we wrote a Matlab script that segments responsive boutons based on the difference between peak vGpH intensity during the first stimulation and baseline intensity prior to stimulation ($\Delta F = F_{\text{peak}} - F_{\text{baseline}}$). An intensity threshold for ΔF was selected to resolve individual boutons and exclude those with ΔF below 5%. The same threshold was used for all conditions in one independent experiment (i.e., one neuron preparation with control vs. DISC1-depleted conditions). This threshold value was minimally adjusted (less than 10% change) across all independent experiments described in this article. Binarized boutons were then slightly dilated (**Figure 1B**) to ensure that vGpH fluorescence was captured in its totality even after minor lateral movement or change in shape. Time series with minor x–y drifts (originating from the stage) were re-aligned using a script previously described (Thevathasan et al., 2013). Segmented boutons were then size gated, with gating parameters kept constant across all experiments. vGpH fluorescence intensity was then extracted in each segmented bouton across the time series and divided by the signal after NH_4Cl to normalize for vGpH expression (**Figure 1C**). This segmentation strategy ensures that the same boutons are analyzed during the two consecutive AP trains. vGpH traces with significant baseline drifts between the first and second stimulation or after Baf application were excluded. A similar segmentation approach was used to analyze SyGC3 Ca^{2+} signals. SV exocytic rates were obtained by measuring the slope of the vGpH rise during the second stimulation (in the presence of Baf). The first six time points (during stimulation) were used for linear regression analysis. To measure endocytic rates, the vGpH trace during the first stimulation was subtracted from that obtained during the second stimulation. The resulting trace is a measure of endocytosis (**Figure 1D**). Endocytic rates were measured by linear fitting of six time points chosen after stimulation onset when endocytosis kicks in. Presynaptic localization, abundance and density of Cav2.1 or Cav2.2 were analyzed with a modified version of a Matlab script described previously (Poon et al., 2014). All Matlab scripts are available upon request.

Immunoblotting

Cultured primary neurons or HEK293T cells were washed with ice-cold PBS and lysed with RIPA buffer (10 mM Tris-HCl pH = 7.2, 150 mM NaCl, 1% TritonX-100, 0.1% SDS, 5 mM EDTA, 0.25% Na-deoxycholate) supplemented with Complete protease inhibitor and PhosphoStop phosphatase inhibitor (Roche). For analysis of hippocampal tissue, the

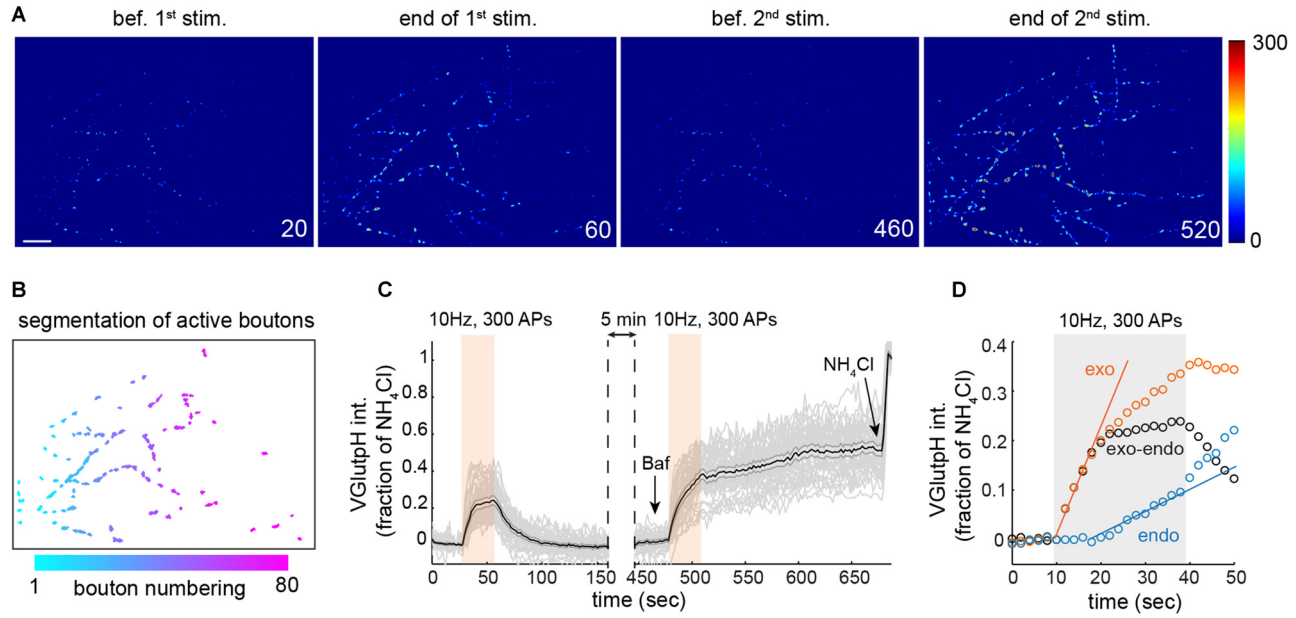

FIGURE 1 | Extracting synaptic vesicle (SV) exo- and endocytic rates by population imaging of vGpH. (A) Snapshots of rat hippocampal neurons (DIV 15) expressing vGpH and stimulated with two consecutive trains of action potentials (APs; 300 APs, 10 Hz) before (first two images) and after (last two images) addition of Bafilomycin (Baf). Time is in sec. scale bar: 10 μm. **(B)** Automated segmentation of active boutons based on vGpH responses after the first stimulation. **(C)** Individual (gray) and average vGpH (black) traces derived from segmented boutons. Shaded errorbar indicates 95% confidence interval. **(D)** Measurement of exo- and endocytic rates based on vGpH responses before and after Baf (see text).

hippocampi from P10 mice were harvested and homogenized in RIPA buffer using a Dounce tissue homogenizer. Lysates were cleared by centrifugation and boiled in Laemmli sample buffer. Equal amount of total proteins were loaded. Samples were then analyzed by SDS-PAGE, transferred onto nitrocellulose membranes, probed with appropriate primary and HRP-labeled secondary antibodies and revealed by enhanced chemiluminescence.

Whole-Cell Patch Clamp Recordings of Cav2.1 and Cav2.2 Currents

Cav2.1 or Cav2.2, the auxiliary subunits (GFP-β_{2a} and $\alpha_2\delta_1$) and DISC1 were transiently transfected in HEK 293 cells using the calcium phosphate method (Huang et al., 2012). Whole-cell patch-clamp recordings were performed within 36–72 h after transfection. The external solution contained (in mM) 10 HEPES, 140 TEA-$MeSO_3$ and 5 $BaCl_2$ (pH 7.4, 300–310 mOsm). The glass pipette solution was backfilled with pipette solution (in mM) 10 HEPES, 5 CsCl, 138 Cs-$MeSO_3$, 0.5 EGTA, 1 $MgCl_2$, 2 mg/ml MgATP (pH 7.3, 290–300 mOsm). HEK 293 cells were held at −90 mV using the Axopatch 700B amplifier (Axon Instruments). The series resistance for all recordings was less than 5 MΩ; 70–80% compensation on serial resistance and cell membrane capacitance were applied. A P/4 protocol was used to subtract leakage current. All recordings were obtained with an Axon Digidata 1440A data acquisition system, sampled at 5–50 kHz and low pass-filtered at 1 kHz or 6 kHz. The I-V curves were obtained from 10 mV voltage-steps ranging from −50 to 40 mV and fitted with a modified Boltzmann equation:

$$I = G_{\max}(E_{\text{rev}} - V)/\left(1 + e^{\frac{V_{1/2\text{act}} - V}{k_{\text{act}}}}\right)$$

where, I = current density (in pA/pF), $G_{\max}$ = maximum conductance (in nS/pF), E_{rev} = reversal potential, V = measured potential, $V_{1/2\text{act}}$ = midpoint voltage for current activation, and k_{act} = the slope factor.

We used a tail protocol to measure current density; cells were depolarized using 10 mV voltage steps, from −60 to 60 mV. Following depolarization, tail currents were evoked with a 10 ms pulse at −50 mV. The data were fitted with single Boltzmann equation:

$$I = I_{\min} + (I_{\max} - I_{\min})/\left(1 + e^{\frac{V_{1/2\text{inact}} - V}{k_{\text{inact}}}}\right)$$

where, $I_{\max}$ and $I_{\min}$ = maximal and minimal current respectively, $V_{1/2\text{inact}}$ = the half-maximal voltage for current inactivation, k_{inact} = slope of inactivation curve.

Statistics

The experimental design of this study implies that data collected at individual synaptic terminals are clustered according to neuron preparations and imaged fields. Galbraith et al. (2010) demonstrated that such clustering can adversely affect statistical inference when not accounted for. In order to

probe for clustering effects (i.e., intra-field correlations), we tested whether bouton responses significantly vary from field to field. For this, we conducted Wald tests of the null hypothesis of no difference in mean outcome across fields within each condition, which revealed (p-value < 0.0001) strong intra-field correlation. To account for these correlations, we performed our statistical analysis in the framework of linear mixed models (Laird and Ware, 1982) with normally-distributed random field effects and preparation fixed effects. In experiments involving one genetically-modified condition and one control group, we tested the null hypothesis of no difference between the mean outcome of the groups via 2-sample t-tests. In experiments involving two genetically-modified conditions and one control group, we tested the null hypothesis of no difference between the mean outcome of each group and the control group jointly using Wald tests. All tests were performed at the 5% level of statistical significance and carried out using the statistical software Stata version 13.2. Because our statistical approach (linear mixed model) is not a standard practice when analyzing synaptic properties, we compared the p-values obtained with our method with those measured by the more common field averaging approach, where the information of a field is collapsed to a single independent observation by taking the mean of bouton responses. Both methods are valid and gave comparable results (**Supplementary Table T1**), although the field averaging approach is less statistically efficient as it diminishes the information that can be obtained from the data by reducing individual measurements in a field to one observation (Galbraith et al., 2010).

RESULTS

DISC1 Loss-of-Function Slows Down SV Cycling

We opted for an imaging approach based on the synaptic tracer vGpH to explore the impact of DISC1 on the SV cycle. vGpH consists of the pH-sensitive GFP variant pHluorin (Miesenbock et al., 1998) fused to the SV-resident glutamate transporter vGlut1. pHluorin, which faces the acidic lumen of SVs, undergoes a ∼20-fold increase in fluorescence intensity when exposed to the neutral pH of the extracellular milieu after membrane fusion. (Sankaranarayanan et al., 2000). Following glutamate discharge and vGpH re-uptake, SVs are rapidly re-acidified and vGpH fluorescence is quenched. This property has made vGpH a valuable tool to monitor both exo- and endocytosis of SVs at single synapses.

Due to the inherent variability in the properties of individual synaptic boutons (Ariel et al., 2013) we measured SV cycling in large synapse populations. For this, we developed an image analysis algorithm that identifies all responding boutons in a given field (**Figures 1A,B**), and imaged 16–18 fields from at six independent rat hippocampal neuron cultures, yielding close to a thousand synaptic boutons for each condition. We employed this algorithm to monitor SV cycling in response to a stimulation paradigm that consists of two consecutive trains of APs (Fernandez-Alfonso and Ryan, 2004; Burrone et al., 2006). The amplitude of the first vGpH transient is governed by the relative rates of SV exo- and endocytosis during stimulation (**Figure 1C**). To separate the contributions of exo- and endocytosis, we blocked SV re-acidification with the vacuolar H^+ ATPase inhibitor Bafilomycin (Baf) during the second stimulation, which allows selective measurement of SV exocytosis (**Figure 1C**). To account for cell-to-cell variation in vGpH expression, we normalized each trace based on the vGpH signal measured after NH_4Cl addition (**Figure 1C**). The endocytic component of SV cycling was then computed by subtracting the first vGpH transient from the vGpH response after Baf treatment (**Figure 1D**). Synaptic traces with baseline drifts between the first and second stimulation or after Baf addition were excluded from the analysis (see "Materials and Methods" Section). Exocytosis largely dominates at the onset of stimulation, while endocytosis kicks in towards the end of the AP train. Exo- and endocytic rates were finally obtained by linear fitting of the exo- and endo traces (**Figure 1D**). Exocytic rates are about three times higher than endocytic rates under this stimulation protocol. To evaluate the variability of bouton responses across fields and neuron preparations, we compiled exocytic rates from six independent experiments (**Supplementary Figure S1**). Statistical analysis of these responses revealed substantial field to field variation (see "Materials and Methods" Section), implying that the information collected from each bouton does not constitute an independent measurement. To compare synaptic responses in different fields and conditions we used a statistical approach that accounts for correlations within fields and variations in neuron preparations (see "Materials and Methods" Section and **Supplementary Table T1**).

We then silenced the DISC1 gene using a published shRNA sequence (shRNA-E), targeting exon 2 (Duan et al., 2007) and a new shRNA sequence (shRNA-A) targeting exon 9. These two shRNAs target regions of the *DISC1* gene that are fully conserved in rodents and are thus expected to silence rat and mouse *DISC1* with the same efficiency. To probe the effect of these shRNAs on DISC1 protein levels, we used an antibody raised against the C-terminus of mouse DISC1, which has previously been validated in a *DISC1* KO mouse (Kuroda et al., 2011). In our hands, this antibody poorly reacts with rat DISC1 (not shown). In mouse hippocampal neurons, however, it detects one major protein at ∼100 kDa corresponding to the predicted full length DISC1 (Kuroda et al., 2011) and which is substantially reduced in both shRNA-E and -A transduced cells (**Figure 2A**).

Next, we probed the impact of these shRNAs on the SV cycle in rat hippocampal neurons. We initially chose to work with rat, rather than mouse neurons, because we can harvest substantially more cells from a rat embryonic litter. vGpH signals in shRNA-E and -A expressing neurons display a slower rise and lower amplitude during the first and second stimulation, relative to control cells expressing a scramble shRNA (**Figure 2B**). Analysis of exocytosis shows

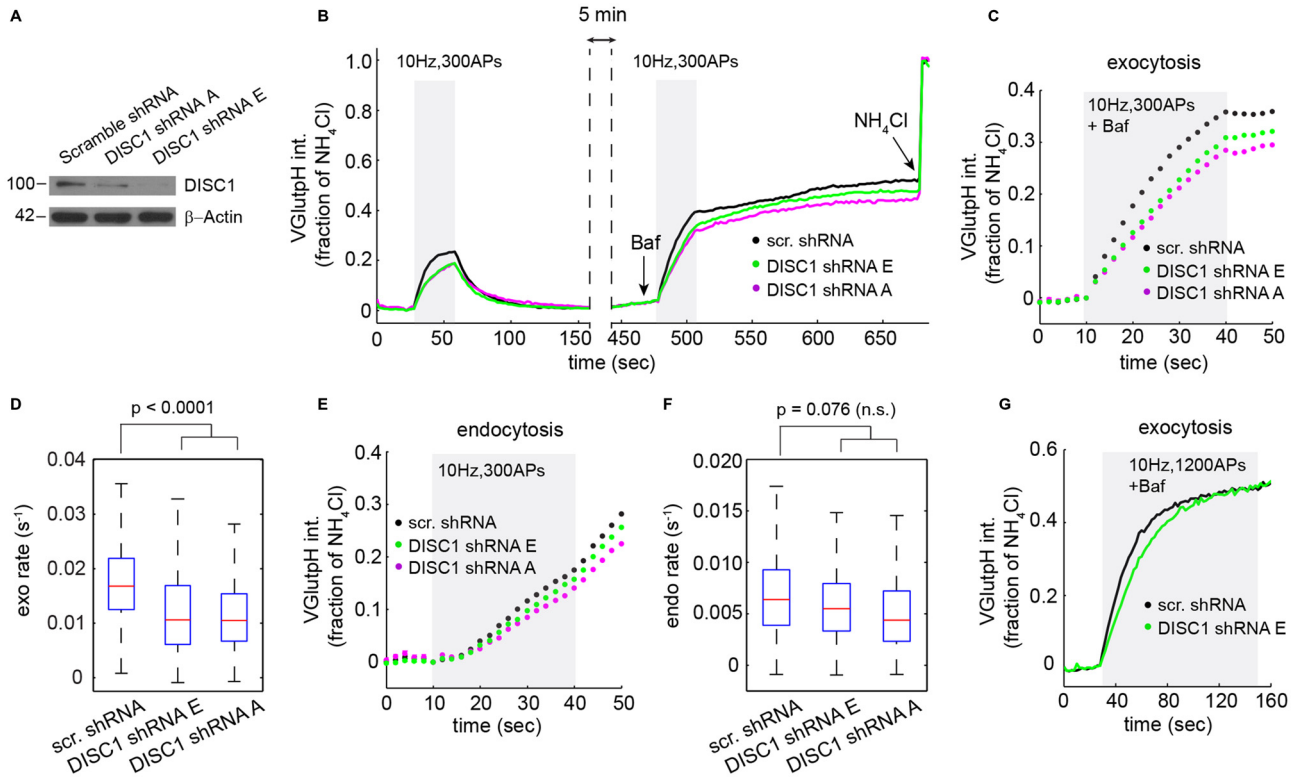

FIGURE 2 | DISC1 silencing by RNAi slows down SV exocytosis. (A) Immunoblot analysis of DISC1 in mouse hippocampal neurons (DIV 8) transduced with scramble, DISC1-A and DISC1-E shRNAs. **(B)** Average vGpH traces derived from neurons expressing scr (1204 boutons, 18 fields), -E (960 boutons, 18 fields) and -A (924 boutons, 16 fields) shRNAs from six independent experiments. **(C,D)** Analysis of SV exocytosis after Baf treatment. **(C)** Exocytic profiles of neurons expressing the indicated shRNAs. **(D)** Boxplot of exocytic rates. **(E,F)** Analysis of SV endocytosis. **(E)** Endocytic profiles. **(F)** Boxplot of endocytic rates. **(G)** Exocytic profile of cells expressing the indicated shRNAs in response to a stimulation (1200 APs, 10 Hz) that depletes the total releasable pool.

substantial synapse-to-synapse variation in all conditions, but reveals a marked decrease in exocytic rates (**Figures 2C,D**) and amplitudes (**Figure 2C**) in both shRNA-E and -A expressing neurons. DISC1 silencing also resulted in slightly slower SV endocytosis, although this effect did not reach statistical significance (**Figures 2E,F**).

Reduced amplitude of the exocytic response prompted us to test whether DISC1 also regulates the size of the total releasable pool. For this, we applied a stimulus strong enough (1200 APs at 10 Hz) to maximally deplete releasable SVs from presynaptic terminals (Ariel and Ryan, 2010). Under this stimulation regime, vGpH responses reached the same plateau in DISC1-silenced and control neurons, albeit with different kinetics, arguing against an effect on the total releasable pool but confirming the stimulatory function of DISC1 in SV exocytosis (**Figure 2G**).

To rule out the possibility of RNAi off-target effects—shRNA-E has recently been suggested to inhibit neuron migration in the developing cortex independently of DISC1 (Tsuboi et al., 2015)—we examined SV cycling in a *DISC1* KO mouse that lacks exons 2 and 3 of the *DISC1* gene (Kuroda et al., 2011). Homozygous $DISC1^{\Delta 2-3/\Delta 2-3}$ mice show no detectable levels of the major isoform of DISC1 (**Figure 3A**). Hippocampal neurons derived from $DISC1^{\Delta 2-3/\Delta 2-3}$ mice display SV cycling defects that are remarkably similar to these observed with RNAi. The rates and amplitudes of exocytic responses were substantially reduced relative to wt cells (**Figures 3B–D**), while endocytic rates were marginally, but not significantly diminished (**Figures 3E,F**). Together, these results show that both genetic ablation and RNAi knockdown of DISC1 selectively disrupts SV exocytosis at glutamatergic synapses with no detectable impact on the total releasable pool.

DISC1 Stimulates Ca^{2+} Influx and Regulates Cav2.2-Dependent SV Release

Because SV exocytosis is initiated by Ca^{2+} influx through VGCCs, we measured evoked Ca^{2+} transients at presynaptic terminals using the SV-targeted Ca^{2+} sensor SyGC3 (Li et al., 2011). Ca^{2+} signals evoked by 300 APs (10 Hz) or 200 APs (20 Hz) show a rapid rise and partial decay during the stimulus (**Figures 4A,B,D,E**), as observed by others (Li et al., 2011). These Ca^{2+} transients were significantly reduced in shRNA-E and -A expressing neurons, under the same stimulation conditions used for vGpH measurements (**Figures 4A,C**), or in response to a higher frequency stimulus (**Figure 4B**). Similarly,

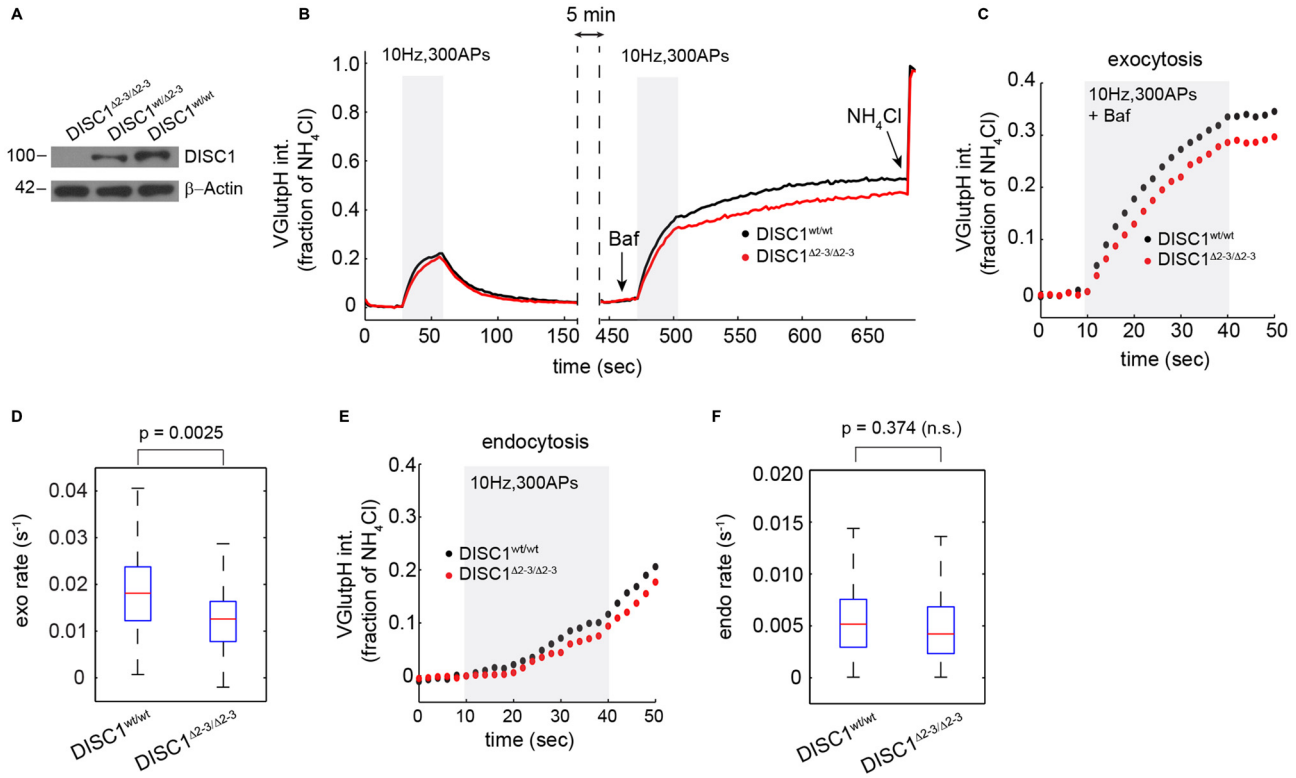

FIGURE 3 | Attenuated SV release in hippocampal neurons from DISC1$^{\Delta 2\text{-}3/\Delta 2\text{-}3}$ mice. (A) Immunoblot analysis of DISC1 in hippocampal lysates prepared from P10 *DISC1*$^{\Delta 2-3/\Delta 2-3}$, *DISC1*$^{wt/\Delta\ 2-3}$ and *DISC1*$^{wt/wt}$ mice, confirming the ablation of full-length DISC1 (~100 kD). **(B)** Average vGpH traces in *DISC1*$^{wt/wt}$ (575 boutons, 7 fields) and *DISC1*$^{\Delta 2-3/\Delta 2-3}$ (682 boutons, 9 fields) neurons in response to two consecutive trains of APs and obtained from two independent experiments. **(C,D)** Analysis of SV exocytosis from vGpH responses after Baf. Average kinetics **(C)** and rates **(D)** of vGpH exocytic responses. **(E,F)** Analysis of SV endocytosis. Average kinetics **(E)** and rates **(F)** of vGpH endocytic responses.

DISC1$^{\Delta 2-3/\Delta 2-3}$ neurons show lowered Ca^{2+} transients compared to wt cells (**Figures 4D–F**). We were concerned that, under such prolonged stimulations, Ca^{2+} concentration in terminals might reach levels that partially saturate SyGC3. Ca^{2+} signals were therefore also examined in response to shorter stimulations (20 APs, 20 Hz) under conditions well below SyGC3 saturation (Tian et al., 2009; Akerboom et al., 2012). A clear decrease in the amplitude of Ca^{2+} transients was also observed in DISC1-silenced neurons under this stimulation regime (**Figure 4G**). Together, these Ca^{2+} imaging data hint at a Ca^{2+} influx defect in DISC1-inactivated cells, although abnormal clearance of Ca^{2+} from the presynaptic terminal could also be involved (see "Discussion" Section).

To determine whether reduced Ca^{2+} influx is the primary cause of SV cycling defects, we attempted to rescue SV exocytosis in DISC1-silenced neurons by elevating extracellular Ca^{2+} concentration. Shifting extracellular Ca^{2+} concentration from 2 to 4 mM increases AP-induced Ca^{2+} entry (Ariel and Ryan, 2010) and restored the vGpH response (**Figure 4H**), in line with a role of DISC1 in facilitating Ca^{2+} influx.

At central synapses, the P/Q-type (Cav2.1) and N-type (Cav2.2) Ca^{2+} channels are the main sources of Ca^{2+} for initiation of SV exocytosis (Catterall et al., 2013). We used channel-specific toxins to determine the contribution of each subtype to SV release in hippocampal neurons. ω-Conotoxin GVIA (an N-type blocker) reduced SV exocytic rates by 73 ± 5% (**Figures 5A,B**), while ω-Agatoxin TK (a P/Q-type blocker) resulted in a 42 ± 3% decrease in SV exocytic rates (**Figures 5C,D**), in a good agreement with a recent study (Ariel et al., 2013). Note that in these experiments, exocytic rates were approximated by measuring the initial slope of the vGpH response in the absence of Baf (see **Figure 1D**). Importantly, blockade of Cav2.2 almost completely occluded the effect of DISC1 silencing on SV exocytosis (**Figures 5A,B,E**). Blockade of Cav2.1, on the other hand, slightly increased the inhibitory impact of DISC1 knockdown on SV release rates (**Figures 5C–E**). We conclude from these results that DISC1 selectively stimulates Cav2.2-dependent SV release at hippocampal synapses.

We then asked whether DISC1 regulates Cav2.2 activity by controlling its presynaptic localization and/or abundance. Co-localization studies of endogenous Cav2.2 with the active zone marker bassoon revealed extensive presence of Cav2.2 in synaptic boutons, both in control and DISC1-silenced neurons (**Supplementary Figures S2A–C**). We found no significant difference between these two groups in the fraction of boutons

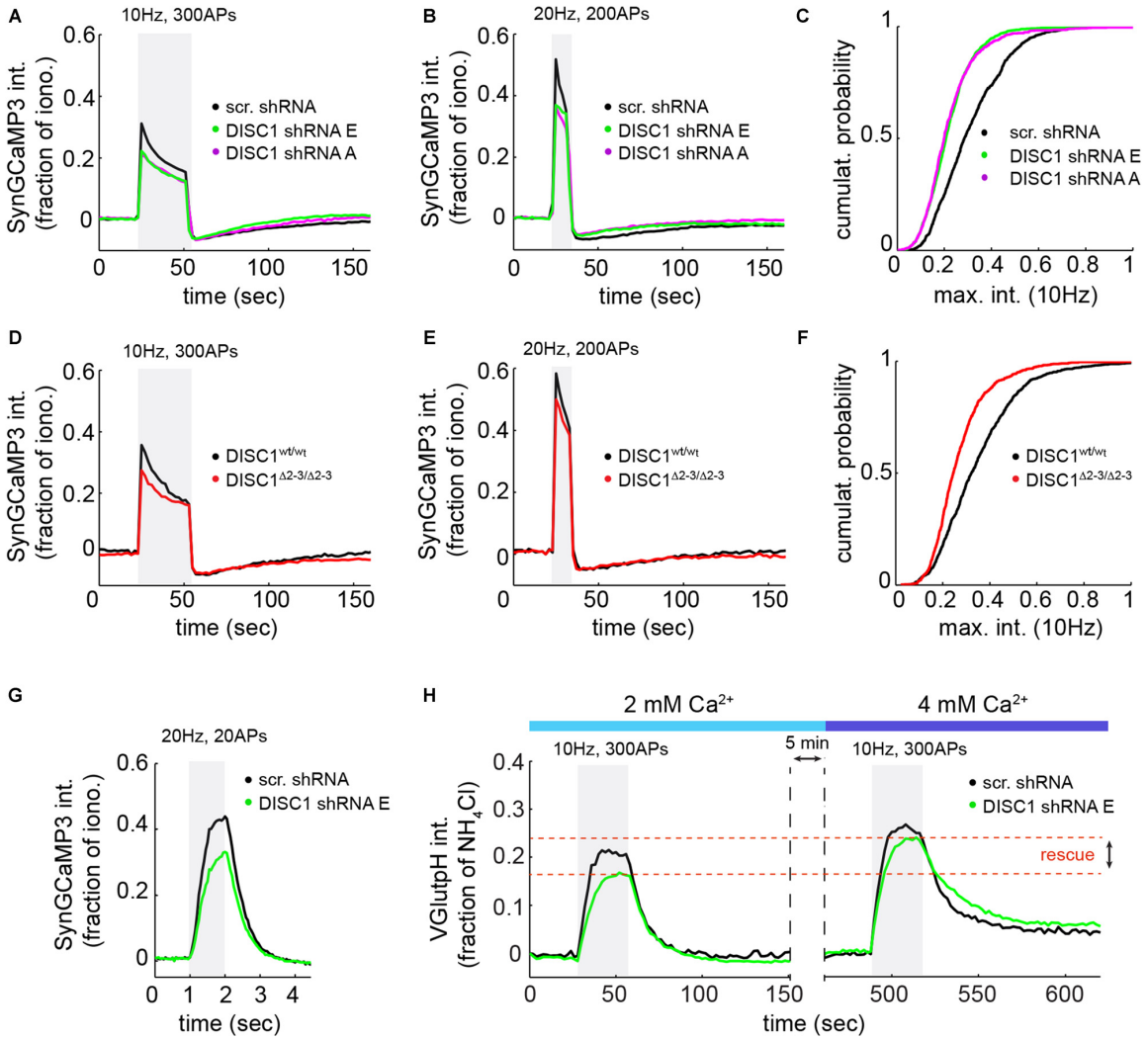

FIGURE 4 | DISC1 loss-of-function reduces evoked Ca^{2+} transients at nerve terminals. SyGC3 imaging in rat hippocampal neurons (DIV14–16) in response two different trains of APs. **(A)** Average Ca^{2+} transients in neurons expressing scr (1052 boutons, 15 fields, 5 experiments (exps)), DISC1-E (1836 boutons, 9 fields, 3 exps) and -A (754 boutons, 11 fields, 3 exps) shRNAs, in response to 300 APs, 10 Hz. The DISC1-E and DISC-A groups are significantly different than the scr group ($p = 0.0057$). **(B)** Average Ca^{2+} transients in neurons expressing scr (861 boutons, 9 fields, 5 exps), DISC1-E (2118 boutons, 7 fields, 3 exps) and -A (1549 boutons, 9 fields, 3 exps) shRNAs, in response to 200 APs, 20 Hz. **(C)** Cumulative probability of SyGC3 peak intensity from individual boutons corresponding to **(A)**. **(D)** Average Ca^{2+} transients in *DISC1* $^{wt/wt}$ (1090 boutons, 11 fields, 3 exps) and *DISC1* $^{\Delta 2-3/\Delta 2-3}$ (727 boutons, 9 fields, 3 exps) neurons, in response to 300 APs, 10 Hz. The *DISC1* $^{wt/wt}$ and *DISC1* $^{\Delta 2-3/\Delta 2-3}$ groups are statistically different ($p = 0.0182$). **(E)** Average Ca^{2+} transients in *DISC1* $^{wt/wt}$ (1365 boutons, 9 fields, 3 exps) and *DISC1* $^{\Delta 2-3/\Delta 2-3}$ (1233 boutons, 8 fields, 3 exps) neurons, in response to 200 APs, 20 Hz. **(F)** Cumulative probability of SyGC3 peak intensity from individual boutons corresponding to **(D)**. **(G)** Average Ca^{2+} transients in neurons expressing scr (290 boutons, 6 fields, 2 exps), and DISC1-E (390 boutons, 6 fields, 2 exps) shRNAs, in response to 20 APs, 20 Hz. The scr and DISC1-E groups are statistically different ($p = 0.0036$). **(H)** Average vGpH traces in scr (180 boutons, 5 fields, 2 exps) and DISC1-E (488 boutons, 6 fields, 2 exps) shRNA-expressing neurons during two consecutive trains of APs (300 AP, 10 Hz) in the presence of 2 or 4 mM extracellular Ca^{2+}.

containing Cav2.2, or in the intensity of Cav2.2 staining in presynaptic terminals (**Supplementary Figures S2B,C**). Nor did we find evidence for altered presynaptic localization and intensity of Cav2.1 (**Supplementary Figures S2D–F** or reduced density of presynaptic terminals (**Supplementary Figure S2G**) in DISC1 knockdown neurons. Thus, synaptic targeting and abundance of Cav2 channels does not seem to be regulated by DISC1.

We finally examined the effect of DISC1 on Cav2 currents by whole cell patch-clamp recordings. Co-transfection of recombinant DISC1 (**Figure 6A**) in HEK293T cells together with Cav2.2 and its auxiliary subunits (see "Materials and Methods" Section) resulted in a 27% increase in Cav2.2 peak current density (**Figures 6B,C**). Likewise, tail current density of Cav2.2 was substantially elevated in DISC1-overexpressing cells (**Figures 6D,E**). Current density can be

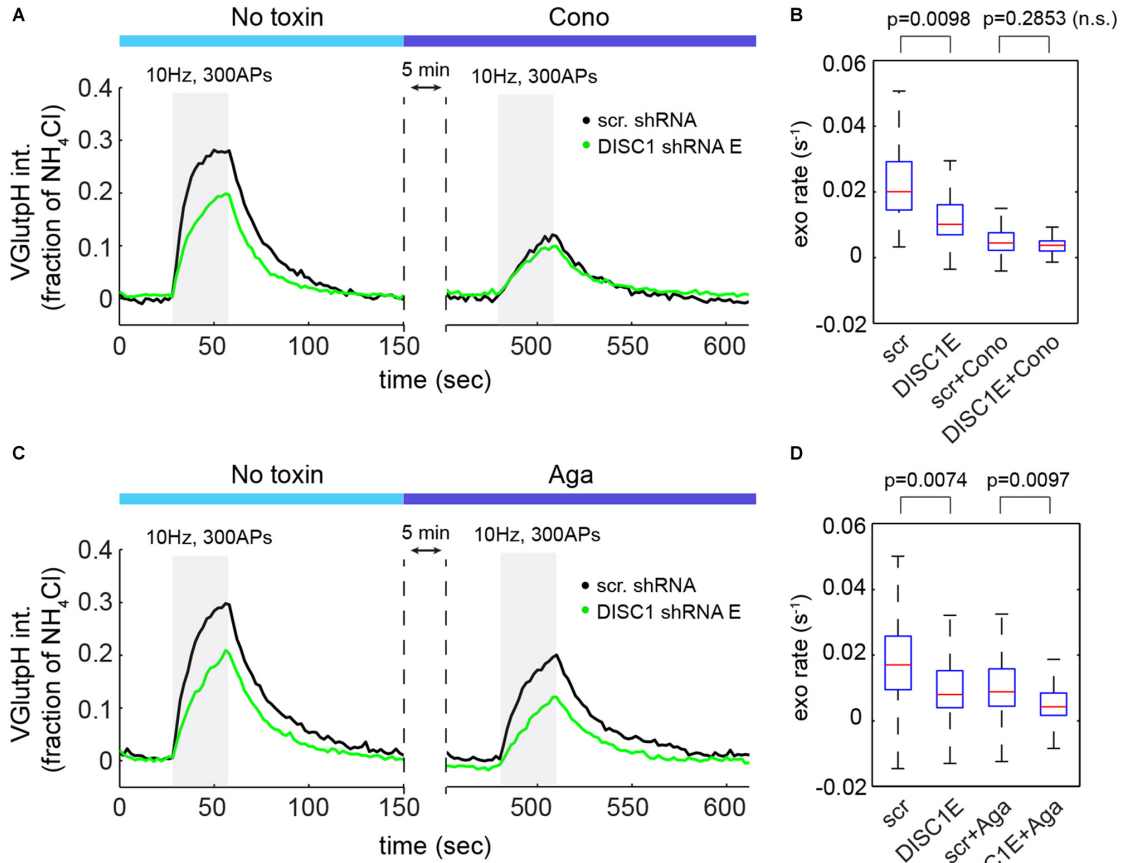

E

% inhibition of exo rate by DISC1 KD	before toxin	after toxin
Cono	43.9%	16.5%
Aga	43.4%	49.5%

FIGURE 5 | DISC1 regulates Cav2.2-dependent SV exocytosis. (A) Average vGpH traces in scr (101 boutons, 6 fields, 2 exps) and DISC1-E (87 boutons, 5 fields, 2 exps) shRNA-expressing neurons during consecutive trains of APs (300 AP, 10 Hz) in the absence or presence of the Cav2.2 blocker ω-Conotoxin GVIA (125 nM). **(B)** Boxplot of SV exocytic rates before and after ω-Conotoxin GVIA application. Exocytic rates were measured by linear fitting of the first six time points of the vGpH response. **(C)** Average vGpH traces in scr (1294 boutons, 9 fields, 3 exps) and DISC1-E (1282 boutons, 9 fields, 3 exps) shRNA-expressing neurons during consecutive trains of APs (300 AP, 10 Hz) in the absence or presence of the Cav2.1 blocker ω-Agatoxin TK (125 nM). **(D)** Boxplot of SV exocytic rates before and after ω-Agatoxin TK application. **(E)** Table showing the percentage of inhibition of exocytosis rate by DISC1 knockdown before and after Cav2.2- or Cav2.1 blockade.

affected by a change in channel gating or by the number of channels at the cell surface. To test the first possibility, we examined the voltage-dependent properties of Cav2.2 current activation and saw no difference between control and DISC1-overexpressing cells (**Figure 6F**). This suggests that DISC1 promotes surface delivery and/or stabilize surface expression of Cav2.2. Recording of Cav2.1 currents revealed a similar, voltage-independent, potentiation effect of DISC1 (**Figures 6G–K**). Thus, DISC1 equally augments both Cav2.2 and Cav2.1 currents in this heterologous system, presumably by increasing surface expression of these Ca^{2+} channels. These results also imply the presence of an additional layer of regulation in hippocampal neurons that restricts the activity of DISC1 to Cav2.2-dependent SV exocytosis.

DISCUSSION

We used here two independent gene-targeting approaches together with large-scale imaging of presynaptic function to determine the impact of the mental disease gene *DISC1* on the glutamate release machinery. Our results show that DISC1 accelerates SV exocytosis and thus enhances presynaptic performance. This boosting effect is mediated by N-type Ca^{2+} channels, establishing the first link between DISC1 and VGCC activity.

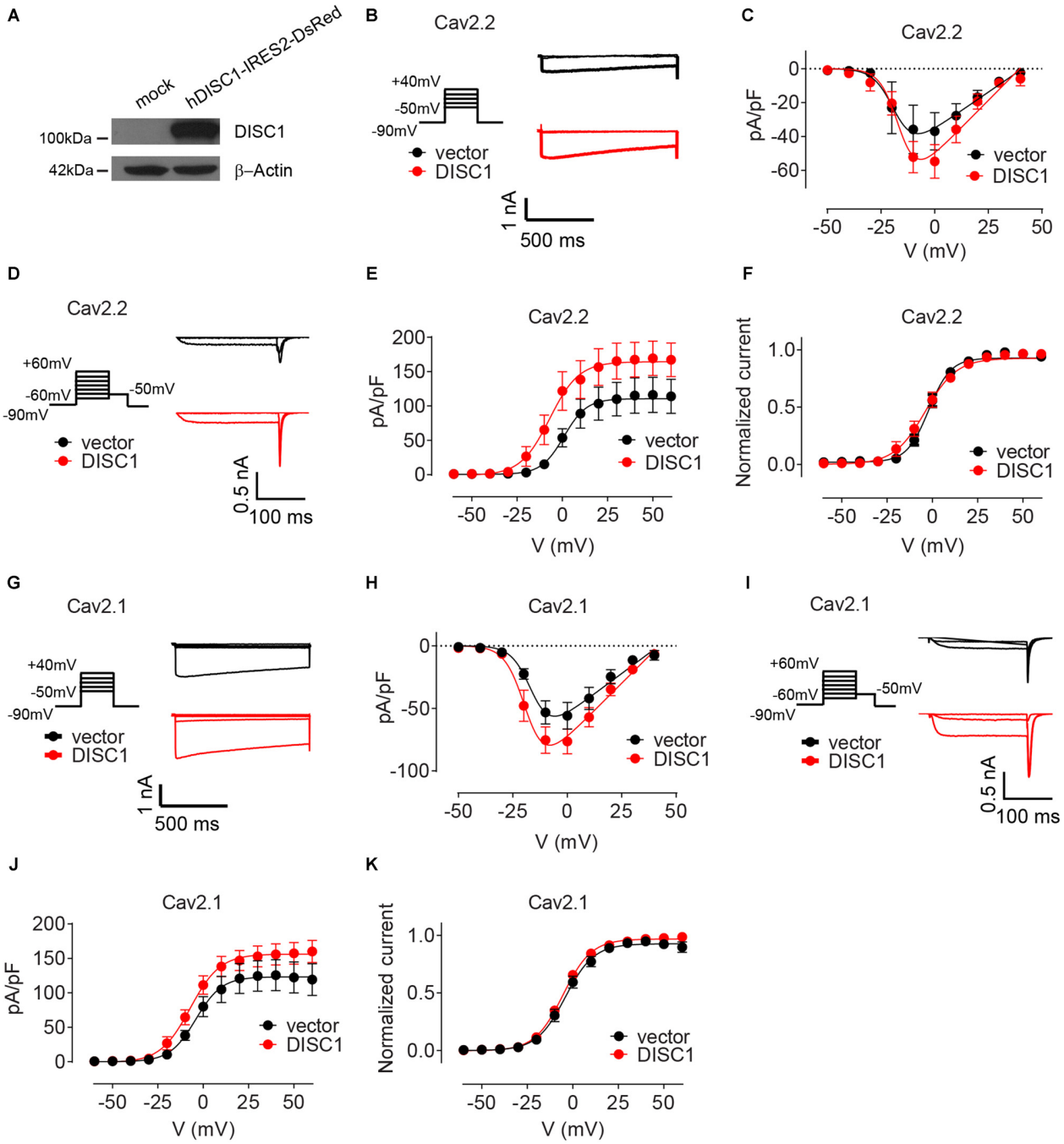

FIGURE 6 | DISC1 enhances Cav2.2 and Cav2.1 currents. (A) Western blot showing expression of ectopic (human) DISC1 in HEK293 cells. **(B,C)** Cav2.2 Current-voltage (I-V) curves for hDISC1-expressing and control cells. **(B)** Stimulation protocol and individual current responses shown at three different voltages (−30, 0 and 30 mV) **(C)**. Average I-V plots for hDISC1 (peak = 54.2 ± 4.5 pA/pF, 13 cells) and control (peak = 39.2 ± 4.9 pA/pF, 12 cells), $p = 0.033$. **(D–F)** Cav2.2 activation curves in response to the tail protocol. **(D)** Illustration of the tail protocol and individual tail currents measured at −50 mV after three different voltage steps (−20, 0 and 40 mV). **(E)** Average current density based on tail currents for DISC1 (164.3 ± 7.3 pA/pF, 12 cells) and control (110.5 ± 6.3 pA/pF, 12 cells), $^*p < 0.001$. **(F)** Normalized activation curve from tail currents showing no significant difference between DISC1 (V_{50}: −6.98 ± 3.43 mV, 12 cells) and control (V_{50}: 0.86 ± 3.62 mV, 12 cells), $p = 0.13$. **(G,H)** Cav2.1 Current-voltage (I-V) curves for hDISC1-expressing and control cells. **(G)** Stimulation protocol and individual current responses shown at three different voltages (−30, 0 and 30 mV). **(H)** Average I-V plots for hDISC1 (peak = 79.9 ± 8.3 pA/pF, 15 cells) and control (peak = 56.3 ± 7.4 pA/pF, 13 cells), $p = 0.046$. **(I–K)** Cav2.1 activation curves in response to the tail protocol. **(I)** Illustration of the tail protocol and individual tail currents measured at −50 mV after three different voltage steps (−20, 0 and 40 mV). **(J)** Average current density based on tail currents for DISC1 (156.3 ± 5.7 pA/pF, 25 cells) and control (123.2 ± 7.4 pA/pF, 17 cells), $^*p = 0.003$. **(K)** Normalized activation curve from tail currents showing no significant difference between DISC1 (V_{50}: −5.39 ± 0.49 mV, 24 cells) and control (V_{50}: −4.41 ± 0.93 mV, 17 cells), $p = 0.31$.

DISC1 inactivation in hippocampal neurons results in decreased Ca^{2+} transients at hippocampal terminals in response to AP firing, consistent with a deficit in Ca^{2+} entry. Because these Ca^{2+} signals are shaped by both Ca^{2+} entry and clearance processes, we cannot exclude a role of DISC1 in regulating Ca^{2+} extrusion or buffering. A stimulatory effect of DISC1 on Ca^{2+} entry is further supported, however, by its positive impact on Cav2.2 and Cav2.1 currents, the two main VGCCs underlying the initiation of neurotransmission at hippocampal synapses. How DISC1 enhances Cav2 currents is unclear. The lack of an effect on gating suggests that DISC1 promotes surface expression of these Ca^{2+} channels, although we cannot exclude a role of DISC1 in regulating single-channel conductance or open probability. Our immunolocalization studies revealed no detectable impact of DISC1 on presynaptic abundance of Cav2 channels. This does not rule out, however, the possibility that DISC1 regulates the number of functional Ca^{2+} channels at the surface of the terminal.

Although overexpression of DISC1 enhances both Cav2.1 and Cav2.2 currents in a heterologous system, our findings point to a selective influence of DISC1 on Cav2.2-dependent SV exocytosis. How is this selectivity achieved? It is possible that both Cav2.1 and Cav2.2 compete for DISC1 regulation at presynaptic terminals. The dominant contribution of Cav2.2 to SV release probably results (at least in part) from increased levels of Cav2.2 (relative to Cav2.1) at hippocampal terminals (Ariel et al., 2013). Thus, preferential regulation of Cav2.2 by endogenous levels of DISC1 combined with greater abundance of Cav2.2 may explain why DISC1-dependent SV exocytosis appears to be exclusively mediated by Cav2.2. Specificity could also arise, however, from functions of DISC1 downstream of Ca^{2+} entry. For example, DISC1 could be involved in positioning Cav2.2 in close proximity to the SV release machinery at the active zone, a process that dictates speed and fidelity of neurotransmission. While the role of Ca^{2+} entry in SV exocytosis is undisputed, its impact on SV endocytosis remains somewhat controversial. Recent evidence suggests, however, that Ca^{2+} couples rates of SV exo- and endocytosis and optimizes endocytic rates during AP bursts (Armbruster et al., 2013). We observed reduced endocytic rates in both DISC1-silenced and *DISC1*$^{\Delta 2-3/\Delta 2-3}$ neurons. Although this effect was small and did not reach statistical significance, our results suggest that the influence of DISC1 on Cav2.2 impacts both exo- and endocytosis of SVs at hippocampal terminals.

Our findings extend on two recent studies implicating DISC1 in presynaptic function. In glutamatergic neurons differentiated from human iPS cells and derived from members of a family with a frameshift mutation in DISC1, deficits in SV release were observed after KCl-induced depolarization (Wen et al., 2014). In a separate report, RNAi knockdown of DISC1 in layer 2/3 neocortical neurons increases paired-pulse facilitation and appears to reduce probability of glutamate release (Maher and Loturco, 2012). Collectively, these results clearly identify DISC1 as a positive modulator of glutamate release.

The efficacy of neurotransmitter release determines not only the strength of synaptic excitation, but also dictates various forms of short-term plasticity (Abbott and Regehr, 2004), suggesting broad functions of DISC1 in synaptic computation and neural circuit performance. Although we have not directly measured release probability (P_r), the impact of DISC1 on Ca^{2+} entry and SV cycling suggests a positive influence on P_r (see Maher and Loturco, 2012). Because synaptic facilitation and depression depend largely on the initial P_r (high P_r favors depression while low P_r favors facilitation), our results predict altered short-term plasticity in DISC1-deficient neural circuits. Of interest, abnormal short-term plasticity has been associated with deficits in moment-to-moment information processing and working memory, two hallmarks of schizophrenia (Crabtree and Gogos, 2014). Reduced efficacy in glutamate release may also be relevant for forms of long-term potentiation (LTP) that have clear presynaptic components, such as LTP at the perforant path-granule cell synapse in the dentate gyrus (Errington et al., 1987). Notably, this form of LTP is impaired in *DISC1*$^{\Delta 2-3/\Delta 2-3}$ mice—a stronger tetanic stimulus is required for the expression of LTP (Kuroda et al., 2011). Our findings suggest that this LTP deficit could be due to a failure of the presynaptic terminal to undergo activity-dependent increase in release probability.

Several genes encoding VGCC subunits, including *CACNA1C, CACNB2* and *CACNA1I* have repeatedly been associated with schizophrenia and other psychiatric disorders (Ferreira et al., 2008; Cross-Disorder Group of the Psychiatric Genomics, 2013; Hamshere et al., 2013; Ripke et al., 2013; Schizophrenia Working Group of the Psychiatric Genomics, 2014). Although *CACNA1A* (Cav2.1) and *CACNA1B* (Cav2.2) are not typically associated with risk loci, *RIM1* (also called *RIMS1*)—a presynaptic scaffold that regulates density of P/Q- and N-type Ca^{2+} channels and SV docking at the active zone (Han et al., 2011)—was recently identified as a candidate gene for schizophrenia in the largest GWAS study conducted to date (Schizophrenia Working Group of the Psychiatric Genomics, 2014). Together these findings point to neurotransmitter release as a central process targeted in schizophrenia.

In conclusion, our results shed light on a novel mechanism by which a major susceptibility gene for mental illness enhances the efficacy of glutamate release, and provide further support for a central role of glutamate neurotransmission in schizophrenia and other major mood disorders.

AUTHOR CONTRIBUTIONS

WT and JVT performed and analyzed all imaging and biochemical experiments. QL performed and analyzed whole-cell patch-clamp recordings. MB carried out the statistical analysis. KBL made the original observation implicating DISC1 in SV cycling. KKu and KKa made the *DISC1* Δ2–3 mouse and the DISC1 C-terminus antibody. WT and MF wrote Matlab scripts. TWS and MF supervised the project. MF wrote the article.

ACKNOWLEDGMENTS

We thank Bo Lu for critical reading of the manuscript. We are in debt to Durgadevi Alagappan and Tan Li-Ting for excellent technical assistance. This work was supported by a grant to MF from the Ministry of Education Academic Research Fund (MOE2013-T2-1-053).

SUPPLEMENTARY MATERIAL

The Supplementary Material for this article can be found online at: http://journal.frontiersin.org/article/10.3389/fnsyn.2016.00015/abstract

FIGURE S1 | Variability of SV exocytic responses. Scatter plot showing SV exocytic rates in individual boutons across six (color-coded) independent preparations. Each preparation comprises three fields colored light to dark. These rates were measured in hippocampal neurons (DIV14–16) expressing scr shRNA and correspond to the data shown in **Figure 2**.

FIGURE S2 | Presynaptic localization and abundance of Cav2 channels are unaffected by DISC1 silencing. (A,D) Immunolocalization of endogenous Cav2.2 **(A)** or Cav2.1 **(D)** and bassoon in rat hippocampal neurons (DIV 14–15) expressing scr and DISC1-E shRNAs. Arrowheads indicate boutons positive for Cav2.2 and bassoon **(A)** or Cav2.1 and bassoon **(D)**. Scale bar 10 μm. **(B)** Percentage of Cav2.2-positive boutons in scr (5 cells) and DISC1-E (5 cells) shRNA-expressing neurons. **(C)** Cav2.2 fluorescence intensity measured at individual presynaptic boutons (based on bassoon staining) in **(B)**. **(E)** Percentage of Cav2.1-positive boutons in scr (8 cells) and DISC1-E (8 cells) shRNA-expressing neurons. **(F)** Cav2.1 fluorescence intensity measured at individual presynaptic boutons (based on bassoon staining) in **(E)**. **(G)** Quantification of the density of presynaptic terminals (based on bassoon staining) in neurons expressing scr (24 cells), DISC1–E (21 cells) and -A (17 cells) shRNAs from four independent experiments.

TABLE T1 | Statistical analysis of synaptic responses. Column 1: datasets. Column 2: *p* values derived from the field averaging approach, with each field weighted according to its number of boutons (see "Materials and Methods" Section). Column 3: *p* values derived from the linear mixed model, where intra-field correlations and variations in neuron preparations are taken into account (see "Materials and Methods" Section).

REFERENCES

Abbott, L. F., and Regehr, W. G. (2004). Synaptic computation. *Nature* 431, 796–803. doi: 10.1038/nature03010

Akerboom, J., Chen, T. W., Wardill, T. J., Tian, L., Marvin, J. S., Mutlu, S., et al. (2012). Optimization of a GCaMP calcium indicator for neural activity imaging. *J. Neurosci.* 32, 13819–13840. doi: 10.1523/jneurosci.2601-12.2012

Ariel, P., Hoppa, M. B., and Ryan, T. A. (2013). Intrinsic variability in Pv, RRP size, Ca^{2+} channel repertoire and presynaptic potentiation in individual synaptic boutons. *Front. Synaptic Neurosci.* 4:9. doi: 10.3389/fnsyn.2012.00009

Ariel, P., and Ryan, T. A. (2010). Optical mapping of release properties in synapses. *Front. Neural Circuits* 4:18. doi: 10.3389/fncir.2010.00018

Armbruster, M., Messa, M., Ferguson, S. M., De Camilli, P., and Ryan, T. A. (2013). Dynamin phosphorylation controls optimization of endocytosis for brief action potential bursts. *Elife* 2:e00845. doi: 10.7554/elife.00845

Burrone, J., Li, Z., and Murthy, V. N. (2006). Studying vesicle cycling in presynaptic terminals using the genetically encoded probe synaptopHluorin. *Nat. Protoc.* 1, 2970–2978. doi: 10.1038/nprot.2006.449

Catterall, W. A., Leal, K., and Nanou, E. (2013). Calcium channels and short-term synaptic plasticity. *J. Biol. Chem.* 288, 10742–10749. doi: 10.1074/jbc.r112.411645

Chubb, J. E., Bradshaw, N. J., Soares, D. C., Porteous, D. J., and Millar, J. K. (2008). The DISC locus in psychiatric illness. *Mol. Psychiatry* 13, 36–64. doi: 10.1038/sj.mp.4002106

Clapcote, S. J., Lipina, T. V., Millar, J. K., Mackie, S., Christie, S., Ogawa, F., et al. (2007). Behavioral phenotypes of Disc1 missense mutations in mice. *Neuron* 54, 387–402. doi: 10.1016/j.neuron.2007.04.015

Crabtree, G. W., and Gogos, J. A. (2014). Synaptic plasticity, neural circuits and the emerging role of altered short-term information processing in schizophrenia. *Front. Synaptic Neurosci.* 6:28. doi: 10.3389/fnsyn.2014.00028

Cross-Disorder Group of the Psychiatric Genomics, C. (2013). Identification of risk loci with shared effects on five major psychiatric disorders: a genome-wide analysis. *Lancet* 381, 1371–1379. doi: 10.1016/s0140-6736(12)62129-1

Cross-Disorder Group of the Psychiatric Genomics, C., Lee, S. H., Ripke, S., Neale, B. M., Faraone, S. V., Purcell, S. M., et al. (2013). Genetic relationship between five psychiatric disorders estimated from genome-wide SNPs. *Nat. Genet.* 45, 984–994. doi: 10.1038/ng.2711

Duan, X., Chang, J. H., Ge, S., Faulkner, R. L., Kim, J. Y., Kitabatake, Y., et al. (2007). Disrupted-In-Schizophrenia 1 regulates integration of newly generated neurons in the adult brain. *Cell* 130, 1146–1158. doi: 10.1016/j.cell.2007.07.010

Ekelund, J., Hennah, W., Hiekkalinna, T., Parker, A., Meyer, J., Lonnqvist, J., et al. (2004). Replication of 1q42 linkage in Finnish schizophrenia pedigrees. *Mol. Psychiatry* 9, 1037–1041. doi: 10.1038/sj.mp.4001536

Ekelund, J., Hovatta, I., Parker, A., Paunio, T., Varilo, T., Martin, R., et al. (2001). Chromosome 1 loci in Finnish schizophrenia families. *Hum. Mol. Genet.* 10, 1611–1617. doi: 10.1093/hmg/10.15.1611

Errington, M. L., Lynch, M. A., and Bliss, T. V. (1987). Long-term potentiation in the dentate gyrus: induction and increased glutamate release are blocked by D(-)aminophosphonovalerate. *Neuroscience* 20, 279–284. doi: 10.1016/0306-4522(87)90019-4

Fernandez-Alfonso, T., and Ryan, T. A. (2004). The kinetics of synaptic vesicle pool depletion at CNS synaptic terminals. *Neuron* 41, 943–953. doi: 10.1016/s0896-6273(04)00113-8

Ferreira, M. A., O'donovan, M. C., Meng, Y. A., Jones, I. R., Ruderfer, D. M., Jones, L., et al. (2008). Collaborative genome-wide association analysis supports a role for ANK3 and CACNA1C in bipolar disorder. *Nat. Genet.* 40, 1056–1058. doi: 10.1038/ng.209

Fromer, M., Pocklington, A. J., Kavanagh, D. H., Williams, H. J., Dwyer, S., Gormley, P., et al. (2014). De novo mutations in schizophrenia implicate synaptic networks. *Nature* 506, 179–184. doi: 10.1038/nature12929

Galbraith, S., Daniel, J. A., and Vissel, B. (2010). A study of clustered data and approaches to its analysis. *J. Neurosci.* 30, 10601–10608. doi: 10.1523/jneurosci.0362-10.2010

Garcia-Alvarez, G., Lu, B., Yap, K. A., Wong, L. C., Thevathasan, J. V., Lim, L., et al. (2015). STIM2 regulates PKA-dependent phosphorylation and trafficking of AMPARs. *Mol. Biol. Cell* 26, 1141–1159. doi: 10.1091/mbc.e14-07-1222

Glessner, J. T., Reilly, M. P., Kim, C. E., Takahashi, N., Albano, A., Hou, C., et al. (2010). Strong synaptic transmission impact by copy number variations in schizophrenia. *Proc. Natl. Acad. Sci. U S A* 107, 10584–10589. doi: 10.1073/pnas.1000274107

Hamshere, M. L., Walters, J. T., Smith, R., Richards, A. L., Green, E., Grozeva, D., et al. (2013). Genome-wide significant associations in schizophrenia to ITIH3/4, CACNA1C and SDCCAG8 and extensive replication of associations reported by the Schizophrenia PGC. *Mol. Psychiatry* 18, 708–712. doi: 10.1038/mp.2012.67

Han, Y., Kaeser, P. S., Sudhof, T. C., and Schneggenburger, R. (2011). RIM determines Ca^{2+} channel density and vesicle docking at the

presynaptic active zone. *Neuron* 69, 304–316. doi: 10.1016/j.neuron.2010.12.014

Hikida, T., Jaaro-Peled, H., Seshadri, S., Oishi, K., Hookway, C., Kong, S., et al. (2007). Dominant-negative DISC1 transgenic mice display schizophrenia-associated phenotypes detected by measures translatable to humans. *Proc. Natl. Acad. Sci. U S A* 104, 14501–14506. doi: 10.1073/pnas.0704774104

Howes, O., Mccutcheon, R., and Stone, J. (2015). Glutamate and dopamine in schizophrenia: an update for the 21st century. *J. Psychopharmacol.* 29, 97–115. doi: 10.1177/0269881114563634

Huang, H., Tan, B. Z., Shen, Y., Tao, J., Jiang, F., Sung, Y. Y., et al. (2012). RNA editing of the IQ domain in Ca(v)1.3 channels modulates their Ca^{2+}-dependent inactivation. *Neuron* 73, 304–316. doi: 10.1016/j.neuron.2011.11.022

Huettner, J. E., and Baughman, R. W. (1986). Primary culture of identified neurons from the visual cortex of postnatal rats. *J. Neurosci.* 6, 3044–3060.

International Schizophrenia, C., Purcell, S. M., Wray, N. R., Stone, J. L., Visscher, P. M., O'donovan, M. C., et al. (2009). Common polygenic variation contributes to risk of schizophrenia and bipolar disorder. *Nature* 460, 748–752. doi: 10.1038/nature08185

Kaech, S., and Banker, G. (2006). Culturing hippocampal neurons. *Nat. Protoc.* 1, 2406–2415. doi: 10.1038/nprot.2006.356

Kamiya, A., Kubo, K., Tomoda, T., Takaki, M., Youn, R., Ozeki, Y., et al. (2005). A schizophrenia-associated mutation of DISC1 perturbs cerebral cortex development. *Nat. Cell Biol.* 7, 1167–1178. doi: 10.1038/ncb1328

Kilpinen, H., Ylisaukko-Oja, T., Hennah, W., Palo, O. M., Varilo, T., Vanhala, R., et al. (2008). Association of DISC1 with autism and Asperger syndrome. *Mol. Psychiatry* 13, 187–196. doi: 10.1038/sj.mp.4002031

Kubo, K., Tomita, K., Uto, A., Kuroda, K., Seshadri, S., Cohen, J., et al. (2010). Migration defects by DISC1 knockdown in C57BL/6, 129X1/SvJ and ICR strains via in utero gene transfer and virus-mediated RNAi. *Biochem. Biophys. Res. Commun.* 400, 631–637. doi: 10.1016/j.bbrc.2010.08.117

Kuroda, K., Yamada, S., Tanaka, M., Iizuka, M., Yano, H., Mori, D., et al. (2011). Behavioral alterations associated with targeted disruption of exons 2 and 3 of the Disc1 gene in the mouse. *Hum. Mol. Genet.* 20, 4666–4683. doi: 10.1093/hmg/ddr400

Laird, N. M., and Ware, J. H. (1982). Random-effects models for longitudinal data. *Biometrics* 38, 963–974.

Lee, F. H., Fadel, M. P., Preston-Maher, K., Cordes, S. P., Clapcote, S. J., Price, D. J., et al. (2011). Disc1 point mutations in mice affect development of the cerebral cortex. *J. Neurosci.* 31, 3197–3206. doi: 10.1523/jneurosci.4219-10.2011

Li, H., Foss, S. M., Dobryy, Y. L., Park, C. K., Hires, S. A., Shaner, N. C., et al. (2011). Concurrent imaging of synaptic vesicle recycling and calcium dynamics. *Front. Mol. Neurosci.* 4:34. doi: 10.3389/fnmol.2011.00034

Maher, B. J., and Loturco, J. J. (2012). Disrupted-in-schizophrenia (DISC1) functions presynaptically at glutamatergic synapses. *PLoS One* 7:e34053. doi: 10.1371/journal.pone.0034053

Mao, Y., Ge, X., Frank, C. L., Madison, J. M., Koehler, A. N., Doud, M. K., et al. (2009). Disrupted in schizophrenia 1 regulates neuronal progenitor proliferation via modulation of GSK3beta/beta-catenin signaling. *Cell* 136, 1017–1031. doi: 10.1016/j.cell.2008.12.044

Miesenbock, G., De Angelis, D. A., and Rothman, J. E. (1998). Visualizing secretion and synaptic transmission with pH-sensitive green fluorescent proteins. *Nature* 394, 192–195. doi: 10.1038/28190

Millar, J. K., Christie, S., Anderson, S., Lawson, D., Hsiao-Wei Loh, D., Devon, R. S., et al. (2001). Genomic structure and localisation within a linkage hotspot of Disrupted In Schizophrenia 1, a gene disrupted by a translocation segregating with schizophrenia. *Mol. Psychiatry* 6, 173–178. doi: 10.1038/sj.mp.4000784

Millar, J. K., Pickard, B. S., Mackie, S., James, R., Christie, S., Buchanan, S. R., et al. (2005). DISC1 and PDE4B are interacting genetic factors in schizophrenia that regulate cAMP signaling. *Science* 310, 1187–1191. doi: 10.1126/science.1112915

Millar, J. K., Wilson-Annan, J. C., Anderson, S., Christie, S., Taylor, M. S., Semple, C. A., et al. (2000). Disruption of two novel genes by a translocation co-segregating with schizophrenia. *Hum. Mol. Genet.* 9, 1415–1423. doi: 10.1093/hmg/9.9.1415

Moskvina, V., Craddock, N., Holmans, P., Nikolov, I., Pahwa, J. S., Green, E., et al. (2009). Gene-wide analyses of genome-wide association data sets: evidence for multiple common risk alleles for schizophrenia and bipolar disorder and for overlap in genetic risk. *Mol. Psychiatry* 14, 252–260. doi: 10.1038/mp.2008.133

Niwa, M., Kamiya, A., Murai, R., Kubo, K., Gruber, A. J., Tomita, K., et al. (2010). Knockdown of DISC1 by in utero gene transfer disturbs postnatal dopaminergic maturation in the frontal cortex and leads to adult behavioral deficits. *Neuron* 65, 480–489. doi: 10.1016/j.neuron.2010.01.019

Pletnikov, M. V., Ayhan, Y., Nikolskaia, O., Xu, Y., Ovanesov, M. V., Huang, H., et al. (2008). Inducible expression of mutant human DISC1 in mice is associated with brain and behavioral abnormalities reminiscent of schizophrenia. *Mol. Psychiatry* 13, 173–186. doi: 10.1038/sj.mp.4002079

Poon, V. Y., Goh, C., Voorhoeve, P. M., and Fivaz, M. (2014). High-content imaging of presynaptic assembly. *Front. Cell Neurosci.* 8:66. doi: 10.3389/fncel.2014.00066

Ripke, S., O'dushlaine, C., Chambert, K., Moran, J. L., Kahler, A. K., Akterin, S., et al. (2013). Genome-wide association analysis identifies 13 new risk loci for schizophrenia. *Nat. Genet.* 45, 1150–1159. doi: 10.1038/ng.2742

Sachs, N. A., Sawa, A., Holmes, S. E., Ross, C. A., Delisi, L. E., and Margolis, R. L. (2005). A frameshift mutation in Disrupted in Schizophrenia 1 in an American family with schizophrenia and schizoaffective disorder. *Mol. Psychiatry* 10, 758–764. doi: 10.1038/sj.mp.4001667

Sankaranarayanan, S., De Angelis, D., Rothman, J. E., and Ryan, T. A. (2000). The use of pHluorins for optical measurements of presynaptic activity. *Biophys. J.* 79, 2199–2208. doi: 10.1016/s0006-3495(00)76468-x

Schizophrenia Working Group of the Psychiatric Genomics, C. (2014). Biological insights from 108 schizophrenia-associated genetic loci. *Nature* 511, 421–427. doi: 10.1038/nature13595

Shen, S., Lang, B., Nakamoto, C., Zhang, F., Pu, J., Kuan, S. L., et al. (2008). Schizophrenia-related neural and behavioral phenotypes in transgenic mice expressing truncated Disc1. *J. Neurosci.* 28, 10893–10904. doi: 10.1523/jneurosci.3299-08.2008

Shinoda, T., Taya, S., Tsuboi, D., Hikita, T., Matsuzawa, R., Kuroda, S., et al. (2007). DISC1 regulates neurotrophin-induced axon elongation via interaction with Grb2. *J. Neurosci.* 27, 4–14. doi: 10.1523/jneurosci.3825-06.2007

Singh, K. K., Ge, X., Mao, Y., Drane, L., Meletis, K., Samuels, B. A., et al. (2010). Dixdc1 is a critical regulator of DISC1 and embryonic cortical development. *Neuron* 67, 33–48. doi: 10.1016/j.neuron.2010.06.002

St Clair, D., Blackwood, D., Muir, W., Carothers, A., Walker, M., Spowart, G., et al. (1990). Association within a family of a balanced autosomal translocation with major mental illness. *Lancet* 336, 13–16. doi: 10.1016/0140-6736(90)91520-k

Steinecke, A., Gampe, C., Valkova, C., Kaether, C., and Bolz, J. (2012). Disrupted-in-Schizophrenia 1 (DISC1) is necessary for the correct migration of cortical interneurons. *J. Neurosci.* 32, 738–745. doi: 10.1523/jneurosci.5036-11.2012

Thevathasan, J. V., Tan, E., Zheng, H., Lin, Y. C., Li, Y., Inoue, T., et al. (2013). The small GTPase HRas shapes local PI3K signals through positive feedback and regulates persistent membrane extension in migrating fibroblasts. *Mol. Biol. Cell* 24, 2228–2237. doi: 10.1091/mbc.E12-12-0905

Tian, L., Hires, S. A., Mao, T., Huber, D., Chiappe, M. E., Chalasani, S. H., et al. (2009). Imaging neural activity in worms, flies and mice with improved GCaMP calcium indicators. *Nat. Methods* 6, 875–881. doi: 10.1038/nmeth.1398

Tiscornia, G., Singer, O., and Verma, I. M. (2006). Production and purification of lentiviral vectors. *Nat. Protoc.* 1, 241–245. doi: 10.1038/nprot.2006.37

Tsuboi, D., Kuroda, K., Tanaka, M., Namba, T., Iizuka, Y., Taya, S., et al. (2015). Disrupted-in-schizophrenia 1 regulates transport of ITPR1 mRNA for synaptic plasticity. *Nat. Neurosci.* 18, 698–707. doi: 10.1038/nn.3984

Voglmaier, S. M., Kam, K., Yang, H., Fortin, D. L., Hua, Z., Nicoll, R. A., et al. (2006). Distinct endocytic pathways control the rate and extent of synaptic vesicle protein recycling. *Neuron* 51, 71–84. doi: 10.1016/j.neuron.2006.05.027

Wen, Z., Nguyen, H. N., Guo, Z., Lalli, M. A., Wang, X., Su, Y., et al. (2014). Synaptic dysregulation in a human iPS cell model of mental disorders. *Nature* 515, 414–418. doi: 10.1038/nature13716

Conflict of Interest Statement: The authors declare that the research was conducted in the absence of any commercial or financial relationships that could be construed as a potential conflict of interest.

frontiers in Synaptic Neuroscience

ORIGINAL RESEARCH
published: 26 July 2016
doi: 10.3389/fnsyn.2016.00021

Visualizing Presynaptic Calcium Dynamics and Vesicle Fusion with a Single Genetically Encoded Reporter at Individual Synapses

*Rachel E. Jackson and Juan Burrone**

Centre for Developmental Neurobiology, King's College London, London, UK

Synaptic transmission depends on the influx of calcium into the presynaptic compartment, which drives neurotransmitter release. Genetically encoded reporters are widely used tools to understand these processes, particularly pHluorin-based reporters that report vesicle exocytosis and endocytosis through pH dependent changes in fluorescence, and genetically encoded calcium indicators (GECIs) that exhibit changes in fluorescence upon binding to calcium. The recent expansion of the color palette of available indicators has made it possible to image multiple probes simultaneously within a cell. We have constructed a single molecule reporter capable of concurrent imaging of both presynaptic calcium influx and exocytosis, by fusion of sypHy, the vesicle associated protein synaptophysin containing a GFP-based pHluorin sensor, with the red-shifted GECI R-GECO1. Due to the fixed stoichiometry of the two probes, the ratio of the two responses can also be measured, providing an all optical correlate of the calcium dependence of release. Here, we have characterized stimulus-evoked sypHy-RGECO responses of hippocampal synapses *in vitro*, exploring the effects of different stimulus strengths and frequencies as well as variations in external calcium concentrations. By combining live sypHy-RGECO imaging with *post hoc* fixation and immunofluorescence, we have also investigated correlations between structural and functional properties of synapses.

Keywords: presynaptic, calcium, neurotransmitter release, pHluorin, RGECO, vesicle

OPEN ACCESS

Edited by:
Marc Fivaz,
Duke-NUS Graduate Medical School, Singapore

Reviewed by:
Kirill Volynski,
University College London, UK
Michael Alan Cousin,
University of Edinburgh, UK

****Correspondence:***
Juan Burrone
juan.burrone@kcl.ac.uk

Received: *14 May 2016*
Accepted: *13 July 2016*
Published: *26 July 2016*

Citation:
Jackson RE and Burrone J (2016) Visualizing Presynaptic Calcium Dynamics and Vesicle Fusion with a Single Genetically Encoded Reporter at Individual Synapses. Front. Synaptic Neurosci. 8:21. doi: 10.3389/fnsyn.2016.00021

INTRODUCTION

Synaptic transmission depends on the influx of calcium into the presynaptic compartment, driving the release of vesicles containing neurotransmitter, which will bind to receptors on the postsynaptic cell. Electrophysiological studies have been fundamental in understanding the relationship between presynaptic calcium and neurotransmitter release (Dodge and Rahamimoff, 1967) but are limited in spatial resolution and cannot provide information about individual presynaptic terminals, unless employed at large synapses that can be accessed directly (Heidelberger and Matthews, 1992; Schneggenburger and Neher, 2000; Vyleta and Jonas, 2014). For studying individual synapses, optical strategies using either chemical indicators or genetically encoded reporters have therefore become the method of choice. Genetically encoded reporters offer the advantage that neural activity can be monitored in defined populations of cells, both *in vitro* and *in vivo*, and the probe can be localized to specific subcellular compartments (reviewed in Broussard et al., 2014).

The largest family of single color genetically encoded calcium indicators (GECIs) is the GCaMP family, based on a circularly permuted GFP linked to calmodulin (CaM) and it's binding peptide M13 (Nakai et al., 2001). The original sensor has undergone multiple rounds of both random and structure-guided mutagenesis to improve stability, brightness, signal to noise ratio and kinetics (Tian et al., 2009; Akerboom et al., 2012; Chen et al., 2013) and several variants have been effectively targeted to the neuronal presynaptic terminal by fusion with synaptophysin (Dreosti et al., 2009; Li et al., 2011; Nikolaou et al., 2012). To enable multicolor imaging in single cells, red-shifted GECIs have been developed, including RCaMP (Akerboom et al., 2013) and R-GECO1 (Zhao Y. et al., 2011), for which a presynaptically targeted version (SyRGECO) has also been characterized (Walker et al., 2013). Much like the GCaMPs, red GECIs are constantly evolving, with new variants recently produced in both RCaMP and R-GECO families (Inoue et al., 2015; Dana et al., 2016).

The most widely used reporters of synaptic vesicle exocytosis and endocytosis consist of a synaptic vesicle protein fused to pHluorin, a pH-sensitive form of GFP (Miesenbock et al., 1998). Crucially in these constructs, pHluorin is localized to the acidic lumen of synaptic vesicles, so that its fluorescence is quenched at rest, but increases by up to 20-fold upon fusion with the plasma membrane and exposure to the more basic pH of the extracellular medium (Sankaranarayanan et al., 2000). Several variants exist including fusions to the intraluminal domains of VAMP2, known as synaptopHluorin, (Miesenbock et al., 1998), VGLUT1 (Voglmaier et al., 2006), and synaptophysin, known as sypHy (Granseth et al., 2006). Recently, efforts have been made to improve the normalization of presynaptic pHluorin responses, which are complicated by the presence of a fraction of the protein at the cell surface, particularly for synaptopHluorin and sypHy. At rest, surface stranded protein dominates the baseline fluorescence due to its increased brightness compared to quenched protein localized to synaptic vesicles and is highly variable between boutons, preventing the use of baseline fluorescence as a normalizing factor for exocytic responses. By fusing tdimer2 to the C-terminus of sypHy Rose et al. (2013) generated ratio-sypHy, in which the red fluorescence provides an invariant signal proportional to the expression of the probe rather than the surface fraction. The ratio of green to red fluorescence is fixed and allows normalization of sypHy responses to the red baseline, simplifying comparisons across cells with different expression levels and at different depths within a tissue. Finally, red-shifted reporters of vesicle fusion have also been generated, including VGLUT-2XmOr2 (Li et al., 2011), synaptobrevin 2-mOrange (Ramirez et al., 2012), and sypHTomato (Li and Tsien, 2012), again offering the possibility of combined imaging with other spectrally distinct reporters.

Despite the development of these tools, relatively few studies have been carried out in which both presynaptic calcium influx and vesicle exocytosis have been imaged in the same small, en-passant presynaptic terminals. Ermolyuk et al. (2012) used FM dyes to monitor vesicle exocytosis in conjunction with a calcium indicator introduced via a patch pipette, to examine the major parameters of presynaptic function including the size of the RRP, the probability of single vesicle fusion, calcium influx and the overall release probability of the synapse. Whilst this elegant study was highly informative, the techniques used are limited to relatively small numbers of cells and cannot be transferred to an *in vivo* situation. With genetically encoded reporters, visualization of both calcium influx and neurotransmitter release has been achieved by co-expression of a red-shifted reporter of vesicle exocytosis, either VGLUT-mOr2 or sypHTomato, with a green calcium indicator, such as members of the GCaMP family (Li et al., 2011; Li and Tsien, 2012). However, in this situation the two probes were expressed separately, resulting in possible differences in the level of expression of each reporter and in their subcellular location. Crucially, it also precludes the use of a ratiometric approach to measuring sypHy responses (Rose et al., 2013), complicating the direct comparison of responses across cells.

We have generated a new genetically encoded probe that brings together the measure of calcium and of exocytosis, in addition to a ratiometric measure of sypHy signals. To do this we combined sypHy, a well characterized pHluorin sensor of synaptic vesicle exocytosis (Granseth et al., 2006), with the red-shifted calcium indicator R-GECO1 (Zhao Y. et al., 2011) in a single molecule (sypHy-RGECO) to enable concurrent imaging of calcium influx and neurotransmitter release. The fixed 1:1 ratio of the two reporter molecules allows not only the normalization of sypHy signals to baseline or maximum RGECO fluorescence, but also the use of the ratio of the two responses as a measure of the calcium dependence of release at individual synapses. We systematically varied the number and frequency of action potentials, as well as the external calcium concentrations, and measured sypHy and RGECO signals in individual synapses. We found that while the amplitude of both responses changed, the distribution of the ratios remained constant. Interestingly, the calcium dependence of release was found to vary considerably between synapses, even within the same cell, suggesting the sensitivity of neurotransmitter release to calcium is synapse-specific. We also combined live sypHy-RGECO imaging with immunofluorescence for structural markers and observed that the amplitudes of calcium influx and exocytosis at individual synapses were positively correlated with the levels of the active zone protein RIM but were less well correlated with levels of the synaptic vesicle calcium sensor synaptotagmin-1.

MATERIALS AND METHODS

Generation of syn::sypHy-RGECO Plasmid

SypHy was amplified by PCR using primers containing HindIII and NotI restriction sites from CMV::sypHy A4 (a gift from Leon Lagnado, Addgene plasmid # 24478). The resulting PCR fragment was subcloned in to a modified version of the pEGFP-N2 plasmid (Clontech Laboratories, USA), in which the CMV promoter had been replaced with the human synapsin I promoter. To amplify RGECO from SyRGECO (Walker et al., 2013), a forward primer containing an XmaI site followed by a 5 amino acid linker (GSGGT) was used in conjunction with a reverse primer containing a NotI site. When subcloned into these

sites in the syn::sypHy-EGFP-N2 plasmid the EGFP was replaced to generate syn::sypHy-RGECO.

Hippocampal Neuronal Culture and Transfection

Dissociated hippocampal neurons were prepared from Sprague–Dawley rats at embryonic day 18. Dissected hippocampi were treated with 5 mg/ml trypsin (Worthington, UK) for 5 min at 37 and triturated with fire-polished Pasteur pipettes. Neurons were plated on 18mm glass coverslips (Hecht Assistent, Germany) or 35 mm Grid500 μ-dishes (Ibidi, Germany) coated with poly-D-lysine (50 μg/ml) and laminin (20 μg/ml, both Sigma–Aldrich, UK). Cultures media were maintained in neurobasal media supplemented with 2% B27, 2% fetal bovine serum, 1% glutamax (all ThemoFisher Scientific, UK) and 1 % penicillin/streptomycin (Sigma), at 37°C in a humidified incubator with 5% CO_2. After 3 days *in vitro* (DIV) the media was exchanged for serum-free media. At 7DIV neurons were transfected with sypHy-RGECO using Effectene (QIAGEN, UK). After transfection neurons were maintained in serum-free media without antibiotics. Only schedule 1 procedures performed by a competent individual were used in these studies, which are exempt under the Animals (Scientific Procedures) Act 1986.

Imaging of sypHy-RGECO

Neurons were imaged at 17–21DIV in HEPES buffered saline (HBS; 139 mM NaCl, 2.5 mM KCl, 10 mM HEPES, 10 mM D-Glucose, 2 mM $CaCl_2$, 1.3 mM $MgCl_2$; pH 7.3, 290 mOsmol) with 2,3-dioxo-6-nitro-1,2,3,4-tetrahydrobenzo[*f*]quinoxaline-7-sulfonamide (NBQX), 0.025 mM amino-5-phosphonovaleric acid (APV) and 6-imino-3-(4-methoxyphenyl)-1(6*H*)-pyridazinebutanoic acid hydrobromide (Gabazine) (all Tocris, UK). Coverslips were placed in a field stimulation chamber containing platinum electrodes (RC49-MFS, Warner Instruments, USA). For Ibidi dishes a stimulation insert (RC-37WS, Warner Instruments) was placed inside the dish. Neurons were imaged on an inverted Olympus IX71 microscope, equipped with a 60x/1.42 NA oil objective. Imaging was performed with a dual band-pass filter set optimized for EGFP and mCherry (Chroma, cat number 59022) and with LED excitation light sources of 470 and 585 nm (CoolLED, UK) for pHluorin and RGECO fluorophores, respectively. Time-lapse images were acquired at approximately 9.4 Hz using an Evolve 512 EMCCD camera (Photometrics, USA) controlled by Slidebook software (Intelligent Imaging Innovations, USA). Each frame consisted of a 20 ms exposure of the 470 and 585 nm LEDs sequentially, at 50 and 70% power, respectively, with 2 × 2 binning. Stimulation consisted of 1 ms 80 V pulses, which approximate single APs (Zhao C. et al., 2011), delivered by an SD9 Stimulator (Grass Technologies, USA), controlled by Slidebook. At the end of the imaging session 200 μM ionomycin was applied (Cayman Chemicals, USA) in either standard HBS, or HBS in which 50 mM of NaCl was replaced with 50 mM NH4Cl, to maximize sypHy-RGECO fluorescence. Neurons in Ibidi dishes were fixed in 4% PFA + 1% sucrose after imaging and were not treated with ionomycin. For calculations of surface fluorescence, synapses were imaged in HBS pH5.5 and HBS pH7.4 ±50 mM NH_4Cl and the surface fraction calculated as $(G_{pH7.4}-G_{pH5.5})/(G_{max}-G_{pH5.5})$. Synapses in which the surface fraction was calculated to be >100% were not included (<1% of synapses).

Analysis of Live Images

Images were analyzed using custom written Matlab codes (Mathworks, USA). Regions of interest (ROIs, 6 × 6 pixels) were selected for each puncta of sypHy fluorescence. Mean background-subtracted fluorescence intensity values were calculated for each ROI in both sypHy (G) and RGECO (R) channels. Traces were smoothed by averaging over a sliding window of 4 frames. Baseline fluorescence (G_0 and R_0) was measured as the average of ten frames prior to the stimulus. ΔG and ΔR values were calculated by the change in signal intensity from the baseline, with the peak responses defined as the maximum ΔG and ΔR within 40 frames of the stimulus. Puncta in which the ΔR response to the first 10 AP 20 Hz stimulus was greater than three times the standard deviation of the baseline were considered responding synapses and were analyzed in further images or stimulation conditions. ΔG and ΔR values for each synapse were averaged across trials and any synapse in which the mean peak response did not reach 3 SDs of the mean baseline in either channel were also discarded. Before pooling, mean ΔG and ΔR responses were normalized to either R_0 or R_{max}, defined as the average of 10 images in 200 μM ionomycin.

Immunofluorescence

After fixation cells were permeabilized with 0.2% Triton X-100 in PBS for 5 min, washed three times in PBS and placed in blocking solution (3% BSA in PBS + 0.05% NaN_3) for 60 min at room temperature (RT), or for longer at 4°C. Cells were incubated in primary antibodies diluted in blocking solution for 60 min at RT then washed five times in PBS. Secondary antibodies in blocking solution were applied for 60 min at RT and cells were washed five times in PBS. Cells were mounted using Ibidi mounting medium.

Cells were stained with chicken anti-GFP (1:1000, Abcam, UK) to amplify the sypHy signal, and either rabbit anti-RIM1/2 (1:500, Synaptic Systems, Germany) or mouse anti Synaptogmin-1 (1:100, Synaptic Systems). Appropriate secondary antibodies tagged with Alexa 488 or 647 (ThermoFisher Scientific) were used at 1:1000.

Fixed Cell Imaging and Analysis

The regions previously imaged live were located using the grid coordinates and imaged on an inverted Nikon Eclipse Ti spectral confocal microscope equipped with a 60x/1.40 NA oil objective using NIS Elements software. Excitation wavelengths were 405, 488, and 636 nm with bandpass emission filters set to 425–475 nm, 500–550 nm, and 662–737 nm. Microscope settings were kept the same for all images of the same antibodies. Z-stacks were generated from 0.15 μm optical sections, and maximum projections were produced in Image-J. To align the live and fixed images landmarks were selected in the GFP channel of both images, followed by affine transformation of the fixed image. ROIs from the live image were scaled and overlaid on the

registered GFP image for manual confirmation of the position. The GFP image was then thresholded using the 'Moments' algorithm in ImageJ to produce a mask, which was applied to the other channels of the fixed image to avoid the inclusion of neighboring puncta in the ROI. Intensity values for each ROI were then calculated from the masked images.

Statistical Analysis

Mean responses are displayed ±SEM unless otherwise stated, and n = the total number of synapses. As data are not normally distributed, non-parametric statistical tests have been used.

RESULTS

To generate a single molecule reporter of both presynaptic calcium influx and synaptic vesicle exocytosis, the R-GECO1 fragment was amplified from SyRGECO (Walker et al., 2013) and subcloned downstream of sypHy (Granseth et al., 2006) with a short linker sequence. The whole sequence was placed under control of the human synapsin I promoter to drive expression in neurons. The resultant syn::sypHy-R-GECO1 plasmid will hereafter be referred to as sypHy-RGECO (**Figure 1A**). With this probe, presynaptic calcium influx is reported by an increase in red fluorescence and exocytosis of synaptic vesicles by an increase in green fluorescence (**Figure 1A**). In dissociated hippocampal neurons transfected with sypHy-RGECO, punctate fluorescence in presynaptic boutons was observed in both green and red channels (**Figure 1B**). A field stimulation of 10 action potentials (APs) at 20 Hz was applied and individual boutons responded with increases in fluorescence in both channels (**Figure 1C**), the amplitudes of which (ΔG and ΔR) were highly correlated (**Figure 1D**).

In order to pool responses from multiple cells or synapses, baseline fluorescence is often used to normalize reporter responses. However, for pHluorins this value can be dominated by protein localized to the plasma membrane, which is approximately 20-fold brighter than the quenched vesicular protein (Sankaranarayanan et al., 2000), and is highly variable between synapses. One method that has been used to overcome this problem involved fusion of the red fluorescent protein tdimer2 to the C-terminus of sypHy, generating a reporter termed ratio-sypHy (Rose et al., 2013). The fixed stoichiometry of the two fluorophores in this probe allowed normalization of the sypHy signals to the tdimer2 fluorescence. Using the same reasoning, RGECO can be used not only as a calcium indicator, but to normalize both ΔG and ΔR responses. As baseline RGECO fluorescence (R_0) is relatively dim, we applied ionomycin in 2mM extracellular calcium to maximize the RGECO signal within the bouton (R_{max}). Both values (R_0 and R_{max}) were highly correlated (Supplementary Figure S1A) and were subsequently used as a normalizing factor for sypHy and RGECO responses. After ionomycin treatment, sypHy fluorescence also gradually increased to a plateau presumably due to vesicle release caused by the large influx of calcium. The maximum fluorescence in green and red channels was also highly correlated, reflecting the fixed ratio of the two fluorophores at all synapses (Supplementary Figure S1B). A similar correlation was observed when ionomycin treatment was combined with application of HBS containing 50mM NH_4Cl to alkalinize all compartments and maximize sypHy fluorescence (Supplementary Figure S1C). This contrasts with the less tight correlations observed between the baseline fluorescence values of the two channels, G_0 and R_0 (Supplementary Figure S1D), and between G_0 and G_{max} (Supplementary Figure S1E), which are likely affected by heterogeneity in the baseline fluorescence of sypHy. To directly measure the surface fraction of sypHy-RGECO, we compared the difference in sypHy fluorescence in external solutions at pH5.5 and pH7.4 to the sypHy fluorescence maximized by application of 50mM NH_4Cl. The surface fraction varied between synapses (Supplementary Figure S1F, mean = 30.8%, median = 24.8%) and was slightly higher than that reported for ratio-sypHy (median f_{surf} = 20%, Rose et al., 2013). This may be due to the fact that as basal RGECO fluorescence is low, it was necessary to identify transfected cells using basal sypHy fluorescence, potentially biasing toward brighter cells with higher surface fractions.

SypHy-RGECO responses to a 10 AP stimulus from multiple cells were normalized and pooled, and a positive non-linear correlation between $\Delta G/R_{max}$ and $\Delta R/R_{max}$ was observed (**Figure 1E**), as expected from the non-linear relationship between calcium and exocytosis (Dodge and Rahamimoff, 1967) and similar to that seen in other imaging studies (Zhao C. et al., 2011; Ariel et al., 2012; Ermolyuk et al., 2012). The spread of the responses suggested that individual synapses differed in the amount of neurotransmitter released for a given influx of calcium, which can be evaluated by the ratio ΔG/ΔR. We observed a range of ratio values, the majority of which fell within a normal distribution, although a small number of synapses displayed very high release in comparison to calcium influx, an order of magnitude higher than the lowest ratios (**Figure 1F**). Thus, there is heterogeneity in the calcium dependence of release between synapses.

When using ratiometric imaging, differential bleaching of the fluorophores could pose a potential problem. In boutons imaged without stimulation, sypHy fluorescence decayed by only 2% during the imaging period. This decay could be fit with a double exponential, with time constants of 1.64 s and 3172 s (Supplementary Figure S2A). Frames within the first time constant were therefore disregarded and frames from 1 s before the stimulus were used to calculate baseline fluorescence. The slow phase of bleaching, which accounted for 98.5% of the decay, had a negligible effect on either baseline fluorescence or maximum ΔG amplitude and was not corrected for, although this would need to be considered if imaging over a long period or using this probe to measure vesicular endocytosis rates. RGECO did not exhibit bleaching, instead showing an initial rapid increase in fluorescence that plateaued, the reasons for which will be discussed in more detail below (Supplementary Figure S2B). The rapid initial changes in fluorescence suggested that sequential images may be affected by differential bleaching. To test this, cells were stimulated with 10 AP stimuli five times, with a 1 min interval between images. The average ΔG and ΔR responses both decreased over the trials, with a slightly greater decrease in the calcium response (Supplementary Figure S2C).

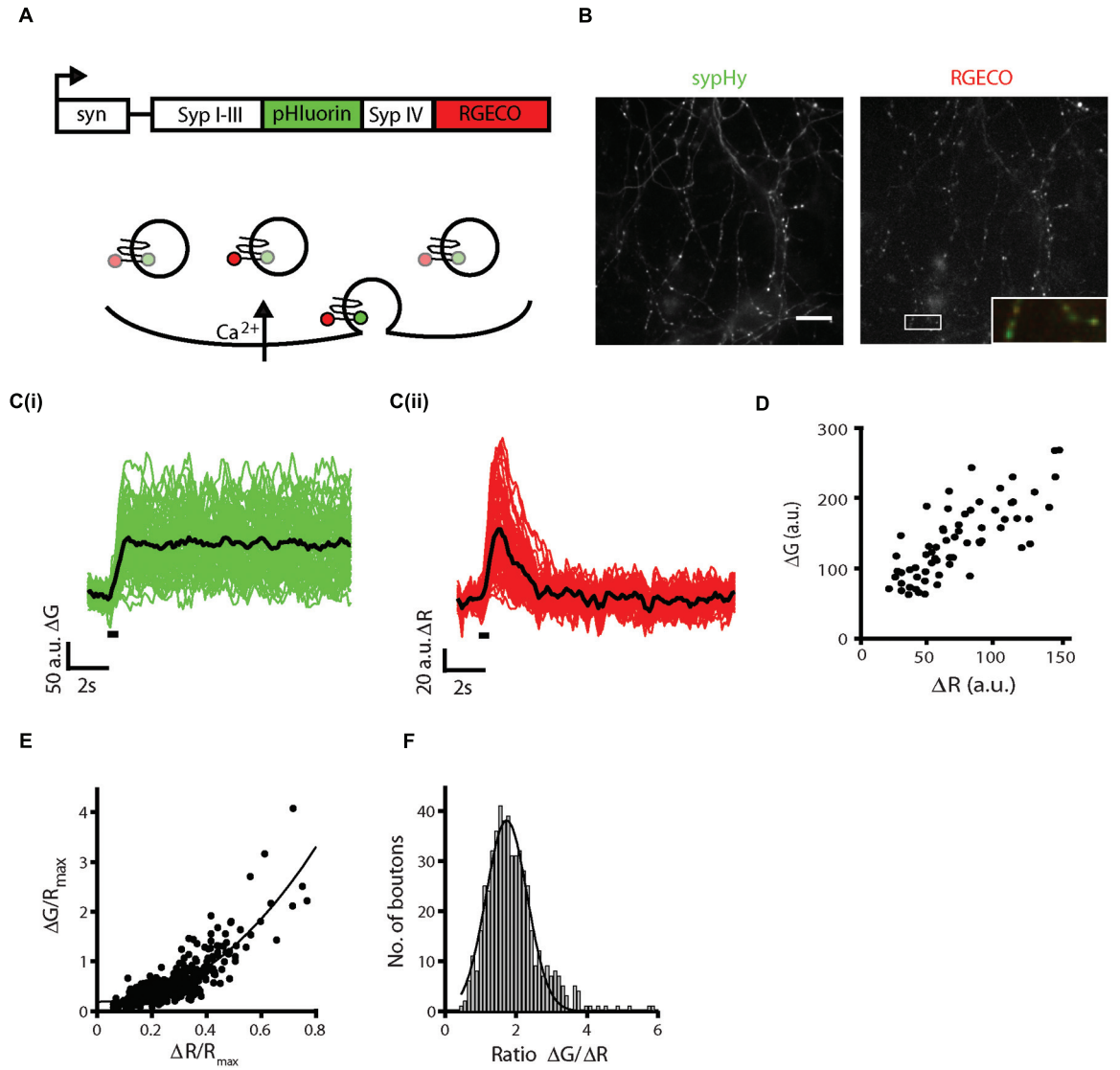

FIGURE 1 | Generation and characterization of sypHy-RGECO. (A) Schematic of the sypHy-RGECO construct and its function. Presynaptic calcium influx is reported by an increase in RGECO fluorescence, situated on the cytoplasmic tail of synaptophysin, whilst exocytosis is reported by an increase in pHluorin fluorescence situated in the vesicle lumen. **(B)** Representative images of a dissociated hippocampal cell expressing sypHy-RGECO. Scale bar 20 μm. Inset shows merge of the two channels for the boxed region. **(C)** Changes in sypHy (**i**, ΔG) and RGECO (**ii**, ΔR) fluorescence in response to a field stimulus of 10 APs at 20 Hz. ($n = 65$ synapses from 1 coverslip, traces representing individual synapse responses shown in green/red, mean response of all synapses shown in black, stimulation period shown by black bar). **(D)** ΔG and ΔR responses are correlated (Spearman's rank correlation $r_s = 0.766$, $p < 0.001$). **(E)** Cells were stimulated five times with a 10 AP 20 Hz stimulus. A mean response across trials was calculated and normalized to the maximum RGECO fluorescence in 200 μM ionomycin for each synapse. $\Delta G/R_{max}$ and $\Delta R/R_{max}$ responses from multiple cells show a non-linear correlation ($r_s = 0.727$, $p < 0.0001$, $n = 526$ synapses, from 9 coverslips and 5 independent cultures). The black line shows a fit to a power function of the form ax^b+c, where $b = 2.18$. **(F)** Distribution of values for the ratio $\Delta G/\Delta R$, a measure of the calcium dependence of release (for the same synapses as in **E**).

The reasons for these decreases are not clear, and may be different for the two responses. RGECO did not exhibit bleaching across trials, whilst the baseline fluorescence of sypHy decreased by approximately 20% (Supplementary Figure S2C). It has previously been suggested that GECIs targeted to the presynaptic compartment can exhibit rundown in responses (Walker et al., 2013), whereas the responses of synaptic pHluorins are similar across repeated trials (Burrone et al., 2006). However, the ratio of the two responses remained relatively stable across trials, increasing by only 9% between the first and fifth repeat (Supplementary Figure S2C). To avoid any inherent bias due to the effect of repeated trials we interspersed different stimulation conditions, such as number or frequency of AP stimuli.

It has previously been reported that R-GECO1 displays photoactivation when illuminated with 488 nm light (Akerboom et al., 2013), which may explain the increase in red fluorescence

observed in unstimulated boutons (Supplementary Figure S2B). To examine if this phenomenon affected sypHy-RGECO calcium responses, single channel images, illuminated with 585 nm light only, were compared to our usual imaging conditions, alternating 470 and 585 nm light. ΔR responses were larger in images taken with 585 nm light only (Supplementary Figure S2C, upper trace), although when scaled for comparison, the kinetics of the response were the same in both imaging conditions (Supplementary Figure S2C, lower trace). The response amplitudes and baseline fluorescence in single channel and two channel images were highly correlated and, importantly, scaled linearly (Supplementary Figures S2D,E). These results suggested that in our imaging conditions, fast alterations between blue and green excitation light reduces the size of the RGECO responses in a multiplicative manner, without the introduction of non-linear artifacts.

To characterize the sypHy-RGECO response to different stimulus strengths, stimuli ranging from 1 AP to 20 AP at 20 Hz were delivered by field stimulation. Both responses increased linearly over the range of stimulus strengths tested (**Figures 2A,B**), as has been previously reported for SyRGECO (Walker et al., 2013). Peak ΔG and ΔR responses to different numbers of action potentials also showed a strong linear correlation (**Figure 2C**). The mean ratio between vesicle exocytosis and calcium influx did not differ between 5, 10, and 20 AP stimuli (**Figure 2D**). The mean ratio was significantly increased at lower stimulus strengths, although many synapses that responded at higher stimulus strengths fell below the detection threshold in the 1 AP and 2 AP stimuli, potentially biasing toward synapses with higher release probabilities in these groups. At higher numbers of APs, the longer stimulation times required would begin to overlap with the endocytosis and reacidification of synaptic vesicles, making the amplitude of sypHy responses harder to interpret. However, to check for potential saturation of the probe we also delivered 40 and 100 AP stimuli at 20 Hz. The calcium response indicated by RGECO was saturated at 40 APs and displayed no further increase in amplitude to a 100 AP stimulus, whilst sypHy responses continued to increase with longer stimulation trains (Supplementary Figure S3).

We next tested the effect of changing the external calcium concentration, recording sypHy-RGECO responses in both 0.5 mM and 2 mM calcium for the same set of synapses. As expected, both the calcium influx and level of vesicle release were significantly reduced in 0.5 mM calcium (**Figure 3A**), although the positive correlation between the two responses was maintained (**Figure 3B**). For synapses which responded above threshold in both conditions, the distribution of ΔG/ΔR ratios was not significantly different between the two concentrations (**Figure 3C**), although the ratios measured for 0.5 mM calcium showed a skewed distribution toward higher values. This discrepancy is likely due to the saturation of the vesicular sensor of exocytosis for higher calcium concentrations, as reported previously (Ermolyuk et al., 2012).

Calcium influx at the presynaptic terminal is predominantly mediated by $Ca_V2.1$ and 2.2 channels, with some contribution from $Ca_V2.3$ (Takahashi and Momiyama, 1993; Wheeler et al., 1994; Gasparini et al., 2001). The contribution of different channel subtypes to the presynaptic calcium signal varies not only between synapses, but also with stimulation frequency (Ricoy and Frerking, 2014). We stimulated neurons expressing sypHy-RGECO with 10 APs at 5, 20, and 83 Hz, to examine whether stimulation frequency affected the relationship between ΔG and ΔR responses. Pooled ΔG and ΔR responses across all frequencies showed the expected non-linear relationship (**Figure 3D**). Both calcium influx and vesicle exocytosis were significantly reduced at 83 Hz stimulation, which could be due to the failure of the cell to fire action potentials at high frequency, or to the inactivation of calcium channels (**Figures 3D,E**). However, the distributions of ΔG/ΔR ratios were indistinguishable between stimulation frequencies (**Figure 3F**), suggesting frequency did not alter the relationship between calcium influx and vesicle release.

Synaptic boutons are heterogeneous in both structural and functional parameters. Studies of the relationship between the two show that bouton volume is a poor predictor of functional properties such as presynaptic calcium influx and the synaptic probability of release (Ermolyuk et al., 2012; Holderith et al., 2012), whereas active zone size strongly correlates with function (Holderith et al., 2012). Additionally, levels of the active zone proteins RIM1/2 are highly correlated with active zone size (Holderith et al., 2012). To examine the relationship between sypHy-RGECO responses and active zone size, neurons were first imaged live, whilst stimulating with 10 APs at 20 Hz, and subsequently fixed and stained for RIM1/2. Live and fixed images were aligned to allow the comparison of functional and structural data from individual identified synapses (**Figure 4A** and Supplementary Figure S4). We observed significant positive correlations between RIM levels and both sypHy and RGECO responses (**Figure 4Bi,ii**). Whilst significant, these correlations are weaker than those found in ultrastructural studies, most likely due to limitations in the alignment process and the lower resolution of light microscopy. Interestingly, RIM levels also correlated significantly, albeit weakly, with the ratio ΔG/ΔR (**Figure 4Biii**), possibly reflecting the role of RIM, along with RIM binding protein (RBP), in localizing calcium channels to the active zone (Kaeser et al., 2011), vesicle docking (Han et al., 2011) and coupling of calcium channels to release (Kaeser et al., 2012).

Similar correlations were also carried out with staining for the putative calcium sensor for synchronous neurotransmitter release, synaptotagmin-1 (Syt1) (Geppert et al., 1994; Fernandez-Chacon et al., 2001). We found that the levels of Syt1 were positively correlated with the magnitude of the RGECO response, and showed a trend toward a positive correlation with neurotransmitter release that did not reach significance (**Figures 4Ci,ii**). However, the ratio of release to calcium influx at each synapse was not related to the level of Syt1 (**Figure 4Ciii**). As the neurons were stimulated with a train of APs at high frequency (20 Hz), both synchronous and asynchronous forms of release are expected to operate (Hagler and Goda, 2001), and thus the levels of other calcium sensors may be more important in determining the total release that occurs in response to this type of stimulus. Furthermore, approximately

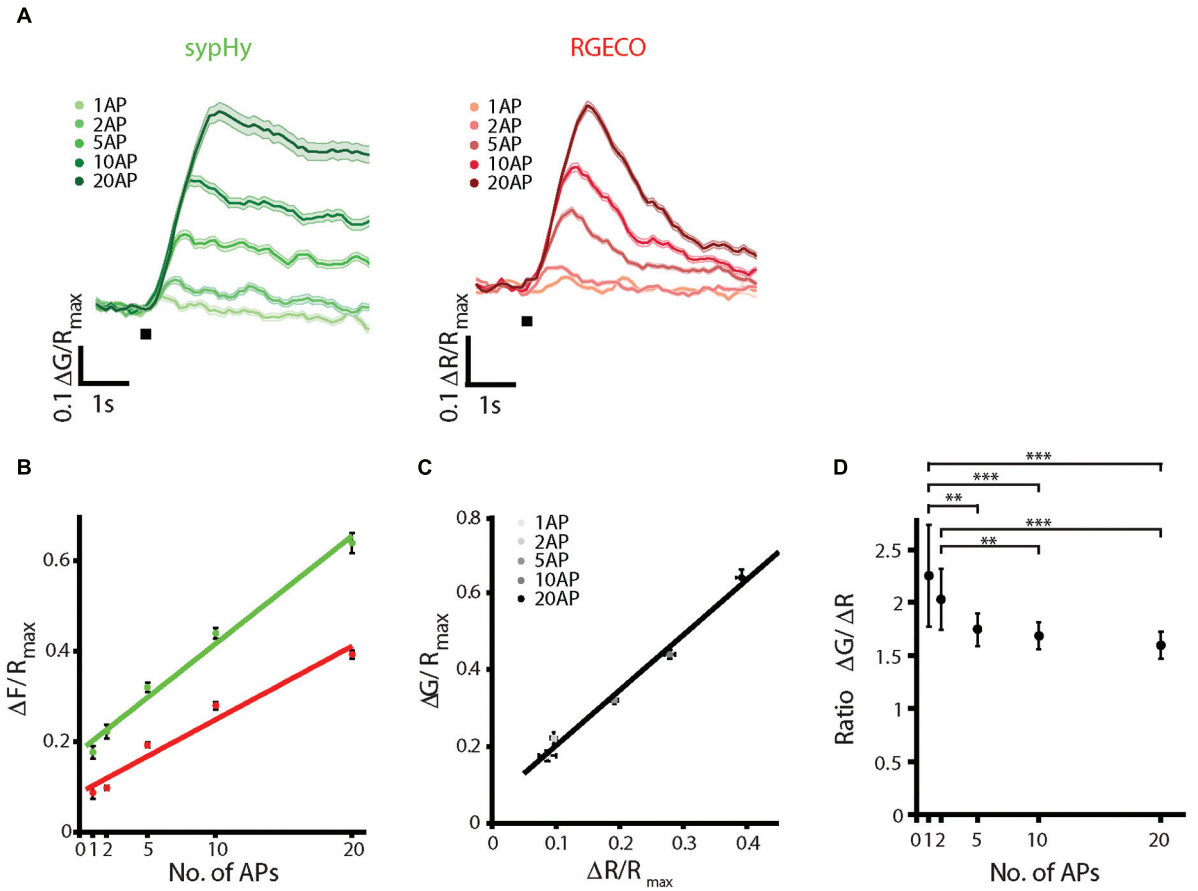

FIGURE 2 | SypHy-RGECO responses to different stimulus strengths. A range of AP stimuli were delivered by field stimulation at 20 Hz. Each stimulus was repeated twice, varying the order in which different numbers of APs were given, and a mean of the two responses was taken. **(A)** Mean sypHy and RGECO responses to different numbers of APs, the black bar indicates the start of stimulation. **(B)** Peak $\Delta G/R_{max}$ (green) and $\Delta R/R_{max}$ responses (red) increase linearly over the range of AP stimuli tested (colored lines indicate linear regression fit: sypHy, green, $r^2 = 0.986$, RGECO, red, $r^2 = 0.961$). **(C)** Correlation between peak $\Delta G/R_{max}$ and $\Delta R/R_{max}$ responses over the range of APs tested (black line indicates linear fit, $r^2 = 0.989$). **(D)** Ratio $\Delta G/\Delta R$ for each of the stimulus strengths tested. Only the ratios for 1 and 2 APs show a significant difference from the other stimuli (one way ANOVA,$^{**}p < 0.01$,$^{***}p < 0.001$). All plots show mean ±SEM, $n = 171$ synapses from 4 coverslips and two independent cultures.

20% of total Syt1 is found on the surface of the bouton, not on vesicles (Fernandez-Alfonso et al., 2006), thus the level of Syt1 present at the bouton may not accurately reflect the size of the vesicle pool. Together, our data is in broad agreement with the general principle that synapses that have larger active zones also show higher levels of calcium influx and neurotransmitter release. Although the overall levels of Syt1 at the synapse also broadly correlated with these functional measures, they were a worse predictor of synapse function than RIM.

DISCUSSION

We have generated a single molecule reporter, sypHy-RGECO, for concurrent imaging of presynaptic calcium influx and synaptic vesicle recycling. This hybrid molecule consisted of a red calcium indicator, R-GECO1 (Zhao Y. et al., 2011), fused to the C-terminus of sypHy, a reporter of vesicle exocytosis and endocytosis (Granseth et al., 2006). Combining the two reporters in one molecule offers several advantages. First, it provides two independent readouts of presynaptic function, without the need for co-expression of multiple probes. Second, as the probes are not separated spatially and a fixed ratio of the two fluorophores is present at all synapses, it provides a way of normalizing sypHy signals across synapses and cells, in a manner similar to that employed for ratio-sypHy (Rose et al., 2013). This is particularly important for sypHy signals, where resting levels of fluorescence vary quite dramatically from bouton to bouton and do not correlate directly with the amount probe at the synapse, but rather to its surface levels. Finally, the fixed stoichiometry also allows a direct comparison of the two fluorescence responses, thereby providing a direct measure of the calcium dependence of release within single presynaptic boutons.

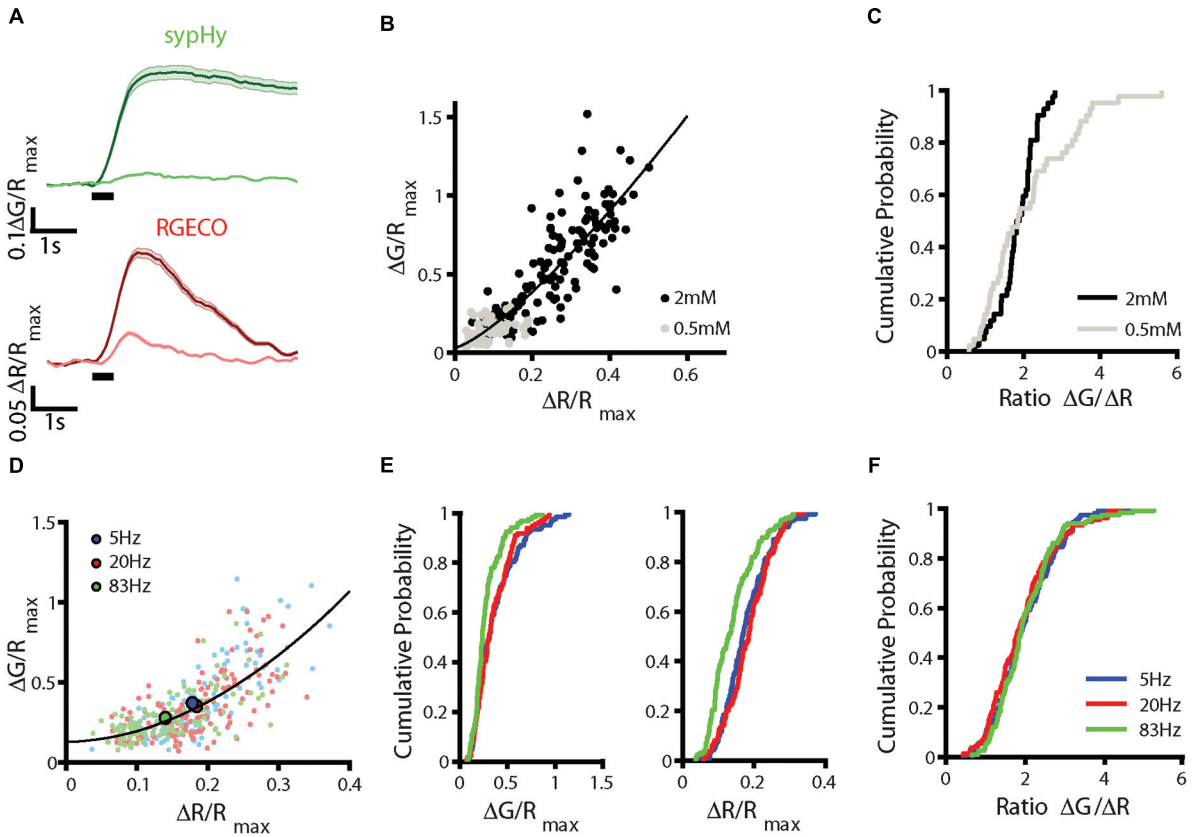

FIGURE 3 | Effects of altering stimulation conditions. (A–C) Dissociated hippocampal neurons in external solution (HBS) containing 0.5 mM calcium were stimulated with a train of 10 APs at 20 Hz repeated five times 1 min apart. The solution was replaced with HBS containing 2 mM calcium and the stimulus set repeated. Responses across trials were averaged for each synapse. **(A)** Fluorescence changes in sypHy (upper traces) and RGECO (lower traces) in 0.5 and 2 mM. Traces show mean ± SEM for $n = 131$ synapses from 3 coverslips from 3 independent cultures. **(B)** Correlation between peak $\Delta G/R_{max}$ and $\Delta R/R_{max}$ responses for these synapses (Spearman's rank correlation $r_s = 0.873$, $p < 0.001$, the black line indicates a fit to a power function of the form ax^b+c, where $b = 1.30$.) **(C)** Distribution of $\Delta G/\Delta R$ ratios for synapses which responded above threshold at both calcium concentrations, ratios shown are averaged from the last two 0.5 mM trials (gray) and the first two 2 mM trials (black) ($n = 47$ synapses). The distribution is not significantly different between concentrations (Kolmogorov–Smirnov test, $p = 0.093$). **(D–F)** Hippocampal neurons were stimulated with 10 APs at 5, 20, and 83 Hz. Each set of stimuli was repeated three times, varying the order in which the frequencies were delivered and the mean of the trials was calculated. **(D)** Correlation between peak $\Delta G/R_{max}$ and $\Delta R/R_{max}$ values at 5 Hz (blue), 20 Hz (red), and 83 Hz (green). Mean responses to each frequency are shown in the larger, brighter points ($n = 134$ synapses from 3 coverslips and three independent cultures, the black line indicates a fit to a power function of the form ax^b+c, where $b = 1.91$). **(E)** Distribution of $\Delta G/R_{max}$ (left) and $\Delta R/R_{max}$ (right) responses for these synapses show a decrease in the responses at 83 Hz compared to 20 Hz (Kolmogorov–Smirnov test, $\Delta G/R_{max}$ $p = 0.0013$, $\Delta R/R_{max}$ $p < 0.001$) but no change in the response at 5 Hz (Kolmogorov–Smirnov test $\Delta G/R_{max}$ $p = 0.537$, $\Delta R/R_{max}$ $p = 0.240$). **(F)** The distribution of $\Delta G/\Delta R$ ratios does not change between stimulus frequencies (Kolmogorov–Smirnov test 5 Hz $p = 0.703$, 83 Hz $p = 0.282$).

We observed a strong non-linear correlation between calcium influx and vesicle exocytosis across synapses that was maintained in response to different stimulation conditions, in agreement with many previous studies (Ariel et al., 2012; Ermolyuk et al., 2012). Using the ratio of the sypHy response to the RGECO response ($\Delta G/\Delta R$), we were also able to measure the calcium-dependence of release at individual presynaptic boutons, a feature that has been difficult to study in these small CNS synapses. Interestingly, we observed heterogeneity in this value, suggesting that calcium triggers vesicle fusion with different efficiencies at different synapses. It is not yet clear what underlies this variation, as the distribution of $\Delta G/\Delta R$ ratios did not change significantly under different stimulation conditions, such as stimulation frequency and extracellular calcium, despite changes in the amplitude of both calcium and exocytosis signals. A possible source of this variation may be the repertoire of presynaptic calcium channel subtypes, which can vary between synapses (Reid et al., 1997; Nimmervoll et al., 2013). In support of this, individual boutons displayed differential sensitivity to pharmacological blockade of $Ca_V2.1$ and 2.2 channels in both calcium influx measured by GCaMP3 and exocytosis measured by sypHTomato, when these reporters were co-expressed in the same cell (Li and Tsien, 2012). Similarly, in another study in which calcium and vesicle dynamics were imaged in separate cells, pharmacological inhibition of $Ca_V2.1$ or 2.2 led to variable blockade of neurotransmitter release between individual synapses, although this did not alter the relationship between calcium and exocytosis measured across the synapse population (Ariel et al., 2012). However, neither

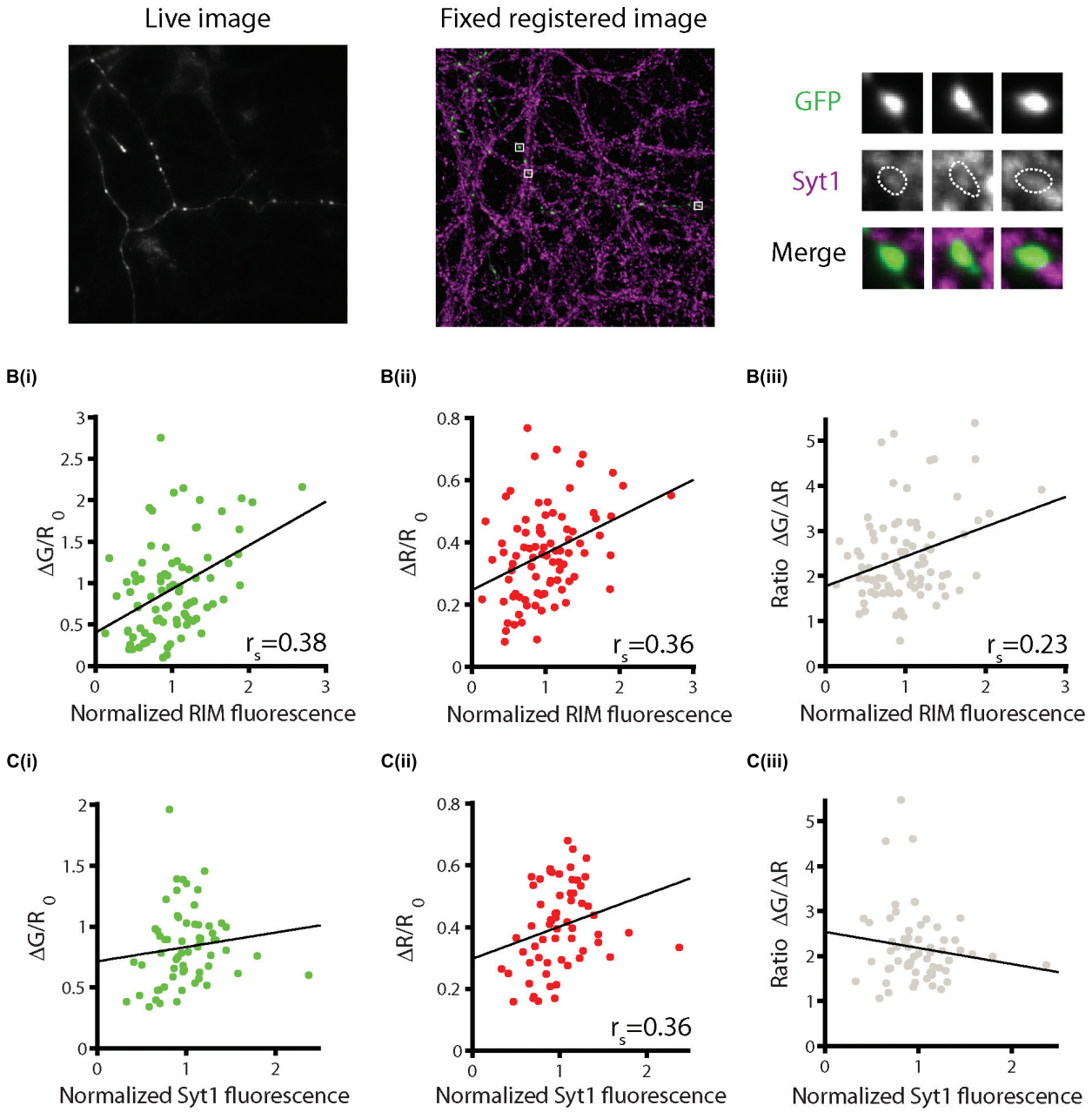

FIGURE 4 | Combining functional imaging with sypHy-RGECO and immunofluorescence. Neurons were stimulated five times with 10 APs at 20 Hz and the responses averaged across trials. Cells were then fixed and stained for presynaptic markers and imaged using confocal microscopy. Live and fixed images were registered and fluorescence intensities for individual synapses were measured. **(A)** Example of a live image of the green channel of sypHy-RGECO (left) and fixed image (middle) of GFP and synaptotagmin-1 (Syt1) for the same cell. Right, magnified view of individual synapses. **(B)** Positive correlations between levels of RIM and sypHy responses (**i**, green, $p < 0.001$), RGECO responses (**ii**, red, $p < 0.001$), and the $\Delta G/\Delta R$ ratio (**iii**, gray, $p = 0.039$), ($n = 85$ synapses from 3 dishes from independent cultures). **(C)** Levels of Syt1 are not significantly correlated with sypHy responses (**i**, $p = 0.059$), or the $\Delta G/\Delta R$ ratio (**iii**, $p = 0.323$), but are correlated with the calcium response (**ii**, $p = 0.005$) ($n = 62$ synapses from three dishes from independent cultures).

of these studies directly examined the relationship between channel subtypes and the calcium dependence of release in individual boutons, which could be addressed using sypHy-RGECO.

An alternative possibility is that individual boutons differ in the levels or components of the molecular machinery that links calcium influx to vesicle release. Of the markers that we examined using *post hoc* immunofluorescence, the level of the

calcium sensor synaptotagmin-1 was not related to the ΔG/ΔR ratio, although a weak correlation was observed with the level of RIM, an active zone protein with roles in the localization of calcium channels and vesicle docking (Han et al., 2011). Whilst absolute RIM levels are only weakly predictive of the ratio, it is possible that more nuanced features such as the size and shape of the active zone relative to the bouton volume, and positioning of elements such as calcium channels within it may affect the calcium dependence of release at individual synapses. Combining functional imaging with structural imaging by immunofluorescence, super-resolution, or electron microscopy will enable investigation of these possibilities. Such methods could also be used to examine if differences in the calcium dependence of release exist in different cell types, or to study the relationship between presynaptic function and postsynaptic properties at individual connections.

Finally, it would be interesting to examine if the calcium dependence of release is fixed for an individual synapse or is subject to regulation. Calcium influx and vesicle exocytosis have been measured individually after chronic changes in network activity, and the changes observed indicate that the relationship between the two is not altered at the population level following homeostatic plasticity (Zhao C. et al., 2011). However, this is yet to be studied simultaneously in single synapses. Furthermore, it is unknown if short-term plasticity mechanisms involve changes in the efficiency with which calcium triggers vesicle fusion. Tools such as sypHy-RGECO will enable optical interrogation of these questions.

Several spectrally distinct genetically encoded reporters of calcium and vesicle recycling have been developed, offering the opportunity to combine probes with different characteristics. We selected to combine sypHy and R-GECO1 for several reasons; synaptophysin has previously been shown to tolerate addition of both pHluorin in the intravesicular loop with a second fluorophore at the C-terminus (Rose et al., 2013), and both sypHy and SyRGECO have previously been characterized individually (Granseth et al., 2006; Walker et al., 2013). SypHy has a superior signal-to-noise ratio than synaptopHluorin and whilst VGLUT-pHluorin offers further improvement in this aspect (Voglmaier et al., 2006), there is a risk that VGLUT1 overexpression may cause an increase in quantal content (Wojcik et al., 2004; Wilson et al., 2005), and therefore alter the strength of synaptic connections. Additionally, although VGLUT based probes have been used in inhibitory neurons, it may impart GABAergic boutons with unwanted properties resulting from the overexpression of a transporter not usually found in these neurons. R-GECO1 is a sensitive calcium indicator with a wide dynamic range that exhibits a larger fluorescence change to field stimuli than the RCaMP1 sensors (Akerboom et al., 2013; Walker et al., 2013). RCaMP2 (Inoue et al., 2015) offers greater sensitivity than R-GECO1 but saturates at approximately 8 APS and was therefore less suitable for combination with sypHy, for which longer stimulus trains are typically used. The ΔF/F responses of R-GECO1 are also linear over a greater range of calcium concentrations than RCaMP1 sensors (Akerboom et al., 2013). When combined in the single molecule sypHy-RGECO, both reporters displayed a linear increase in the amplitude of the response across the range of 1–20 AP stimuli delivered at 20 Hz, but at higher stimulus strengths the RGECO response became saturated. Whilst sypHy responses continued to increase to both 40 and 100 AP stimuli, the amplitude of these responses will be affected by the decrease in fluorescence caused by endocytosis and reacidifcation of vesicles. The dynamic ranges of the two reporters are therefore well matched and suited to reporting activity up to 20 action potentials.

One potential disadvantage of combining R-GECO1 with green sensors of vesicle exocytosis is its photoswitching behavior in response to 488 nm light (Akerboom et al., 2013). Indeed, we found that blue light exposure in our imaging conditions did cause an offset in the basal RGECO fluorescence, as well as a reduction in the calcium response. However, these decreases scaled linearly with the original R-GECO1 response, and both the kinetics of the calcium transient and the range of responses across synapses were preserved. SypHy-RGECO is therefore a useful addition to the expanding toolbox of genetically encoded reporters, and will enable a detailed study of the relationship between calcium influx and vesicle dynamics at individual synapses. Whilst we have shown proof of principle in hippocampal synapses *in vitro*, this reporter could also be used to study these processes in more intact systems, such as brain slices and *in vivo*.

AUTHOR CONTRIBUTIONS

JB and RJ designed experiments, RJ performed experiments, analyzed data, and drafted the manuscript, JB and RJ edited and approved the manuscript.

FUNDING

This work was funded by an ERC consolidator grant, a Wellcome Trust Investigator award and a Lister Institute Prize to JB.

ACKNOWLEDGMENTS

We would like to thank Mideia Kotsogianni for the preparation of dissociated hippocampal cultures, Robert E. Campbell for the R-GECO1 plasmid (Addgene plasmid 32444) and Leon Lagnado for the sypHy plasmid (Addgene plasmid 24478).

SUPPLEMENTARY MATERIAL

The Supplementary Material for this article can be found online at: http://journal.frontiersin.org/article/10.3389/fnsyn.2016.00021

REFERENCES

Akerboom, J., Carreras Calderon, N. Tian, L., Wabnig, S., Prigge, M., Tolo, J., et al. (2013). Genetically encoded calcium indicators for multi-color neural activity imaging and combination with optogenetics. *Front. Mol. Neurosci.* 6:2. doi: 10.3389/fnmol.2013.00002

Akerboom, J., Chen, T. W., Wardill, T. J., Tian, L., Marvin, J. S., Mutlu, S., et al. (2012). Optimization of a GCaMP calcium indicator for neural activity imaging. *J. Neurosci.* 32, 13819–13840. doi: 10.1523/JNEUROSCI.2601-12.2012

Ariel, P., Hoppa, M. B., and Ryan, T. A., (2012). Intrinsic variability in Pv, RRP size, Ca(2^+) channel repertoire, and presynaptic potentiation in individual synaptic boutons. *Front. Synaptic Neurosci.* 4:9. doi: 10.3389/fnsyn.2012.00009

Broussard, G. J., Liang, R., and Tian, L. (2014). Monitoring activity in neural circuits with genetically encoded indicators. *Front. Mol. Neurosci.* 7:97. doi: 10.3389/fnmol.2014.00097

Burrone, J., Li, Z., and Murthy, V. N., (2006). Studying vesicle cycling in presynaptic terminals using the genetically encoded probe synaptopHluorin. *Nat. Protoc.* 1, 2970–2978. doi: 10.1038/nprot.2006.449

Chen, T. W., Wardill, T. J., Sun, Y., Pulver, S. R., Renninger, S. L., Baohan, A., et al. (2013). Ultrasensitive fluorescent proteins for imaging neuronal activity. *Nature* 499, 295–300. doi: 10.1038/nature12354

Dana, H., Mohar, B., Sun, Y., Narayan, S., Gordus, A., Hasseman, J. P., et al. (2016). Sensitive red protein calcium indicators for imaging neural activity. *Elife* 5:e12727. doi: 10.7554/eLife.12727

Dodge, F. A. Jr., and Rahamimoff, R. (1967). Co-operative action a calcium ions in transmitter release at the neuromuscular junction. *J. Physiol.* 193, 419–432. doi: 10.1113/jphysiol.1967.sp008367

Dreosti, E., Odermatt, B., Dorostkar, M. M., and Lagnado, L. (2009). A genetically encoded reporter of synaptic activity in vivo. *Nat. Methods* 6, 883–889. doi: 10.1038/nmeth.1399

Ermolyuk, Y. S., Alder, F. G., Henneberger, C., Rusakov, D. A., Kullmann, D. M., and Volynski, K. E. (2012). Independent regulation of basal neurotransmitter release efficacy by variable Ca^{2+} influx and bouton size at small central synapses. *PLoS Biol.* 10:e1001396. doi: 10.1371/journal.pbio.1001396

Fernandez-Alfonso, T., Kwan, R., and Ryan, T. A., (2006). Synaptic vesicles interchange their membrane proteins with a large surface reservoir during recycling. *Neuron* 51, 179–186. doi: 10.1016/j.neuron.2006.06.008

Fernandez-Chacon, R., Konigstorfer, A., Gerber, S. H., Garcia, J., Matos, M. F., Stevens, C. F., et al. (2001). Synaptotagmin I functions as a calcium regulator of release probability. *Nature* 410, 41–49. doi: 10.1038/35065004

Gasparini, S., Kasyanov, A. M., Pietrobon, D., Voronin, L. L., and Cherubini, E. (2001). Presynaptic R-type calcium channels contribute to fast excitatory synaptic transmission in the rat hippocampus. *J. Neurosci.* 21, 8715–8721.

Geppert, M., Goda, Y., Hammer, R. E., Li, C., Rosahl, T. W., Stevens, C. F., et al. (1994). Synaptotagmin I: a major Ca^{2+} sensor for transmitter release at a central synapse. *Cell* 79, 717–727. doi: 10.1016/0092-8674(94)90556-8

Granseth, B., Odermatt, B., Royle, S. J., and Lagnado, L. (2006). Clathrin-mediated endocytosis is the dominant mechanism of vesicle retrieval at hippocampal synapses. *Neuron* 51, 773–786. doi: 10.1016/j.neuron.2006.08.029

Hagler, D. J. Jr., and Goda, Y. (2001). Properties of synchronous and asynchronous release during pulse train depression in cultured hippocampal neurons. *J. Neurophysiol.* 85, 2324–2334.

Han, Y., Kaeser, P. S., Sudhof, T. C., and Schneggenburger, R. (2011). RIM determines Ca^{2+} channel density and vesicle docking at the presynaptic active zone. *Neuron* 69, 304–316. doi: 10.1016/j.neuron.2010.12.014

Heidelberger, R., and Matthews, G. (1992). Calcium influx and calcium current in single synaptic terminals of goldfish retinal bipolar neurons. *J. Physiol.* 447, 235–256. doi: 10.1113/jphysiol.1992.sp019000

Holderith, N., Lorincz, A., Katona, G., Rozsa, B., Kulik, A., Watanabe, M., et al. (2012). Release probability of hippocampal glutamatergic terminals scales with the size of the active zone. *Nat. Neurosci.* 15, 988–997. doi: 10.1038/nn.3137

Inoue, M., Takeuchi, A., Horigane, S., Ohkura, M., Gengyo-Ando, K., Fujii, H., et al. (2015). Rational design of a high-affinity, fast, red calcium indicator R-CaMP2. *Nat. Methods* 12, 64–70. doi: 10.1038/nmeth.3185

Kaeser, P. S., Deng, L., Fan, M., and Sudhof, T. C., (2012). RIM genes differentially contribute to organizing presynaptic release sites. *Proc. Natl. Acad. Sci. U.S.A.* 109, 11830–11835. doi: 10.1073/pnas.1209318109

Kaeser, P. S., Deng, L., Wang, Y., Dulubova, I., Liu, X., Rizo, J., et al. (2011). RIM proteins tether Ca^{2+} channels to presynaptic active zones via a direct PDZ-domain interaction. *Cell* 144, 282–295. doi: 10.1016/j.cell.2010.12.029

Li, H., Foss, S. M., Dobryy, Y. L., Park, C. K., Hires, S. A., Shaner, N. C., et al. (2011). Concurrent imaging of synaptic vesicle recycling and calcium dynamics. *Front. Mol. Neurosci.* 4:34. doi: 10.3389/fnmol.2011.00034

Li, Y., and Tsien, R. W., (2012). pHTomato, a red, genetically encoded indicator that enables multiplex interrogation of synaptic activity. *Nat. Neurosci.* 15, 1047–1053. doi: 10.1038/nn.3126

Miesenbock, G., De Angelis, D. A., and Rothman, J. E. (1998). Visualizing secretion and synaptic transmission with pH-sensitive green fluorescent proteins. *Nature* 394, 192–195. doi: 10.1038/28190

Nakai, J., Ohkura, M., and Imoto, K. (2001). A high signal-to-noise Ca(2^+) probe composed of a single green fluorescent protein. *Nat. Biotechnol.* 19, 137–141. doi: 10.1038/84397

Nikolaou, N., Lowe, A. S., Walker, A. S., Abbas, F., Hunter, P. R., Thompson, I. D., et al. (2012). Parametric functional maps of visual inputs to the tectum. *Neuron* 76, 317–324. doi: 10.1016/j.neuron.2012.08.040

Nimmervoll, B., Flucher, B. E., and Obermair, G. J. (2013). Dominance of P/Q-type calcium channels in depolarization-induced presynaptic FM dye release in cultured hippocampal neurons. *Neuroscience* 253, 330–340. doi: 10.1016/j.neuroscience.2013.08.052

Ramirez, D. M., Khvotchev, M., Trauterman, B., and Kavalali, E. T. (2012). Vti1a identifies a vesicle pool that preferentially recycles at rest and maintains spontaneous neurotransmission. *Neuron* 73, 121–134. doi: 10.1016/j.neuron.2011.10.034

Reid, C. A., Clements, J. D., and Bekkers, J. M. (1997). Nonuniform distribution of Ca^{2+} channel subtypes on presynaptic terminals of excitatory synapses in hippocampal cultures. *J. Neurosci.* 17, 2738–2745.

Ricoy, U. M., and Frerking, M. E. (2014). Distinct roles for Cav2.1-2.3 in activity-dependent synaptic dynamics. *J. Neurophysiol.* 111, 2404–2413. doi: 10.1152/jn.00335.2013

Rose, T., Schoenenberger, P., Jezek, K., and Oertner, T. G. (2013). Developmental refinement of vesicle cycling at Schaffer collateral synapses. *Neuron* 77, 1109–1121. doi: 10.1016/j.neuron.2013.01.021

Sankaranarayanan, S., De Angelis, D., Rothman, J. E., and Ryan, T. A. (2000). The use of pHluorins for optical measurements of presynaptic activity. *Biophys. J.* 79, 2199–2208. doi: 10.1016/S0006-3495(00)76468-X

Schneggenburger, R., and Neher, E. (2000). Intracellular calcium dependence of transmitter release rates at a fast central synapse. *Nature* 406, 889–893. doi: 10.1038/35022702

Takahashi, T., and Momiyama, A. (1993). Different types of calcium channels mediate central synaptic transmission. *Nature* 366, 156–158. doi: 10.1038/366156a0

Tian, L., Hires, S. A., Mao, T., Huber, D., Chiappe, M. E., Chalasani, S. H., et al. (2009). Imaging neural activity in worms, flies and mice with improved GCaMP calcium indicators. *Nat. Methods* 6, 875–881. doi: 10.1038/nmeth.1398

Voglmaier, S. M., Kam, K., Yang, H., Fortin, D. L., Hua, Z., Nicoll, R. A., et al. (2006). Distinct endocytic pathways control the rate and extent of synaptic vesicle protein recycling. *Neuron* 51, 71–84. doi: 10.1016/j.neuron.2006.05.027

Vyleta, N. P., and Jonas, P. (2014). Loose coupling between Ca^{2+} channels and release sensors at a plastic hippocampal synapse. *Science* 343, 665–670. doi: 10.1126/science.1244811

Walker, A. S., Burrone, J., and Meyer, M. P. (2013). Functional imaging in the zebrafish retinotectal system using RGECO. *Front. Neural Circ.* 7:34. doi: 10.3389/fncir.2013.00034

Wheeler, D. B., Randall, A., and Tsien, R. W. (1994). Roles of N-type and Q-type Ca^{2+} channels in supporting hippocampal synaptic transmission. *Science* 264, 107–111. doi: 10.1126/science.7832825

Wilson, N. R., Kang, J., Hueske, E. V., Leung, T., Varoqui, H., Murnick, J. G., et al. (2005). Presynaptic regulation of quantal size by the vesicular glutamate transporter VGLUT1. *J. Neurosci.* 25, 6221–6234. doi: 10.1523/JNEUROSCI.3003-04.2005

Wojcik, S. M., Rhee, J. S., Herzog, E., Sigler, A., Jahn, R., Takamori, S., et al. (2004). An essential role for vesicular glutamate transporter 1 (VGLUT1) in postnatal development and control of quantal size. *Proc. Natl. Acad. Sci. U.S.A.* 101, 7158–7163. doi: 10.1073/pnas.0401764101

Zhao, C., Dreosti, E., and Lagnado, L. (2011). Homeostatic synaptic plasticity through changes in presynaptic calcium influx. *J. Neurosci.* 31, 7492–7496. doi: 10.1523/JNEUROSCI.6636-10.2011

Zhao, Y., Araki, S., Wu, J., Teramoto, T., Chang, Y. F., Nakano, M., et al. (2011). An expanded palette of genetically encoded Ca^{2+} indicators. *Science* 333, 1888–1891. doi: 10.1126/science.1208592

Conflict of Interest Statement: The authors declare that the research was conducted in the absence of any commercial or financial relationships that could be construed as a potential conflict of interest.

frontiers in Synaptic Neuroscience

METHODS
published: 19 August 2016
doi: 10.3389/fnsyn.2016.00024

Flash-and-Freeze: Coordinating Optogenetic Stimulation with Rapid Freezing to Visualize Membrane Dynamics at Synapses with Millisecond Resolution

Shigeki Watanabe [1, 2]*

[1] Department of Cell Biology, Johns Hopkins University, Baltimore, MD, USA, [2] The Solomon H. Snyder Department of Neuroscience, Johns Hopkins University, Baltimore, MD, USA

Electron microscopy depicts subcellular structures at synapses exquisitely but only captures static images. To visualize membrane dynamics, we have developed a novel technique, called flash-and-freeze, which induces neuronal activity with a flash of light and captures the membrane dynamics by rapid freezing. For characterizing membrane movements during synaptic transmission, a light-sensitive cation channel, channelrhodopsin, is heterologously expressed in mouse hippocampal neurons or in *Caenorhabditis elegans* motor neurons. A brief pulse of blue light activates channelrhodopsin and induces an action potential, leading to synaptic transmission. Following the light stimulation, neurons are frozen at different time intervals ranging from 10 ms to 20 s. Electron micrographs are then acquired from each time point to visualize the morphological changes. Using this approach, we have characterized a novel form of endocytosis, ultrafast endocytosis, which rapidly removes excess membrane added to the surface during neurotransmission. The flash-and-freeze approach can be adapted to study other cellular phenomena that can be induced by light-sensitive genetic or pharmacological tools.

Keywords: flash-and-freeze, synaptic transmission, synaptic cell biology, synaptic vesicle exocytosis, synaptic vesicles, optogenetics, high-pressure freezing, electron microscopy

OPEN ACCESS

Edited by:
George Augustine,
Nanyang Technologicial University, Singapore

Reviewed by:
Tom Reese,
National Institutes of Health, USA
Ruud Toonen,
Vrije Universiteit Amsterdam, Netherlands

***Correspondence:**
Shigeki Watanabe
shigeki.watanabe@jhmi.edu

Received: *25 May 2016*
Accepted: *03 August 2016*
Published: *19 August 2016*

Citation:
Watanabe S (2016) Flash-and-Freeze: Coordinating Optogenetic Stimulation with Rapid Freezing to Visualize Membrane Dynamics at Synapses with Millisecond Resolution. Front. Synaptic Neurosci. 8:24. doi: 10.3389/fnsyn.2016.00024

INTRODUCTION

Imaging Neurons

To process information at synapses, membrane trafficking takes place on a millisecond time scale. When a nerve impulse arrives at synaptic terminals, synaptic vesicles fuse with the plasma membrane within 1 ms (Heuser and Reese, 1981). Subsequently, vesicle membrane and proteins are recovered from the plasma membrane to reconstitute new vesicles (Dittman and Ryan, 2009; Saheki and De Camilli, 2012). One major challenge in studying membrane dynamics at synapses is visualizing these rapid events at the spatial resolution necessary to resolve individual vesicles and temporal resolution relevant to synaptic functions. Several methods have been developed over the years including electrophysiological, optical, and electron microscopy methods.

Capacitance measurements of synaptic terminals allow monitoring of membrane flux at the plasma membrane with sub-millisecond temporal resolution (Hamill et al., 1981; Neher and Marty, 1982). The capacitance across a membrane is proportional to the membrane area.

Direct patch-clamping of synaptic boutons shows an increase in the capacitance during exocytosis and a decrease during endocytosis (von Gersdorff and Matthews, 1994; Sun et al., 2002; Delvendahl et al., 2016). This method has a single vesicle sensitivity. However, it is blind to the locations of the membrane insertion and removal. Furthermore, membrane trafficking within the cytosol cannot be visualized by this technique.

Optical imaging methods aim to label functional pools of vesicles in the terminals and visualize their fates. The spatial resolution of optical microscopy is limited to ∼200 nm by the diffraction of light. Because synaptic vesicles are small (∼40 nm in diameter) and hundreds of these vesicles are clustered in a confined space, optical microscopy cannot resolve individual vesicles in the terminal. Therefore, several tricks have been developed to visualize specific subsets of vesicles. For example, fluid phase markers like dextran, ferritin, and quantum dots can be applied exogenously to label endocytosed vesicles and visualize their dynamics in the terminal (Zhang et al., 2007b; Park et al., 2012). Similarly, lipophilic dyes like FM dyes and mCling can be internalized via endocytosis and mark the newly reconstituted vesicles (Betz et al., 1992; Revelo et al., 2014). Finally, pH-sensitive fluorescent molecules such as pHluorin (Miesenböck et al., 1998) can be used to monitor synaptic vesicle cycle. Fluorescence from pHlourin is quenched in the lumen of synaptic vesicles due to the low pH. When exposed to the extracellular space by exocytosis, the protein becomes fluorescent. The pHluorin molecules are quenched again once they are internalized and vesicles are fully re-acidified. These techniques allow visualization of particular vesicles (Sankaranarayanan and Ryan, 2000; Balaji and Ryan, 2007; Armbruster et al., 2013). However, like in the capacitance measurement, it is difficult to visualize intracellular trafficking events, limiting the interpretation of the results.

Electron microscopy, on the other hand, depicts all the membrane-bound structures within the terminal, but only captures a static image. To overcome this limitation, neurons are typically stimulated and fixed at defined time points after the stimulation (Ceccarelli et al., 1972; Heuser and Reese, 1973; Ferguson et al., 2007; Clayton et al., 2008; Matthews and Sterling, 2008; Hoopmann et al., 2010; Schikorski, 2014; Wu et al., 2014). However, the temporal resolution is limited to seconds to minutes for two reasons. First, to ensure the capture of endocytic events, neurons are often stimulated with prolonged intense stimulation that lasts seconds to minutes. Second, diffusion and reaction of aldehyde-based chemicals are slow, requiring an additional time. To visualize membrane dynamics on a millisecond time scale, Heuser and Reese developed the "freeze slammer," which freezes tissues near instantaneously following electrical stimulation (Heuser et al., 1979; Heuser and Reese, 1981). Using this device, they were able to observe vesicles fusing with the plasma membrane 5 ms after an electrical pulse (Heuser and Reese, 1981; Heuser et al., 1979). Although individual images are static, membrane dynamics can be visualized in electron micrographs by inducing a particular activity and freezing neurons at multiple defined time points.

The freeze slamming approach allows visualization of membrane dynamics at the temporal resolution relevant to synaptic functions, but it has two major drawbacks. First, the specimen must be physically attached to the electrical wire, and thus experiments can only be performed *ex vivo*. Second, only the surface of specimens (∼5 μm) can be frozen without ice crystal damage. These two factors limit its utility as a versatile tool for studying membrane trafficking at synapses. To overcome these limitations, we have developed a novel technique, flash-and-freeze, that combines optogenetics with high-pressure freezing (Watanabe et al., 2013a,b, 2014a). With this technique, non-invasive light stimulation is used to induce synaptic transmission. Specimens as thick as 200 μm can be properly frozen without ice crystal formation. Therefore, intact animals like *Caenorhabditis elegans* (*C. elegans* hereafter) or an entire population of neurons in a dish can be studied. Here, I will describe the methods in detail and discuss its potential applications in synaptic cell biology.

High-Pressure Freezing

An electron microscope operates under high vacuum to avoid the scattering of electrons by gaseous molecules in the air. Thus, to observe a specimen in a transmission electron microscope, it must be fixed and dehydrated. In addition, electron beam must penetrate through the specimen, requiring extremely flat specimens with a thickness of ∼30–70 nm. For this reason, the specimen is embedded in plastic and sectioned ultrathin. The sample preparation for electron microscopy often leads to the generation of artifacts. Fixation using aldehyde-based chemicals cross-links proteins and aggregates them. Worse yet, this reaction can induce fusion of synaptic vesicles (Smith and Reese, 1980). Furthermore, dehydration leads to the shrinkage of the membrane-bound structures and the overall changes in the morphological architecture of the cells. Therefore, a better approach must be used to study membrane trafficking events at synapses.

One approach to avoid these artifacts is to immobilize cells physically by rapid freezing. The freezing process, however, leads to formation of ice crystals that can damage the cellular architecture by directly penetrating through the membrane. Alternatively, the solutes segregated from ice crystals can burst membrane due to the local changes in the osmotic pressure. To prevent water molecules from forming ice crystals, a freezing rate of at least 10,000 K/s must be achieved. At this rate, water molecules cannot rearrange to form ice crystals and are frozen in an unordered state. The cooling rate by liquid nitrogen can exceed 16,000 K/s. Unfortunately, the heat conductance of water is poor, reducing the rate to 1000 K/s within 10 μm from the point of the contact. Under high pressure (2100 bar), however, a freezing rate of 100 K/s is sufficient to freeze water in an unordered state due to the supercooling effect (Moor, 1987; Dubochet, 2007). Thus, high-pressure freezing allows freezing of tissues up to 200 μm thickness or intact animals like *C. elegans*, (∼70 μm thick) without ice crystal damage.

Optogenetics

To visualize membrane dynamics during neurotransmission, neurons must be stimulated and frozen at defined time points after stimulation. In the freeze slammer, specimens are physically attached to the stimulating wire, limiting the specimen choice.

Furthermore, the configuration of the high-pressure freezer makes it difficult to apply electrical field stimulation. To overcome these limitations, we have coupled optogenetics with high-pressure freezing. Channelrhodopsin is a light-sensitive cation channel isolated from *Chlamydomonas reinhardtii* (Nagel et al., 2003). A flash of blue light opens the channel, allowing cations to flow into the cell, thereby depolarizing it. When the channel is heterologously expressed in neurons, a short pulse of light triggers an action potential, leading to synaptic transmission (Boyden et al., 2005; Nagel et al., 2005). Therefore, non-invasive stimulation can be applied to a population of neurons in a dish or intact animals.

To couple optogenetic stimulation with high-pressure freezing ("flash-and-freeze"), we have developed a device that interfaces with the computer of high-pressure freezer as well as with an LED (Watanabe et al., 2013a,b, 2014a). This device allows application of light pulses at defined time points before the specimen is frozen (see Section Materials and Methods). Using this approach, we can visualize the membrane trafficking events at synapses with a millisecond temporal resolution.

MATERIALS AND METHODS

All experiments are performed according to the guidelines for the animal use by the National Institute of Health. The animal protocol is approved by the Animal Care and Use Committee at Johns Hopkins University, School of Medicine. The graphical representations of the workflow is shown in **Figure 1**. The step-by-step protocol can be found in the Supplementary information.

Cell Cultures

For flash-and-freeze experiments, specimens must be mounted on a substrate that is translucent like a glass coverslip but can withstand the extreme pressure application. Sapphire disks are ideal substrates, meeting these two criteria. In addition, thermal conductivity of sapphire is extremely high, particularly at low temperature, making it the perfect substrate. For culturing cells on sapphire disks, the following procedures are performed. First, we sputter carbon on one side of 6 mm sapphire disks so that we can distinguish the surface that the cells are cultured on. Then, we scratch out a letter "4" on the carbon-coated surface with a diamond scribe. Alternatively, a finder grid can be placed on a sapphire disk as a mask. The sapphire disks are baked at 120°C overnight. After a brief dip in ethanol, two sapphire disks are placed in each well of a 12-well plate and air-dried in a biosafety cabinet. Poly-D-Lysine solution (acetic acid 3 parts, rat tail collagen 1 part, and poly-D-lysine 1 part) is applied directly on each sapphire disk. After 5 min, the excess solution is removed, and the plates are dried under the laminar flow. Prior to use, the 12-well plates containing sapphire disks are sterilized by exposure to UV light for 20 min.

For hippocampal cultures, we first culture astrocytes as a feeder layer and then plate the neurons on top of the astrocytes. Mouse brains are dissected out from newborn C57/BL6J mice immediately after decapitation. Cortices and hippocampi are isolated from each brain, in cold HBSS solution. For the astrocyte feeder layer, cortices are treated with 0.05% Trypsin-EDTA for 20 min at 37°C. The dissociated astrocytes are then cultured in DMEM containing 10% FBS and 0.1% penicillin-streptomycin for 2 weeks in a T-75 flask. Then astrocytes are transferred to the 12-well plate containing sapphire disks (5×10^4/ well) and grown for a week. Astrocyte mitosis is arrested a few hours before neuron plating using fluorodeoxyuridine (80 mm). Media are exchanged with Neurobasal, a media containing 2% B27, 1% glutamax, and 0.1% penicillin-streptomycin, prior to neuron plating. Isolated hippocampi are treated with papain (20 U/ ml) for 1 h and plated (5×10^4/well) on top of the feeder layer. Neurons are allowed to grow for 2–3 weeks. On DIV1-3, neurons are infected with lentivirus containing Channelrhodopsin expressed from the neuron specific synapsin promoter.

Caenorhabditis elegans

Transgenic animals expressing ChIEF, a variant of channelrhodopsin-2, are grown on an agar plate (50 mm) seeded with 250 µl of *E. coli* OP50. Larval stage 4 (L4) transgenic animals are transferred to agar plates seeded with bacteria and 4 µl trans-retinal solution (100 mM) a day prior to the experiment. These animals are kept in the dark before the experiments.

Freezing

We have used three different high-pressure freezers: Leica EM PACT2, HPM100, and ICE. *C. elegans* has been tested in the EM PACT2, whereas neuronal cultures are frozen with the HPM100 or ICE. For the EM PACT2, a membrane carrier with a 100 µm-deep well is used to mount transgenic worms (**Figure 2A**). First, the well of the membrane carrier is filled with M9 worm buffer containing 20% bovine serum albumin (BSA) as cryo-protectant. Approximately 10–15 young adult animals are transferred into the solution. The membrane carrier is then mounted into the modified specimen pod.

To mount cultured neuronal cells, the following procedures are carried out (**Figure 2B**). First, a sapphire disk with neurons is transferred into pre-warmed (37°C) recording solution containing 140 mM NaCl, 2.4 mM KCl, 10 mM HEPES (pH 7.5), 10 mM glucose, 4 mM $CaCl_2$, 1 mM $MgCl_2$, 3 µM NBQX, and 30 µM bicuculline. The addition of NBQX and bicuculline blocks the recurrent network activity following channelrhodopsin stimulation. The sapphire disk is mounted on the countersink of a 6-mm middle plate. A spacer ring (100 µm thickness) is placed on the sapphire disk so that cells are not crushed when the assembly is capped with another sapphire disk. To cap the assembly, a sapphire disk is first dipped in the recording solution so that one side of the disk carries a drop of solution. This sapphire disk is then placed on top of the spacer ring gently so that air bubbles are not trapped in between the disks. Two more spacer rings (200 µm each) are then placed to fill up the remaining space. The excess solution should be removed by gently tapping with a small piece of filter paper. The middle plate assembly is then sandwiched between two transparent plastic half cylinders. Note that light is shone

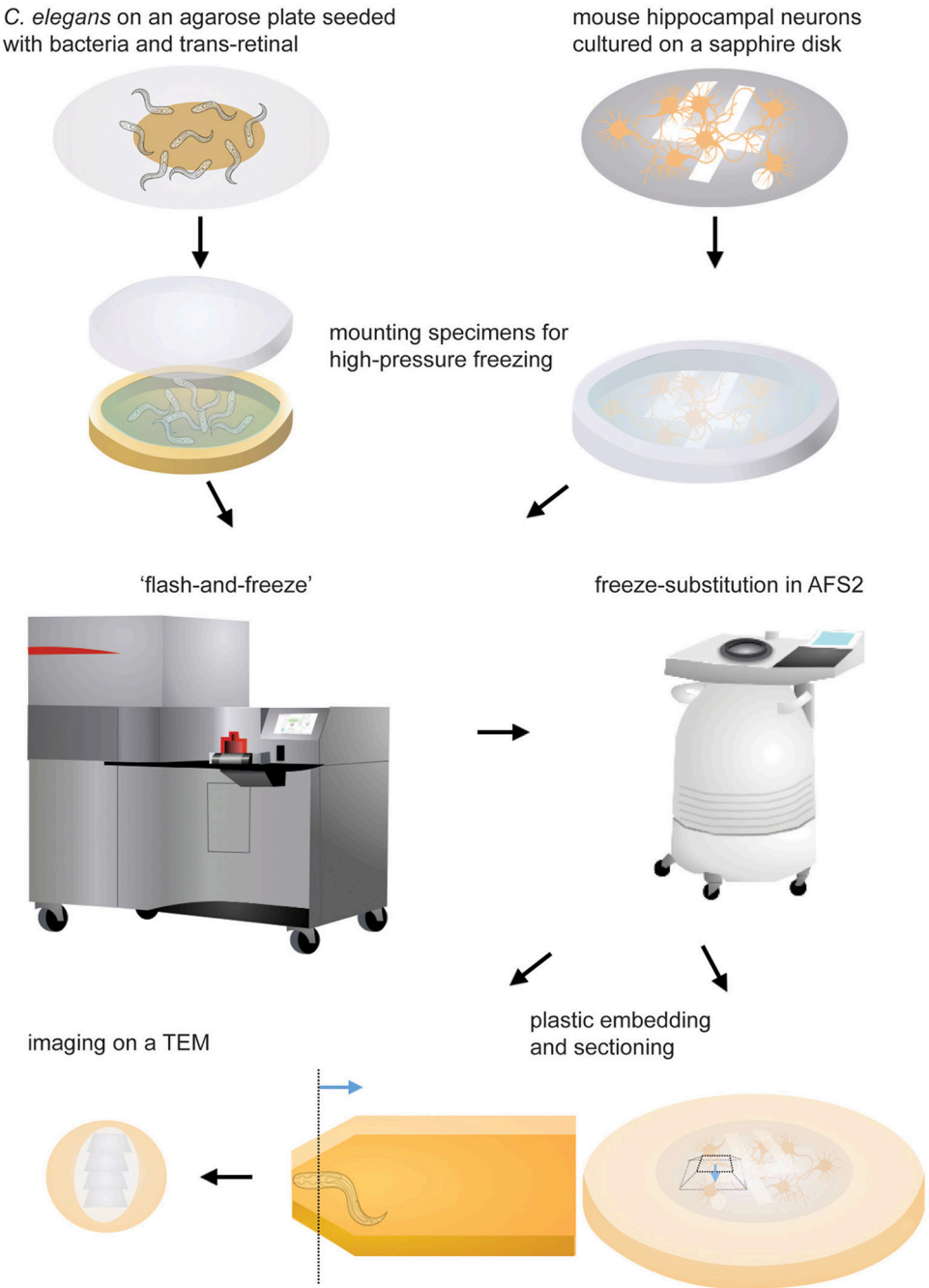

FIGURE 1 | Schematic drawings showing the experimental procedures. Specimens are mounted in the appropriate carrier and frozen immediately following light stimulation. The freeze-substition is carried out in an automated freeze-substitution unit. Once the freeze-substitution is complete, specimens are embedded in resin and cured for 48 h. The region of interest (the dotted line) is located using a stereoscope. The blue line indicates the direction of sectioning. The ultrathin sections are mounted on a grid and imaged on a transmission electron microscope.

from the bottom side of the specimen assembly in the HPM100 while it is from the top in the ICE. The video demonstrating sample loading can be found on the Leica website (http://www.leica-microsystems.com/science-lab/video-tutorials-filling-and-assembling-of-different-carriers-for-high-pressure-freezing/).

Programming Light Stimulation

The modifications we have made for the EM PACT2 are described in detail in previous publications (Watanabe et al., 2013a,b, 2014a). For controlling the light stimulation and freezing, we constructed an Arudino Uno based device that sends out 5V TTL signals to the LED and the high-pressure freezer at the

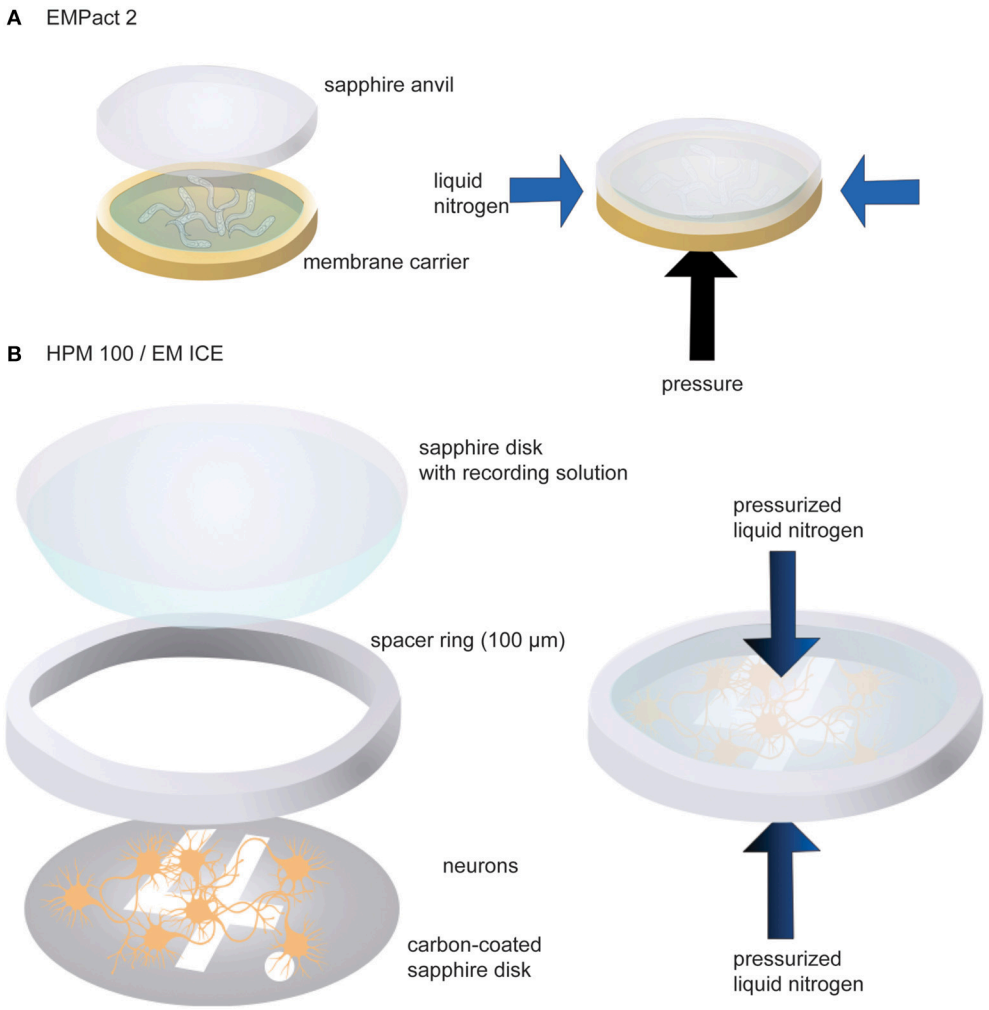

FIGURE 2 | Schematic drawings showing sample loading in the EM PACT2 (A) and in the HPM 100 or the EM ICE (B). For the EM PACT2, the membrane carrier must be sealed with a sapphire anvil before the experiments. Typically, the liquid is slightly overfilled so that no air bubbles are trapped when sealing with the sapphire anvil. For the HPM 100 and the EM ICE, liquid should be carried with the top sapphire disk to seal the assembly with no bubbles. For the EM PACT2, the pressure is applied from the bottom of the membrane carrier while liquid nitrogen is applied from the side of the specimen. For the HPM 100 and the EM ICE, pressurized liquid nitrogen is applied to the specimen from both sides.

desired time point. This device is driven by custom firmware to produce any pattern of light pulses (i.e., single stimulus, 10 Hz stimulation) and send out the "start" signal that triggers the freezing process (this device can be purchased from Marine Reef International). Once the signal is sent, the freezer applies hydraulic fluid to the specimen and pressurize the specimen. When the pressure reaches 2000 bar, the liquid nitrogen is immediately applied to the specimen. The initiation of this freezing process needs to be timed so that the desired time interval between the light stimulation and freezing is achieved. To monitor the precise timing when the pressure is applied to the specimen, we installed an accelerometer on the sample holder (also known as a "specimen bayonet"). When the pressure is applied to the specimen, the sample holder jolts, producing a distinctive peak in the accelerometer recording. We found that it requires about 170 ms for the EM PACT2 to apply the pressure to the specimen after sending the 'start' signal. After the pressure is applied to the specimen, the specimen is frozen to −20°C in 8 ms, according to standard thermodynamic equations. To account for the variability in timing, we calculate the actual time interval *post-hoc* based on the pressure peak recorded by the accelerometer. We have found the actual time interval to typically be within 33.6 ± 4.6 ms of the intended time.

To introduce light stimulation capability in the HPM100, a similar Arudino Uno based device was constructed. The operation of the HPM100 is fundamentally different from that of the EM PACT2 in that pressurized liquid nitrogen is applied to the specimen instead of a hydraulic fluid. After sending the "start" signal, it takes 370 ms to compress the liquid nitrogen. The pressurized liquid nitrogen reaches the specimen in precisely 72 ms. The specimen is frozen to −20°C in 8 ms from the time the pressurized liquid nitrogen hits the specimen surface. Therefore, a total of 450 ms delay is expected. To monitor the precise timing, light stimulation device record the internal signal of the machine

that opens the liquid nitrogen valve in each shot. This signal initiates almost invariably at 370 ms after the start signal. The actual timing of the freeze is adjusted *post-hoc* based on the valve opening signal.

For EM ICE, Leica microsystems has integrated the light stimulation control into the freezer. The machine is capable of freezing specimen at the desired timing after the light stimulation with 1–2 ms variability.

Freeze-Substitution

Following high-pressure freezing, vitrified water from the specimen must be substituted with organic solvent to avoid crystallization of vitrified water as the specimen warms up to room temperature for further processing. The freeze-substitution is carried out in cryotubes containing fixatives (1% osmium tetroxide, 1% glutaraldehyde, 1% milliQ water in anhydrous acetone) using an automated freeze-substitution unit (Leica AFS2). The cryotubes containing fixatives are stored under liquid nitrogen to avoid the cross-reaction between osmium tetroxide and glutaraldehyde. The sapphire disks containing the cells typically remain associated with the middle plate. To release the sapphire disks, the middle plate is quickly transferred to a cup containing acetone, which is precooled to −90°C in AFS. Once the middle plate reaches −90°C in the acetone, the sapphire disk often dissociates from the middle plate spontaneously. If not, it can be released by a gentle tap. The sapphire disk is then transferred into the cryotube containing the fixatives at −90°C. For *C. elegans*, the frozen specimens can be transferred under liquid nitrogen into the cryotubes containing fixatives. The tubes should be transferred quickly into the AFS. The following program is used for the freeze-substitution: −90°C for 5–30 h, 5°C/h to −20°C, 12 h at −20°C, 10°C/h to 20°C. The cryotubes are agitated at least twice a day during the substitution process.

Plastic Embedding

Once the freeze-substitution is complete, specimens are embedded in Epon/Araldite resin. The resin is as composed of 4.4 g Araldite 502, 6.2 g Eponate 12, 12.2 g dodecenyl succinic anhydrite (DDSA), and 0.8 ml benzyldimethylamine (BDMA). First, the fixative solution is carefully removed from the cryotube, and specimens are washed with acetone a few times. Specimens are then treated with 0.1% uranyl acetate in acetone for 1 h to enhance the membrane contrast. Following several acetone washes, infiltration is carried out in the same cryotubes on an orbital shaker: 30% for 2–5 h, 70% for 3–6 h, and 90% overnight at room temperature. The next day, specimens are transferred into the caps of BEEM capsules containing 100% Epon/Araldite resin. The resin is replaced three times (2 h each). The specimens are cured in an oven (60°C) for 48 h.

Sectioning

For observation in a transmission electron microscope, specimens must be sliced thin so that electrons can penetrate through the tissue and generate an image. Ultrathin sections (40 nm) of specimens are cut using a diamond knife and collected on pioloform-coated single slot grids. For *C. elegans*, we orient the animal so that it is perpendicular to the sectioning surface (**Figure 1**, bottom). We trim the animal to the reflex of the gonad using a glass knife. We collect ribbons of 250 sections from each animal. For mouse hippocampal neurons, we first remove the sapphire disks from the sample by submerging them in the liquid nitrogen for a few seconds. About 40 sections are cut from the exposed surface (**Figure 1**, bottom) and collected. These sections are stained with 2.5% uranyl acetate in 70% methanol for 4 min prior to imaging.

Imaging

A transmission electron microscope is operated at 80–120 keV. Images are acquired with a digital camera. Roughly 200–300 images are collected from each time point.

Image Analysis

The morphological analysis is performed in ImageJ using a custom-written macro. This macro records X- and Y-coordinates of hand-traced membrane structures such as the plasma membrane, active zone, membrane invaginations, synaptic vesicles, dense-core vesicles, large vesicles, and endosomes. The positional information is first exported as text files and then imported into MATLAB (MathWorks). We have written scripts in MATLAB to analyze the coordinates and calculate several statistics: distribution of vesicles from the plasma membrane, distribution of vesicles from the active zone, diameter of vesicles, and number of vesicles. A normality test is performed on these data, and *P*-values are calculated using student's *T*-test for normally distributed data and Mann–Whitney *U*-test for skewed data. The confidence level is set at 95%. For multiple comparisons, the Bonferroni correction is applied.

RESULTS

Accuracy of Timing

To test the accuracy of the timing for light stimulation, we applied a single stimulus and froze tissues at desired time points. We calculated the actual time at which the specimens were frozen by monitoring the time when the pressure was applied to the specimens. The pressure application can be monitored using an accelerometer for EM PACT 2 (Watanabe et al., 2013b, 2014a). For HPM 100, we recorded the signal that triggers opening of the valve that allows pressurized liquid nitrogen to pass through because specimens are frozen exactly 80 ms after the valve opening (see Section Materials and Methods; Watanabe et al., 2013a). On the EM ICE, we can measure the interval between the end of the desired stimulation program and the time at which the sensor, which is located close to the specimen, reaches 0°C. The sensor is placed before the specimen, and it requires additional 3-6 ms for the specimen to experience the same magnitude of cooling.

We recorded the values from each machine on at least three different experimental days. Out of 52 shots taken on the EM PACT2 (4 experiments, 13 shots/experiment), the desired time point was achieved in only 5 shots (**Figure 3**). The actual timing was variable, ranging from −102 to 110 ms. Because of this variability, the actual timing is always calculated *post-hoc* for each shot on the EM PACT2. On the HPM100, nearly two thirds of the shots (57/90) achieved the desired time point (3 experiments,

30 shots/experiment). The rest were either 5 ms before or after the desired time point, indicating that the variation is small in the HPM 100. However, the signal for the valve opening is measured at 5 ms time interval (200 Hz), and thus each recording has an uncertainty of ±2.5 ms. The EM ICE, on the other hand, records the temperature and pressure sensors' signals at 2000 Hz. The data from the EM ICE indicated that 56 out of 72 shots (3 experiments, 24 shots/experiment) landed between 1.5 and 2.5 ms after the desired time point. The maximum delay was 4 ms, and this maximum delay occurred on the very first shot on each experimental day. The rest of the shots were within 1.5–3.5 ms after the desired time point (average = 2.2 ± 0.08 ms). Given that the additional 3 ms is required to freeze specimens at 5 μm deep from the surface, a total of 4.5–6.5 ms is expected. These results indicate that millisecond temporal control can be achieved in HPM 100 and EM ICE.

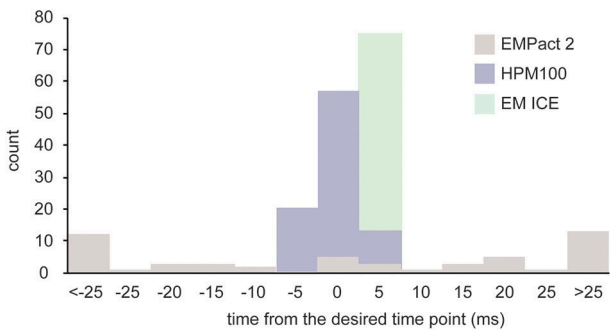

FIGURE 3 | A bar graph showing the time difference between the desired time point and the actual time point at which specimens are frozen. The variation is largest in the EM PACT2, with the average delay of 33.6 ± 4.6 ms ($N = 4$ experiments; $n = 52$ shots). The average delay of the HPM100 is 1.9 ± 0.3 ms ($N = 3$ experiments; $n = 90$ shots) while that of the EM ICE is 2.2 ± 0.1 ($N = 3$ experiments; $n = 72$ shots).

Exocytosis

To further test the accuracy of the timing, we stimulated *C. elegans* neuromuscular junctions for 20 ms and froze them at the end of the pulse using the EM PACT2. Based on the electrophysiological recordings, channelrhodopsin induced neurotransmission is close to the peak at this time point in the *C. elegans* motor neurons (Watanabe et al., 2013b). From a total of 13 shots taken, only 1 shot achieved this time point. To further test the accuracy, we also imaged the samples that were frozen 10 ms before the onset of the light pulse and 30 ms after the end of the light pulse, as calculated *post-hoc*. We were able to capture exocytic omega figures at neuromuscular junctions frozen 20 ms after the light onset (**Figure 4A**). However, these structures were not observed in the samples frozen 10 ms before the light onset or 30 ms after the end of the light pulse. These results indicate that the EM PACT2, although unreliable, can be used to capture fast membrane dynamics at synaptic terminals.

To test if the exocytic omega figures can be captured with the HPM 100 and the EM ICE, we froze mouse hippocampal neurons expressing channelrhodopsin. We applied a single 10 ms light pulse to the specimen and froze it 5 ms after the end of the light pulse. In the neurons frozen on the HPM 100, we found at least one omega figure in 19% of synapses at this time point (**Figure 4B**; 193 profiles; Watanabe et al., 2013a). Similarly, omega figures were captured in 18% of synapses by EM ICE (**Figure 4C**; 105 profiles). These results indicate that the flash-and-freeze approach can reliably capture the membrane dynamics at synapses with milliseconds temporal resolution.

DISCUSSION

Comparisons among Three Instruments

To visualize membrane dynamics at synapses, we developed a technique, "flash-and-freeze," which couples optogenetic stimulation of neurons with high-pressure freezing. Here, we

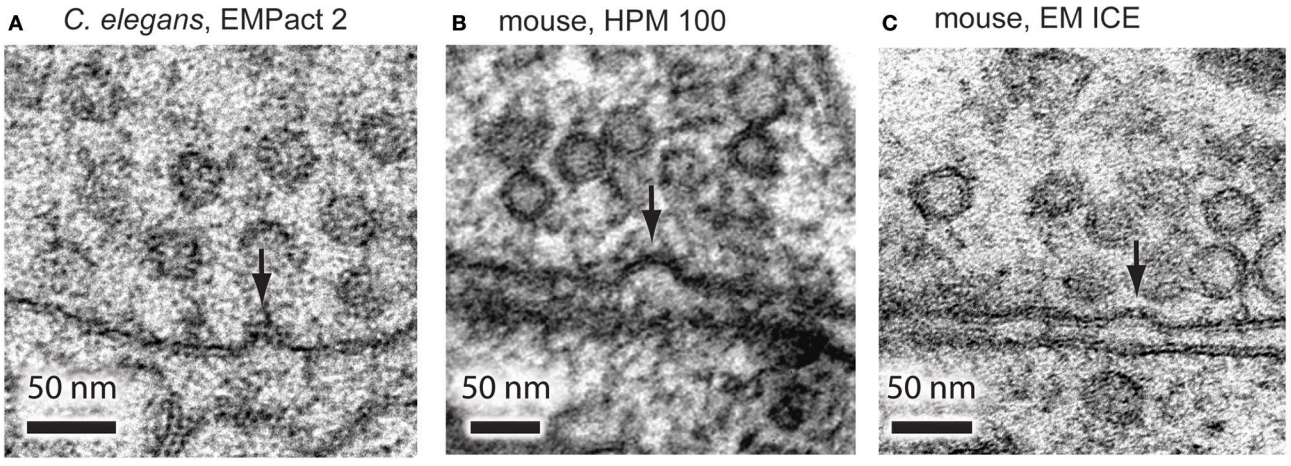

FIGURE 4 | Representative micrographs showing exocytic omega figures from the flash-and-freeze experiments. (A) *C. elegans* neuromuscular junctions, stimulated for 20 ms, and frozen at the end of the light pulse. Mouse hippocampal neurons, stimulated for 10 ms, frozen 5 ms after the end of the pulse using HPM 100 **(B)**, and EM ICE **(C)**. These structures are rarely observed in non-stimulated control or in specimens frozen at later time points after the stimulation.

compared three instruments that allow such experiments: EM PACT2, HPM100, and EM ICE. There are advantages and disadvantages for each instrument. The major advantage of the EM PACT 2 is in its potential application - higher intensity of ultraviolet light can be applied to specimens because light only has to penetrate through a clear sapphire anvil. Most caged compounds are uncaged with ultraviolet light. In both HPM100 and EM ICE, light must travel through an optical fiber and penetrate through a plastic sample holder that absorbs ultraviolet light. Thus, experiments using caged compound are more feasible in the EM PACT2. However, the EM PACT2 required many trials before the desired time point was reached. Besides the unreliability, the major disadvantage of the EM PACT2 is the size of the specimen cup. A specimen cup has a dimension of 1.6 mm diameter $\times$ 100 or 200 μm depth. Cells must be cultured on sapphire disks with a diameter of 1.4 mm. These small sapphire disks float in culture media, making it difficult to culture cells. On the other hand, sapphire disks as large as 6 mm can be loaded into the HPM100 or the EM ICE. Both the HPM100 and the EM ICE are essentially comparable in terms of the freezing quality and the temporal precision of light stimulation. However, HPM100 is more flexible in terms of its potential applications, as the light stimulation device and programs are customizable. With the expansion in the repertoire of optogenetic tools or light-sensitive compounds, cellular activity can be controlled using different wavelengths of light, and it is possible to develop a multi-color system for the HPM100. The major disadvantages of HPM 100 are that it requires an external device and that the actual freezing point must be calculated based on when the liquid nitrogen valve opens each time. On the contrary, EM ICE does not require a custom device or an external light source—everything is integrated. Furthermore, it achieves the most precise control of the light stimulation and the fastest freezing rate, requiring only 3 ms from the initial temperature drop to -20°C. Despite these differences among instruments, exocytosis of synaptic vesicles, which occurs on a millisecond time scale, were captured in all three instruments, suggesting that any of these machines are compatible with flash-and-freeze experiments. Therefore, the choice should be made depending on the potential applications.

Potential Applications

The flash-and-freeze approach can be applied to study many cell biological problems. We have been using channelrhodopsin to stimulate neuronal activity and capture membrane dynamics at synapses. Neuronal activity or cellular functions can be manipulated using light-sensitive molecules such as bacterial opsins (Han and Boyden, 2007; Zhang et al., 2007a; Berthold et al., 2008; Chow et al., 2010), caged compounds (Walker et al., 1986; Tsien et al., 1987; Milburn et al., 1989; Adams and Tsien, 1993; Wieboldt et al., 1994), light-sensitive proteins (Levskaya et al., 2009; Wu et al., 2009; Yazawa et al., 2009; Idevall-Hagren et al., 2012; Zhou et al., 2012; Guntas et al., 2015), and photo-isomerizable molecule (Banghart et al., 2004; Kramer et al., 2009). These tools can be used to inhibit or activate neuronal activity, protein function, lipid composition, signaling cascades, and ion composition in vesicular structures. The morphological changes that take place during these manipulations can be preserved through the flash-and-freeze approach and visualized with a millisecond temporal resolution. Furthermore, there are neurons like photoreceptors that are naturally sensitive to light. The flash-and-freeze approach can be readily adapted to address the mechanism underlying tonic release of neurotransmitters from these terminals and how exocytosis is mediated by synaptic ribbons, electron dense proteinaceous protrusion in the center of the active zone (LoGiudice and Matthews, 2009).

Potential Difficulties

Membrane dynamics are inferred by observing the membrane morphology at defined time points, but individual electron micrographs still capture static images of cells. The flash-and-freeze technique cannot follow the membrane dynamics in a single cell. Therefore, to reconstruct the membrane dynamics, hundreds of images must be acquired and analyzed from each time point. For membrane trafficking at synapses, an even higher number may be required due to the heterogeneity in the release probability (Rosenmund and Stevens, 1996)—not every action potential leads to fusion of synaptic vesicles. We have estimated that about 20–30% of synapses are activated with a single light pulse in mouse hippocampal neurons (Watanabe et al., 2013a, 2014b). To produce data with statistical significance, we have analyzed over 10,000 images. These analyses were performed blind to genotypes and time points, and thus the average frequency of morphological features at a particular time point can be determined from these images. To expedite analysis and increase the statistical power, automation is in an immediate need. However, with the recent advances in methods for automated image acquisition and analysis (Potter et al., 1999; Denk and Horstmann, 2004; Knott et al., 2008; Hayworth et al., 2014), achieving such a goal is likely within reach.

AUTHOR CONTRIBUTIONS

SW performed all the experiments, analyzed the data, and wrote the manuscript.

ACKNOWLEDGMENTS

I would like to thank Erik Jorgensen, Christian Rosenmund, and all the members in their laboratories for the help in performing the original experiments. The light stimulation device for Leica EM PACT 2 and HPM 100 is designed and developed by M. Wayne Davis. I would like to thank the Grass Foundation and the Marine Biological Laboratory at Woods Hole for space, equipment and funding for performing these experiments. I would like to thank Sumana Raychaudhuri and Edward Hujber for a critical reading of the manuscript. The research is supported by Johns Hopkins University startup fund.

SUPPLEMENTARY MATERIAL

The Supplementary Material for this article can be found online at: http://journal.frontiersin.org/article/10.3389/fnsyn.2016.00024

REFERENCES

Adams, S. R., and Tsien, R. Y. (1993). Controlling cell chemistry with caged compounds. *Annu. Rev. Physiol.* 55, 755–784. doi: 10.1146/annurev.ph.55.030193.003543

Armbruster, M., Messa, M., Ferguson, S. M., De Camilli, P., and Ryan, T. A. (2013). Dynamin phosphorylation controls optimization of endocytosis for brief action potential bursts. *Elife* 2:e00845. doi: 10.7554/eLife.00845

Balaji, J., and Ryan, T. A. (2007). Single-vesicle imaging reveals that synaptic vesicle exocytosis and endocytosis are coupled by a single stochastic mode. *Proc. Natl. Acad. Sci. U.S.A.* 104, 20576–20581. doi: 10.1073/pnas.0707574105

Banghart, M., Borges, K., Isacoff, E., Trauner, D., and Kramer, R. H. (2004). Light-activated ion channels for remote control of neuronal firing. *Nat. Neurosci.* 7, 1381–1386. doi: 10.1038/nn1356

Berthold, P., Tsunoda, S. P., Ernst, O. P., Mages, W., Gradmann, D., and Hegemann, P. (2008). Channelrhodopsin-1 initiates phototaxis and photophobic responses in chlamydomonas by immediate light-induced depolarization. *Plant Cell* 20, 1665–1677. doi: 10.1105/tpc.108.057919

Betz, W. J., Mao, F., and Bewick, G. S. (1992). Activity-dependent fluorescent staining and destaining of living vertebrate motor nerve terminals. *J. Neurosci.* 12, 363–375.

Boyden, E. S., Zhang, F., Bamberg, E., Nagel, G., and Deisseroth, K. (2005). Millisecond-timescale, genetically targeted optical control of neural activity. *Nat. Neurosci.* 8, 1263–1268. doi: 10.1038/nn1525

Ceccarelli, B., Hurlbut, W. P., and Mauro, A. (1972). Depletion of vesicles from frog neuromuscular junctions by prolonged tetanic stimulation. *J. Cell Biol.* 54, 30–38. doi: 10.1083/jcb.54.1.30

Chow, B. Y., Han, X., Dobry, A. S., Qian, X., Chuong, A. S., Li, M., et al. (2010). High-performance genetically targetable optical neural silencing by light-driven proton pumps. *Nature* 463, 98–102. doi: 10.1038/nature08652

Clayton, E. L., Evans, G. J. O., and Cousin, M. A. (2008). Bulk synaptic vesicle endocytosis is rapidly triggered during strong stimulation. *J. Neurosci.* 28, 6627–6632. doi: 10.1523/JNEUROSCI.1445-08.2008

Delvendahl, I., Vyleta, N. P., von Gersdorff, H., and Hallermann, S. (2016). Fast, temperature-sensitive and clathrin-independent endocytosis at central synapses. *Neuron* 90, 492–498. doi: 10.1016/j.neuron.2016.03.013

Denk, W., and Horstmann, H. (2004). Serial block-face scanning electron microscopy to reconstruct three-dimensional tissue nanostructure. *PLoS Biol.* 2:e329. doi: 10.1371/journal.pbio.0020329

Dittman, J., and Ryan, T. A. (2009). Molecular circuitry of endocytosis at nerve terminals. *Annu. Rev. Cell Dev. Biol.* 25, 133–160. doi: 10.1146/annurev.cellbio.042308.113302

Dubochet, J. (2007). The physics of rapid cooling and its implications for cryoimmobilization of cells. *Methods Cell Biol.* 79, 7–21. doi: 10.1016/s0091-679x(06)79001-x

Ferguson, S. M., Brasnjo, G., Hayashi, M., Wölfel, M., Collesi, C., Giovedi, S., et al. (2007). A selective activity-dependent requirement for dynamin 1 in synaptic vesicle endocytosis. *Science* 316, 570–574. doi: 10.1126/science.1140621

Guntas, G., Hallett, R. A., Zimmerman, S. P., Williams, T., Yumerefendi, H., Bear, J. E., et al. (2015). Engineering an improved light-induced dimer (iLID) for controlling the localization and activity of signaling proteins. *Proc. Natl. Acad. Sci. U.S.A.* 112, 112–117. doi: 10.1073/pnas.1417910112

Hamill, O. P., Marty, A., Neher, E., Sakmann, B., and Sigworth, F. J. (1981). Improved patch-clamp techniques for high-resolution current recording from cells and cell-free membrane patches. *Pflügers Arch.* 391, 85–100. doi: 10.1007/BF00656997

Han, X., and Boyden, E. S. (2007). Multiple-color optical activation, silencing, and desynchronization of neural activity, with single-spike temporal resolution. *PLoS ONE* 2:e299. doi: 10.1371/journal.pone.0000299

Hayworth, K. J., Morgan, J. L., Schalek, R., Berger, D. R., Hildebrand, D. G. C., and Lichtman, J. W. (2014). Imaging ATUM ultrathin section libraries with WaferMapper: a multi-scale approach to EM reconstruction of neural circuits. *Front. Neural Circuits* 8:68. doi: 10.3389/fncir.2014.00068

Heuser, J. E., and Reese, T. S. (1973). Evidence for recycling of synaptic vesicle membrane during transmitter release at the frog neuromuscular junction. *J. Cell Biol.* 57, 315–344. doi: 10.1083/jcb.57.2.315

Heuser, J. E., and Reese, T. S. (1981). Structural changes after transmitter release at the frog neuromuscular junction. *J. Cell Biol.* 88, 564–580. doi: 10.1083/jcb.88.3.564

Heuser, J. E., Reese, T. S., Dennis, M. J., Jan, Y., Jan, L., and Evans, L. (1979). Synaptic vesicle exocytosis captured by quick freezing and correlated with quantal transmitter release. *J. Cell Biol.* 81, 275–300. doi: 10.1083/jcb.81.2.275

Hoopmann, P., Punge, A., Barysch, S. V., Westphal, V., Bückers, J., Opazo, F., et al. (2010). Endosomal sorting of readily releasable synaptic vesicles. *Proc. Natl. Acad. Sci. U.S.A.* 107, 19055–19060. doi: 10.1073/pnas.1007037107

Idevall-Hagren, O., Dickson, E. J., Hille, B., Toomre, D. K., and De Camilli, P. (2012). Optogenetic control of phosphoinositide metabolism. *Proc. Natl. Acad. Sci. U.S.A.* 109, E2316–E2323. doi: 10.1073/pnas.1211305109

Knott, G., Marchman, H., Wall, D., and Lich, B. (2008). Serial section scanning electron microscopy of adult brain tissue using focused ion beam milling. *J. Neurosci.* 28, 2959–2964. doi: 10.1523/JNEUROSCI.3189-07.2008

Kramer, R. H., Fortin, D. L., and Trauner, D. (2009). New photochemical tools for controlling neuronal activity. *Curr. Opin. Neurobiol.* 19, 544–552. doi: 10.1016/j.conb.2009.09.004

Levskaya, A., Weiner, O. D., Lim, W. A., and Voigt, C. A. (2009). Spatiotemporal control of cell signalling using a light-switchable protein interaction. *Nature* 461, 997–1001. doi: 10.1038/nature08446

LoGiudice, L., and Matthews, G. (2009). The role of ribbons at sensory synapses. *Neuroscientist* 15, 380–391. doi: 10.1177/1073858408331373

Matthews, G., and Sterling, P. (2008). Evidence that vesicles undergo compound fusion on the synaptic ribbon. *J. Neurosci.* 28, 5403–5411. doi: 10.1523/JNEUROSCI.0935-08.2008

Miesenböck, G., De Angelis, D. A., and Rothman, J. E. (1998). Visualizing secretion and synaptic transmission with pH-sensitive green fluorescent proteins. *Nature* 394, 192–195. doi: 10.1038/28190

Milburn, T., Matsubara, N., Billington, A. P., Udgaonkar, J. B., Walker, J. W., Carpenter, B. K., et al. (1989). Synthesis, photochemistry, and biological activity of a caged photolabile acetylcholine receptor ligand. *Biochemistry* 28, 49–55. doi: 10.1021/bi00427a008

Moor, H. (1987). "Theory and practice of high pressure freezing," in *Cryotechiniques in Biological Electron Microscopy*, eds R. A. Steinbrecht and K. Zierold (Berlin: Springer-Verlag), 175–191.

Nagel, G., Brauner, M., Liewald, J. F., Adeishvili, N., Bamberg, E., and Gottschalk, A. (2005). Light activation of channelrhodopsin-2 in excitable cells of *Caenorhabditis elegans* triggers rapid behavioral responses. *Curr. Biol.* 15, 2279–2284. doi: 10.1016/j.cub.2005.11.032

Nagel, G., Szellas, T., Huhn, W., Kateriya, S., Adeishvili, N., Berthold, P., et al. (2003). Channelrhodopsin-2, a directly light-gated cation-selective membrane channel. *Proc. Natl. Acad. Sci. U.S.A.* 100, 13940–13945. doi: 10.1073/pnas.1936192100

Neher, E., and Marty, A. (1982). Discrete changes of cell membrane capacitance observed under conditions of enhanced secretion in bovine adrenal chromaffin cells. *Proc. Natl. Acad. Sci.U.S.A.* 79, 6712–6716. doi: 10.1073/pnas.79.21.6712

Park, H., Li, Y., and Tsien, R. W. (2012). Influence of synaptic vesicle position on release probability and exocytotic fusion mode. *Science* 335, 1362–1366. doi: 10.1126/science.1216937

Potter, C. S., Chu, H., Frey, B., Green, C., Kisseberth, N., Madden, T. J., et al. (1999). Leginon: a system for fully automated acquisition of 1000 electron micrographs a day. *Ultramicroscopy* 77, 153–161. doi: 10.1016/S0304-3991(99)00043-1

Revelo, N. H., Kamin, D., Truckenbrodt, S., Wong, A. B., Reuter-Jessen, K., Reisinger, E., et al. (2014). A new probe for super-resolution imaging of membranes elucidates trafficking pathways. *J. Cell Biol.* 205, 591–606. doi: 10.1083/jcb.201402066

Rosenmund, C., and Stevens, C. F. (1996). Definition of the readily releasable pool of vesicles at hippocampal synapses. *Neuron* 16, 1197–1207. doi: 10.1016/S0896-6273(00)80146-4

Saheki, Y., and De Camilli, P. (2012). Synaptic vesicle endocytosis. *Cold Spring Harb. Perspect. Biol.* 4:a005645. doi: 10.1101/cshperspect.a005645

Sankaranarayanan, S., and Ryan, T. A. (2000). Real-time measurements of vesicle-SNARE recycling in synapses of the central nervous system. *Nat. Cell Biol.* 2, 197–204. doi: 10.1038/35008615

Schikorski, T. (2014). Readily releasable vesicles recycle at the active zone of hippocampal synapses. *Proc. Natl. Acad. Sci. U.S.A.* 111, 5415–5420. doi: 10.1073/pnas.1321541111

Smith, J. E., and Reese, T. S. (1980). Use of aldehyde fixatives to determine the rate of synaptic transmitter release. *J. Exp. Biol.* 89, 19–29.

Sun, J.-Y., Wu, X.-S., and Wu, L.-G. (2002). Single and multiple vesicle fusion induce different rates of endocytosis at a central synapse. *Nature* 417, 555–559. doi: 10.1038/417555a

Tsien, R. W., Fox, A. P., Hess, P., McCleskey, E. W., Nilius, B., Nowycky, M. C., et al. (1987). Multiple types of calcium channel in excitable cells. *Soc. Gen. Physiol. Ser.* 41, 167–187.

von Gersdorff, H., and Matthews, G. (1994). Dynamics of synaptic vesicle fusion and membrane retrieval in synaptic terminals. *Nature* 367, 735–739. doi: 10.1038/367735a0

Walker, J. W., McCray, J. A., and Hess, G. P. (1986). Photolabile protecting groups for an acetylcholine receptor ligand. Synthesis and photochemistry of a new class of o-nitrobenzyl derivatives and their effects on receptor function. *Biochemistry* 25, 1799–1805. doi: 10.1021/bi00355a052

Watanabe, S., Davis, M. W., and Jorgensen, E. M. (2014a). "Flash-and-freeze electron microscopy: coupling optogenetics with high-pressure freezing," in *Nanoscale Imaging of Synapses,* eds U. V. Nägerl and A. Triller (New York, NY: Springer), 43–57.

Watanabe, S., Liu, Q., Davis, M. W., Hollopeter, G., Thomas, N., Jorgensen, N. B., et al. (2013b). Ultrafast endocytosis at *Caenorhabditis elegans* neuromuscular junctions. *Elife* 2:e00723. doi: 10.7554/eLife.00723

Watanabe, S., Rost, B. R., Camacho-Pérez, M., Davis, M. W., Söhl-Kielczynski, B., Rosenmund, C., et al. (2013a). Ultrafast endocytosis at mouse hippocampal synapses. *Nature* 504, 242–247. doi: 10.1038/nature 12809

Watanabe, S., Trimbuch, T., Camacho-Pérez, M., Rost, B. R., Brokowski, B., Söhl-Kielczynski, B., et al. (2014b). Clathrin regenerates synaptic vesicles from endosomes. *Nature* 515, 228–233. doi: 10.1038/nature 13846

Wieboldt, R., Gee, K. R., Niu, L., Ramesh, D., Carpenter, B. K., and Hess, G. P. (1994). Photolabile precursors of glutamate: synthesis, photochemical properties, and activation of glutamate receptors on a microsecond time scale. *Proc. Natl. Acad. Sci. U.S.A.* 91, 8752–8756. doi: 10.1073/pnas.91.19.8752

Wu, Y. I., Frey, D., Lungu, O. I., Jaehrig, A., Schlichting, I., Kuhlman, B., et al. (2009). A genetically encoded photoactivatable Rac controls the motility of living cells. *Nature* 461, 104–108. doi: 10.1038/nature08241

Wu, Y., O'Toole, E. T., Girard, M., Ritter, B., Messa, M., Liu, X., et al. (2014). A dynamin 1-, dynamin 3- and clathrin-independent pathway of synaptic vesicle recycling mediated by bulk endocytosis. *Elife* 3:e01621. doi: 10.7554/eLife.01621

Yazawa, M., Sadaghiani, A. M., Hsueh, B., and Dolmetsch, R. E. (2009). Induction of protein-protein interactions in live cells using light. *Nat. Biotechnol.* 27, 941–945. doi: 10.1038/nbt.1569

Zhang, F., Wang, L.-P., Brauner, M., Liewald, J. F., Kay, K., Watzke, N., et al. (2007a). Multimodal fast optical interrogation of neural circuitry. *Nature* 446, 633–639. doi: 10.1038/nature05744

Zhang, Q., Cao, Y.-Q., and Tsien, R. W. (2007b). Quantum dots provide an optical signal specific to full collapse fusion of synaptic vesicles. *Proc. Natl. Acad. Sci. U.S.A.* 104, 17843–17848. doi: 10.1073/pnas.0706906104

Zhou, X. X., Chung, H. K., Lam, A. J., and Lin, M. Z. (2012). Optical control of protein activity by fluorescent protein domains. *Science* 338, 810–814. doi: 10.1126/science.1226854

Conflict of Interest Statement: The author declares that the research was conducted in the absence of any commercial or financial relationships that could be construed as a potential conflict of interest.

frontiers in Synaptic Neuroscience

PERSPECTIVE
published: 19 August 2016
doi: 10.3389/fnsyn.2016.00023

The Postsynaptic Density: There Is More than Meets the Eye

Ayse Dosemeci[1], Richard J. Weinberg[2], Thomas S. Reese[1] and Jung-Hwa Tao-Cheng[3]*

[1] Laboratory of Neurobiology, National Institute of Neurological Disorders and Stroke (NINDS), National Institutes of Health (NIH), Bethesda, MD, USA, [2] Department of Cell Biology and Physiology, University of North Carolina, Chapel Hill, Chapel Hill, NC, USA, [3] Electron Microscopy Facility, National Institute of Neurological Disorders and Stroke (NINDS), National Institutes of Health (NIH), Bethesda, MD, USA

The postsynaptic density (PSD), apparent in electron micrographs as a dense lamina just beneath the postsynaptic membrane, includes a deeper layer, the "pallium", containing a scaffold of Shank and Homer proteins. Though poorly defined in traditionally prepared thin-section electron micrographs, the pallium becomes denser and more conspicuous during intense synaptic activity, due to the reversible addition of CaMKII and other proteins. In this Perspective article, we review the significance of CaMKII-mediated recruitment of proteins to the pallium with respect to both the trafficking of receptors and the remodeling of spine shape that follow synaptic stimulation. We suggest that the level and duration of CaMKII translocation and activation in the pallium will shape activity-induced changes in the spine.

Keywords: postsynaptic density, PSD, pallium, electron microscopy, EM, Shank, Homer, CaMKII

OPEN ACCESS

Edited by:
George Augustine, Nanyang Technologicial University (NTU), Singapore

Reviewed by:
Eric Hanse, University of Gothenburg, Sweden
Anne McKinney, McGill University, Canada

****Correspondence:***
Ayse Dosemeci
dosemeca@mail.nih.gov

Received: *17 May 2016*
Accepted: *25 July 2016*
Published: *19 August 2016*

Citation:
Dosemeci A, Weinberg RJ, Reese TS and Tao-Cheng J-H (2016) The Postsynaptic Density: There Is More than Meets the Eye. Front. Synaptic Neurosci. 8:23. doi: 10.3389/fnsyn.2016.00023

Excitatory glutamatergic synapses examined with the electron microscope typically display a pronounced postsynaptic density (PSD), which appears in conventional electron micrographs as an approximately 30 nm thick electron-dense structure applied to the postsynaptic membrane (Palay, 1956). The large majority of excitatory synapses in the vertebrate CNS release glutamate as neurotransmitter. Ionotropic glutamate receptors concentrate at the PSD, where specialized molecules anchor them and regulate their trafficking; modulation of their expression and trafficking plays a key role in synaptic plasticity. Decades of research show that much of the story of this modulation resides in the PSD.

Using special stains, Valtschanoff and Weinberg (2001) uncovered a distinct layer ~50 nm thick immediately adjacent and deep to the PSD. Though previously reported, this "subsynaptic web" (DeRobertis, 1964) had been largely ignored for decades, because it is difficult to distinguish from the rest of the spine cytoplasm after standard histological procedures. Extending this work, Petralia et al. (2005) reported high levels of immunoEM label for both Shank and Homer in the same region, which was referred to as the "subjacent" area.

The subsynaptic web becomes more prominent after short bouts of stimulation, reflecting the reversible incorporation of additional proteins. Because this part of the PSD comprises different proteins and displays a more labile organization than the "core" layer lining the synaptic membrane, it merits a distinct name; we propose to designate this separate structural and functional layer of the PSD as its *pallium* or mantle (**Figure 1**). Here we present a perspective on PSD structure that highlights potential functions carried out in the pallium.

CORE LAYER OF THE PSD

Though highly variable, PSDs in the rodent forebrain contain on average 300–400 copies of PSD-95 and related membrane-associated guanylate kinase (MAGUK) molecules (Chen et al., 2005;

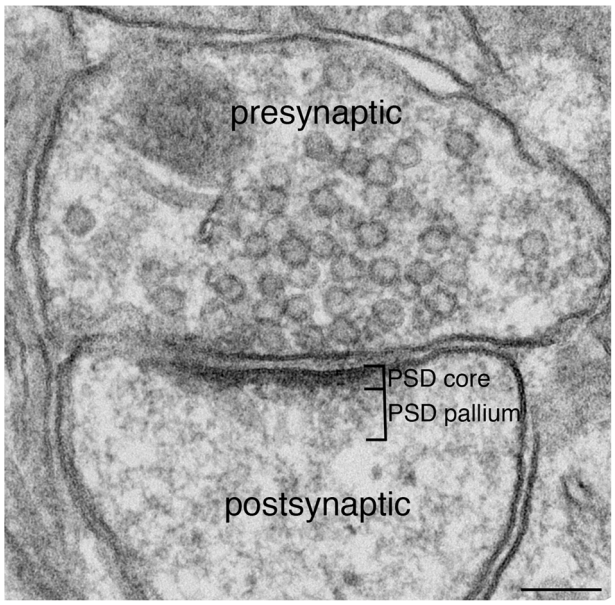

FIGURE 1 | Excitatory synapse. Excitatory glutamatergic synapses typically display a prominent electron-dense zone juxtaposed to the postsynaptic membrane, traditionally known as the postsynaptic density (PSD). Extending deeper from the PSD core is a specialized region we call the PSD pallium. Scale bar: 0.1 μm.

BOX 1 | Major scaffold proteins in the PSD.

Names used in the present article are listed along with synonyms.

MAGUKs (membrane-associated guanylate kinases).

The most abundant MAGUK at the mammalian PSD is **PSD-95** (DLG4, SAP90); others include SAP97 (DLG1), PSD-93 (DLG2, Chapsyn-110), and SAP102 (DLG3).

GKAP (guanylate kinase-associated protein) also called SAPAP (SAP90/PSD-95-associated protein), or disks large-associated protein.

Shank (SH3 and multiple ankyrin repeat domains protein) also called ProSAP (Proline-rich synapse-associated protein), Synamon and CortBP (Cortactin binding protein).

Homer also called Vesl, Cupidin, and PSD-Zip45.

Sugiyama et al., 2005). PSD-95 is localized in the core layer of the PSD. Comparing immunogold labeling with antibodies against its N- and C-termini shows that PSD-95 is oriented with its N-terminus near the plane of the postsynaptic membrane and its C-terminus deep in the spine (Chen et al., 2008). Electron microscopic tomography reveals vertical filaments extending from the postsynaptic membrane in numbers and dimensions expected for PSD-95 (Chen et al., 2008), and these filaments are depleted by acute knockdown of PSD-95 (Chen et al., 2011). Thus, PSD-95-containing filaments oriented vertically to the postsynaptic membrane represent a major structural component of the core layer (Chen et al., 2008). This close apposition to the membrane puts PSD-95 in a position to bind neurotransmitter receptors. Indeed, there is substantial evidence indicating the association of PSD-95 with both NMDA and AMPA types of glutamate receptors.

EM tomography also reveals filaments of different lengths, oriented parallel to the postsynaptic membrane, that appear to contact the deep (C-terminal) ends of PSD-95 filaments (Chen et al., 2008). The dimensions of one frequently-encountered type of horizontal filament corresponds to that expected for guanylate kinase-associated protein (GKAP), consistent with biochemical work demonstrating that GKAP can bind PSD-95 near its C-terminal (Kim et al., 1997). GKAP is in the PSD at a ratio of approximately one GKAP for two PSD-95s (Lowenthal et al., 2015) so a layer of GKAP cross-linked with PSD-95 could provide an interface between the core layer and the pallium of the PSD. Like PSD-95 (Yang et al., 2011), GKAP stays put during brief stimulation (Tao-Cheng et al., 2015). Thus, the dense matrix of PSD-95/MAGUK filaments capped by GKAPs provides a stable platform for the subjacent pallium.

PALLIAL LAYER OF THE PSD

Early biochemical analyses indicated that the PSD complex contains several types of scaffolding molecules in addition to MAGUKs and GKAPs (**Box 1**). Two-hybrid and co-immunoprecipitation experiments led to the identification of the Shank/ProSAP family of proteins, which bind to GKAPs (Boeckers et al., 1999a,b; Naisbitt et al., 1999). Similar two-hybrid studies identified the Homer family of proteins as binding partners for Shanks and the two types of proteins were shown to co-immunoprecipitate from brain extracts (Tu et al., 1999). Both Shank and Homer family proteins are highly enriched in PSD fractions (Xiao et al., 1998; Naisbitt et al., 1999) and co-purify as large complexes, with PSD-95, GKAP and other PSD constituents (Collins et al., 2006; Dosemeci et al., 2007).

While biochemical studies identify Shank and Homer as part of the PSD complex, immunoEM studies show that label for these proteins concentrates outside the electron-dense material conventionally defined as the PSD (**Figure 2**). Although the reported distributions of label for these proteins differ somewhat between groups, immunoEM studies typically find that much of the postsynaptic immunogold label for both Shank and Homer lie in a layer immediately below the PSD core (Tu et al., 1999; Valtschanoff and Weinberg, 2001; Petralia et al., 2005; Rostaing et al., 2006; Tao-Cheng et al., 2010, 2014a).

These data imply that a network containing Shanks and Homer extends the PSD scaffold well beyond the classically recognized electron-dense material. This second layer, which we term the *pallium*, is likely pegged to the PSD core through GKAPs, which can simultaneously associate with PSD-95 and Shanks. *In vitro* studies report that Shanks can associate with each other through their SAM domains to form sheet-like structures (Baron et al., 2006) and Homers can polymerize into tetramers that can cross-link Shanks (Hayashi et al., 2009). Furthermore, purified C-terminal Shank and Homer form a mesh-like matrix when mixed together (Hayashi et al., 2009). Thus, Shank and Homer proteins in the pallium are likely to form an extended scaffold. The side of this scaffold facing the cleft is continuous

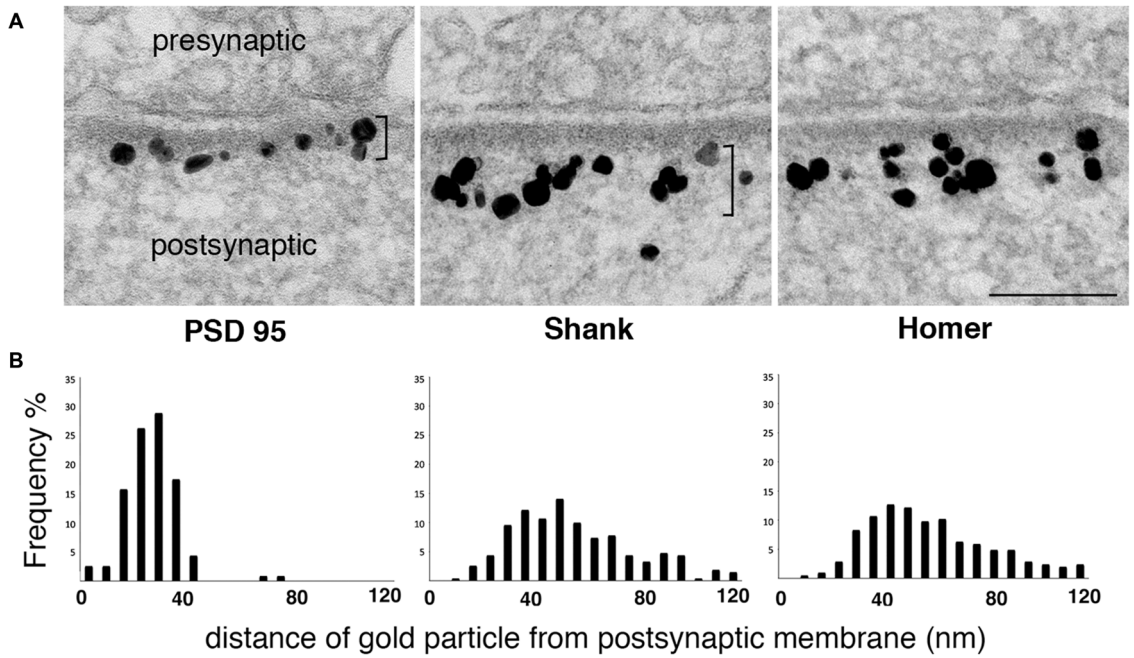

FIGURE 2 | Label for two PSD scaffold proteins, Shank and Homer, lies mostly outside the PSD core. (A) Electron micrographs of asymmetric synapses in cultured hippocampal neurons immunogold labeled with antibodies for three major PSD scaffold proteins. Silver-enhanced gold label appears as black particles of heterogeneous size (EM in middle panel from Tao-Cheng et al., 2015). The PSD core with PSD-95 label and the PSD pallium with Shank and Homer labels are marked by brackets on the left and middle panels respectively. Scale bar: 0.1 μm. **(B)** Frequency histograms depicting the distribution of label at the postsynaptic compartment in a typical experiment. While label for PSD-95 is within the electron-dense material, label for Shank and Homer is concentrated in a deeper region we designate as the *pallium* of the PSD.

with the PSD core, whereas the cytoplasmic side, characterized by an extremely rough surface (Petersen et al., 2003) merges imperceptibly into the central zone of the spine head.

ACTIVITY-INDUCED CHANGES AT THE PALLIUM

The Pallium Becomes More Electron-Dense as CaMKII Accumulates

Thin-section EM of cultured hippocampal neurons reveals increased electron density at the pallium under excitatory conditions (**Figure 3**: top panels), a phenomenon we have described as PSD "thickening" (Dosemeci et al., 2001). The increase in electron density likely reflects the addition of proteins, and immunoEM shows significant increase in CaMKII immunolabel within the PSD complex under excitatory conditions (**Figure 3**: bottom panels, Dosemeci et al., 2001). Similar morphological changes at the PSD, accompanied by the accumulation of CaMKII and other proteins, also occur under the excitotoxic conditions promoted by ischemia (Suzuki et al., 1994; Hu et al., 1998; Martone et al., 1999). The duration of the morphological and compositional changes at the PSD appears to vary according to the type of stimulation; importantly, more sustained modification is observed following an LTP-inducing protocol (Otmakhov et al., 2004).

Role of CaMKII as a Kinase

CaMKII, a Ca^{2+}-regulated serine-threonine protein kinase, is present at very high concentrations in neurons, with a relative abundance reaching ∼1–2% of total protein in the cerebral cortex and hippocampus (Erondu and Kennedy, 1985). Within neurons, CaMKII is especially prominent in the PSD pallium (Petralia et al., 2005; Ding et al., 2013). Activation of CaMKII plays a pivotal role in certain types of synaptic modification, most notably NMDA-dependent LTP (reviews: Lisman et al., 2012; Shonesy et al., 2014).

The CaMKII holoenzyme is a dodecamer made of individually active subunits, with α- and β-isoforms prevalent in brain. Subunits within a single holoenzyme can phosphorylate one another, a process called autophosphorylation. Upon autophosphorylation in the presence of Ca^{2+}, CaMKII becomes autonomous, allowing enzymatic activity to persist beyond the duration of Ca^{2+} elevation (reviews: Hell, 2014; Shonesy et al., 2014). Autonomous CaMKII can remain at the PSD pallium after the cessation of excitatory stimuli (Dosemeci et al., 2002; Otmakhov et al., 2004). Continued co-localization of autonomous CaMKII with its substrates at the pallium would counteract dephosphorylation by phosphatases and thus help maintain phosphorylation of CaMKII substrates.

The accumulation and activation of CaMKII at the pallium triggers further changes at the PSD. Some of these have been studied in depth, such as the incorporation of AMPA receptors

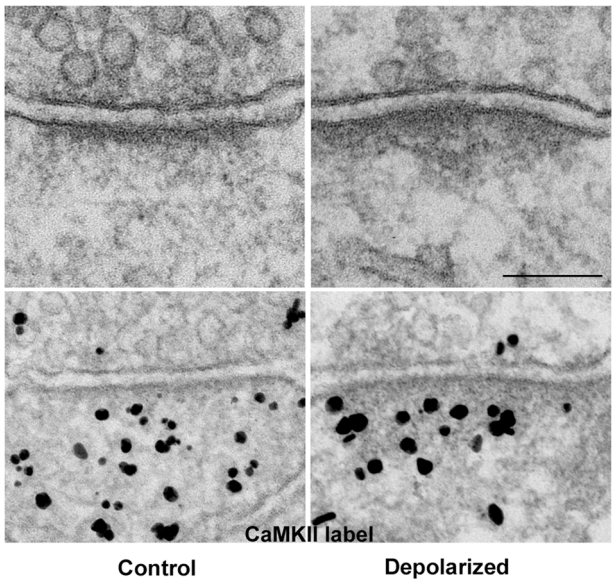

FIGURE 3 | The PSD pallium becomes electron-dense as CaMKII and other proteins are recruited under excitatory conditions. Electron micrographs of asymmetric synapses in cultured hippocampal neurons under basal conditions (left) and after depolarization in medium containing high K^+ (right). Upon intense synaptic activity the pallium of the PSD becomes electron-dense due to the accumulation of proteins, including CaMKII (bottom panels). Scale bar: 0.1 μm.

into the postsynaptic membrane (review: Lisman et al., 2012). ImmunoEM studies also reveal activity-induced increases in the levels of a number of proteins at the pallium, including SynGAP, AIDA-1 and Shanks, in parallel with CaMKII. Importantly, the redistribution of all these PSD components is blocked by the application of a specific CaMKII inhibitor (Yang et al., 2013; Tao-Cheng et al., 2014b; Dosemeci et al., 2016), indicating that the activation of CaMKII is required for the redistribution of these PSD components.

Role of CaMKII as a Dynamic Structural Element

In addition to its function as a protein kinase, accumulating evidence suggests that CaMKII in the pallium may act as a scaffold. Bingol et al. (2010) show that activity-induced translocation of autophosphorylated α-CaMKII, but not its kinase activity, is responsible for the translocation of proteasomes into synapses. Similarly, activity-induced CaMKII translocation is responsible for parallel accumulation of the deubiquitinase CYLD, specific for K63-linked polyubiquitins, to the PSD (Thein et al., 2014). Since K63-linked polyubiquitination inhibits interaction of proteins with proteasomes (Nathan et al., 2013) CYLD activity is expected to facilitate protein binding to proteasomes. Thus, CaMKII accumulated at the pallium appears to constitute a structural platform that brings together components that may work synergistically to promote local degradation of proteins.

Activity-induced translocation of CaMKII also may mediate modifications in spine morphology. CaMKII holoenzymes at the spine cytoplasm serve as actin bundling elements (Okamoto et al., 2007) and dissociation of CaMKII from F-actin upon autophosphorylation destabilizes the actin cytoskeleton (Kim et al., 2015). Thus the translocation of CaMKII from the actin network to the PSD pallium can trigger synchronized changes at the PSD and actin cytoskeleton.

SynGAP Levels Decrease in the PSD Core and Increase in the Pallium

SynGAP is an enzymatic regulator of Ras, a small GTPase. However, as one of the most abundant proteins at the PSD (at levels exceeding even those of PSD-95, its binding partner at the PSD core), SynGAP is likely to also play a non-enzymatic role. ImmunoEM shows that SynGAP label is concentrated at the PSD core (Yang et al., 2011, 2013). After strong depolarization, labeling for SynGAP significantly decreases at the PSD core while increasing at the pallium (Yang et al., 2011, 2013). Under the same conditions, label for PSD-95 does not change its localization at the PSD (Yang et al., 2011), implying dissociation of the two molecules. Further studies indicate that the release of SynGAP from PSD-95 and its exit from the PSD core require CaMKII-mediated phosphorylation (Yang et al., 2013; Araki et al., 2015).

NMDA- or high K^+-induced changes in the distribution of SynGAP are reversed within 30 min after cessation of the excitatory conditions. In contrast, a stimulation protocol (glycine in the absence of Mg^{2+}) that leads to sustained increases in synaptic efficacy (chem-LTP) also leads to a sustained exclusion of SynGAP from the spine (Araki et al., 2015) indicating a correlation between LTP and the removal of SynGAP. It appears likely that a wide range of excitatory stimuli promotes translocation of SynGAP out of the PSD core, but that only under LTP-promoting conditions is the molecule removed on a long-term basis. The extent and maintenance of SynGAP phosphorylation at the pallium may determine its subsequent movement. In this regard, it is interesting that SynGAP is most efficiently phosphorylated by the autonomous form of CaMKII in the absence of Ca^{2+} (Dosemeci and Jaffe, 2010).

What might be the functional implications of activity-induced redistribution of SynGAP at the PSD? Both SynGAP and members of the transmembrane AMPA receptor regulatory protein family (TARPs) can bind to the same PDZ domains on PSD-95 (Kim et al., 1998; Schnell et al., 2002; Dakoji et al., 2003) and thus may compete for association with PSD-95. Considering its high abundance in the PSD, SynGAP is likely to block TARP binding to PDZ domains on PSD-95 under basal conditions. Thus, the removal of SynGAP during activity may be a prerequisite for the anchoring of AMPA receptors to the PSD, explaining the well-documented role of SynGAP as an inhibitor of AMPA receptor insertion (Rumbaugh et al., 2006). This function may account for the remarkable abundance of SynGAP at the PSD.

AIDA-1 Levels Decrease in the PSD Core and Increase in the Pallium

Quantitative mass spectrometric analysis of PSD fractions reveals that Amyloid-β protein precursor Intracellular Domain-

Associated 1 (AIDA-1, also known as EB-1 and ANKS1B) is a major component of the PSD complex, with a PSD-95/AIDA-1/GKAP stoichiometry of 2:1:1 (Lowenthal et al., 2015). Like SynGAP, AIDA-1 binds directly to PSD-95 at the same domains that bind TARPs (Jordan et al., 2007) and therefore could also interfere with the anchoring of AMPA receptors. By immunoEM, the AIDA-1 label is mostly located within the PSD core at rest (Jacob et al., 2010; Dosemeci et al., 2015). Under excitatory conditions AIDA-1 label at the PSD core is significantly reduced with a concomitant increase at the pallium (Dosemeci et al., 2015). The reversible CaMKII-mediated redistribution of AIDA-1 at the PSD under excitatory conditions (Dosemeci et al., 2016) parallels that of SynGAP. We speculate that different regulatory mechanisms may trigger dissociation of SynGAP and AIDA-1 from PSD-95.

Shank Levels Increase in the Pallium

Shanks, a protein scaffold family concentrated in the PSD, are encoded by three genes, *Shank1*, *Shank2* and *Shank3*, each giving rise to multiple splice variants. Shank mutations have been linked to autism and other neurodevelopmental/neuropsychiatric disorders (reviews: Grabrucker et al., 2011; Sala et al., 2015). All Shank isoforms have a similar molecular organization, with specialized domains that can associate with GKAPs, Homers, and other Shanks. Analysis of immunoEM data suggests that Shanks at the PSD are organized into a proximal pool, close enough to the interface between the core and pallium to associate with GKAP, and a distal (deeper) pool that may be stabilized through association with Homers and/or with other Shanks. Under excitatory conditions, Shanks accumulate preferentially in the distal pool (Tao-Cheng et al., 2015).

Shanks promote maturation of dendritic spines and the enlargement of spine heads (Sala et al., 2001), although the precise mechanism remains unclear. Considering that changes in spine shape and size involve reorganization of the actin cytoskeleton, it is likely that Shanks regulate spine morphology through interaction with actin. Indeed, Shanks associate with three actin-regulating proteins, Insulin Receptor Substrate Protein 53 (IRSp53), Abp1 and cortactin.

The actin binding protein IRSp53 (also called BAIAP2; see review by Kang et al., 2016) is a major PSD component, with a molar ratio of IRSp53 to PSD-95 of 1:4 (Lowenthal et al., 2015). IRSp53 is located between layers containing Shank and PSD-95, relatively close to the postsynaptic membrane (Burette et al., 2014), where it may function as a linker between the actin cytoskeleton and the plasma membrane (Scita et al., 2008; Burette et al., 2014). Indeed, IRSp53 contains an actin-binding BAR-like domain that can induce changes in membrane curvature (Zhao et al., 2011) and thus may be involved in activity-induced changes in the curvature of the synapse (Burette et al., 2014).

Abp1, which can associate simultaneously with actin and Shanks, may link the actin cytoskeleton to the PSD (Qualmann et al., 2004). Abp1 preferentially interacts with dynamic rather than static F-actin structures (Kessels et al., 2000) and more Abp1 becomes incorporated into Shank-positive synapses during activity (Qualmann et al., 2004). Overexpression of Abp1 increases the density of mushroom-shaped spines; importantly, its association with Shank is necessary for Abp1-mediated regulation of spine morphology (Haeckel et al., 2008).

TABLE 1 | Redistribution of postsynaptic density (PSD) components during activity.

	CaMKII	SynGAP	AIDA-1	Shank	CYLD
Core		decrease	decrease		
Pallium	increase	increase	increase	increase	increase

Changes observed in immunogold label density for selected proteins following treatment of cultured hippocampal neurons with media containing NMDA or high K^+.

Another protein that associates with both Shanks and actin is cortactin, although immunoEM shows that cortactin concentrates mainly at the central region of the spine (Racz and Weinberg, 2004). In contrast to Abp1, cortactin exits the spines during activity (Hering and Sheng, 2003). While Abp1 overexpression increases mushroom spine density (Haeckel et al., 2008), cortactin overexpression causes elongation of spines (Hering and Sheng, 2003).

The above considerations lead us to suggest a model for activity-induced modification of spine morphology: under basal conditions, cytosolic Shanks within the spine are pegged to the actin cytoskeleton through cortactin and held outside of the pallium. During activity, CaMKII-mediated phosphorylation releases Shanks from cortactin. The Shank thus released accumulates at the pallium, while cortactin exits the spine. Shank accumulated at the pallium could then recruit Abp1 to promote remodeling of the actin cytoskeleton around the pallium.

ACTIN AND THE PSD

There are several reports that filaments of F-actin, the primary cytoskeletal component of the spine, contact the PSD (Gulley and Reese, 1981; Landis and Reese, 1983; Fifková, 1985), especially at its periphery (Burette et al., 2012), though these contacts are likely highly variable, considering the dynamic nature of F-actin. While the molecular basis of the attachment of actin filaments to the PSD remains uncertain, a number of PSD molecules are plausible candidates. As discussed above, two Shank binding proteins, IRSp53 and Abp1, may provide a link between the PSD and the actin cytoskeleton.

Yet another point of interaction of actin with the PSD may be through the ubiquitous actin binding protein α-actinin. *In vitro* assays show that α-actinin can form a ternary complex with the PSD proteins, densin and CaMKII (Walikonis et al., 2001). Loss of α-actinin-2 in rat hippocampal neurons creates an increased density of immature, filopodia-like protrusions that fail to mature into a mushroom-shaped spine during development (Hodges et al., 2014).

CONCLUSION

The pallium is an extension of the electron-dense PSD core, demarcated by strong immunolabeling for two PSD

scaffold proteins, Shank and Homer. This specialized zone, sandwiched between the electron-dense PSD core and the actin "spinoskeleton", is highly dynamic, exhibiting striking changes during synaptic activity. Under conditions of strong excitation, the pallium becomes electron-dense, with the addition of CaMKII and several other proteins (**Table 1**). Activation and/or translocation of CaMKII is necessary for the recruitment of other components to the pallium.

The pallium can be viewed as a hub where several proteins converge during activity. Accumulating evidence on the movements of individual proteins suggests a mechanism for concerted insertion of receptors to the PSD and re-organization of the actin spinoskeleton, both mediated by CaMKII. Upon synaptic stimulation, translocation and activation of CaMKII cause SynGAP and AIDA-1 to move out of the PSD core and accumulate at the pallium (Yang et al., 2013; Dosemeci et al., 2015, 2016). We propose that the movement of SynGAP (and perhaps also of AIDA-1) vacates "slots" on PSD-95, providing a window of opportunity for the insertion of AMPA receptors. Simultaneous CaMKII-mediated accumulation of Shanks at the pallium (Tao-Cheng et al., 2014b), on the other hand, may enable actin reorganization around the PSD. CaMKII also acts as a dynamic structural element whose activity-induced translocation changes the molecular organization within the spine. Dissociation of CaMKII from F-actin causes destabilization and reorganization of the actin cytoskeleton (Kim et al., 2015). Subsequent accumulation of CaMKII at the pallium docks elements that regulate protein turnover (Bingol et al., 2010; Thein et al., 2014).

In summary, activation of CaMKII and its translocation to the pallium under excitatory conditions trigger a chain of events poised to elicit profound effects on the organization of the PSD complex and of the actin cytoskeleton that could synchronize receptor trafficking with changes in spine morphology. We speculate that the degree and duration of CaMKII accumulation and activity at the pallium, promoted by different types of excitatory stimuli, may determine the type and level of synaptic modification.

AUTHOR CONTRIBUTIONS

All authors contributed to the writing of the manuscript.

ACKNOWLEDGMENTS

We would like to thank Dr. John Lisman for stimulating discussions and for a critical reading of the manuscript. This work was supported by the Intramural Research Program of the National Institute of Neurological Disorders and Stroke (NINDS)/National Institutes of Health (NIH) and NINDS/NIH NS 039444 grant to RJW.

REFERENCES

Araki, Y., Zeng, M., Zhang, M., and Huganir, R. L. (2015). Rapid dispersion of SynGAP from synaptic spines triggers AMPA receptor insertion and spine enlargement during LTP. *Neuron* 85, 173–189. doi: 10.1016/j.neuron.2014.12.023

Baron, M. K., Boeckers, T. M., Vaida, B., Faham, S., Gingery, M., Sawaya, M. R., et al. (2006). An architectural framework that may lie at the core of the postsynaptic density. *Science* 311, 531–535. doi: 10.1126/science.1118995

Bingol, B., Wang, C. F., Arnott, D., Cheng, D., Peng, J., and Sheng, M. (2010). Autophosphorylated CaMKIIα acts as a scaffold to recruit proteasomes to dendritic spines. *Cell* 140, 567–578. doi: 10.1016/j.cell.2010.01.024

Boeckers, T. M., Kreutz, M. R., Winter, C., Zuschratter, W., Smalla, K. H., Sanmarti-Vila, L., et al. (1999a). Proline-rich synapse-associated protein-1/cortactin binding protein 1 (ProSAP1/CortBP1) is a PDZ-domain protein highly enriched in the postsynaptic density. *J. Neurosci.* 19, 6506–6518.

Boeckers, T. M., Winter, C., Smalla, K. H., Kreutz, M. R., Bockmann, J., Seidenbecher, C., et al. (1999b). Proline-rich synapse-associated proteins ProSAP1 and ProSAP2 interact with synaptic proteins of the SAPAP/GKAP family. *Biochem. Biophys. Res. Commun.* 264, 247–252. doi: 10.1006/bbrc.1999.1489

Burette, A. C., Lesperance, T., Crum, J., Martone, M., Volkmann, N., Ellisman, M. H., et al. (2012). Electron tomographic analysis of synaptic ultrastructure. *J. Comp. Neurol.* 520, 2697–2711. doi: 10.1002/cne.23067

Burette, A. C., Park, H., and Weinberg, R. J. (2014). Postsynaptic distribution of IRSp53 in spiny excitatory and inhibitory neurons. *J. Comp. Neurol.* 522, 2164–2178. doi: 10.1002/cne.23526

Chen, X., Nelson, C. D., Li, X., Winters, C. A., Azzam, R., Sousa, A. A., et al. (2011). PSD-95 is required to sustain the molecular organization of the postsynaptic density. *J. Neurosci.* 31, 6329–6338. doi: 10.1523/JNEUROSCI.5968-10.2011

Chen, X., Vinade, L., Leapman, R. D., Petersen, J. D., Nakagawa, T., Phillips, T. M., et al. (2005). Mass of the postsynaptic density and enumeration of three key molecules. *Proc. Natl. Acad. Sci. U S A* 102, 11551–11556. doi: 10.1073/pnas.0505359102

Chen, X., Winters, C., Azzam, R., Li, X., Galbraith, J. A., Leapman, R. D., et al. (2008). Organization of the core structure of the postsynaptic density. *Proc. Natl. Acad. Sci. U S A* 105, 4453–4458. doi: 10.1073/pnas.0800897105

Collins, M. O., Husi, H., Yu, L., Brandon, J. M., Anderson, C. N., Blackstock, W. P., et al. (2006). Molecular characterization and comparison of the components and multiprotein complexes in the postsynaptic proteome. *J. Neurochem.* 97, 16–23. doi: 10.1111/j.1471-4159.2005.03507.x

Dakoji, S., Tomita, S., Karimzadegan, S., Nicoll, R. A., and Bredt, D. S. (2003). Interaction of transmembrane AMPA receptor regulatory proteins with multiple membrane associated guanylate kinases. *Neuropharmacology* 45, 849–856. doi: 10.1016/s0028-3908(03)00267-3

DeRobertis, E. D. P. (1964). "International series of monographs on pure and applied biology. Division, modern trends in physiological sciences," in *Histophysiology of Synapses and Neurosecretion* (Vol. 20), eds P. Alexander and Z. M. Bacq (Oxford: Pergamon Press), 34–42.

Ding, J. D., Kennedy, M. B., and Weinberg, R. J. (2013). Subcellular organization of camkii in rat hippocampal pyramidal neurons. *J. Comp. Neurol.* 521, 3570–3583. doi: 10.1002/cne.23372

Dosemeci, A., and Jaffe, H. (2010). Regulation of phosphorylation at the postsynaptic density during different activity states of Ca^{2+}/calmodulin-dependent protein kinase II. *Biochem. Biophys. Res. Commun.* 391, 78–84. doi: 10.1016/j.bbrc.2009.10.167

Dosemeci, A., Makusky, A. J., Jankowska-Stephens, E., Yang, X., Slotta, D. J., and Markey, S. P. (2007). Composition of the synaptic PSD-95 complex. *Mol. Cell. Proteomics* 6, 1749–1760. doi: 10.1074/mcp.M700040-MCP200

Dosemeci, A., Tao-Cheng, J. H., Vinade, L., Winters, C. A., Pozzo-Miller, L., and Reese, T. S. (2001). Glutamate-induced transient modification of the postsynaptic density. *Proc. Natl. Acad. Sci. U S A* 98, 10428–10432. doi: 10.1073/pnas.181336998

Dosemeci, A., Toy, D., Burch, A., Bayer, K. U., and Tao-Cheng, J. H. (2016). CaMKII-mediated displacement of AIDA-1 out of the postsynaptic density core. *FEBS Lett.* doi: 10.1002/1873-3468.12334 [Epub ahead of print].

Dosemeci, A., Toy, D., Reese, T. S., and Tao-Cheng, J. H. (2015). AIDA-1 moves out of the postsynaptic density core under excitatory conditions. *PLoS One* 10:e0137216. doi: 10.1371/journal.pone.0137216

Dosemeci, A., Vinade, L., Winters, C. A., Reese, T. S., and Tao-Cheng, J. H. (2002). Inhibition of phosphatase activity prolongs NMDA-induced modification of the postsynaptic density. *J. Neurocytol.* 31, 605–612. doi: 10.1023/A:1025735410738

Erondu, N. E., and Kennedy, M. B. (1985). Regional distribution of type II Ca^{2+}/calmodulin-dependent protein kinase in rat brain. *J. Neurosci.* 5, 3270–3277.

Fifková, E. (1985). Actin in the nervous system. *Brain Res.* 356, 187–215. doi: 10.1016/0165-0173(85)90012-8

Grabrucker, A. M., Schmeisser, M. J., Schoen, M., and Boeckers, T. M. (2011). Postsynaptic ProSAP/Shank scaffolds in the cross-hair of synaptopathies. *Trends Cell Biol.* 21, 594–603. doi: 10.1016/j.tcb.2011.07.003

Gulley, R. L., and Reese, T. S. (1981). Cytoskeletal organization at the postsynaptic complex. *J. Cell Biol.* 91, 298–302. doi: 10.1083/jcb.91.1.298

Haeckel, A., Ahuja, R., Gundelfinger, E. D., Qualmann, B., and Kessels, M. M. (2008). The actin-binding protein Abp1 controls dendritic spine morphology and is important for spine head and synapse formation. *J. Neurosci.* 28, 10031–10044. doi: 10.1523/jneurosci.0336-08.2008

Hayashi, M. K., Tang, C., Verpelli, C., Narayanan, R., Stearns, M. H., Xu, R. M., et al. (2009). The postsynaptic density proteins Homer and Shank form a polymeric network structure. *Cell* 137, 159–171. doi: 10.1016/j.cell.2009.01.050

Hell, J. W. (2014). CaMKII: claiming center stage in postsynaptic function and organization. *Neuron* 81, 249–265. doi: 10.1016/j.neuron.2013.12.024

Hering, H., and Sheng, M. (2003). Activity-dependent redistribution and essential role of cortactin in dendritic spine morphogenesis. *J. Neurosci.* 23, 11759–11769.

Hodges, J. L., Vilchez, S. M., Asmussen, H., Whitmore, L. A., and Horwitz, A. R. (2014). α-Actinin-2 mediates spine morphology and assembly of the post-synaptic density in hippocampal neurons. *PLoS One* 9:e101770. doi: 10.1371/journal.pone.0101770

Hu, B. R., Park, M., Martone, M. E., Fischer, W. H., Ellisman, M. H., and Zivin, J. A. (1998). Assembly of proteins to postsynaptic densities after transient cerebral ischemia. *J. Neurosci.* 18, 625–633.

Jacob, A. L., Jordan, B. A., and Weinberg, R. J. (2010). Organization of amyloid-beta protein precursor intracellular domain-associated protein-1 in the rat brain. *J. Comp. Neurol.* 518, 3221–3236. doi: 10.1002/cne.22394

Jordan, B. A., Fernholz, B. D., Khatri, L., and Ziff, E. B. (2007). Activity-dependent AIDA-1 nuclear signaling regulates nucleolar numbers and protein synthesis in neurons. *Nat. Neurosci.* 10, 427–435. doi: 10.1038/nn1867

Kang, J., Park, H., and Kim, E. (2016). IRSp53/BAIAP2 in dendritic spine development, NMDA receptor regulation and psychiatric disorders. *Neuropharmacology* 100, 27–39. doi: 10.1016/j.neuropharm.2015.06.019

Kessels, M. M., Engqvist-Goldstein, A. E., and Drubin, D. G. (2000). Association of mouse actin-binding protein 1 (mAbp1/SH3P7), an Src kinase target, with dynamic regions of the cortical actin cytoskeleton in response to Rac1 activation. *Mol. Biol. Cell* 11, 393–412. doi: 10.1091/mbc.11.1.393

Kim, K., Lakhanpal, G., Lu, H. E., Khan, M., Suzuki, A., Hayashi, M. K., et al. (2015). A temporary gating of actin remodeling during synaptic plasticity consists of the interplay between the kinase and structural functions of CaMKII. *Neuron* 87, 813–826. doi: 10.1016/j.neuron.2015.07.023

Kim, J. H., Liao, D., Lau, L. F., and Huganir, R. L. (1998). SynGAP: a synaptic RasGAP that associates with the PSD-95/SAP90 protein family. *Neuron* 20, 683–691. doi: 10.1016/s0896-6273(00)81008-9

Kim, E., Naisbitt, S., Hsueh, Y. P., Rao, A., Rothschild, A., Craig, A. M., et al. (1997). GKAP, a novel synaptic protein that interacts with the guanylate kinase-like domain of the PSD-95/SAP90 family of channel clustering molecules. *J. Cell Biol.* 136, 669–678. doi: 10.1083/jcb.136.3.669

Landis, D. M., and Reese, T. S. (1983). Cytoplasmic organization in cerebellar dendritic spines. *J. Cell Biol.* 97, 1169–1178. doi: 10.1083/jcb.97.4.1169

Lisman, J., Yasuda, R., and Raghavachari, S. (2012). Mechanisms of CaMKII action in long-term potentiation. *Nat. Rev. Neurosci.* 13, 169–182. doi: 10.1038/nrn3192

Lowenthal, M. S., Markey, S. P., and Dosemeci, A. (2015). Quantitative mass spectrometry measurements reveal stoichiometry of principal postsynaptic density proteins. *J. Proteome Res.* 14, 2528–2538. doi: 10.1021/acs.jproteome.5b00109

Martone, M. E., Jones, Y. Z., Young, S. J., Ellisman, M. H., Zivin, J. A., and Hu, B. R. (1999). Modification of postsynaptic densities after transient cerebral ischemia: a quantitative and three-dimensional ultrastructural study. *J. Neurosci.* 19, 1988–1997.

Naisbitt, S., Kim, E., Tu, J. C., Xiao, B., Sala, C., Valtschanoff, J., et al. (1999). Shank, a novel family of postsynaptic density proteins that binds to the NMDA receptor/PSD-95/GKAP complex and cortactin. *Neuron* 23, 569–582. doi: 10.1016/s0896-6273(00)80809-0

Nathan, J. A., Kim, H. T., Ting, L., Gygi, S. P., and Goldberg, A. L. (2013). Why do cellular proteins linked to K63-polyubiquitin chains not associate with proteasomes? *EMBO J.* 32, 552–565. doi: 10.1038/emboj.2012.354

Okamoto, K., Narayanan, R., Lee, S. H., Murata, K., and Hayashi, Y. (2007). The role of CaMKII as an F-actin-bundling protein crucial for maintenance of dendritic spine structure. *Proc. Natl. Acad. Sci. U S A* 104, 6418–6423. doi: 10.1073/pnas.0701656104

Otmakhov, N., Tao-Cheng, J. H., Carpenter, S., Asrican, B., Dosemeci, A., Reese, T. S., et al. (2004). Persistent accumulation of calcium/calmodulin-dependent protein kinase II in dendritic spines after induction of NMDA receptor-dependent chemical long-term potentiation. *J. Neurosci.* 24, 9324–9331. doi: 10.1523/JNEUROSCI.2350-04.2004

Palay, S. L. (1956). Synapses in the central nervous system. *J. Biophys. Biochem. Cytol.* 2, 193–202. doi: 10.1083/jcb.2.4.193

Petersen, J. D., Chen, X., Vinade, L., Dosemeci, A., Lisman, J. E., and Reese, T. S. (2003). Distribution of postsynaptic density (PSD)-95 and Ca^{2+}/calmodulin-dependent protein kinase II at the PSD. *J. Neurosci.* 23, 11270–11278.

Petralia, R. S., Sans, N., Wang, Y. X., and Wenthold, R. J. (2005). Ontogeny of postsynaptic density proteins at glutamatergic synapses. *Mol. Cell. Neurosci.* 29, 436–452. doi: 10.1016/j.mcn.2005.03.013

Qualmann, B., Boeckers, T. M., Jeromin, M., Gundelfinger, E. D., and Kessels, M. M. (2004). Linkage of the actin cytoskeleton to the postsynaptic density via direct interactions of Abp1 with the ProSAP/Shank family. *J. Neurosci.* 24, 2481–2495. doi: 10.1523/JNEUROSCI.5479-03.2004

Racz, B., and Weinberg, R. J. (2004). The subcellular organization of cortactin in hippocampus. *J. Neurosci.* 24, 10310–10317. doi: 10.1523/JNEUROSCI.2080-04.2004

Rostaing, P., Real, E., Siksou, L., Lechaire, J. P., Boudier, T., Boeckers, T. M., et al. (2006). Analysis of synaptic ultrastructure without fixative using high-pressure freezing and tomography. *Eur. J. Neurosci.* 24, 3463–3474. doi: 10.1111/j.1460-9568.2006.05234.x

Rumbaugh, G., Adams, J. P., Kim, J. H., and Huganir, R. L. (2006). SynGAP regulates synaptic strength and mitogen-activated protein kinases in cultured neurons. *Proc. Natl. Acad. Sci. U S A* 103, 4344–4351. doi: 10.1073/pnas.0600084103

Sala, C., Piëch, V., Wilson, N. R., Passafaro, M., Liu, G., and Sheng, M. (2001). Regulation of dendritic spine morphology and synaptic function by Shank and Homer. *Neuron* 31, 115–130. doi: 10.1016/s0896-6273(01)00339-7

Sala, C., Vicidomini, C., Bigi, I., Mossa, A., and Verpelli, C. (2015). Shank synaptic scaffold proteins: keys to understanding the pathogenesis of autism and other synaptic disorders. *J. Neurochem.* 135, 849–858. doi: 10.1111/jnc.13232

Schnell, E., Sizemore, M., Karimzadegan, S., Chen, L., Bredt, D. S., and Nicoll, R. A. (2002). Direct interactions between PSD-95 and stargazin control synaptic AMPA receptor number. *Proc. Natl. Acad. Sci. U S A* 99, 13902–13907. doi: 10.1073/pnas.172511199

Scita, G., Confalonieri, S., Lappalainen, P., and Suetsugu, S. (2008). IRSp53: crossing the road of membrane and actin dynamics in the formation of membrane protrusions. *Trends Cell Biol.* 18, 52–60. doi: 10.1016/j.tcb.2007.12.002

Shonesy, B. C., Jalan-Sakrikar, N., Cavener, V. S., and Colbran, R. J. (2014). CaMKII: a molecular substrate for synaptic plasticity and memory. *Prog. Mol. Biol. Transl. Sci.* 122, 61–87. doi: 10.1016/B978-0-12-420170-5.00003-9

Sugiyama, Y., Kawabata, I., Sobue, K., and Okabe, S. (2005). Determination of absolute protein numbers in single synapses by a GFP-based calibration technique. *Nat. Methods* 2, 677–684. doi: 10.1038/nmeth783

Suzuki, T., Okumura-Noji, K., Tanaka, R., and Tada, T. (1994). Rapid translocation of cytosolic Ca^{2+}/calmodulin-dependent protein kinase II into postsynaptic density after decapitation. *J. Neurochem.* 63, 1529–1537. doi: 10.1046/j.1471-4159.1994.63041529.x

Tao-Cheng, J. H., Dosemeci, A., Gallant, P. E., Smith, C., and Reese, T. (2010). Activity induced changes in the distribution of Shanks at hippocampal synapses. *Neuroscience* 168, 11–17. doi: 10.1016/j.neuroscience.2010.03.041

Tao-Cheng, J. H., Thein, S., Yang, Y., Reese, T. S., and Gallant, P. E. (2014a). Homer is concentrated at the postsynaptic density and does not redistribute after acute synaptic stimulation. *Neuroscience* 266, 80–90. doi: 10.1016/j.neuroscience.2014.01.066

Tao-Cheng, J. H., Yang, Y., Bayer, K. U., Reese, T. S., and Dosemeci, A. (2014b). NMDA-induced accumulation of Shank at the postsynaptic density is mediated by CaMKII. *Biochem. Biophys. Res. Commun.* 450, 808–811. doi: 10.1016/j.bbrc.2014.06.049

Tao-Cheng, J. H., Yang, Y., Reese, T. S., and Dosemeci, A. (2015). Differential distribution of Shank and GKAP at the postsynaptic density. *PLoS One* 10:e0118750. doi: 10.1371/journal.pone.0118750

Thein, S., Tao-Cheng, J. H., Li, Y., Bayer, K. U., Reese, T. S., and Dosemeci, A. (2014). CaMKII mediates recruitment and activation of the deubiquitinase CYLD at the postsynaptic density. *PLoS One* 9:e91312. doi: 10.1371/journal.pone.0091312

Tu, J. C., Xiao, B., Naisbitt, S., Yuan, J. P., Petralia, R. S., Brakeman, P., et al. (1999). Coupling of mGluR/Homer and PSD-95 complexes by the Shank family of postsynaptic density proteins. *Neuron* 23, 583–592. doi: 10.1016/s0896-6273(00)80810-7

Valtschanoff, J. G., and Weinberg, R. J. (2001). Laminar organization of the NMDA receptor complex within the postsynaptic density. *J. Neurosci.* 21, 1211–1217.

Walikonis, R. S., Oguni, A., Khorosheva, E. M., Jeng, C. J., Asuncion, F. J., and Kennedy, M. B. (2001). Densin-180 forms a ternary complex with the α-subunit of Ca^{2+}/calmodulin-dependent protein kinase II and α-actinin. *J. Neurosci.* 21, 423–433.

Xiao, B., Tu, J. C., Petralia, R. S., Yuan, J. P., Doan, A., Breder, C. D., et al. (1998). Homer regulates the association of group 1 metabotropic glutamate receptors with multivalent complexes of homer-related, synaptic proteins. *Neuron* 21, 707–716. doi: 10.1016/s0896-6273(00)80588-7

Yang, Y., Tao-Cheng, J. H., Bayer, K. U., Reese, T. S., and Dosemeci, A. (2013). Camkii-mediated phosphorylation regulates distributions of Syngap-α1 and -α2 at the postsynaptic density. *PLoS One* 8:e71795. doi: 10.1371/journal.pone.0071795

Yang, Y., Tao-Cheng, J. H., Reese, T. S., and Dosemeci, A. (2011). SynGAP moves out of the core of the postsynaptic density upon depolarization. *Neuroscience* 192, 132–139. doi: 10.1016/j.neuroscience.2011.06.061

Zhao, H., Pykalainen, A., and Lappalainen, P. (2011). I-BAR domain proteins: linking actin and plasma membrane dynamics. *Curr. Opin. Cell Biol.* 23, 14–21. doi: 10.1016/j.ceb.2010.10.005

Conflict of Interest Statement: The authors declare that the research was conducted in the absence of any commercial or financial relationships that could be construed as a potential conflict of interest.

frontiers in Synaptic Neuroscience

REVIEW
published: 05 August 2016
doi: 10.3389/fnsyn.2016.00022

Optogenetic Monitoring of Synaptic Activity with Genetically Encoded Voltage Indicators

Ryuichi Nakajima[1†], *Arong Jung*[1,2†], *Bong-June Yoon*[2] *and Bradley J. Baker*[1,3*]

[1] Center for Functional Connectomics, Korea Institute of Science and Technology, Seongbuk-gu, Seoul, South Korea, [2] College of Life Sciences and Biotechnology, Korea University, Seongbuk-gu, Seoul, South Korea, [3] Department of Neuroscience, Korea University of Science and Technology, Daejeon, South Korea

The age of genetically encoded voltage indicators (GEVIs) has matured to the point that changes in membrane potential can now be observed optically *in vivo*. Improving the signal size and speed of these voltage sensors has been the primary driving forces during this maturation process. As a result, there is a wide range of probes using different voltage detecting mechanisms and fluorescent reporters. As the use of these probes transitions from optically reporting membrane potential in single, cultured cells to imaging populations of cells in slice and/or *in vivo*, a new challenge emerges—optically resolving the different types of neuronal activity. While improvements in speed and signal size are still needed, optimizing the voltage range and the subcellular expression (i.e., soma only) of the probe are becoming more important. In this review, we will examine the ability of recently developed probes to report synaptic activity in slice and *in vivo*. The voltage-sensing fluorescent protein (VSFP) family of voltage sensors, ArcLight, ASAP-1, and the rhodopsin family of probes are all good at reporting changes in membrane potential, but all have difficulty distinguishing subthreshold depolarizations from action potentials and detecting neuronal inhibition when imaging populations of cells. Finally, we will offer a few possible ways to improve the optical resolution of the various types of neuronal activities.

Keywords: genetically-encoded voltage indicators, synaptic activity, optogenetics, brain slices, *in vivo*

OPEN ACCESS

Edited by:
George Augustine, Nanyang Technological University, Singapore

Reviewed by:
Jason D. Shepherd, University of Utah, USA
Christian Wilms, Scientifica Ltd., UK

***Correspondence:**
Bradley J. Baker
bradley.baker19@gmail.com

†These authors have contributed equally to this work.

Received: *06 May 2016*
Accepted: *25 July 2016*
Published: *05 August 2016*

Citation:
Nakajima R, Jung A, Yoon B-J and Baker BJ (2016) Optogenetic Monitoring of Synaptic Activity with Genetically Encoded Voltage Indicators. Front. Synaptic Neurosci. 8:22. doi: 10.3389/fnsyn.2016.00022

INTRODUCTION

As developers of genetically-encoded voltage indicators (GEVIs) we are often asked for our best probe. Until recently, a good GEVI would have been any that gave a voltage-dependent, optical signal in mammalian cells (Dimitrov et al., 2007; Lundby et al., 2008, 2010; Perron et al., 2009a,b). Now the experimenter has several probes to choose from that differ in their voltage-dependencies, speed, signal size, and brightness (Akemann et al., 2012; Jin et al., 2012; Kralj et al., 2012; Han et al., 2013; St-Pierre et al., 2014; Zou et al., 2014; Gong et al., 2015; Piao et al., 2015; Abdelfattah et al., 2016). The combinations of these varying characteristics result in strengths and weaknesses of every GEVI available. There is no perfect probe that can optically resolve action potentials, synaptic activity, and neuronal inhibition *in vivo*. Some GEVIs will give large, voltage-dependent optical signals but are very dim limiting their usefulness *in vivo*. Others will give large optical signals but are very slow reducing their ability to resolve fast firing action potentials. So now, when asked which is the best probe, the answer is simply another question. What do you want to measure? To fit with the theme of this edition, we will assume that the answer to that question is synaptic activity.

Several reviews have been published comparing the signal size, speed, and brightness of the GEVIs currently available at the time of publication (Wachowiak and Knöpfel, 2009; Akemann et al., 2012, 2015; Knöpfel, 2012; Mutoh et al., 2012; Perron et al., 2012; Mutoh and Knöpfel, 2013; Emiliani et al., 2015; Knöpfel et al., 2015; St-Pierre et al., 2015; Storace et al., 2015b, 2016; Antic et al., 2016). In this review, we will shift the focus to one of the lesser considered characteristics of a GEVI, the voltage-sensitivity of the probe. Of course, the other characteristics, especially signal size and brightness, are still important, but the range and steepness of the voltage sensitivity of the optical response have extremely important consequences on which type of neuronal activity a GEVI reports well. For instance, a GEVI with a voltage range from −20 mV to +30 mV would be perfect for monitoring action potentials but not ideal for observing synaptic potentials. Even the shape of the slope of the optical response over the voltage range of the probe will affect its performance. The consequences of the slope and voltage range should also be considered when choosing probes for monitoring neuronal activity.

A BRIEF DESCRIPTION OF CURRENTLY AVAILABLE GEVIs

There now exist several GEVIs with multiple mechanisms of converting membrane potential changes into an optical signal. These GEVIs fall into two main classes. One class utilizes bacterial rhodopsin to detect alterations in voltage, while the other class relies on a voltage-sensing domain (VSD) from voltage-sensing proteins. Another viable alternative for optical, neuronal recordings is hybrid voltage sensor (hVOS) which consists of a genetically encoded component, a farnesylated fluorescent protein (FP), and a quenching compound, dipicrylamine (DPA; Chanda et al., 2005; Wang et al., 2010, 2012; Ghitani et al., 2015). The requirement for the treatment with an exogenous chemical limits hVOS use *in vivo* but still has value for imaging voltage in slice preparations.

The molecular schematics of representative probes from these classes and their corresponding voltage ranges are shown in **Figure 1**. The voltage range of a generic mammalian neuron is color coded to represent different neuronal activities. The inhibitory postsynaptic potential (IPSP) voltage range is shown in blue. The excitatory postsynaptic potential (EPSP) voltage range is shown in yellow. Voltages corresponding to action potentials are color coded red. As can be seen from **Figure 1**, the slopes of these optical voltage responses are significantly different. This is an important consideration when measuring synaptic potentials. For instance, Butterfly 1.2 has nearly reached its maximal fluorescent change at −40 mV which would imply that differentiating subthreshold potentials from action potentials will be very difficult.

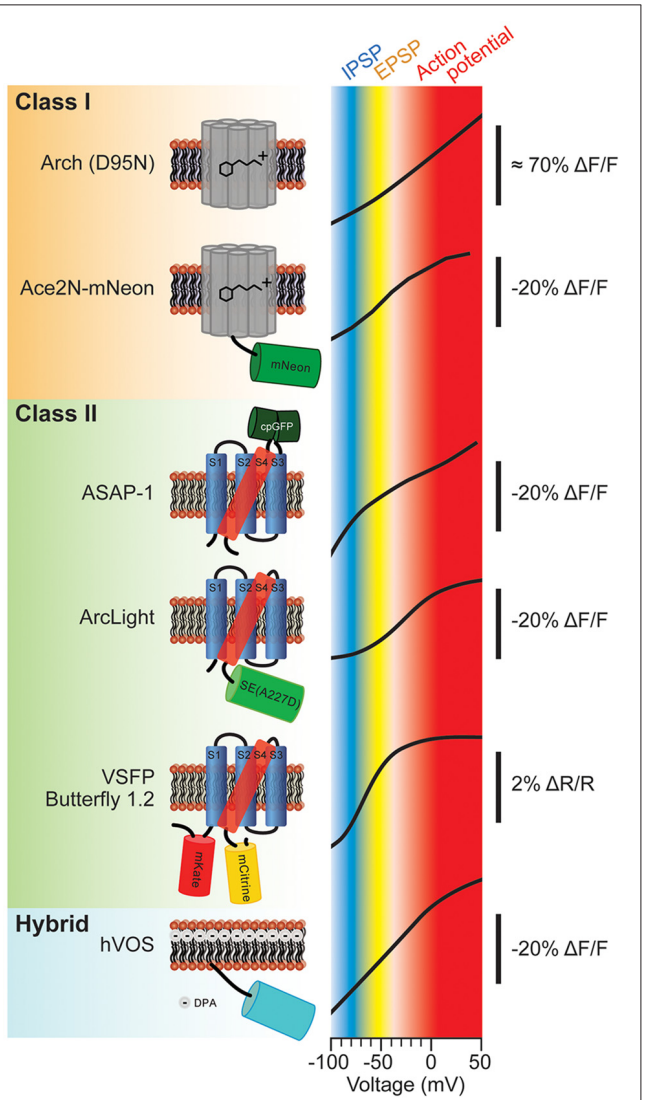

FIGURE 1 | Various types of genetically-encoded voltage indicators (GEVIs) and their voltage sensitivities. The voltage sensitivities of different GEVIs are compared. Typical voltage ranges of inhibitory postsynaptic potential (IPSP), excitatory postsynaptic potential (EPSP) and action potential are indicated as blue, yellow and red, respectively. The vertical scale bar with minus ΔF/F indicates that the fluorescence dims upon depolarization of the plasma membrane. The voltage-sensitivity curves were as reported in: Arch (D95N; modified with permision from Kralj et al., 2012, Figures 3B, 5); Ace2N-mNeon (modified with permission from Gong et al., 2015, Figure 1D); ASAP-1 (modified with permission from St-Pierre et al., 2014, Figure 1D); ArcLight (modified with permission from Jin et al., 2012, Figure 1C); Butterfly 1.2 (modified with permission from Akemann et al., 2012, Figure 2C); hybrid voltage sensor (hVOS; modified with permission from Chanda et al., 2005, Figure 1D).

Class I—The Rhodopsin-Based Probes

Channel rhodopsin has revolutionized neuroscience. The rhodopsin-based voltage sensors are promising to do the same thing for imaging membrane potential. First developed in Adam Cohen's lab, the intrinsic fluorescence of rhodopsin as a Schiff base being protonated or deprotonated in response to voltage was used to image changes in membrane potential (Maclaurin et al., 2013). This probe, Arch, was extremely fast having a tau under 1 ms. The fast optical response is due in part to the fact that the chromophore resides in the voltage field

enabling a nearly instantaneous response. The signal size was also large giving roughly a 70% ΔF/F optical signal per 100 mV membrane depolarization (Kralj et al., 2012; **Figure 1**, Arch (D95N)).

Arch excelled in speed and signal size but suffered from some serious weaknesses. The first weakness was that the original version had an associated, light-induced current. The D95N mutation drastically reduced this current but also resulted in a slower probe (Kralj et al., 2012). The second weakness was that it does not traffic well to the plasma membrane. Even with the addition of endoplasmic reticulum and Golgi network release motifs, every image of a rhodopsin probe in the literature exhibits high intracellular fluorescence (Kralj et al., 2012; Flytzanis et al., 2014; Gong et al., 2014, 2015; Hochbaum et al., 2014; Hou et al., 2014). The third and most devastating weakness was that Arch is very dim. The best versions of Arch and related probes are still at least 5× dimmer than the green fluorescent protein (GFP) requiring exceptionally strong illumination, at least 700× the light intensity required for ASAP-1 to visualize the probe activity (Flytzanis et al., 2014; St-Pierre et al., 2014).

The weak fluorescence of Arch limits its use to single cell in culture studies or to *C. elegans* (Kralj et al., 2012; Flytzanis et al., 2014) for two main reasons. The first is that the intrinsic fluorescence of higher order neuro-systems will mask the fluorescence of Arch-type probes. The second is that ΔF in addition to ΔF/F is an important characteristic of the GEVI when it comes to the signal to noise ratio. An example of this is shown in **Figure 2**. The HEK cell in **Figure 2** is expressing a GEVI from which the ΔF and the ΔF/F traces from three different light levels are shown (Lee et al., 2016). As can be seen from this comparison, a high ΔF/F value can be achieved by a large change in fluorescence or a small change in fluorescence when the probe is dim. Notice the increased noise in trace 3, a telltale sign of poor expression/dim fluorescence.

An ingenious solution to compensate for the poor fluorescence of the rhodopsin voltage probes was developed

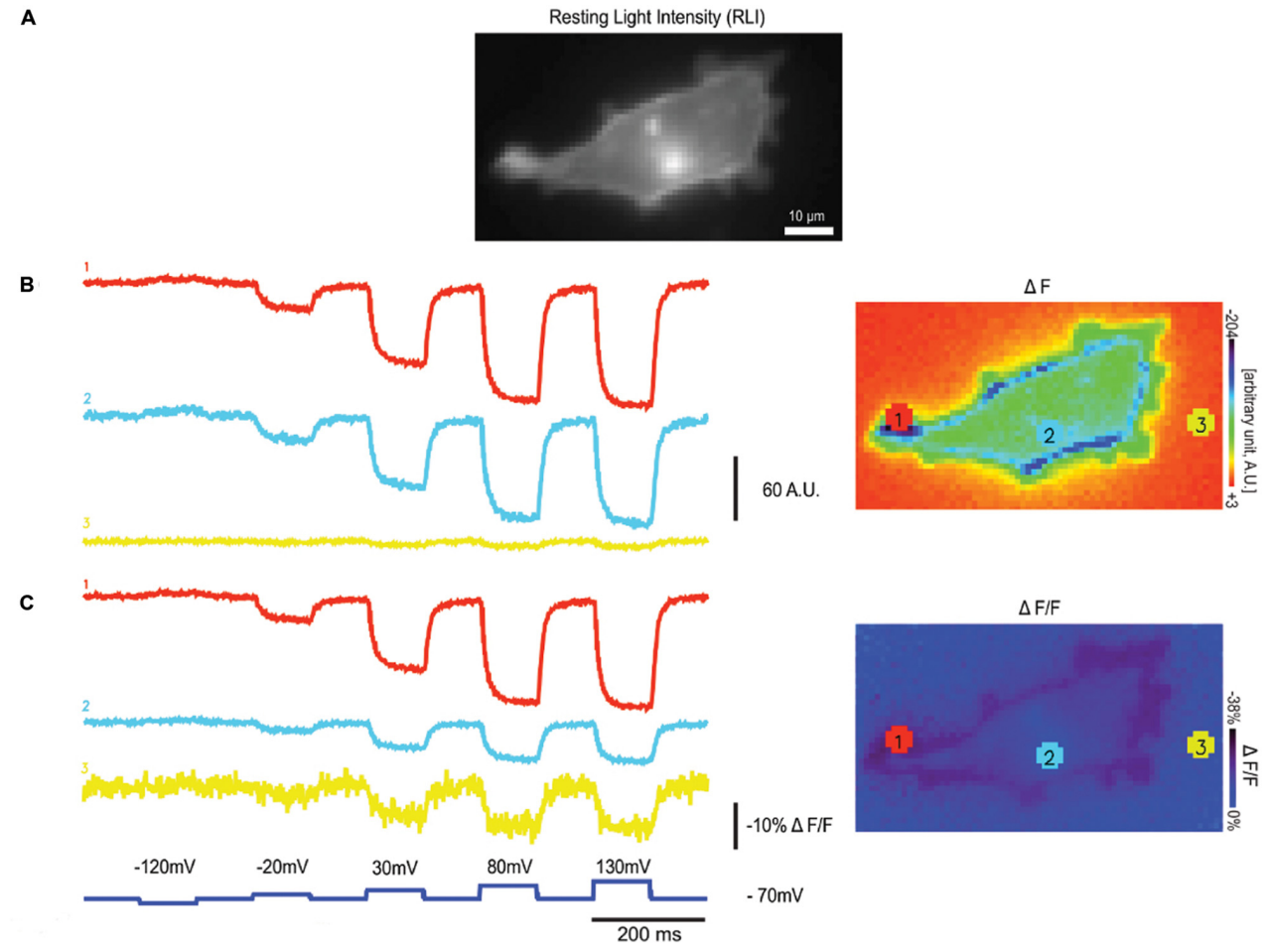

FIGURE 2 | Varying light levels affect ΔF and ΔF/F values. (A) An HEK 293 cell expressing a single fluorescent protein (FP) based GEVI, Bongwoori, is shown in resting light intensity (RLI), **(B)** the fluorescence traces of averaged ΔF (F_x-F_0) values from three different regions with varying intensity, **(C)** the fluorescence traces showing averaged ΔF/F values from the same regions in (**B**; modified with permission from Lee et al., 2016, Figure 6).

simultaneously by the Adam Cohen and Mark Schnitzer laboratories. By fusing an FP to the rhodopsin protein, förster resonance energy transfer (FRET) enabled the rhodopsin chromophore to affect the fluorescence of the fused FP. This design reduced the excitation light intensity needed to visualize the GEVI while maintaining the speed of the optical response since the voltage-sensing chromophore was still in the voltage field. These probes could also cover different wavelengths since many different FPs could be fused to rhodopsin and give a signal (Gong et al., 2014; Zou et al., 2014). While this made the rhodopsin probes better, the optical signal sometimes could only indirectly report neuronal activity by determining the frequency of the noise in the optical recording (See Supplementary Figure 5 in Gong et al., 2014). Now, an exciting new version using the FP, mNeonGreen, has recently been reported (Gong et al., 2015). mNeonGreen is a very bright FP (Shaner et al., 2013) enabling Ace2N-mNeon to resolve action potentials *in vivo* in both flies and mice.

Class II—VSD Containing GEVIs

The second class of GEVIs is also the oldest. The original GEVI, Flash (Siegel and Isacoff, 1997), was the result of inserting GFP downstream of the pore domain of the voltage-gated potassium channel, Shaker. Like the rhodopsin-based probes, the first generation of VSD-based probes had significant drawbacks making them useless in mammalian cells (Baker et al., 2007). The main problem was that the GEVIs did not traffic to the plasma membrane. In 2007, one of the biggest advancements in GEVI development was achieved by the Knöpfel laboratory when they fused FPs to the VSD of the voltage-sensing phosphatase gene from *Ciona intestinalis* (Murata et al., 2005). This probe, voltage-sensing fluorescent protein (VSFP) 2.1 trafficked well to the plasma membrane which resulted in the first voltage-dependent optical signals from cultured neurons (Dimitrov et al., 2007).

Another issue with VSD-based GEVIs is that the chromophore resides outside of the voltage field so the optical signal relies on the conformational change of the VSD. These probes are therefore generally slower than the rhodopsin-based probes, but a recently developed red-shifted GEVI is extremely fast having taus under 1 ms (Abdelfattah et al., 2016).

There are three different designs for GEVIs that utilize a VSD. The first design uses a FRET pair flanking the VSD. An example is Butterfly 1.2 (Akemann et al., 2012). This probe is somewhat slow and gives a very small optical signal, less than 3% $\Delta F/F$ per 100 mV depolarization. A butterfly style probe that gives a faster and larger optical signal was developed last year called Nabi (Sung et al., 2015). An advantage of FRET-based probes is that the ratiometric imaging can remove movement artifacts due to respiration and blood flow *in vivo*. Theoretically, a ratiometric measurement could also be used to determine the absolute value of the membrane potential since the ratio is concentration independent. In practice, however, the relative fluorescence of the two chromophores differ substantially resulting in a potential increase in the noise for the analysis of the optical signal. Often the experimenter should only analyze the brighter signal (Wilt et al., 2013). It is also difficult to only excite the donor chromophore and not the acceptor as well. These factors combined with the relatively low signal size of FRET-based probes prohibit any reliable absolute measurement of membrane potential.

The second design involves a circularly-permuted fluorescent protein (cpFP) attached to the VSD. Initial designs fused the cpFP downstream of the VSD so that the chromophore was in the cytoplasm (Gautam et al., 2009; Barnett et al., 2012). Electrik PK gave very small signals less than 1% $\Delta F/F$ per 100 mV depolarization but were very fast having a tau under 2 ms. A substantial increase in signal size was achieved when the cpFP was placed between the S3 transmembrane segment and the S4 transmembrane segment of the VSD putting the chromophore outside of the cell (St-Pierre et al., 2014). This probe, ASAP-1, is one of the better GEVIs giving a fast and robust optical signal (tau = 1–2 ms and about 20% $\Delta F/F$ per 100 mV depolarization in HEK cells). ASAP-1 has a very broad voltage range which is virtually linear over much of the physiologically relevant potentials of neurons.

The third design of GEVIs that utilize a VSD simply fuses the FP at the carboxy-terminus which puts the chromophore in the cytoplasm. During a systematic test of different FPs fused at different linker lengths from the VSD done in collaboration by Vincent Pieribone's lab and Larry Cohen's lab, a point mutation on the outside of the FP, Super Ecliptic pHlorin (Miesenbock et al., 1998; Ng et al., 2002) converted an alanine to an aspartic acid improving the optical signal 15 fold from 1% $\Delta F/F$ to 15% per 100 mV depolarization of the plasma membrane (Jin et al., 2012). This negative charge on the outside of the β-can seems to affect the fluorescence of a neighboring chromophore when S4 moves since mutations that favor the monomeric form of the FP reduce the voltage-dependent optical signal substantially (Kang and Baker, 2016). Further development of ArcLight has gotten signals as high as 40% $\Delta F/F$ per 100 mV depolarization step (Han et al., 2013). While ArcLight has the drawback of being slow, its brightness and signal size make it one of the better probes for imaging *in vivo* and in slice. In 2015, two publications improving the speed of this sensor were published. One dramatically improved the off rate called Arclightening but reduced the signal size to under 10% $\Delta F/F$ per 100 mV depolarization (Treger et al., 2015). The other, Bongwoori, improved the speed of the sensor and shifted the voltage response to more positive potentials which improved the resolution of action potentials but decreased the signal size for synaptic potentials (Piao et al., 2015). The reduced optical signal response for sub-threshold potentials gives Bongwoori a better "contrast" for optically resolving action potentials.

A final design for researchers to consider when choosing a GEVI is the genetically encoded, hVOS (Chanda et al., 2005; Wang et al., 2010, 2012; Ghitani et al., 2015). First developed in the Bezanilla lab, hVOS consists of an FP anchored to the plasma membrane with the addition of a small charged molecule, DPA, that binds to the plasma membrane effectively acting as a fluorescent quencher. Since DPA is a lipophilic anion, the quenching agent will move from the outer surface of the plasma membrane to the inner surface upon membrane depolarizations

generating a voltage-responsive fluorescent signal. Like the other sensors, hVOS also has drawbacks which are primarily due to the fact that an exogenous chemical must be administered to the sample to be imaged. This is not a trivial process since too much DPA will significantly increase the capacitance of the plasma membrane and alter the neuronal activity of the cell. However, once the appropriate conditions are determined, hVOS gives optical signals for subthreshold potentials as well as action potentials in slice from populations of cells (Wang et al., 2012) or individual cells when expression of the FP is sparser (Ghitani et al., 2015).

SYNAPTIC ACTIVITY MONITORING IN SLICES WITH GEVIs

Brain slices are invaluable for studying in detail the cellular, molecular, and circuitry activity of neuronal functions (Ting et al., 2014). GEVIs can expand this information since every pixel potentially becomes an electrode. There are not many examples of synaptic potential recordings from GEVIs in slice. Most examples are proof-of-principle type of recordings in the original publication of a new sensor to demonstrate its potential. The VSFP family of GEVIs are the most published recordings in brain slice (Akemann et al., 2013; Scott et al., 2014; Carandini et al., 2015; Empson et al., 2015; Mutoh et al., 2015). Here, we compare optical synaptic recordings in brain slices from VSFP Butterfly 1.2 and hVOS.

FRET Signals of Butterfly in Cortical Brain Slices

Figure 3A shows the population imaging in coronal cortical slices prepared from a mouse brain electroporated *in utero* with VSFP-Butterfly 1.2 (Akemann et al., 2012). To explore voltage imaging from populations of cells, cortical slices were imaged at low magnification while delivering a single electrical stimulus (**Figure 3A**, left panel). The amplitude of the evoked optical signal ranged from 1 to 1.5% $\Delta R/R_0$ (**Figure 3A**). Disinhibition with 25 mM gabazine increased the signal to 11% $\Delta R/R_0$ (Akemann et al., 2012). Since VSFP-Butterfly 1.2 is a FRET probe, the ratio of the fluorescent change can be reported, but in slice the advantage of a ratiometric recording is of lesser value since movement artifacts due to respiration and blood flow do not exist. Despite this advantage, the voltage-dependent change in fluorescence is quite small, less than 0.5% $\Delta F/F$ which requires multiple trials to improve the signal to noise ratio.

hVOS Signal in the Hippocampal Slice

Figure 3B shows the hVOS signal in a hippocampal slice. The electrical stimulation evoked clear fluorescence changes only when 4 μM DPA was present. This concentration of DPA provided excellent signal up to 2 h with minimum pharmacological action (Wang et al., 2010). The hVOS probe fluorescence decreases with membrane depolarization because DPA moves to the inner surface of the cell membrane where hVOS probes are anchored; the arrival of DPA quenches the probe fluorescence. Responses of approximately 1–3% could be seen throughout the field of view (Wang et al., 2012).

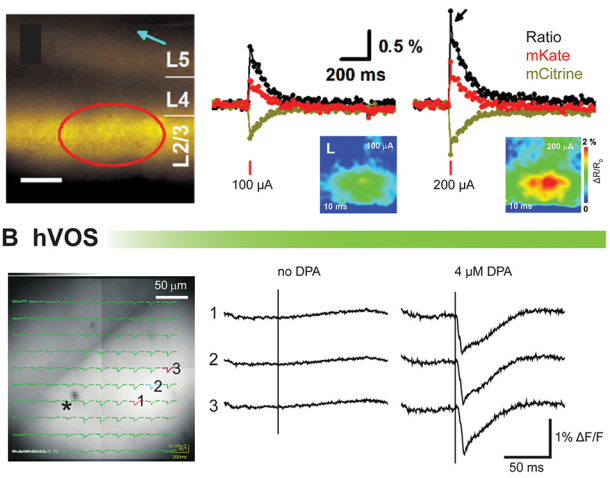

FIGURE 3 | Comparison of voltage indicators for synaptic imaging in brain slices. (A) Fluorescence and ratiometric signals of voltage-sensing fluorescent protein (VSFP) Butterfly 1.2 in cortical brain slices (modified with persmission from Akemann et al., 2012, Figures 3I,J). Left: wide-field fluorescence image with indicated position of the stimulation electrode (blue arrow). Scale bar, 150 μm. Middle and right: a single-pulse synaptic stimulus (middle: 100 μA; right: 200 μA) induced a depolarizing response as indicated by a transient decrease in mCitrine (yellow) and increase in mKate2 (red) emission from the pixels indicated by a red circle. The ratio of the two emission spectra is in black. **(B)** Stimulus-evoked fluorescence changes ($\Delta F/F$) and their dipicrylamine (DPA) dependence (modified with permission from Wang et al., 2012, Figure 3). A slice expressing hVOS 1.5 from mouse hippocampus. All recordings were from the striatum-radiatum (sr) of the CA1 region. Left: a slice from hVOS 1.5 line 602 with images and fluorescence traces superimposed. Traces are from the three numbered locations before and after addition of DPA. The stimulation site is indicated by the asterisk. All traces of hVOS signals are averages of 10 trials.

VSFP-Butterfly 1.2, and hVOS can all generate an optical signal corresponding to synaptic responses in acute brain slices. hVOS has the larger $\Delta F/F$. VSFP-Butterfly 1.2 does not require additional drug application to detect voltage changes in the neuron. Other sensors can also give optical signals in slice but those recordings have focused on action potentials in individual cells and are not shown here. The brightness, signal size, and voltage range of ASAP-1 make it a potentially useful sensor for imaging synaptic potentials in slice. While there are no reports in the literature of ArcLight being used to analyze neuronal activity in brain slices, the brightness, signal size and voltage-sensitivity are also ideal for optically recording synaptic potentials.

SYNAPTIC ACTIVITY MONITORING *IN VIVO* WITH GEVIs

While slice recordings are extremely valuable for deciphering neuronal circuitry, the ultimate goal of voltage imaging is to detect neuronal activity in a behaving animal. This is an ambitious endeavor with very few examples, but some GEVIs

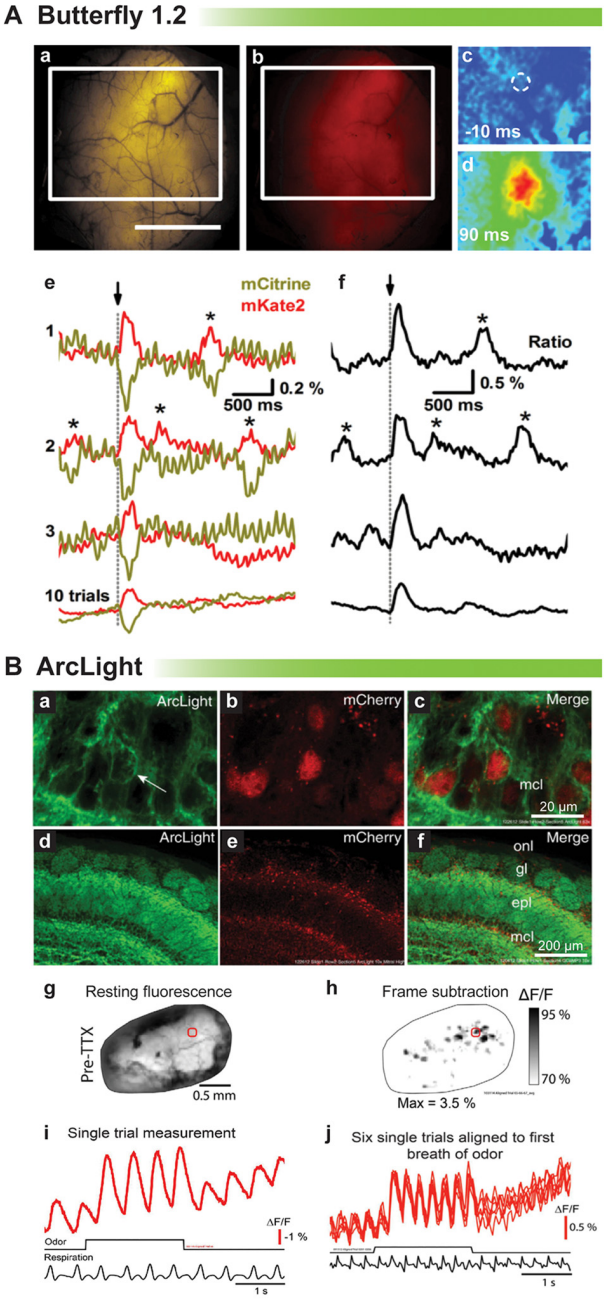

FIGURE 4 | Comparison of voltage indicators for synaptic imaging *in vivo*. **(A)** Butterfly 1.2 signal in the somatosensory cortex during whisker stimulation (modified with permission from Akemann et al., 2012, Figures 6B,D,E). **(a,b)** Fluorescence image of mCitrine **(a)** and mKate2 **(b)** from a mouse expressing VSFP-Butterfly 1.2. White rectangle indicates area imaged in **(c)**. Scale bar, 2 mm. **(c,d)** Ratio images obtained at times before and after brief deflection of the D1 whisker performed at time 0. **(c)** 10 ms before **(d)** 90 ms after the deflection. **(e)** Single-sweep (1, 2, and 3) mCitrine (yellow) and mKate2 (red) optical signals sampled from the region of interest indicated by white circle in **(c)**, together with the 10-trial average (bottom). Asterisks mark signals corresponding to potential spontaneously occurring voltage transients. **(f)** Ratio ($\Delta R/R_0$) signals corresponding to the traces in **(e)**. **(B)** Odor-evoked signals of ArcLight in olfactory bulb (modified with permission from Storace et al., 2015a, Figures 1, 2). **(a–c)** High magnification confocal

(*Continued*)

FIGURE 4 | Continued
images of ArcLight demonstrate membrane localization (arrow). The FP, mCherry, is localized to the nucleus to facilitate identification of transduced neurons. **(d–f)** Low magnification of the olfactory bulb—onl, olfactory nerve layer; gl, glomerular layer; epl, external plexiform layer; mcl, mitral cell layer. **(g)** Wide-field resting fluorescence intensity. **(h)** Glomerular patterns of activation after odor stimulation. **(i)** Odor-evoked optical signals from the region of interest marked with a red circle in **(g,h)**. **(j)** Six unfiltered single trials aligned to the first sniff of odorant.

are now capable of giving a robust signal that allows *in vivo* imaging.

Proof of principle for *in vivo* voltage imaging was established by the Knöpfel lab using the VSFP family of probes (Akemann et al., 2012, 2013). **Figure 4A** shows single trial responses in the barrel cortex during whisker stimulation. Clearly, a stimulus evoked voltage signal could be detected in single trials even though the signal size is very small. Asterisks denote potential spontaneous voltage transients. However, unlike the stimulus evoked optical response, these potential transients exhibit different start times and kinetics. Having a low signal to noise ratio undermines the confidence in reliably detecting neuronal activity trial to trial (Carandini et al., 2015). Another drawback with VSFP Butterfly 1.2 is that the $V_{1/2}$ is roughly −70 mV with maximal fluorescent change occurring at −40 mV (**Figure 1**) making it virtually impossible to distinguish synaptic activity from action potentials based solely on signal size.

ArcLight has also been tested *in vivo* in mice and flies (Cao et al., 2013; Storace et al., 2015a). The $V_{1/2}$ for ArcLight is around −30 mV making it ideal to detect neuronal activity in flies whose action potentials range from a resting potential of −40 mV to a final excitation of −10 mV. As a side note this is why our probe, Bongwoori, should not be used for imaging neuronal activity in flies since the $V_{1/2}$ has been shifted to around 0 mV (Piao et al., 2015). **Figure 4B** shows a recording from a mouse expressing ArcLight in the olfactory bulb. As can be seen, respiration causes an optical artifact, but since ArcLight gives a large signal, identifying regions of the olfactory bulb responding to an odor is still possible. Again, though, it is not possible to resolve synaptic activity from action potentials.

The rhodopsin-based GEVIs have also been shown to elicit an optical signal *in vivo*. An example is shown in **Figure 5A** from the Gradinaru lab (Flytzanis et al., 2014). With the dim fluorescence of the GEVI, Archer, *C. elegans* is one of the few multicellular organisms one would be able to record from. After odorant stimulation, there is a slight variation in the ΔF compared to control. While there appears to be a slight signal, the low signal to noise ratio again undermines one's confidence in being able to reliably detect neuronal activity from trial to trial.

The last example of *in vivo* recordings is the best example of resolving action potentials. Ace2N-4AA-mNeon has been imaged in flies and mice (Gong et al., 2015). This probe is extremely fast showing the best fit of optical data to voltage yet (**Figure 5B**). The red arrow shows an optical response to a 5 mV

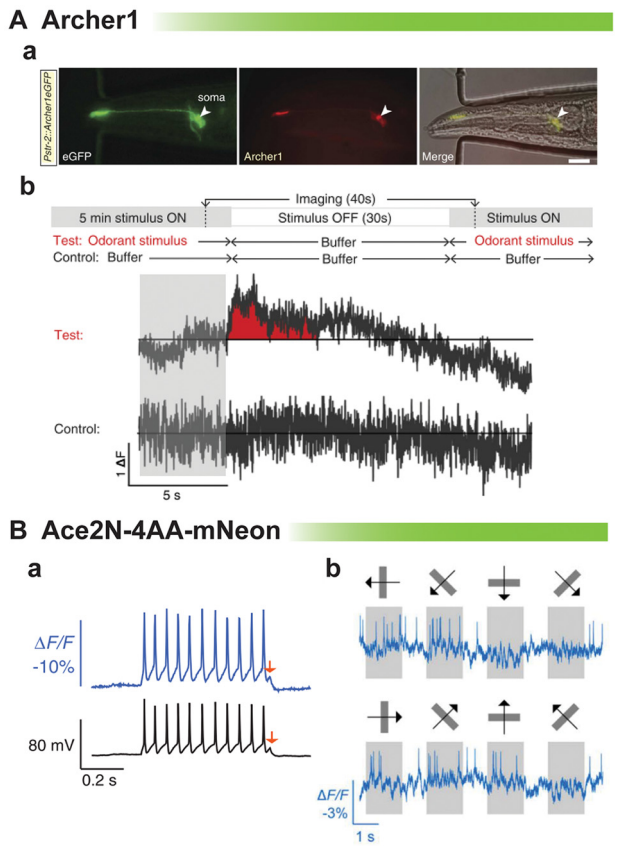

FIGURE 5 | Comparison of rhodopsin-based voltage indicators for synaptic imaging *in vivo*. **(A)** Archer1 expressed in worms. **(a)** *C. elegans* expressing Archer1 shows fluorescence (λ = 655 nm; I = 880 mWmm^{-2}, 100 ms exposure). Scale bar, 20 mm. **(b)** Top: experimental conditions: worms are stimulated with odorant (Isoamyl alcohol, IAA) for 5 min, flow is switched to buffer (S Basal) for 30 s, and then odorant flow is restored. The control conditions are performed on the same worm. Bottom traces: imaging of Archer1 fluorescence (250 Hz) (modified with permission from Flytzanis et al., 2014, Figures 5B,C). **(B)** Imaging single action potentials and subthreshold membrane voltage by Ace2N-4AA-mNeon (modified with permission from Gong et al., 2015, Figures 2A, 3D). **(a)** Optical resolution of action potentials of cultured hippocampal neurons under current clamp exhibiting best fit of optical data to electrical recording to date. Arrow denotes 5 mV depolarization. **(b)** Optical traces from a cortical V1→LM neuron in an awake mouse, showing visually evoked responses to drifting gratings.

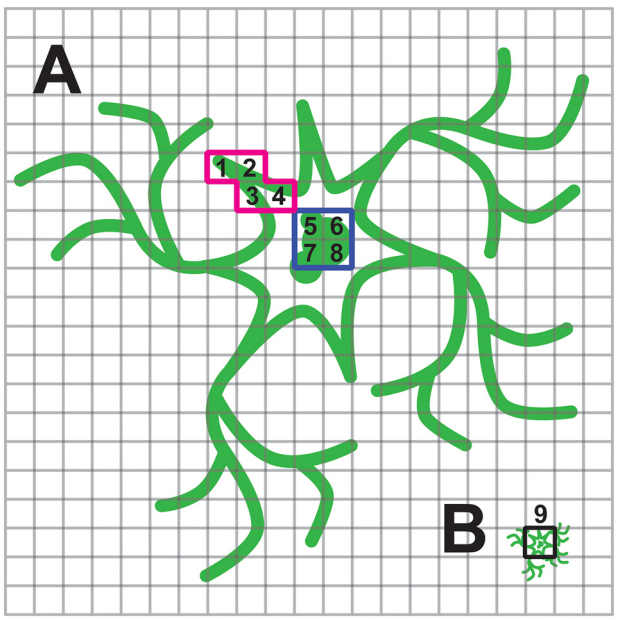

FIGURE 6 | Consequence of internal fluorescence when imaging population of cells. **(A)** Schematic of a neuron under high magnification with plasma membrane and internal fluorescence in green. The cell is projected onto multiple pixels enabling the experimenter to choose pixels with optical activity. In this example the red, highlighted pixels labeled 1–4 have a large ΔF/F while pixels highlighted in blue, labeled 5–8, exhibit low or no change in fluorescence upon depolarization of the plasma membrane. **(B)** Same cell under low magnification now only projects onto a few pixels. The pixel highlighted in black, labeled 9, is a summation of pixels 1–8 in **(A)**. The experimenter is no longer able to avoid the non-responsive, internal fluorescence.

depolarization. However, comparing the optical signal at the spike to the subthreshold potential, one can see that the optical response is skewed towards action potential activity. This gives a fantastic response when imaging the visual cortex in response to visual stimuli. Action potentials are easily discernible. The ability to optically report synaptic activity is less clear but still promising.

CONCLUSION

GEVIs come in many flavors. As demonstrated, the signal size, speed, and voltage sensitivity affect the neuronal activity a GEVI can resolve. Many probes will give an optical signal in slice and *in vivo* but some signals will be more informative. If the experimenter wants to image any neuronal activity from a population of cells in brain slice, the recommendations would be hVOS, ArcLight, and ASAP-1. All have a broad voltage range, traffic to the membrane well and give relatively large signals. ArcLight and ASAP-1 will have some difficulty in separating synaptic activity from action potentials due to their voltage sensitivities, but this could theoretically be overcome by co-expression of a red calcium sensor to verify action potential activity if the neuron tested has an action potential-induced calcium transient. If one wants to measure neuronal activity of individual cells in slice, then one should also consider Ace2N-4AA-mNeon.

Imaging single cells vs. a population of cells will also affect the choice of GEVI to be used. When imaging single cells, probes with broad voltage ranges will enable the optical detection of inhibition, synaptic potentials, and action potentials. However, these same probes when imaging large populations of cells are potentially less informative since the depolarization of a subgroup of neurons could swamp the small, hyperpolarizing signals from inhibited neurons.

Inefficient trafficking or high intracellular expression will affect the voltage imaging of a population of cells more so than when imaging individual cells. The reason for this is that the spatial representation of the cell under high magnification onto

the pixels of the camera has changed. Under high magnification, a researcher can choose only pixels that correspond to regions of the cell that exhibited a fluorescent response. When imaging a population of cells, a pixel will be less likely to capture only the responsive fluorescence. This situation is depicted in **Figure 6**. When imaging a single cell, it is much easier to avoid the internal, non-responsive fluorescence and maximize the signal to noise ratio.

While the GEVIs currently available have shown significant improvement in their ability to optically detect neuronal activity, there is still much room for improvement. Refining the voltage-sensitivity will enable maximizing the optical signal. For instance, a probe that only responded to hyperpolarization of the plasma membrane would make identifying the inhibited parts of a neuronal circuit much easier. Improving the membrane expression of the GEVI will decrease the nonresponsive fluorescence in a population of cells, thereby improving the signal to noise ratio. Most efforts to improve trafficking involve the addition of endoplasmic reticulum and Golgi release motifs. Codon optimization is another approach which for membrane proteins may be a misnomer. The idea of codon optimization is to use only the most abundant codons for rapid translation of the protein. This has been shown to be effective for cytoplasmic proteins. However, for membrane proteins slowing the translation to allow proper folding and insertion into the translocon may also be important (Norholm et al., 2012; Yu et al., 2015). Finally, limiting the expression of the GEVI to subcellular components (i.e., the soma, dendrites, etc.) could also focus the optical signal to the desired region of the neuron again improving the signal to noise ratio.

AUTHOR CONTRIBUTIONS

RN and AJ wrote the manuscript and contributed figures. B-JY and BJB helped to write the manuscript.

ACKNOWLEDGMENTS

This work was funded by the Korea Institute of Science and Technology (KIST) Institutional Program Multiscale Functional Connectomics, 2E26190 and KIST Institutional Program 2E26170.

REFERENCES

Abdelfattah, A. S., Farhi, S. L., Zhao, Y., Brinks, D., Zou, P., Ruangkittisakul, A., et al. (2016). A bright and fast red fluorescent protein voltage indicator that reports neuronal activity in organotypic brain slices. *J. Neurosci.* 36, 2458–2472. doi: 10.1523/jneurosci.3484-15.2016

Akemann, W., Mutoh, H., Perron, A., Park, Y. K., Iwamoto, Y., and Knöpfel, T. (2012). Imaging neural circuit dynamics with a voltage-sensitive fluorescent protein. *J. Neurophysiol.* 108, 2323–2337. doi: 10.1152/jn.00452.2012

Akemann, W., Sasaki, M., Mutoh, H., Imamura, T., Honkura, N., and Knöpfel, T. (2013). Two-photon voltage imaging using a genetically encoded voltage indicator. *Sci. Rep.* 3:2231. doi: 10.1038/srep02231

Akemann, W., Song, C., Mutoh, H., and Knöpfel, T. (2015). Route to genetically targeted optical electrophysiology: development and applications of voltage-sensitive fluorescent proteins. *Neurophotonics* 2:021008. doi: 10.1117/1.nph.2.2.021008

Antic, S. D., Empson, R. M., and Knöpfel, T. (2016). Voltage imaging to understand connections and functions of neuronal circuits. *J. Neurophysiol.* 116, 135–152. doi: 10.1152/jn.00226.2016

Baker, B. J., Lee, H., Pieribone, V. A., Cohen, L. B., Isacoff, E. Y., Knöpfel, T., et al. (2007). Three fluorescent protein voltage sensors exhibit low plasma membrane expression in mammalian cells. *J. Neurosci. Methods* 161, 32–38. doi: 10.1016/j.jneumeth.2006.10.005

Barnett, L., Platisa, J., Popovic, M., Pieribone, V. A., and Hughes, T. (2012). A fluorescent, genetically-encoded voltage probe capable of resolving action potentials. *PLoS One* 7:e43454. doi: 10.1371/journal.pone.0043454

Cao, G., Platisa, J., Pieribone, V. A., Raccuglia, D., Kunst, M., and Nitabach, M. N. (2013). Genetically targeted optical electrophysiology in intact neural circuits. *Cell* 154, 904–913. doi: 10.1016/j.cell.2013.07.027

Carandini, M., Shimaoka, D., Rossi, L. F., Sato, T. K., Benucci, A., and Knöpfel, T. (2015). Imaging the awake visual cortex with a genetically encoded voltage indicator. *J. Neurosci.* 35, 53–63. doi: 10.1523/jneurosci.0594-14.2015

Chanda, B., Blunck, R., Faria, L. C., Schweizer, F. E., Mody, I., and Bezanilla, F. (2005). A hybrid approach to measuring electrical activity in genetically specified neurons. *Nat. Neurosci.* 8, 1619–1626. doi: 10.1038/nn1558

Dimitrov, D., He, Y., Mutoh, H., Baker, B. J., Cohen, L., Akemann, W., et al. (2007). Engineering and characterization of an enhanced fluorescent protein voltage sensor. *PLoS One* 2:e440. doi: 10.1371/journal.pone.0000440

Emiliani, V., Cohen, A. E., Deisseroth, K., and Hausser, M. (2015). All-optical interrogation of neural circuits. *J. Neurosci.* 35, 13917–13926. doi: 10.1523/jneurosci.2916-15.2015

Empson, R. M., Goulton, C., Scholtz, D., Gallero-Salas, Y., Zeng, H., and Knöpfel, T. (2015). Validation of optical voltage reporting by the genetically encoded voltage indicator VSFP-Butterfly from cortical layer 2/3 pyramidal neurons in mouse brain slices. *Physiol. Rep.* 3:e12468. doi: 10.14814/phy2.12468

Flytzanis, N. C., Bedbrook, C. N., Chiu, H., Engqvist, M. K., Xiao, C., Chan, K. Y., et al. (2014). Archaerhodopsin variants with enhanced voltage-sensitive fluorescence in mammalian and *Caenorhabditis elegans* neurons. *Nat. Commun.* 5:4894. doi: 10.1038/ncomms5894

Gautam, S. G., Perron, A., Mutoh, H., and Knöpfel, T. (2009). Exploration of fluorescent protein voltage probes based on circularly permuted fluorescent proteins. *Front. Neuroeng.* 2:14. doi: 10.3389/neuro.16.014.2009

Ghitani, N., Bayguinov, P. O., Ma, Y., and Jackson, M. B. (2015). Single-trial imaging of spikes and synaptic potentials in single neurons in brain slices with genetically encoded hybrid voltage sensor. *J. Neurophysiol.* 113, 1249–1259. doi: 10.1152/jn.00691.2014

Gong, Y., Huang, C., Li, J. Z., Grewe, B. F., Zhang, Y., Eismann, S., et al. (2015). High-speed recording of neural spikes in awake mice and flies with a fluorescent voltage sensor. *Science* 350, 1361–1366. doi: 10.1126/science.aab0810

Gong, Y., Wagner, M. J., Zhong Li, J., and Schnitzer, M. J. (2014). Imaging neural spiking in brain tissue using FRET-opsin protein voltage sensors. *Nat. Commun.* 5:3674. doi: 10.1038/ncomms4674

Han, Z., Jin, L., Platisa, J., Cohen, L. B., Baker, B. J., and Pieribone, V. A. (2013). Fluorescent protein voltage probes derived from ArcLight that respond to membrane voltage changes with fast kinetics. *PLoS One* 8:e81295. doi: 10.1371/journal.pone.0081295

Hochbaum, D. R., Zhao, Y., Farhi, S. L., Klapoetke, N., Werley, C. A., Kapoor, V., et al. (2014). All-optical electrophysiology in mammalian neurons using engineered microbial rhodopsins. *Nat. Methods* 11, 825–833. doi: 10.1038/nmeth.3000

Hou, J. H., Venkatachalam, V., and Cohen, A. E. (2014). Temporal dynamics of microbial rhodopsin fluorescence reports absolute membrane voltage. *Biophys. J.* 106, 639–648. doi: 10.1016/j.bpj.2013.11.4493

Jin, L., Han, Z., Platisa, J., Wooltorton, J. R., Cohen, L. B., and Pieribone, V. A. (2012). Single action potentials and subthreshold electrical events imaged in

neurons with a fluorescent protein voltage probe. *Neuron* 75, 779–785. doi: 10.1016/j.neuron.2012.06.040

Kang, B. E., and Baker, B. J. (2016). Pado, a fluorescent protein with proton channel activity can optically monitor membrane potential, intracellular pH and map gap junctions. *Sci. Rep.* 6:23865. doi: 10.1038/srep23865

Knöpfel, T. (2012). Genetically encoded optical indicators for the analysis of neuronal circuits. *Nat. Rev. Neurosci.* 13, 687–700. doi: 10.1038/nrn3293

Knöpfel, T., Gallero-Salas, Y., and Song, C. (2015). Genetically encoded voltage indicators for large scale cortical imaging come of age. *Curr. Opin. Chem. Biol.* 27, 75–83. doi: 10.1016/j.cbpa.2015.06.006

Kralj, J. M., Douglass, A. D., Hochbaum, D. R., Maclaurin, D., and Cohen, A. E. (2012). Optical recording of action potentials in mammalian neurons using a microbial rhodopsin. *Nat. Methods* 9, 90–95. doi: 10.1038/nmeth.1782

Lee, S., Piao, H. H., Sepheri-Rad, M., Jung, A., Sung, U., Song, Y. K., et al. (2016). Imaging membrane potential with two types of genetically encoded fluorescent voltage sensors. *J. Vis. Exp.* 4:e53566. doi: 10.3791/53566

Lundby, A., Akemann, W., and Knöpfel, T. (2010). Biophysical characterization of the fluorescent protein voltage probe VSFP2.3 based on the voltage-sensing domain of Ci-VSP. *Eur. Biophys. J.* 39, 1625–1635. doi: 10.1007/s00249-010-0620-0

Lundby, A., Mutoh, H., Dimitrov, D., Akemann, W., and Knöpfel, T. (2008). Engineering of a genetically encodable fluorescent voltage sensor exploiting fast Ci-VSP voltage-sensing movements. *PLoS One* 3:e2514. doi: 10.1371/journal.pone.0002514

Maclaurin, D., Venkatachalam, V., Lee, H., and Cohen, A. E. (2013). Mechanism of voltage-sensitive fluorescence in a microbial rhodopsin. *Proc. Natl. Acad. Sci. U S A.* 110, 5939–5944. doi: 10.1073/pnas.1215595110

Miesenbock, G., De Angelis, D. A., and Rothman, J. E. (1998). Visualizing secretion and synaptic transmission with pH-sensitive green fluorescent proteins. *Nature* 394, 192–195. doi: 10.1038/28190

Murata, Y., Iwasaki, H., Sasaki, M., Inaba, K., and Okamura, Y. (2005). Phosphoinositide phosphatase activity coupled to an intrinsic voltage sensor. *Nature* 435, 1239–1243. doi: 10.1038/nature03650

Mutoh, H., Akemann, W., and Knöpfel, T. (2012). Genetically engineered fluorescent voltage reporters. *ACS. Chem. Neurosci.* 3, 585–592. doi: 10.1021/cn300041b

Mutoh, H., and Knöpfel, T. (2013). Probing neuronal activities with genetically encoded optical indicators: from a historical to a forward-looking perspective. *Pflugers. Arch.* 465, 361–371. doi: 10.1007/s00424-012-1202-z

Mutoh, H., Mishina, Y., Gallero-Salas, Y., and Knöpfel, T. (2015). Comparative performance of a genetically-encoded voltage indicator and a blue voltage sensitive dye for large scale cortical voltage imaging. *Front. Cell. Neurosci.* 9:147. doi: 10.3389/fncel.2015.00147

Ng, M., Roorda, R. D., Lima, S. Q., Zemelman, B. V., Morcillo, P., and Miesenbock, G. (2002). Transmission of olfactory information between three populations of neurons in the antennal lobe of the fly. *Neuron* 36, 463–474. doi: 10.1016/s0896-6273(02)00975-3

Norholm, M. H., Light, S., Virkki, M. T., Elofsson, A., Von Heijne, G., and Daley, D. O. (2012). Manipulating the genetic code for membrane protein production: what have we learnt so far? *Biochim. Biophys. Acta.* 1818, 1091–1096. doi: 10.1016/j.bbamem.2011.08.018

Perron, A., Akemann, W., Mutoh, H., and Knöpfel, T. (2012). Genetically encoded probes for optical imaging of brain electrical activity. *Prog. Brain Res.* 196, 63–77. doi: 10.1016/b978-0-444-59426-6.00004-5

Perron, A., Mutoh, H., Akemann, W., Gautam, S. G., Dimitrov, D., Iwamoto, Y., et al. (2009a). Second and third generation voltage-sensitive fluorescent proteins for monitoring membrane potential. *Front. Mol. Neurosci.* 2:5. doi: 10.3389/neuro.02.005.2009

Perron, A., Mutoh, H., Launey, T., and Knöpfel, T. (2009b). Red-shifted voltage-sensitive fluorescent proteins. *Chem. Biol.* 16, 1268–1277. doi: 10.1016/j.chembiol.2009.11.014

Piao, H. H., Rajakumar, D., Kang, B. E., Kim, E. H., and Baker, B. J. (2015). Combinatorial mutagenesis of the voltage-sensing domain enables the optical resolution of action potentials firing at 60 Hz by a genetically encoded fluorescent sensor of membrane potential. *J. Neurosci.* 35, 372–385. doi: 10.1523/jneurosci.3008-14.2015

Scott, G., Fagerholm, E. D., Mutoh, H., Leech, R., Sharp, D. J., Shew, W. L., et al. (2014). Voltage imaging of waking mouse cortex reveals emergence of critical neuronal dynamics. *J. Neurosci.* 34, 16611–16620. doi: 10.1523/jneurosci.3474-14.2014

Shaner, N. C., Lambert, G. G., Chammas, A., Ni, Y., Cranfill, P. J., Baird, M. A., et al. (2013). A bright monomeric green fluorescent protein derived from Branchiostoma lanceolatum. *Nat. Methods* 10, 407–409. doi: 10.1038/nmeth.2413

Siegel, M. S., and Isacoff, E. Y. (1997). A genetically encoded optical probe of membrane voltage. *Neuron* 19, 735–741. doi: 10.1016/s0896-6273(00)80955-1

Storace, D. A., Braubach, O. R., Jin, L., Cohen, L. B., and Sung, U. (2015a). Monitoring brain activity with protein voltage and calcium sensors. *Sci. Rep.* 5:10212. doi: 10.1038/srep10212

Storace, D., Rad, M. S., Han, Z., Jin, L., Cohen, L. B., Hughes, T., et al. (2015b). Genetically encoded protein sensors of membrane potential. *Adv. Exp. Med. Biol.* 859, 493–509. doi: 10.1007/978-3-319-17641-3_20

Storace, D., Sepehri-Rad, M., Kang, B., Cohen, L. B., Hughes, T., and Baker, B. J. (2016). Toward better genetically encoded sensors of membrane potential. *Trends Neurosci* 39, 277–289. doi: 10.1016/j.tins.2016.02.005

St-Pierre, F., Chavarha, M., and Lin, M. Z. (2015). Designs and sensing mechanisms of genetically encoded fluorescent voltage indicators. *Curr. Opin. Chem. Biol.* 27, 31–38. doi: 10.1016/j.cbpa.2015.05.003

St-Pierre, F., Marshall, J. D., Yang, Y., Gong, Y., Schnitzer, M. J., and Lin, M. Z. (2014). High-fidelity optical reporting of neuronal electrical activity with an ultrafast fluorescent voltage sensor. *Nat. Neurosci.* 17, 884–889. doi: 10.1038/nn.3709

Sung, U., Sepehri-Rad, M., Piao, H. H., Jin, L., Hughes, T., Cohen, L. B., et al. (2015). Developing fast fluorescent protein voltage sensors by optimizing FRET interactions. *PLoS One* 10:e0141585. doi: 10.1371/journal.pone.0141585

Ting, J. T., Daigle, T. L., Chen, Q., and Feng, G. (2014). Acute brain slice methods for adult and aging animals: application of targeted patch clamp analysis and optogenetics. *Methods Mol. Biol.* 1183, 221–242. doi: 10.1007/978-1-4939-1096-0_14

Treger, J. S., Priest, M. F., and Bezanilla, F. (2015). Single-molecule fluorimetry and gating currents inspire an improved optical voltage indicator. *Elife* 4:e10482. doi: 10.7554/elife.10482

Wachowiak, M., and Knöpfel, T. (2009). "Optical imaging of brain activity *in vivo* using genetically encoded probes," in *In Vivo Optical Imaging of Brain Function*, 2nd Edn., ed. R. D. Frostig (Boca Raton, FL: CRC Press/Taylor & Francis), 1–36.

Wang, D., Mcmahon, S., Zhang, Z., and Jackson, M. B. (2012). Hybrid voltage sensor imaging of electrical activity from neurons in hippocampal slices from transgenic mice. *J. Neurophysiol.* 108, 3147–3160. doi: 10.1152/jn.00722.2012

Wang, D., Zhang, Z., Chanda, B., and Jackson, M. B. (2010). Improved probes for hybrid voltage sensor imaging. *Biophys. J.* 99, 2355–2365. doi: 10.1016/j.bpj.2010.07.037

Wilt, B. A., Fitzgerald, J. E., and Schnitzer, M. J. (2013). Photon shot noise limits on optical detection of neuronal spikes and estimation of spike timing. *Biophys. J.* 104, 51–62. doi: 10.1016/j.bpj.2012.07.058

Yu, C. H., Dang, Y., Zhou, Z., Wu, C., Zhao, F., Sachs, M. S., et al. (2015). Codon usage influences the local rate of translation elongation to regulate co-translational protein folding. *Mol. Cell* 59, 744–754. doi: 10.1016/j.molcel.2015.07.018

Zou, P., Zhao, Y., Douglass, A. D., Hochbaum, D. R., Brinks, D., Werley, C. A., et al. (2014). Bright and fast multicoloured voltage reporters via electrochromic FRET. *Nat. Commun.* 5:4625. doi: 10.1038/ncomms5625

Conflict of Interest Statement: The authors declare that the research was conducted in the absence of any commercial or financial relationships that could be construed as a potential conflict of interest.

frontiers in Synaptic Neuroscience

ORIGINAL RESEARCH
published: 22 July 2016
doi: 10.3389/fnsyn.2016.00019

Control of Transmembrane Protein Diffusion within the Postsynaptic Density Assessed by Simultaneous Single-Molecule Tracking and Localization Microscopy

*Tuo P. Li and Thomas A. Blanpied**

Department of Physiology and Program in Neuroscience, University of Maryland School of Medicine, Baltimore, MD, USA

Postsynaptic transmembrane proteins are critical elements of synapses, mediating trans-cellular contact, sensitivity to neurotransmitters and other signaling molecules, and flux of Ca and other ions. Positioning and mobility of each member of this large class of proteins is critical to their individual function at the synapse. One critical example is that the position of glutamate receptors within the postsynaptic density (PSD) strongly modulates their function by aligning or misaligning them with sites of presynaptic vesicle fusion. In addition, the regulated ability of receptors to move in or out of the synapse is critical for activity-dependent plasticity. However, factors that control receptor mobility within the boundaries of the synapse are not well understood. Notably, PSD scaffold molecules accumulate in domains much smaller than the synapse. Within these nanodomains, the density of proteins is considerably higher than that of the synapse as a whole, so high that steric hindrance is expected to reduce receptor mobility substantially. However, while numerical modeling has demonstrated several features of how the varying protein density across the face of a single PSD may modulate receptor motion, there is little experimental information about the extent of this influence. To address this critical aspect of synaptic organizational dynamics, we performed single-molecule tracking of transmembrane proteins using universal point accumulation-for-imaging-in-nanoscale-topography (uPAINT) over PSDs whose internal structure was simultaneously resolved using photoactivated localization microscopy (PALM). The results provide important experimental confirmation that PSD scaffold protein density strongly influences the mobility of transmembrane proteins. A protein with a cytosolic domain that does not bind PSD-95 was still slowed in regions of high PSD-95 density, suggesting that crowding by scaffold molecules and perhaps other proteins is sufficient to stabilize receptors even in the absence of binding. Because numerous proteins thought to be involved in establishing PSD structure are linked to disorders including autism and depression, this motivates further exploration of how PSD nanostructure is created. The combined application PALM and uPAINT should be invaluable for distinguishing the interactions of mobile proteins with their nano-environment both in synapses and other cellular compartments.

Keywords: uPAINT, PALM, synapse, nanodomain, glutamate receptor, macromolecular crowding

Edited by:
George Augustine, Nanyang Technological University, Singapore

Reviewed by:
Michele H. Jacob, Tufts University, USA
Jason D. Shepherd, University of Utah, USA

****Correspondence:***
Thomas A. Blanpied
tblanpied@som.umaryland.edu

Received: *30 April 2016*
Accepted: *05 July 2016*
Published: *22 July 2016*

Citation:
Li TP and Blanpied TA (2016) Control of Transmembrane Protein Diffusion within the Postsynaptic Density Assessed by Simultaneous Single-Molecule Tracking and Localization Microscopy. Front. Synaptic Neurosci. 8:19. doi: 10.3389/fnsyn.2016.00019

INTRODUCTION

Transmembrane proteins such as receptors diffuse on the cell surface to reach their sites of action. In doing so, they must make their way through complex environments typified by varying densities of obstacles and potential binding partners. The average behavior of proteins moving through such environments has been well characterized (Frick et al., 2007). However, on small spatial scales or within small compartments, the local organization of potential interactors will dominate the influence on receptor motion paths (Kusumi et al., 2014). For instance, locally high concentrations of steric obstacles create a phenomenon called macromolecular crowding (Ryan et al., 1988) that can slow mobility and result in anomalous diffusion (Saxton, 1994; Santamaria et al., 2010). Thus, high-resolution information about the distribution of even non-binding obstacles is necessary to understand motion trajectories of transmembrane proteins on small scales.

Perhaps the most complex compartment of the plasma membrane in neurons is the postsynaptic density (PSD). The PSD of glutamatergic synapses concentrates numerous receptor types aligned to the presynaptic active zone. Despite the small size of the average PSD ($\sim$0.08 $\mu m^2 \times$ 50 nm; Harris and Weinberg, 2012), roughly 500 species of proteins can be found in this compartment (Husi et al., 2000; Sheng and Hoogenraad, 2007). Because of the high local density of transmembrane proteins, receptor-binding proteins such as PSD-95, and juxtamembrane cytosolic molecules, protein motion within the membrane at the synapse is likely extremely obstructed (Santamaria et al., 2010). This complicated environment is critical to understand, because protein organization in the PSD directly regulates synaptic transmission in many ways. The number of glutamate receptors present in the PSD sets an upper limit on the strength of the synapse (Huganir and Nicoll, 2013), and receptors exchange continuously by diffusion between the PSD and the perisynaptic plasma membrane (Opazo and Choquet, 2011; Choquet and Triller, 2013). Further, alterations to the PSD are a critical component of activity-driven plasticity mechanisms regulating receptor number (Inoue and Okabe, 2003; Bosch et al., 2014). Thus, understanding mechanisms within the PSD that control motion of glutamate receptors is critical for determining how receptor number is modulated during plasticity.

Even beyond the clear importance of the number of receptors, however, their distribution within the synapse in the plane of the membrane is a vital regulator of synaptic strength (MacGillavry et al., 2011). This is because when glutamatergic vesicles fuse with the presynaptic plasma membrane, the result is a highly concentrated but narrow spike of released neurotransmitter. The rapid dissipation of this spike by glutamate diffusion means that receptors laterally displaced from the site of fusion even by less than 100 nm often fail to activate (Xie et al., 1997; Raghavachari and Lisman, 2004; Santucci and Raghavachari, 2008; Freche et al., 2011). Amplifying this effect, receptors in the PSD are concentrated in $\sim$80 nm subdomains (MacGillavry et al., 2013; Nair et al., 2013) where the principle receptor-binding scaffold PSD-95 is also concentrated (Fukata et al., 2013; MacGillavry et al., 2013). In previous work, we modeled diffusion within PSDs where the heterogeneous distribution of PSD-95 was measured, and found that the clustered nature of this scaffold could strongly limit the ability of transmembrane proteins to enter (or escape) the crowded regions of the PSD (Li et al., 2016). Thus, nanoscale regional variation in protein composition within a single PSD may have strong impact on synaptic transmission by controlling the subsynaptic distribution of receptors.

A major impediment to progress on this issue is the technical challenge of simultaneously measuring the nanoscale distribution of the protein environment while simultaneously measuring protein motion through it. To address this, we developed a combined single-molecule imaging approach that uses single-particle tracking photoactivated localization microscopy (sptPALM; Manley et al., 2008) to map the positions of PSD-95 molecules within the synapse (MacGillavry et al., 2013), while simultaneously tracking the motion of proteins in the plasma membrane by universal point-accumulation-for-imaging-in-nanoscale-topography (uPAINT; Giannone et al., 2010). Using this strategy, we could directly investigate the influence of both obstacle density and protein binding on motion through the PSD. The results provide direct experimental confirmation that macromolecular crowding within the PSD can strongly limit the motion of even small transmembrane proteins, likely helping to establish the distribution and dynamic exchange characteristics of glutamate receptors and other molecules.

MATERIALS AND METHODS

Neuron Culture and Transfection

Dissociated hippocampal neuron cultures were prepared from E18 rat embryos as described previously (Frost et al., 2010). All procedures conformed to the guidelines established by Animal Welfare Act, Public Health Service, and the United States Department of Agriculture, and were approved by the Institutional Animal Care and Use Committee at the University of Maryland, Baltimore. Prior to plating the cells on coverslips, the coverslips were first cleaned as reported previously (MacGillavry et al., 2013), subsequently coated with lateral-drift tracking, yellow-green fluorescent 100 nm beads (F8803; Thermo Fischer Scientific) diluted 1:25,000 in 100% ethanol (dried within 25 min in the hood), and then coated overnight with poly-L-lysine (Sigma). Cells were transfected at DIV10–13 using Lipofectamine 2000 (Thermo Fischer Scientific) and imaged 72–96 h later (unless stated otherwise). Individual coverslips were transfected with 0.5–0.75 μg of cDNA for each expression construct.

Expression Constructs

Plasmid cDNAs were obtained as follows (with original sources): the binding and nonbinding probes, Super ecliptic phluorin (SEP)-transmembrane (TM)-Bind and SEP-TM-Nonbind (Li et al., 2016), the PSD-95-mEos2 replacement plasmid

shrPSD-95-mEos2 (MacGillavry et al., 2013). We have previously measured that this construct produces a mild 1.4× overexpression. Interpretations of the results from the PALM-PAINT assay require control experiments to ensure that the expressed protein is organized similarly to its endogenous counterpart. To this end, we have also compared the PSD-95 nanostructure of untransfected cells and those expressing the replacement construct PSD-95-mEos2 (MacGillavry et al., 2013; Tang et al., in press). These were not different in terms of PSD area, number of subsynaptic nanoclusters, and the size of those nanoclusters. Thus, we believe the mEos2 tag does not affect PSD nanostructure, at least in the absence of severe PSD-95 overexpression. Furthermore, mEos2 is fused at the c-terminal end of the PSD-95, not altering the positions of the various protein-protein interaction motifs. Thus, we believe tagging itself does not affect the interaction of PSD-95 with other proteins.

Two-Color Single-Molecule Imaging

PALM-PAINT, a combination of PALM (Betzig et al., 2006; Hess et al., 2006) and uPAINT (Giannone et al., 2010), was performed through a Photometrics DV2 on an Olympus IX81 ZDC2 inverted microscope that was described by MacGillavry et al. (2013). Cells expressing the indicated constructs were imaged in a previously described extracellular buffer (Li et al., 2016). SEP-containing probes were labeled with ATTO647N-conjugated anti-green fluorescent protein (GFP) nanobodies (GFPBooster-647N, Chromotek), bath applied to a final concentration of 0.5–2 nM once the first stretch of synapses was identified for each coverslip. Cells remained at 25°C for no more than 30 min per imaging session.

We imaged the red and far-red bands by interleaving excitations of 561 and 640 nm. Imaging was conducted at 29 Hz (14.5 Hz per color), with 10-ms duration excitation per frame for 5000–20,000 frames per color. The two emissions were overlaid based on calibration images of TetraSpeck beads (100 nm; Thermo Fischer Scientific) deposited on an acellular coverslip as described by MacGillavry et al. (2013). Yellow-green beads (100 nm) ethanol-diluted and dried onto the coverslips prior to plating the cells (F8803; Thermo Fischer Scientific) were excited and captured once every 1000 frames to monitor lateral drift. To correct lateral drift, we localized fiducials *post hoc* from images of the yellow-green beads. We screened for spurious localizations by the duration of fluorescence and mobility. Namely, the bead ought to be present on the first frame, persist for as long as each imaging session, and displace <100 nm (1 pixel) per 1000 frames. Such a filtering process provided a list of localizations that correspond to fiducials. From this list we calculated the sample lateral drift as the weighted average of the displacements of all fiduciary localizations between each set of 1000 frames. For weights, we used the inverse of the estimated localization uncertainty (Thompson et al., 2002) of each fiducial. The single linear correction in drift we applied to each subset of 1000 frames was the average correction obtained from the estimates of 2–10 fiducials in the field of view.

Single-Molecule Localization, Tracking Analysis, and PSD Nanostructure Analysis

All data analysis was performed offline using custom routines in MATLAB (The MathWorks). The algorithms for determining molecule location and criteria for filtering molecules to be considered for further analysis were applied as previously described (MacGillavry et al., 2013). In addition to filtering by localization precision, elliptical form, and brightness, we also utilized a Voronoi-based segmentation program SR-Tesseler (Levet et al., 2015) to filter out spurious localizations outside of putative neuronal border. Criteria for defining a track were described by Li et al. (2016). Instantaneous effective diffusion coefficients (D_{eff}) at individual track time points were calculated for tracks that persisted at least eight frames (the duration in which the mean mean squared displacement (MSD) was linear; a more detailed description can be found in Lu et al., 2014). For comparing diffusion inside and outside of PSDs, tracks that entered or exited the PSD were divided into two portions, a synaptic and an extrasynaptic subtrack, the D_{eff} of which were calculated by averaging the instantaneous D_{eff} for the tracked localizations therein. For the rare tracks that entered and exited PSDs multiple times, synaptic D_{eff} was determined by averaging the instantaneous D_{eff} of all the tracked locations inside the PSD border; vice versa to calculate the extrasynaptic D_{eff}. To calculate the D_{eff} of subtracks in other cases (e.g., within a particular range of PSD-95 regional density, or below the detection limit of D_{eff}), we calculated the average of instantaneous D_{eff} of localizations meeting the criteria. The lower detection limit of D_{eff} was determined conservatively by calculating the D_{eff} of a theoretical immobile particle displaced as much as the average trajectory error ∼30 nm (Savin and Doyle, 2005; Lu et al., 2014) per time frame, which amounted to 0.003 $\mu m^2/s$; this value is indicated by a gray vertical dotted or dotted-dashed line in cumulative frequency graphs of D_{eff}.

The PALM PSD border was determined by taking the convex hull of the PSD-95 molecular positions. To determine the Gaussian-blurred border of each PSD, we first constructed a 2-dimensional molecular density map of 25 × 25 nm subpixels from PSD-95 molecules for each PSD. We then convolved it with a constant-amplitude Gaussian image profile ($\sigma = 125$ nm, image width = 900 nm) that is similar to an ideal microscope point-spread function with a full-width at half max (FWHM) of ∼250 nm. To determine the FWHM border of the blurred PSD, we thresholded the convolved image at half-maximum intensity. To determine the 95%-border, we thresholded it at 5% of the maximum intensity.

Determination of Regional PSD-95 Density

To quantify the regional density of PSD-95, we measured the number of molecules surrounding each position of a tracked probe molecule. PSD-95 localizations appearing in consecutive frames separated by no more than 200 nm were considered one molecule, and its position was taken from the first frame it appeared. We counted the number of PSD-95 molecules within a 30 nm radius (the average trajectory error) of each position in the track of a probe molecule. Because we wished primarily

to relate D_{eff} to regional density, we used the same tracked locations to calculate each measure. That is, for the regional density of PSD-95 surrounding the probe at each position, we calculated the forward running average of regional densities for eight frames, the same number of frames used to calculate D_{eff}. The absolute density of molecules in all calculations was adjusted by the average expected number of blinks (one) of mEos2 in our experimental conditions (Annibale et al., 2011; MacGillavry et al., 2013). The final density when averaged across synapses is likely somewhat higher than endogenous PSD-95 densities due to the mild (∼1.4-fold) overexpression obtained with our shRNA knockdown/replacement approach. However, we did not attempt to measure the potentially quite variable ratio of endogenous and tagged PSD-95 at each synapse analyzed, and did not take this into account for calculations. Data of immunostaining done in cells not intended for PALM-PAINT showed that endogenous PSD-95 molecules resistant to the knockdown did not form dense clusters outside those formed by the expressed PSD-95 molecules, indicating that though the endogenous PSD-95 might be present in the synapse, they likely raise the absolute number of PSD-95 molecules without changing the spatial variation in regional density.

Statistics

Where means are presented, the accompanying errors are the standard error of the mean; additionally, these data were normally distributed according to the Shapiro-Wilk normality test. Where box-and-whisker plots are presented, the middle bar represents the median, the upper and lower limit of the boxes denote the interquartile range, and the whiskers extend to 5% and 95% of the distribution; additionally, these data were not normally distributed according to the Shapiro-Wilk normality test. Different sets of statistical tests were used for normally and non-normally distributed data. Pairwise statistical tests were performed using unpaired *t*-test with Welch's correction for normally distributed data; they were performed using Mann-Whitney U test for non-normally distributed data. Where two-way analysis of variance (ANOVA) was used, a Bonferroni correction was used for *post hoc* pairwise comparisons. Kolmogorov-Smirnov tests were applied for cumulative frequency distributions. In all cases, means (or medians) were considered significantly different if the test reported $p < 0.05$. Most statistical tests and all graphing were done using Prism (GraphPad Software). Two-way ANOVA was done in MATLAB (The MathWorks).

RESULTS

To perform single-molecule tracking during superresolution imaging of the PSD, we co-transfected 13–17 DIV hippocampal neurons with two cDNA constructs. The first encoded a single-pass TM protein composed of an extracellular SEP, the TM domain, and the intracellular carboxy terminus of stargazin, which enables this protein to bind PSD-95. Thus, we refer to it as SEP-TM-Bind (Li et al., 2016). This was co-transfected with shrPSD-95-mEos2, which expresses shRNA targeting PSD-95 along with an RNAi-resistant, mEos2-tagged PSD-95 (MacGillavry et al., 2013). To track motion of SEP-TM-Bind at the cell surface, we used uPAINT and applied anti-GFP nanobodies carrying Atto647N in the chamber to a final concentration of 0.5–2 nM. Concurrently, we localized the positions of PSD-95-mEos2 using conventional sptPALM methods (**Figure 1A**).

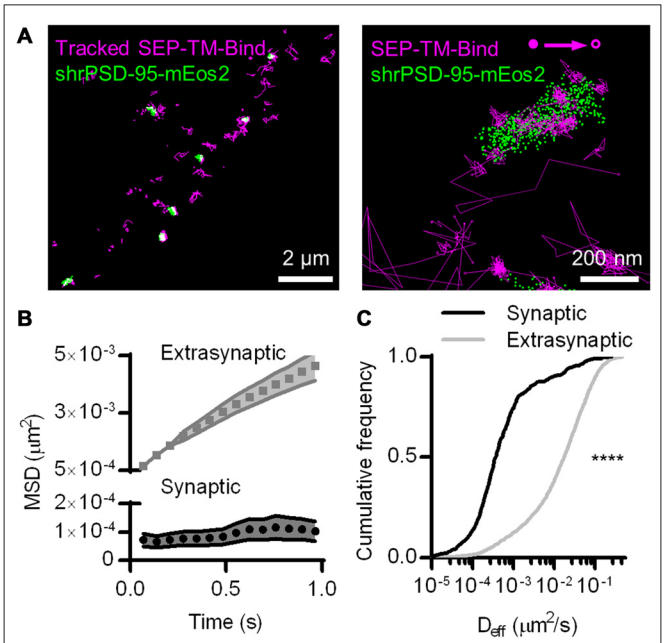

FIGURE 1 | Photoactivated localization microscopy (PALM)-point accumulation-for-imaging-in-nanoscale-topography (PAINT), single-molecule tracking during PALM imaging. (A) (Left) Super ecliptic phluorin (SEP)-TM-Bind molecules tracked for at least eight frames super-imposed on molecules of shrPSD-95, accumulated from 5000–20,000 frames. (Right) A typical example of tracked probes superimposed on positions of shrPSD-95 molecules. The first and last localized positions are indicated as filled and open circles, respectively. **(B)** Mean squared displacement (MSD) over time of connected sub-segments of tracks (subtracks) that are lasted at least 15 frames ($n = 156$ synaptic and 2907 extrasynaptic tracks/113 PSDs/13 fields/11 cells/3 cultures). **(C)** Cumulative frequency distributions of D_{eff} for subtracks that are at least eight frames long ($n = 654$ synaptic and 3349 extrasynaptic tracks/113/13/11/3). ****$p < 0.0001$.

The SEP-TM-Bind probe exhibited clearly different mobility inside and outside of the PSD (**Figure 1A** right), as expected based on the behavior of AMPA-type glutamate receptors (Bats et al., 2007; Hoze et al., 2012), intercellular adhesion molecules such as neuroligin and leucine rich repeat transmembrane neuronal 2 (LRRTM2; Chamma et al., 2016), and NMDA-type glutamate receptors (Dupuis et al., 2014). We compared the diffusion patterns of molecules inside and outside of the PSD, when the PSD border was defined by the convex-hull border of PSD-95 positions. Probes outside of the PSD displayed near-free diffusion as evidenced by an almost linear plot MSD (**Figure 1B**). However, probes within the PSD showed a much slower mobility and appeared highly confined in their motion, as evidenced by saturation of the relationship between MSD and time. This curve approached a plateau

of 104 ± 35 nm^2, suggesting confinement within <60 nm diameter regions of the PSD (Ehlers et al., 2007). The effective diffusion coefficients (D_{eff}) of the synaptic subtracks were ~2 orders of magnitude slower than those of the extrasynaptic subtracks (**Figure 1C**). This differential is similar to that seen for AMPARs (Bats et al., 2007; Hoze et al., 2012), suggesting that AMPAR motion within synapses likely is regulated by mechanisms that also impact many other types of molecules.

The improved resolution of the PSD border obtained by imaging the positions of individual PSD-95 molecules as opposed to using widefield or confocal microscopy should improve discrimination of which molecules are within the synapse. The average PSD area (0.085 ± 0.006 μm^2, n = 263 PSDs/21 neurons) was within the ranges as previously detected by PALM (MacGillavry et al., 2013; Nair et al., 2013) and by electron microscopy (Harris and Stevens, 1989; Schikorski and Stevens, 1997; Shinohara et al., 2008). To test whether diffraction-limited PSD borders could perform as well as PALM of PSDs at segregating synaptic and extrasynaptic probes, we simulated diffraction by blurring the PSD-95 molecular density maps with a Gaussian point-spread function. Taking the FWHM of this intensity distribution as the border of the diffraction-blurred PSDs, as was done by Li et al. (2016), performed nearly as well as the PALM'ed PSD border in segregating synaptic and extrasynaptic probe movements. Taking the 95% border of the blurred PSDs diminished the difference between synaptic and extrasynaptic D_{eff} (**Figure 2**). Thus, how the PSD border is defined in diffraction-limited approaches can influence the accuracy of segregating diffusing molecules in different sub-compartments of the cell.

Synaptic TM Protein Diffusion is not Influenced by PSD Size or Whole-Synapse PSD-95 Density

Interestingly, the D_{eff} distribution within different synapses varied widely, and individual molecules exhibited D_{eff} spanning more than five orders of magnitude. This difference did not stem from neuron-to-neuron variability, as the median synaptic D_{eff} of the binding probes measured in different neurons differed by only up to 2-fold. We reasoned that this broad range of D_{eff} may arise because the diffusion environment within the PSD might vary based on synaptic size or geometry, or because the density of binding sites could influence how likely a probe is able to be bound at any given time. To test this, we first examined the relationship between the area of the PSD and the median D_{eff} of probes found within it. Based on linear regression analysis, we found no statistically significant correlation (**Figure 3A**). However, our previous study found that the fluorescence recovery of these probes after photobleaching spines was negatively correlated with PSD area (Li et al., 2016). Combined with this finding, this suggests that the size of the synapse correlates with the rate with which these probes enter and exit the spine, but does not influence their diffusion within the synapse. To determine whether overall PSD-95 density within the synapse can determine the diffusion

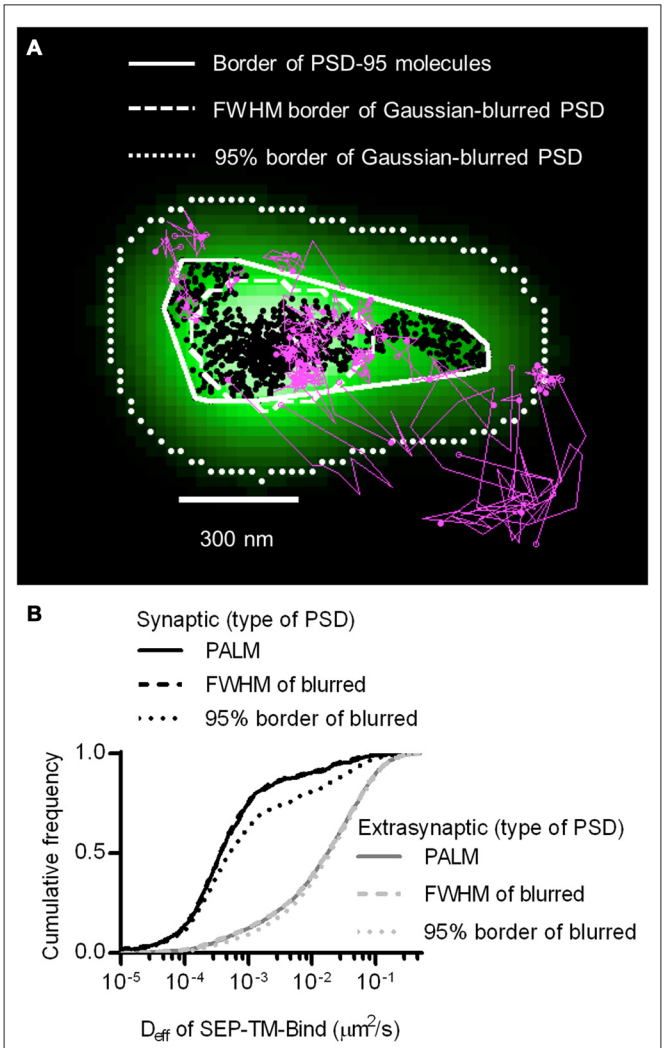

FIGURE 2 | Better discrimination of postsynaptic density (PSD) border reveals strong reduction of mobility within synapses. (A) Typical tracks of the binding probe (magenta) and positions of shrPSD-95 (black circles) super-imposed. Convex hull border of PSD-95 positions (solid line), full-width half max (FWHM) border of Gaussian-blurred shrPSD-95 positions (dashed line), and full-width 5% max (95%) border (dotted lines). **(B)** Cumulative frequency distribution of synaptic (black lines) and extrasynaptic (gray lines) tracks segregated using the synaptic borders of PSDs determined using PALM'ed shrPSD-95 (solid lines), FWHM of Gaussian-blurred shrPSD-95 positions (dashed lines), or full-width 5% max (95% border) of the Gaussian-blurred shrPSD-95 positions (dotted lines) (n = 654 synaptic/3349 extrasynaptic tracks for PALM'ed PSDs, 658/3345 FWHM, 1197/3125 95% border; 113 PSDs, 11 cells, 3 cultures).

of the binding probes, we examined the relationship between the density of PSD-95-mEos2 localizations and the synaptic median D_{eff} of probes in each PSD. The absolute density of localizations in all calculations was adjusted by the average expected number of blinks (one) of mEos2 in our experimental conditions (Annibale et al., 2011; MacGillavry et al., 2013). It should be noted that this measure of density does not incorporate the unknown fraction of total PSD-95 molecules that were mapped, and also ignores the numerous other binding partners of SEP-TM-Bind that may not correlate with the

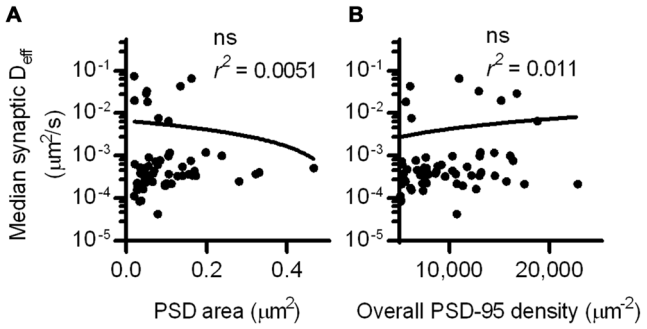

FIGURE 3 | PSD size and density do not correlate with intrasynaptic mobility. (A) PSD area and median D_{eff} within each of the PSDs; linear regression test (n = 113 PSDs/11 cells/3 cultures). **(B)** PSD-95 density and median D_{eff} within each of the PSDs; linear regression test (n = same as in **A**).

measured density of PSD-95-mEos2 as well as the likelihood of slight overexpression compared to endogenous protein level (~1.4×, see MacGillavry et al., 2013). Nevertheless, we found no statistically significant correlation (**Figure 3B**), suggesting that, given these caveats, the overall density of PSD-95 within the PSD does not influence the median diffusion of binding TM proteins in the synapse.

The Control of TM Protein Diffusion by Binding and Steric Hindrance Within the PSD

Though the overall measured density of PSD-95 did not correlate with the diffusion coefficient of SEP-TM-Bind, it would be surprising if this key scaffolding protein did not affect the mobility of its binding partners at all. We thus considered that the distribution of PSD-95 molecules is highly heterogeneous within single synapses (Fukata et al., 2013; MacGillavry et al., 2013; Nair et al., 2013; Broadhead et al., 2016) and can display multiple regions of high density within the synapse. Namely, two synapses of the same PSD-95 density can have very different arrangement of PSD-95 molecules, an organization that could obscure the effect that PSD-95 molecular density can have on the diffusion of probes when measured at the level of the entire synapse. Consistent with this notion, computer modeling has demonstrated that measured arrangements of PSD-95 molecules can prevent a larger fraction of TM proteins from escaping the synapse than homogeneously distributed PSD-95 molecules, without changing the overall density of PSD-95 (Li et al., 2016).

To test whether the density of PSD-95 immediately surrounding the probe can influence its diffusion within the synapse, we defined a subsynaptic metric termed "regional PSD-95 density" to be the number of PSD-95 molecules surrounding a tracked probe position. We measured the regional density using a fixed radius based on the average positional error of the tracked molecules (30 nm, see "Materials and Methods" Section). However, the results of the following analyses depended only very weakly on the radius over the range of 15–80 nm (data not shown). We subdivided tracks into subsegments (subtracks) based on the regional PSD-95 density at each of their positions, and plotted the D_{eff} for subtracks based on their regional density. This analysis revealed that the higher the regional PSD-95 density, the slower the diffusion coefficients of the subtracks in that area of the PSD (**Figures 4A,B**). In fact, the median probe D_{eff} within the synapse was strongly correlated with the regional density of PSD-95 (**Figure 4C**).

The Control of TM Protein Diffusion by Steric Hindrance Alone Within the PSD

At a first glance, this result may not be surprising, as it supports the idea that the more scaffold binding partners there are in the synapse, the more likely the probe will be bound and thus immobilized before diffusing further. However, this effect is more difficult to interpret if we consider that PSD-95 not only binds this probe, but can serve as a steric obstacle. In fact, PSD-95 is a hub for binding many other proteins that can serve as additional obstacles which could, without binding the probe, hinder its diffusion. To isolate the effect of steric hindrance from the combined effect of steric hindrance and

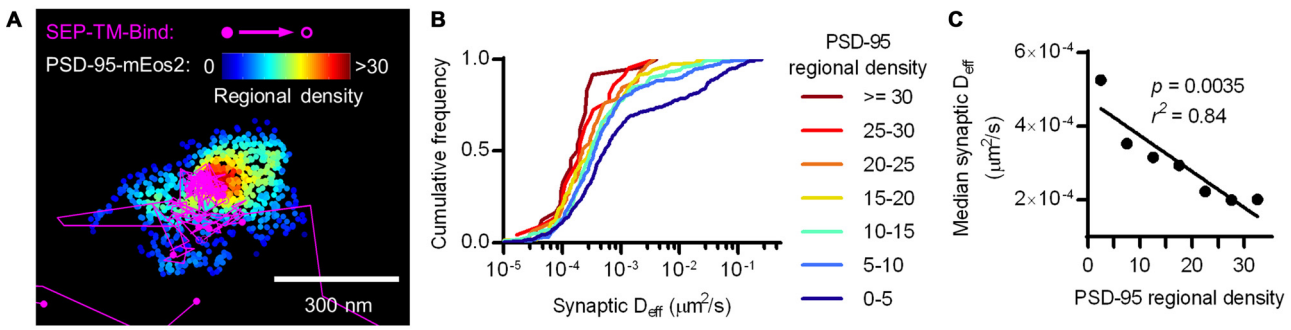

FIGURE 4 | Nanoscale regional density of PSD-95 within the synapse correlates with probe diffusion coefficient. (A) Typical example of tracks and PSD-95 positions. Tracks pseudo-colored purple, PSD-95 positions pseudo-colored by regional density. **(B)** Cumulative frequency distributions of probe D_{eff} binned in increasing regional densites of PSD-95 surrounding the subtracks (n = 448 subtracks in 0–5 PSD-95, 281 in 5–10, 159 in 10–15, 106 in 15–20, 59 in 20–25, 22 in 25–30, 24 in 30+). **(C)** PSD-95 regional density and the median D_{eff} of the binding probe; relationship tested by linear regression.

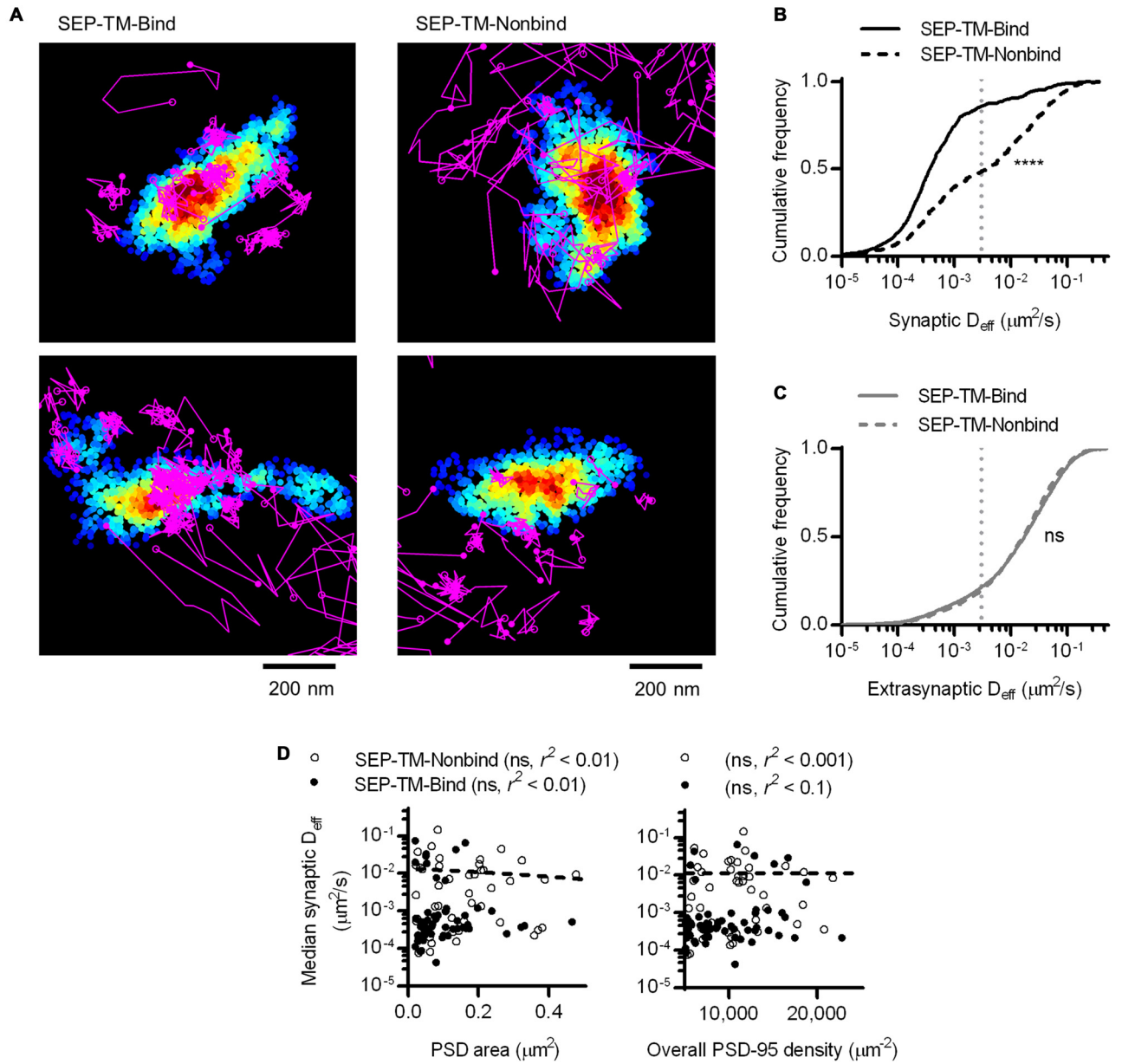

FIGURE 5 | A non-binding transmembrane protein enters and slows within the synapse, but not as much as if it can bind PSD-95. (A) Typical examples of tracked probes (purple) superimposed on shrPSD-95 positions (pseudo-colored on a scale of regional density same as **Figure 4A**; binding probe SEP-TM-Bind (left), nonbinding probe SEP-TM-Nonbind (right). **(B)** Cumulative frequency distributions of the binding probe and nonbinding probe D_{eff} within PSDs ($n = 654$ tracks/113 PSDs/11 cells/3 cultures for SEP-TM-Bind, 519/91/10/3 SEP-TM-Nonbind). **(C)** Cumulative frequency distributions of the binding probe and nonbinding probe D_{eff} outside of PSDs ($n = 3349$ tracks for SEP-TM-Bind, 4470 SEP-TM-Nonbind). **(D)** (Left) PSD area and median D_{eff} within each of the PSDs; linear regression test ($n = 91$ PSDs/10 cells/3 cultures of SEP-TM-Nonbind, same as in **Figure 3** for SEP-TM-Bind). (Right) Overall synaptic PSD-95 density and median D_{eff} within each of the PSDs; linear regression test ($n =$ as in left panel).

probe-scaffold binding, we performed PALM-PAINT on a probe variant that cannot bind to PSD-95 (SEP-TM-Nonbind from Li et al., 2016). Interestingly, SEP-TM-Nonbind still entered synapses and diffused within them, but did not enrich within the PSD nearly as greatly as SEP-TM-Bind (**Figure 5A** and see also Li et al., 2016). Notably, the diffusion of this nonbinding probe within the synapse was dramatically faster than that of the binding probe (**Figure 5B**). On the other hand, the extrasynaptic diffusion of the nonbinding probe was not different from that of the binding probe (**Figure 5C**). It is interesting to note that using sptPALM (i.e., by photoactivating and tracking an mEos3 fusion protein rather than using an anti-GFP PAINT approach as here) there was a very similar mobility differential between the binding and nonbinding probes despite a substantial absolute difference

in D_{eff} arising from the poorer localization precision of the fusion protein compared to the organic dye (Li et al., 2016). Thus, the mobility difference between the two probes is quite robust. Intriguingly, the shoulder-like shape of the cumulative D_{eff} distribution suggests that probes undergo multiple influences on their diffusion within the synapse. However, neither PSD area nor whole-synapse PSD-95 density correlated with probe diffusion within the PSD (**Figure 5D**).

By labeling SEP-tagged TM proteins with nanobodies, we add minimal but appreciable bulk to the extracellular domain of the diffusing entity. SEP is fused to the extracellular domain of the TM probes, adding approximately 3–5 nm of bulk; nanobody labeling of the GFP adds an additional 3–5 nm of bulk. While additional extracellular bulk has previously been shown to slow receptor diffusion (Groc et al., 2007), we expect the effect to be identical for both the binding and the nonbinding probes and thus not change our conclusions about the effect of postsynaptic steric hindrance.

We next considered whether the regional density of PSD-95 immediately surrounding the nonbinding probe can sterically control the probe diffusion. To test this, we first subdivided the tracks into subtracks and binned them into increasing regional densities of PSD-95 molecules, as in **Figure 4B**. This revealed that despite the lack of a PSD-95-binding motif, the probe still diffused more slowly within higher density regions of the PSD (**Figure 6A**). The effect appeared to saturate at low D_{eff} since the mobility of these slowly moving molecules is below our detection limit (0.003 $\mu m^2/s$).

If steric obstruction influences probe mobility, it may influence the overall pattern of probe position within the synapse. We thus compared the fraction of subtracks found in different regional PSD-95 densities (**Figure 6B**). Interestingly, though the binding and the nonbinding probes were distributed similarly through most density values, the nonbinding probes appeared to be preferentially excluded from the highly dense subregions (i.e., >25 regional molecules) of the synapse. Because of the small number of subtracks in these bins, however, this difference was not significant. Note also that the distribution of tracked molecules may not completely faithfully represent the total steady-state distribution of probe molecules, since molecules immobilized in the synapse for long periods are less likely to be recognized by a nanobody and be tracked by uPAINT.

It appeared that regional densities of PSD-95 higher than 10 had minimal effect on diffusion of the nonbinding probe in the D_{eff} range below our detection limit (**Figure 6C**), whereas the regional density of PSD-95 linearly correlated with

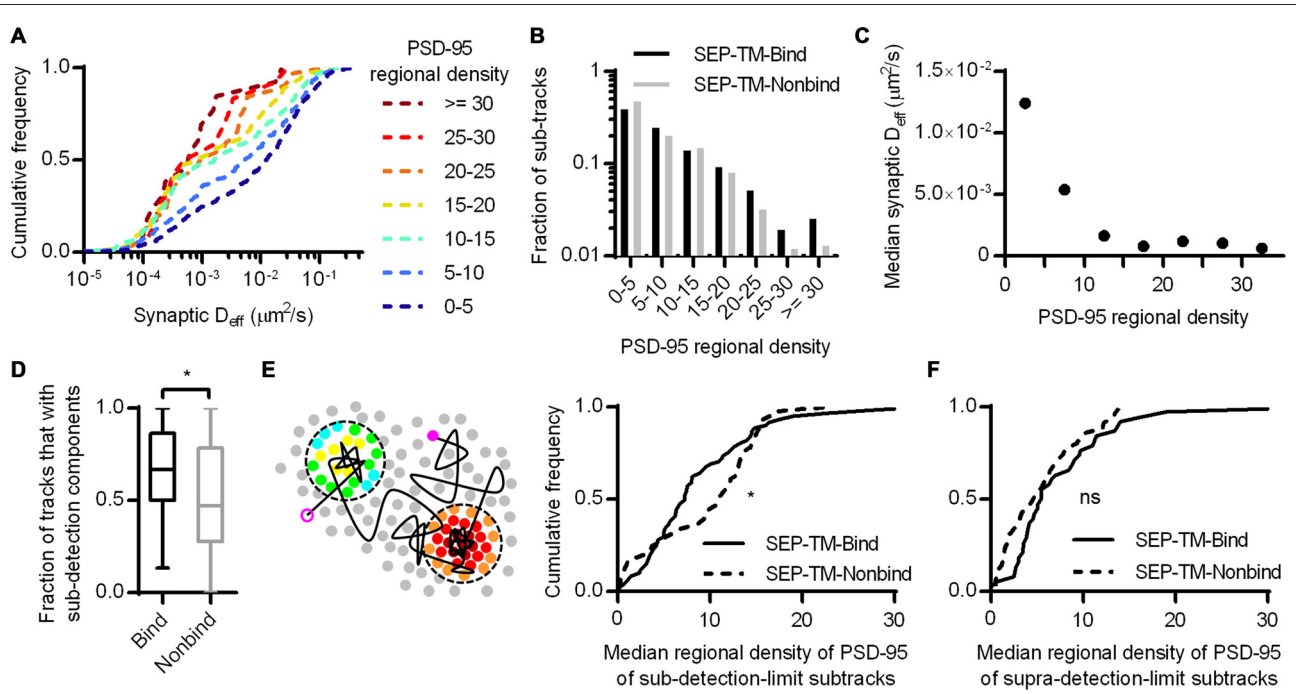

FIGURE 6 | Subsynaptic regional density of PSD-95 influences the mobility of a probe that does not bind PSD-95. (A) Cumulative frequency distributions of the nonbinding probe D_{eff} binned in increasing regional densites of PSD-95 surrounding the subtracks (n = 480 subtracks in 0–5 PSD-95, 204 in 5–10, 148 in 10–15, 81 in 15–20, 32 in 20–25, 12 in 25–30, 13 in 30+). **(B)** Fraction of subtracks in different regional densities of PSD-95. **(C)** PSD-95 regional density and the median D_{eff} of the nonbinding probe. **(D)** Fraction of tracks with subsegments that were slowed below the detection limit per PSD (n = 113 PSDs for SEP-TM-Bind, 91 SEP-TM-Nonbind; *p = 0.0123 Mann-Whitney U test). **(E)** (Left) Cartoon highlighting the PSD-95 molecules surrounding subtrack durations that diffused below the detection limit. The open and closed purple circles indicate the beginning and end of a track, the circles pseudo-colored by regional density were within 30 nm of sub-detection limit subtracks. We calculated the median regional density of PSD-95 of all subtrack durations that diffused below the detection limit with every PSD. (Right) Median regional density of PSD-95 surrounding subtracks that were below the detection limit (n same as in **D**; *p = 0.0325 K-S test). **(F)** Median regional density of PSD-95 surrounding subtracks that above the detection limit (n same as in **D**; ns, Not significant, p = 0.158 K-S test).

the diffusion of the binding probe (**Figures 4B,C**). Thus we wondered whether the two probes required different degrees of steric hindrance in order to be stabilized. To test this, we first noted that during multiple visits to a synapse, or even within a single visit, probe molecules could display both slow and fast periods of motion. Considering only the subtracks within synapses, SEP-TM-Bind had a higher fraction than SEP-TM-Nonbind of these subtracks for which D_{eff} was below the detection limit (**Figure 6D**). This indicates that the binding probes were more often slowed down while within the synapse than were the non-binding probes. We could then further exploit the ability afforded by PALM with uPAINT to examine the very local environment of the molecules as they moved within the synapse. Specifically, we noted that if steric hindrance slows mobility of the both the binding and non-binding probes, but binding is only able to slow SEP-TM-Bind, then SEP-TM-Bind would be expected to show a greater tendency to slow its mobility in relatively less dense PSD subregions. That is, even sparse binding partners could potentially capture and immobilize SEP-TM-Bind whereas higher concentrations of molecules would be required to sterically obstruct SEP-TM-Nonbind. Consistent with this, when we analyzed the sub-detection-limit portion of the nonbinding probe subtracks, we found that these were preferentially in locales of higher regional density of PSD-95 compared to those of the binding probes (**Figure 6E**). Interestingly, the fraction of the subtracks above the detection limit did not show any difference in regional PSD-95 density (**Figure 6F**), with even a trend to the opposite relationship.

Altogether, these results suggest that crowding by scaffold molecules and perhaps other proteins is sufficient to stabilize TM proteins in the absence of binding. How dense does the molecular environment have to be in order to slow the TM probes sterically as much as the combined influence of steric hindrance and probe-scaffold binding? To estimate an answer to this question, we compared the diffusion coefficients of the binding and nonbinding probes within increasing regional densities of PSD-95 (**Figure 7**). As expected based on **Figures 4**, **6**, the synaptic D_{eff} of both probes decreased gradually with increasing PSD-95 regional density. However, the D_{eff} of SEP-TM-Nonbind decreased precipitously over the range of 0–15; yet, it did not decrease further at higher densities. Furthermore, the D_{eff} of SEP-TM-Nonbind plateaued at the D_{eff} value displayed by SEP-TM-Bind at very low PSD-95 densities. Thus, by this analysis, ∼15 PSD-95 molecules per region of 30 nm radius (∼5000 molecules/μm^2) is the threshold beyond which the steric hindrance is as strong as both steric and binding influences combined.

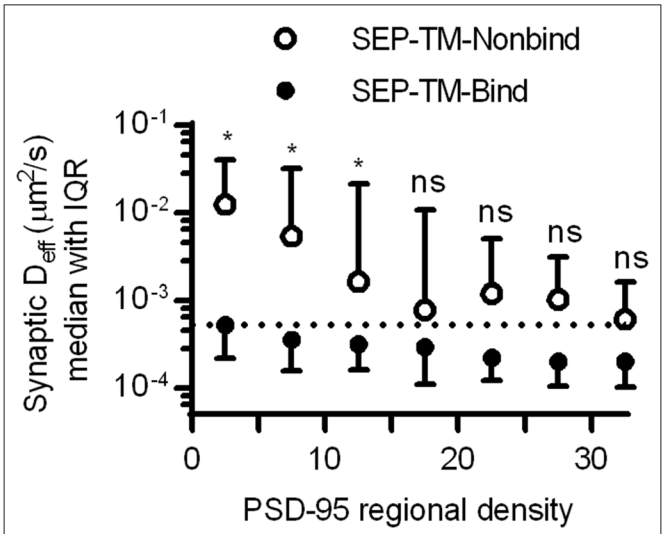

FIGURE 7 | Estimating how dense PSD-95 is when protein mobility is slowed sterically. D_{eff} of SEP-TM-Nonbind and of SEP-TM-Bind within synaptic subregions of different PSD-95 densities (*n* of SEP-TM-Nonbind same as in **Figure 6B**; that of SEP-TM-Bind same as in **Figure 4B**; two-way ANOVA, effect of binding $F_{1,6} = 15.27$, $p < 0.001$; effect of regional PSD-95 density $F_{1,6} = 13.53$, $p < 0.0001$; *post hoc* Bonferroni multiple comparisons tests between probes in increasing regional densities $^*p < 0.05$, ns, Not significant).

DISCUSSION

Using simultaneous single-molecule tracking and localization microscopy enabled by uPAINT and PALM, we demonstrated that the subsynaptic regional density of a scaffold protein PSD-95 can stabilize the surface membrane diffusion and positional organization of a single-pass transmembrane protein probe. The denser the regional density of PSD-95, the slower was the diffusion of the TM probe. This influence was apparent even in the absence of probe-scaffold binding, indicating steric hindrance by macromolecular crowding can complement protein-protein binding interactions in organizing TM proteins within the synapse.

The Roles of Receptor-Scaffold Binding and Macromolecular Crowding in Subsynaptic Organization

The mobility of AMPARs in the synapse is increased when the binding of their accessory subunit Stargazin to PSD-95 is disrupted (Bats et al., 2007; Sainlos et al., 2011), providing strong evidence that receptors are acutely stabilized by PSD-95 binding. However, even in these conditions some stabilization of receptors in the synapse occurs, and our results indicate specifically that even small probes carrying a cytosolic tail unable to bind PSD-95 is still slowed substantially in the synapse. What controls this stabilized fraction even in the absence of binding has been a mystery. Mechanisms such as additional binding interactions have been proposed, which is not unlikely considering that AMPARs have numerous auxiliary subunits (Tomita et al., 2003; Cho et al., 2007; Soto et al., 2009; Kalashnikova et al., 2010; von Engelhardt et al., 2010; Erlenhardt et al., 2016) that can bind to various scaffolding proteins. However, even a cytosolic domain composed of just a GFP-type molecule is slowed within the synapse (Li et al., 2016). Thus, we propose a more general mechanism that likely applies not only to glutamate receptors but also to other TM proteins critically important for synaptic function. In this model, receptor-scaffold binding is a ticket to entry and exit; PSD morphing redistributes even bound

receptors within the synapse; and macromolecular crowding in combination with binding stabilizes the receptors at subsynaptic domains highly packed with other proteins important for synaptic transmission.

Interestingly, though the TM binding probe is much smaller than AMPARs, its distribution of D_{eff} within the synapse appeared as slow as, or even slower than, AMPAR diffusion measured in other studies using dye-conjugated antibodies or quantum-dot-conjugated nanobodies (Nair et al., 2013; Cai et al., 2014). It is possible that these various labeling approaches preferentially sample receptors that exit the synapse and diffuse more freely in the perisynaptic space, which may tend to obscure real differences in the relative numbers of low-D_{eff} molecules that occupy the synapse for long periods. On the other hand, taken at face value, the similarity is consistent with our previous report using sptPALM that a substantial and nearly identical fraction of mEos-tagged AMPARs and binding probes diffused with $D_{eff} < 0.02\ \mu m^2/s$ (Li et al., 2016), further supporting the notion that much of the synapse is so crowded it stabilizes and organizes both large and small TM proteins.

Previously, we demonstrated using partial synapse Fluorescence Recovery after Photobleaching (FRAP), smtPALM alone, and uPAINT alone that the protein bulk of the TM probe decreased its diffusion within the synapse. However, previous approaches were limited in ability to assess how the complex structure within the PSD could influence the mobility and organization of TM proteins in a living synapse. Results from PALM-PAINT indicate that a particular degree of postsynaptic crowding, which we estimate as 5000 molecules/μm^2, can be sufficient to stabilize TM protein diffusion in the absence of binding. This density translates to an average ∼14 nm inter-PSD-95 distance, very similar to the mean nearest-neighbor distance of ∼13 nm between the "vertical filaments" corresponding to PSD-95 as measured in EM tomography (Chen et al., 2008). Note that we deduce this as an average spacing, but could not directly measure it around individual moving probes. The similarity between these values suggests that rather subtle variations in scaffold density across the lateral extent of the synapse could change TM protein mobility substantially. This high density packing is similar to what has been measured for AMPA receptors (e.g., 2000–4000/μm^2, see Levet et al., 2015). Indeed, receptor-scaffold binding may facilitate the assembly of this tight packing. Though the fractional time synaptic AMPARs spend bound to PSD-95 is not known, macromolecular crowding is likely to augment maintenance of this architecture once assembled, because receptors in crowded areas that dissociate from scaffolds will face a longer escape time from the region and thus are more likely to rebind PSD-95.

If domains of high PSD-95 density tend to accumulate not only probes such as used here but also receptors, then their impact on synaptic transmission will depend on where they are with respect to sites of neurotransmitter release (MacGillavry et al., 2011). Recently, we have found that nanoclusters of PSD-95 frequently align transsynaptically with sites of neurotransmitter release, as indicated by their transsynaptic alignment with RIM1/2 molecules which in turn correlate with presynaptic vesicle fusion locations (Tang et al., in press). Thus, we speculate that the enhanced crowding within these high-density subdomains will slow and help limit the escape of receptors from points in the synapse where they are most likely to be activated during neurotransmission.

Crowding within high-density subdomains is likely not due only to postsynaptic scaffolding proteins. Indeed, transmembrane adhesion molecules, which associate with one another across the synaptic cleft, will enhance crowding further in the extracellular, transmembrane, and intracellular domains. The distribution of these adhesion molecules may regulate the alignment between neurotransmitter receptors and release sites, though this is not known. The TM probes employed here share commonalities with some of the intercellular adhesion molecules in size (e.g., single-pass TM proteins) or the ability to bind PSD-95, yet synaptic adhesion proteins display quite divergent patterns of expression within the synapse. SynCAM is distributed in clusters surrounding the border of PSD-95 molecules (Perez de Arce et al., 2015), as are some members of the cadherin/catenin system (Uchida et al., 1996). On the other hand, neuroligin1 and LRRTM2 are inside the synapse and distributed in clusters reminiscent of PSD-95 (Chamma et al., 2016).

Surprisingly, LRRTM2, though smaller in both extracellular and intracellular length than neuroligin1, in fact diffuses slower than neuroligin1 (Chamma et al., 2016). Moreover, LRRTM2 is more compactly distributed and in the synaptic center than the larger neuroligin1, suggesting that LRRTM2 is more likely associated with dense regions of PSD-95 which are often found near the center of the PSD (MacGillavry et al., 2013; Tang et al., in press). This paradoxical result confirms that the arrangements of TM proteins cannot be predicted by their bulk alone. Interestingly, however, AMPARs associate with LRRTM2 through their extracellular domains (de Wit et al., 2009), potentially regulating the mobility of each protein by the addition of further bulk and protein-protein interactions. Further experiments are needed to tease out how the various interactions on diverse synaptic TM protein species dictate one another's spatial arrangement.

The diffusion of TM proteins appeared complicated outside of the synapse particularly within few hundred nanometers from the border of the PSD. In some cases, the nonbinding probe moves over a large area in the extrasynaptic regions, but in other cases, they can appear confined or immobilized as the binding probes. Proteins other than scaffolding proteins can certainly affect the mobility of these probes outside the synapse. Some factors could affect both probes roughly equally: regions with high density of endocytic adaptor molecules (Blanpied et al., 2002; Petralia et al., 2003; Racz et al., 2004), zones of dense cortical cytoskeleton (He et al., 2016), sites of plasma membrane-ER apposition (Spacek and Harris, 1997). In addition, puncta adherens or clusters of adhesion molecules (Perez de Arce et al., 2015) may slow transit of all TM proteins. Less frequently, undetected regions could exist that would selectively affect the

binding probe. For example, small and low-density regions below the PSD detection criteria (<10 molecules and <30 nm in diameter) could be situated within nanometers of the detected PSD border. These could come from small segments of multi-segmented PSDs (Spacek and Hartmann, 1983; Stewart et al., 2005), but these types of PSDs are rare. In addition, though the density of PSD-95 outside the PSD border is quite low (Zhang and Diamond, 2009; Perez de Arce et al., 2015), its extrasynaptic mobility has not been measured and there may be enough PSD-95 in the perisynaptic region to bind and immobilize the binding probes. We speculate that the overall extrasynaptic diffusion of both probes are not different because few extrasynaptic regions selectively affect the binding probe but not the nonbinding probe.

Role of Crowding in Synaptic Plasticity

The many types and time scales of ongoing and triggered PSD plasticity that have been documented (Okabe et al., 1999; Blanpied et al., 2008; MacGillavry et al., 2013; Bosch et al., 2014) suggest that PSD reorganization during plasticity will affect accumulation not just of TM proteins like AMPARs but additional molecules contributing to crowding as well. For instance, PSD-95 content in spines has been shown to decrease transiently after an LTP induction protocol in hippocampal slice cultures (Steiner et al., 2008). This may directly lead to loss of AMPARs as their binding partners are lost. However, the loss of PSD-95 may decrease crowding, which could prompt a net loss of even TM proteins with minimal direct binding to PSD-95 (e.g., desensitized AMPARs uncoupled from stargazin Constals et al., 2015). This further loss of molecular crowders could then further facilitate receptor exit. However, whether the transient loss of spine PSD-95 reflects a disruption of high-density areas of the synapse is unknown.

On the other hand, speculating further, if the transient decrease in synaptic PSD-95 during LTP induction reflects primarily loss from the PSD edge, and thus is not correlated with significant de-crowding at high-density regions, then the continued presence of additional nonbinding proteins at these high-density regions could in fact obstruct the entry of AMPARs to these regions and limit the changes in AMPARs level, at least over certain kinetic phases. Thus, it would be tempting to speculate in this case that the nonbinding proteins could affect LTP induction kinetics but not maintenance, as morphing dynamics and internal mixing of the PSD would eventually enable synapses to reach their new steady state capacity of AMPARs on a time scale of minutes. Resolving these many possibilities in the future will require close examination of the kinetics of protein redistribution and exchange during plasticity.

Advantages and Disadvantages of PALM-PAINT

PALM of the PSD border improves discrimination of those molecules definitively within the synapse proper. However, we suspect that the effect of crowding may have been underestimated in our analysis because spatial and temporal alignment of the uPAINT and PALM data was subject to residual errors that may have diminished a larger underlying effect. The two color channels faced an alignment error of ~6 nm, which would somewhat blur our measurement of regional PSD-95 density around individual tracked locations. In addition, the uPAINT data is subject to error stemming from the finite precision of individual localizations. The Atto647N we used for tracking is a relatively bright organic dye and helps to maximize this precision and thus minimize error in the estimate of D_{eff}. However, brighter, longer-lasting fluorophores could be advantageous. Nanobody-labeled small quantum dots (Wang et al., 2014) have been used to track AMPARs in and around synapses, and have the additional advantage of being so bright as to facilitate tracking in 3D (Cai et al., 2014). However, 3D mapping of the PSD would require high localization numbers and longer imaging durations (Legant et al., 2016; and see below), and the *z* resolution normally obtainable without 4pi detection is usually worse than 100 nm for fluorescent proteins, making this difficult to implement.

In our application of PALM-PAINT, there was only limited temporal relationship between individual tracks (generally lasting <1 s and the PALM map (aggregated over the imaging session of generally 4–6 min)). Though lateral drift was corrected during this time (to an error we estimated as <10 nm), ongoing morphing and internal reorganization of the PSD (Kerr and Blanpied, 2012; MacGillavry et al., 2013) presumably degraded many details of the PSD-95 distribution in our final images. The reduced precision in capturing the true regional density of PSD-95 molecules would diminish the difference we saw between probes in different regional densities, and also reduce the difference between binding and nonbinding probe. Further, probes in a similar subsynaptic space but tracked early vs. late in the mapping might have not truly experienced the same degree of steric hindrance. However, the differences we observed were robust even in the face of these errors. Ideally, to capture the true effect size, one would need to monitor lateral drift continuously (Bon et al., 2015) and achieve more rapid mapping (Huang et al., 2013). However, in structures with low protein copy number, a large fraction of the proteins must be mapped to achieve statistical reliability (MacGillavry et al., 2013; Legant et al., 2016), which may preclude time-lapse imaging except if the protein exchange rate is high compared to the photobleaching rate induced by imaging.

We hope the combined approach of PALM-PAINT will help answer many key questions regarding synapse architecture and plasticity. One key issue is what mechanisms assemble the particular organization of PSD-95, a pattern that appears to dictate receptor number and position (Opazo et al., 2012). One possibility is that the more deeply positioned multi-domain proteins in the PSD, such as the Shank and GKAP families (Valtschanoff and Weinberg, 2001; Dani et al., 2010), may establish a platform of loose spacing with which the more superficial proteins such as PSD-95 may interact (Chen et al., 2008). Interestingly, in this case, a close interaction of the deeper PSD with cytoskeleton (Frost et al., 2010; MacGillavry et al., 2016) may thus provide a link between activity-dependent plasticity of spine and PSD structure. Alternatively, cleft-resident

adhesion molecules have distinct organizational patterns (Perez de Arce et al., 2015; Chamma et al., 2016), that may guide intracellular protein organization in both the presynaptic and postsynaptic cells. Dissecting these possibilities, which require nanoscale resolution of position and mobility of multiple proteins, may be aided by future PALM-PAINT applications.

AUTHOR CONTRIBUTIONS

TPL and TAB designed research; TPL performed research and data analysis; TPL and TAB wrote the article.

FUNDING

This work was supported by the National Institutes of Health Grant F30MH102891 to TPL and R01MH080046 and R01MH096376 to TAB and the Kahlert Foundation to TAB.

ACKNOWLEDGMENTS

We thank Sridhar Raghavachari and members of the Thompson, Jurado, and Blanpied laboratories helpful discussion, and Minerva Contreras for help with cultures.

REFERENCES

Annibale, P., Vanni, S., Scarselli, M., Rothlisberger, U., and Radenovic, A. (2011). Identification of clustering artifacts in photoactivated localization microscopy. *Nat. Methods* 8, 527–528. doi: 10.1038/nmeth.1627

Bats, C., Groc, L., and Choquet, D. (2007). The interaction between Stargazin and PSD-95 regulates AMPA receptor surface trafficking. *Neuron* 53, 719–734. doi: 10.1016/j.neuron.2007.01.030

Betzig, E., Patterson, G. H., Sougrat, R., Lindwasser, O. W., Olenych, S., Bonifacino, J. S., et al. (2006). Imaging intracellular fluorescent proteins at nanometer resolution. *Science* 313, 1642–1645. doi: 10.1126/science.1127344

Blanpied, T. A., Kerr, J. M., and Ehlers, M. D. (2008). Structural plasticity with preserved topology in the postsynaptic protein network. *Proc. Natl. Acad. Sci. U S A* 105, 12587–12592. doi: 10.1073/pnas.0711669105

Blanpied, T. A., Scott, D. B., and Ehlers, M. D. (2002). Dynamics and regulation of clathrin coats at specialized endocytic zones of dendrites and spines. *Neuron* 36, 435–449. doi: 10.1016/s0896-6273(02)00979-0

Bon, P., Bourg, N., Lécart, S., Monneret, S., Fort, E., Wenger, J., et al. (2015). Three-dimensional nanometre localization of nanoparticles to enhance super-resolution microscopy. *Nat. Commun.* 6:7764. doi: 10.1038/ncomms8764

Bosch, M., Castro, J., Saneyoshi, T., Matsuno, H., Sur, M., and Hayashi, Y. (2014). Structural and molecular remodeling of dendritic spine substructures during long-term potentiation. *Neuron* 82, 444–459. doi: 10.1016/j.neuron.2014.03.021

Broadhead, M. J., Horrocks, M. H., Zhu, F., Muresan, L., Benavides-Piccione, R., DeFelipe, J., et al. (2016). PSD95 nanoclusters are postsynaptic building blocks in hippocampus circuits. *Sci. Rep.* 6:24626. doi: 10.1038/srep24626

Cai, E., Ge, P., Lee, S. H., Jeyifous, O., Wang, Y., Liu, Y., et al. (2014). Stable small quantum dots for synaptic receptor tracking on live neurons. *Angew. Chem. Int. Ed Engl.* 53, 12484–12488. doi: 10.1002/anie.201405735

Chamma, I., Letellier, M., Butler, C., Tessier, B., Lim, K. H., Gauthereau, I., et al. (2016). Mapping the dynamics and nanoscale organization of synaptic adhesion proteins using monomeric streptavidin. *Nat. Commun.* 7:10773. doi: 10.1038/ncomms10773

Chen, X., Winters, C., Azzam, R., Li, X., Galbraith, J. A., Leapman, R. D., et al. (2008). Organization of the core structure of the postsynaptic density. *Proc. Natl. Acad. Sci. U S A* 105, 4453–4458. doi: 10.1073/pnas.0800897105

Cho, C. H., St-Gelais, F., Zhang, W., Tomita, S., and Howe, J. R. (2007). Two families of TARP isoforms that have distinct effects on the kinetic properties of AMPA receptors and synaptic currents. *Neuron* 55, 890–904. doi: 10.1016/j.neuron.2007.08.024

Choquet, D., and Triller, A. (2013). The dynamic synapse. *Neuron* 80, 691–703. doi: 10.1016/j.neuron.2013.10.013

Constals, A., Penn, A. C., Compans, B., Toulmé, E., Phillipat, A., Marais, S., et al. (2015). Glutamate-induced AMPA receptor desensitization increases their mobility and modulates short-term plasticity through unbinding from Stargazin. *Neuron* 85, 787–803. doi: 10.1016/j.neuron.2015.01.012

Dani, A., Huang, B., Bergan, J., Dulac, C., and Zhuang, X. (2010). Superresolution imaging of chemical synapses in the brain. *Neuron* 68, 843–856. doi: 10.1016/j.neuron.2010.11.021

de Wit, J., Sylwestrak, E., O'Sullivan, M. L., Otto, S., Tiglio, K., Savas, J. N., et al. (2009). LRRTM2 interacts with Neurexin1 and regulates excitatory synapse formation. *Neuron* 64, 799–806. doi: 10.1016/j.neuron.2009.12.019

Dupuis, J. P., Ladépêche, L., Seth, H., Bard, L., Varela, J., Mikasova, L., et al. (2014). Surface dynamics of GluN2B-NMDA receptors controls plasticity of maturing glutamate synapses. *EMBO J.* 33, 842–861. doi: 10.1002/embj.201386356

Ehlers, M. D., Heine, M., Groc, L., Lee, M. C., and Choquet, D. (2007). Diffusional trapping of GluR1 AMPA receptors by input-specific synaptic activity. *Neuron* 54, 447–460. doi: 10.1016/j.neuron.2007.04.010

Erlenhardt, N., Yu, H., Abiraman, K., Yamasaki, T., Wadiche, J. I., Tomita, S., et al. (2016). Porcupine controls hippocampal AMPAR levels, composition and synaptic transmission. *Cell Rep.* 14, 782–794. doi: 10.1016/j.celrep.2015.12.078

Freche, D., Pannasch, U., Rouach, N., and Holcman, D. (2011). Synapse geometry and receptor dynamics modulate synaptic strength. *PLoS One* 6:e25122. doi: 10.1371/journal.pone.0025122

Frick, M., Schmidt, K., and Nichols, B. J. (2007). Modulation of lateral diffusion in the plasma membrane by protein density. *Curr. Biol.* 17, 462–467. doi: 10.1016/j.cub.2007.01.069

Frost, N. A., Shroff, H., Kong, H., Betzig, E., and Blanpied, T. A. (2010). Single-molecule discrimination of discrete perisynaptic and distributed sites of actin filament assembly within dendritic spines. *Neuron* 67, 86–99. doi: 10.1016/j.neuron.2010.05.026

Fukata, Y., Dimitrov, A., Boncompain, G., Vielemeyer, O., Perez, F., and Fukata, M. (2013). Local palmitoylation cycles define activity-regulated postsynaptic subdomains. *J. Cell Biol.* 202, 145–161. doi: 10.1083/jcb.201302071

Giannone, G., Hosy, E., Levet, F., Constals, A., Schulze, K., Sobolevsky, A. I., et al. (2010). Dynamic superresolution imaging of endogenous proteins on living cells at ultra-high density. *Biophys. J.* 99, 1303–1310. doi: 10.1016/j.bpj.2010.06.005

Groc, L., Lafourcade, M., Heine, M., Renner, M., Racine, V., Sibarita, J. B., et al. (2007). Surface trafficking of neurotransmitter receptor: comparison between single-molecule/quantum dot strategies. *J. Neurosci.* 27, 12433–12437. doi: 10.1523/jneurosci.3349-07.2007

Harris, K. M., and Stevens, J. K. (1989). Dendritic spines of CA 1 pyramidal cells in the rat hippocampus: serial electron microscopy with reference to their biophysical characteristics. *J. Neurosci.* 9, 2982–2997.

Harris, K. M., and Weinberg, R. J. (2012). Ultrastructure of synapses in the mammalian brain. *Cold Spring Harb. Perspect. Biol.* 4:a005587. doi: 10.1101/cshperspect.a005587

He, J., Zhou, R., Wu, Z., Carrasco, M. A., Kurshan, P. T., Farley, J. E., et al. (2016). Prevalent presence of periodic actin-spectrin-based membrane skeleton in a broad range of neuronal cell types and animal species. *Proc. Natl. Acad. Sci. U S A* 113, 6029–6034. doi: 10.1073/pnas.1605707113

Hess, S. T., Girirajan, T. P., and Mason, M. D. (2006). Ultra-high resolution imaging by fluorescence photoactivation localization microscopy. *Biophys. J.* 91, 4258–4272. doi: 10.1529/biophysj.106.091116

Hoze, N., Nair, D., Hosy, E., Sieben, C., Manley, S., Herrmann, A., et al. (2012). Heterogeneity of AMPA receptor trafficking and molecular interactions revealed by superresolution analysis of live cell imaging. *Proc. Natl. Acad. Sci. U S A* 109, 17052–17057. doi: 10.1073/pnas.1204589109

Huang, F., Hartwich, T. M., Rivera-Molina, F. E., Lin, Y., Duim, W. C., Long, J. J., et al. (2013). Video-rate nanoscopy using sCMOS camera-specific single-molecule localization algorithms. *Nat. Methods* 10, 653–658. doi: 10.1038/nmeth.2488

Huganir, R. L., and Nicoll, R. A. (2013). AMPARs and synaptic plasticity: the last 25 years. *Neuron* 80, 704–717. doi: 10.1016/j.neuron.2013.10.025

Husi, H., Ward, M. A., Choudhary, J. S., Blackstock, W. P., and Grant, S. G. (2000). Proteomic analysis of NMDA receptor-adhesion protein signaling complexes. *Nat. Neurosci.* 3, 661–669. doi: 10.1038/76615

Inoue, A., and Okabe, S. (2003). The dynamic organization of postsynaptic proteins: translocating molecules regulate synaptic function. *Curr. Opin. Neurobiol.* 13, 332–340. doi: 10.1016/s0959-4388(03)00077-1

Kalashnikova, E., Lorca, R. A., Kaur, I., Barisone, G. A., Li, B., Ishimaru, T., et al. (2010). SynDIG1: an activity-regulated, AMPA- receptor-interacting transmembrane protein that regulates excitatory synapse development. *Neuron* 65, 80–93. doi: 10.1016/j.neuron.2009.12.021

Kerr, J. M., and Blanpied, T. A. (2012). Subsynaptic AMPA receptor distribution is acutely regulated by actin-driven reorganization of the postsynaptic density. *J. Neurosci.* 32, 658–673. doi: 10.1523/JNEUROSCI.2927-11.2012

Kusumi, A., Tsunoyama, T. A., Hirosawa, K. M., Kasai, R. S., and Fujiwara, T. K. (2014). Tracking single molecules at work in living cells. *Nat. Chem. Biol.* 10, 524–532. doi: 10.1038/nchembio.1558

Legant, W. R., Shao, L., Grimm, J. B., Brown, T. A., Milkie, D. E., Avants, B. B., et al. (2016). High-density three-dimensional localization microscopy across large volumes. *Nat. Methods* 13, 359–365. doi: 10.1038/nmeth.3797

Levet, F., Hosy, E., Kechkar, A., Butler, C., Beghin, A., Choquet, D., et al. (2015). SR-Tesseler: a method to segment and quantify localization-based super-resolution microscopy data. *Nat. Methods* 12, 1065–1071. doi: 10.1038/nmeth.3579

Li, T. P., Song, Y., MacGillavry, H. D., Blanpied, T. A., and Raghavachari, S. (2016). Protein crowding within the postsynaptic density can impede the escape of membrane proteins. *J. Neurosci.* 36, 4276–4295. doi: 10.1523/JNEUROSCI.3154-15.2016

Lu, H. E., MacGillavry, H. D., Frost, N. A., and Blanpied, T. A. (2014). Multiple spatial and kinetic subpopulations of CaMKII in spines and dendrites as resolved by single-molecule tracking PALM. *J. Neurosci.* 34, 7600–7610. doi: 10.1523/JNEUROSCI.4364-13.2014

MacGillavry, H. D., Kerr, J. M., and Blanpied, T. A. (2011). Lateral organization of the postsynaptic density. *Mol. Cell. Neurosci.* 48, 321–331. doi: 10.1016/j.mcn.2011.09.001

MacGillavry, H. D., Kerr, J. M., Kassner, J., Frost, N. A., and Blanpied, T. A. (2016). Shank-cortactin interactions control actin dynamics to maintain flexibility of neuronal spines and synapses. *Eur. J. Neurosci.* 43, 179–193. doi: 10.1111/ejn.13129

MacGillavry, H. D., Song, Y., Raghavachari, S., and Blanpied, T. A. (2013). Nanoscale scaffolding domains within the postsynaptic density concentrate synaptic AMPA receptors. *Neuron* 78, 615–622. doi: 10.1016/j.neuron.2013.03.009

Manley, S., Gillette, J. M., Patterson, G. H., Shroff, H., Hess, H. F., Betzig, E., et al. (2008). High-density mapping of single-molecule trajectories with photoactivated localization microscopy. *Nat. Methods* 5, 155–157. doi: 10.1038/nmeth.1176

Nair, D., Hosy, E., Petersen, J. D., Constals, A., Giannone, G., Choquet, D., et al. (2013). Super-resolution imaging reveals that AMPA receptors inside synapses are dynamically organized in nanodomains regulated by PSD95. *J. Neurosci.* 33, 13204–13224. doi: 10.1523/JNEUROSCI.2381-12.2013

Okabe, S., Kim, H. D., Miwa, A., Kuriu, T., and Okado, H. (1999). Continual remodeling of postsynaptic density and its regulation by synaptic activity. *Nat. Neurosci.* 2, 804–811. doi: 10.1038/12175

Opazo, P., and Choquet, D. (2011). A three-step model for the synaptic recruitment of AMPA receptors. *Mol. Cell. Neurosci.* 46, 1–8. doi: 10.1016/j.mcn.2010.08.014

Opazo, P., Sainlos, M., and Choquet, D. (2012). Regulation of AMPA receptor surface diffusion by PSD-95 slots. *Curr. Opin. Neurobiol.* 22, 453–460. doi: 10.1016/j.conb.2011.10.010

Perez de Arce, K., Schrod, N., Metzbower, S. W., Allgeyer, E., Kong, G. K., Tang, A. H., et al. (2015). Topographic mapping of the synaptic cleft into adhesive nanodomains. *Neuron* 88, 1165–1172. doi: 10.1016/j.neuron.2015.11.011

Petralia, R. S., Wang, Y. X., and Wenthold, R. J. (2003). Internalization at glutamatergic synapses during development. *Eur. J. Neurosci.* 18, 3207–3217. doi: 10.1111/j.1460-9568.2003.03074.x

Racz, B., Blanpied, T. A., Ehlers, M. D., and Weinberg, R. J. (2004). Lateral organization of endocytic machinery in dendritic spines. *Nat. Neurosci.* 7, 917–918. doi: 10.1038/nn1303

Raghavachari, S., and Lisman, J. E. (2004). Properties of quantal transmission at CA1 synapses. *J. Neurophysiol.* 92, 2456–2467. doi: 10.1152/jn.00258.2004

Ryan, T. A., Myers, J., Holowka, D., Baird, B., and Webb, W. W. (1988). Molecular crowding on the cell surface. *Science* 239, 61–64. doi: 10.1126/science.2962287

Sainlos, M., Tigaret, C., Poujol, C., Olivier, N. B., Bard, L., Breillat, C., et al. (2011). Biomimetic divalent ligands for the acute disruption of synaptic AMPAR stabilization. *Nat. Chem. Biol.* 7, 81–91. doi: 10.1038/nchembio.498

Santamaria, F., Gonzalez, J., Augustine, G. J., and Raghavachari, S. (2010). Quantifying the effects of elastic collisions and non-covalent binding on glutamate receptor trafficking in the post-synaptic density. *PLoS Comput. Biol.* 6:e1000780. doi: 10.1371/journal.pcbi.1000780

Santucci, D. M., and Raghavachari, S. (2008). The effects of NR2 subunit-dependent NMDA receptor kinetics on synaptic transmission and CaMKII activation. *PLoS Comput. Biol.* 4:e1000208. doi: 10.1371/journal.pcbi.1000208

Savin, T., and Doyle, P. S. (2005). Static and dynamic errors in particle tracking microrheology. *Biophys. J.* 88, 623–638. doi: 10.1529/biophysj.104.042457

Saxton, M. J. (1994). Anomalous diffusion due to obstacles: a monte carlo study. *Biophys. J.* 66, 394–401. doi: 10.1016/s0006-3495(94)80789-1

Schikorski, T., and Stevens, C. F. (1997). Quantitative ultrastructural analysis of hippocampal excitatory synapses. *J. Neurosci.* 17, 5858–5867.

Sheng, M., and Hoogenraad, C. C. (2007). The postsynaptic architecture of excitatory synapses: a more quantitative view. *Annu. Rev. Biochem.* 76, 823–847. doi: 10.1146/annurev.biochem.76.060805.160029

Shinohara, Y., Hirase, H., Watanabe, M., Itakura, M., Takahashi, M., and Shigemoto, R. (2008). Left-right asymmetry of the hippocampal synapses with differential subunit allocation of glutamate receptors. *Proc. Natl. Acad. Sci. U S A* 105, 19498–19503. doi: 10.1073/pnas.0807461105

Soto, D., Coombs, I. D., Renzi, M., Zonouzi, M., Farrant, M., and Cull-Candy, S. G. (2009). Selective regulation of long-form calcium-permeable AMPA receptors by an atypical TARP, gamma-5. *Nat. Neurosci.* 12, 277–285. doi: 10.1038/nn.2266

Spacek, J., and Harris, K. M. (1997). Three-dimensional organization of smooth endoplasmic reticulum in hippocampal CA1 dendrites and dendritic spines of the immature and mature rat. *J. Neurosci.* 17, 190–203.

Spacek, J., and Hartmann, M. (1983). Three-dimensional analysis of dendritic spines. I. Quantitative observations related to dendritic spine and synaptic morphology in cerebral and cerebellar cortices. *Anat. Embryol. (Berl)* 167, 289–310. doi: 10.1007/bf00298517

Steiner, P., Higley, M. J., Xu, W., Czervionke, B. L., Malenka, R. C., and Sabatini, B. L. (2008). Destabilization of the postsynaptic density by PSD-95 serine 73 phosphorylation inhibits spine growth and synaptic plasticity. *Neuron* 60, 788–802. doi: 10.1016/j.neuron.2008.10.014

Stewart, M. G., Medvedev, N. I., Popov, V. I., Schoepfer, R., Davies, H. A., Murphy, K., et al. (2005). Chemically induced long-term potentiation increases the number of perforated and complex postsynaptic densities but does not alter dendritic spine volume in CA1 of adult mouse hippocampal slices. *Eur. J. Neurosci.* 21, 3368–3378. doi: 10.1111/j.1460-9568.2005.04174.x

Tang, A.-H., Chen, H., Li, T. P., Metzbower, S. R., MacGillavry, H. D., and Blanpied, T. A. (in press). A transsynaptic nanocolumn aligns neuotransmitter release to receptors. *Nature*

Thompson, R. E., Larson, D. R., and Webb, W. W. (2002). Precise nanometer localization analysis for individual fluorescent probes. *Biophys. J.* 82, 2775–2783. doi: 10.1016/s0006-3495(02)75618-x

Tomita, S., Chen, L., Kawasaki, Y., Petralia, R. S., Wenthold, R. J., Nicoll, R. A., et al. (2003). Functional studies and distribution define a family of transmembrane AMPA receptor regulatory proteins. *J. Cell Biol.* 161, 805–816. doi: 10.1083/jcb.200212116

Uchida, N., Honjo, Y., Johnson, K. R., Wheelock, M. J., and Takeichi, M. (1996). The catenin/cadherin adhesion system is localized in synaptic junctions bordering transmitter release zones. *J. Cell Biol.* 135, 767–779. doi: 10.1083/jcb.135.3.767

Valtschanoff, J. G., and Weinberg, R. J. (2001). Laminar organization of the NMDA receptor complex within the postsynaptic density. *J. Neurosci.* 21, 1211–1217.

von Engelhardt, J., Mack, V., Sprengel, R., Kavenstock, N., Li, K. W., Stern-Bach, Y., et al. (2010). CKAMP44: a brain-specific protein attenuating short-term synaptic plasticity in the dentate gyrus. *Science* 327, 1518–1522. doi: 10.1126/science.1184178

Wang, Y., Cai, E., Rosenkranz, T., Ge, P., Teng, K. W., Lim, S. J., et al. (2014). Small quantum dots conjugated to nanobodies as immunofluorescence probes for nanometric microscopy. *Bioconjug. Chem.* 25, 2205–2211. doi: 10.1021/bc5004179

Xie, X., Liaw, J.-S., Baudry, M., and Berger, T. W. (1997). Novel expression mechanism for synaptic potentiation: alignment of presynaptic release site and postsynaptic receptor. *Proc. Natl. Acad. Sci. U S A* 94, 6983–6988. doi: 10.1073/pnas.94.13.6983

Zhang, J., and Diamond, J. S. (2009). Subunit- and pathway-specific localization of NMDA receptors and scaffolding proteins at ganglion cell synapses in rat retina. *J. Neurosci.* 29, 4274–4286. doi: 10.1523/JNEUROSCI.5602-08.2009

Conflict of Interest Statement: The authors declare that the research was conducted in the absence of any commercial or financial relationships that could be construed as a potential conflict of interest.

frontiers in Synaptic Neuroscience

REVIEW
published: 28 July 2016
doi: 10.3389/fnsyn.2016.00020

The Emergence of NMDA Receptor Metabotropic Function: Insights from Imaging

Kim Dore[1], *Jonathan Aow*[2] *and Roberto Malinow*[1]*

[1] Center for Neural Circuits and Behavior, Department of Neuroscience and Section for Neurobiology, Division of Biology, University of California at San Diego, San Diego, CA, USA, [2] Genome Institute of Singapore, Singapore, Singapore

The NMDA receptor (R) participates in many important physiological and pathological processes. For example, its activation is required for both long-term potentiation (LTP) and long-term depression (LTD) of synaptic transmission, cellular models of learning and memory. Furthermore, it may play a role in the actions of amyloid-beta on synapses as well as in the signaling leading to cell death following stroke. Until recently, these processes were thought to be mediated by ion-flux through the receptor. Using a combination of imaging and electrophysiological approaches, ion-flux independent functions of the NMDAR were recently examined. In this review, we will discuss the role of metabotropic NMDAR function in LTD and synaptic dysfunction.

Keywords: ion-flux independent, FRET-FLIM, long-term depression (LTD), NMDAR interactions with CaMKII, amyloid-beta induced depression, PP1, excitotoxicity

INTRODUCTION

Transmembrane receptors have traditionally been divided into two classes: ionotropic and metabotropic. Ionotropic glutamate receptors (iGluRs) form channels that allow the passage of ions into the cell to drive signaling, while metabotropic glutamate receptors (mGluRs) generate downstream effects without ion-flux. The boundary between these two classes is not completely distinct, as there has been evidence that several iGluRs are capable of producing effects in the absence of ion-flux. For example, the N-terminal domain of GluA2, a subunit of the AMPA receptor (AMPAR), is sufficient to promote spine formation in hippocampal neurons (Passafaro et al., 2003). Another iGluR, the kainate receptor, can modulate GABA transmission without ion-flux (Rodríguez-Moreno and Lerma, 1998).

The NMDA receptor (NMDAR), a member of the iGluR family, is ubiquitously expressed and plays numerous roles in the brain (Traynelis et al., 2010). Given its ability to conduct calcium ions (Ca^{2+}) well, it has been assumed that downstream signaling triggered by NMDARs was mediated by Ca^{2+} influx and increased cytoplasmic Ca^{2+}. However, to allow Ca^{2+} entry through the receptor, several conditions have to be fulfilled: (1) glutamate must bind to GluN2 subunits; (2) glycine, the co-agonist must bind to GluN1 subunits; and (3) neurons must be sufficiently depolarized to eliminate the voltage-dependent magnesium ion (Mg^{2+}) block of the channel. During high-frequency stimulation (HFS) these three conditions are met resulting in long-term potentiation (LTP; Bliss and Collingridge, 1993). For long-term depression (LTD), however, the role of the NMDAR is not as clear. A long-standing model has proposed that while LTP requires a large increase in cytoplasmic Ca^{2+}, a moderate rise in cytoplasmic Ca^{2+} would produce LTD (Lisman, 1989; Malenka, 1994). However, several recent studies indicate that NMDARs can induce LTD without ion-flow through the receptor

OPEN ACCESS

Edited by:
George Augustine,
Nanyang Technological University,
Singapore

Reviewed by:
Kei Cho,
University of Bristol, UK
William N. Green,
University of Chicago, USA

***Correspondence:**
Roberto Malinow
rmalinow@ucsd.edu

Received: 25 April 2016
Accepted: 06 July 2016
Published: 28 July 2016

Citation:
Dore K, Aow J and Malinow R (2016) The Emergence of NMDA Receptor Metabotropic Function: Insights from Imaging. Front. Synaptic Neurosci. 8:20. doi: 10.3389/fnsyn.2016.00020

(Nabavi et al., 2013; Dore et al., 2015; Stein et al., 2015; Carter and Jahr, 2016). Other publications have shown that excitotoxicity as well as amyloid-beta-induced synaptic depression depend on NMDAR activity but are likewise independent of ion-flow (Kessels et al., 2013; Tamburri et al., 2013; Birnbaum et al., 2015; Weilinger et al., 2016). In this review, we will discuss how these studies probed NMDAR metabotropic activity with an emphasis on the imaging techniques used.

NMDAR-DEPENDENT LTD CAN BE INDUCED INDEPENDENTLY OF ION-FLUX

Interestingly, evidence for ion-flux independent LTD can be observed in data from older literature. Over 20 years ago, data were published indicating that MK-801, which blocks NMDAR channels, blocked LTP but failed to block LTD (Mayford et al., 1995). A similar effect was obtained by a different group (Scanziani et al., 1996). Surprisingly, these observations were not discussed in either study. The ion-flux dependence of LTD was recently examined more closely (Nabavi et al., 2013). Low-frequency stimulation (LFS) produced LTD in the presence of either MK-801 or 7-chloro-kynurenate (7CK, a competitive GluN1 antagonist; see **Figure 1A**) but not APV (a competitive GluN2 antagonist); all three antagonists effectively blocked ion-flux through the NMDAR. Moreover, LTD was observed in experiments in which intracellular Ca^{2+} was clamped to basal levels, suggesting that a rise in intracellular Ca^{2+} is not required for LTD. It was thus proposed that glutamate binding to the NMDAR could induce a conformational change in the cytoplasmic domain of the NMDAR that triggers downstream signaling resulting in LTD.

To test if ligand binding could drive movement of the NMDAR intracellular domain, FRET-FLIM [Forster resonance energy transfer measured by fluorescence lifetime imaging of the FRET donor, see **Toolbox** and (Wallrabe and Periasamy, 2005; Yasuda, 2006)] was employed (Dore et al., 2015). Recombinant GluN1 subunits of the NMDAR were tagged with GFP or mCherry at their carboxyl(c)-terminus and co-expressed in neurons. As the magnitude of FRET is very sensitive to the distance and orientation of the interacting fluorophores, nanometer-scale changes in distance can be reliably detected. Bath application or uncaging of glutamate in the presence of MK-801 or 7CK, but not APV, produced a transient change in FRET consistent with conformational movement of the NMDAR cytoplasmic domain (**Figure 1B**). Infusing neurons with a GluN1 c-terminus antibody through a patch pipette blocked the ligand-driven FRET change as well as LTD, suggesting that this conformational change is required for LTD induction.

Downstream signaling events were also examined using FRET-FLIM (Aow et al., 2015). Protein-phosphatase 1 (PP1) is one of the first molecules whose activity was shown to be required for LTD (Mulkey et al., 1993) and it co-immunoprecipitates with the NMDAR complex (Husi et al., 2000). FRET between GluN1-GFP and PP1-mCherry, observed in baseline conditions, was transiently reduced during chemical LTD induction. This ligand-driven decrease in FRET required NMDAR conformational movement but not PP1 activity (Aow et al., 2015). It is possible that the transient movement of PP1 relative to the NMDAR cytoplasmic domain exposes the catalytic active site of PP1 to a target unavailable under basal conditions. One potential target is calcium-calmodulin dependent protein kinase II (CaMKII; Strack et al., 1997), which is recruited to the NMDAR complex during LTP stimuli (Otmakhov et al., 2004) and whose activity is required for both LTP (Malenka et al., 1989; Malinow et al., 1989; Silva et al., 1992) and LTD (Coultrap et al., 2014). By monitoring FRET between fluorescently-tagged GluN1 and CaMKII, a delayed decrease in the NMDAR-CaMKII interaction was observed during ion-flux independent LTD (Aow et al., 2015). This effect depended on PP1 activity and was not seen with a CaMKII mutant that cannot be dephosphorylated at Thr-286 (CaMKII-Thr-286-Asp), suggesting that dephosphorylation of Thr-286 is necessary to modify the NMDAR-CaMKII interaction (Aow et al., 2015). Co-immunoprecipitation experiments additionally revealed that the amount of total CaMKII bound to the NMDAR was unaffected by ion-flow independent LTD, whereas levels of phosphorylated Thr-286 were reduced both during and after LTD induction (Aow et al., 2015). These results are consistent with a model for ion-flux independent LTD in which glutamate binding to the NMDAR induces a conformational change in the NMDAR intracellular domain that facilitates PP1 access to and dephosphorylation of CaMKII at Thr-286, thereby repositioning the CaMKII holoenzyme within the NMDAR complex. The relocated CaMKII could in turn potentially act on a novel site of the GluA1 subunit (Ser-567) that undergoes phosphorylation during LTD (Coultrap et al., 2014). Consistent with this model, CaMKII phosphorylation of GluA1-Ser-567 does not require Ca^{2+} or calmodulin (Coultrap et al., 2014). Ultimately, this process could increase AMPAR endocytosis (Lüscher et al., 1999; Lin et al., 2000; Kim et al., 2001; Shi et al., 2001) and lead to depressed synaptic transmission.

Ion-flow independent NMDAR activation of downstream signaling pathways has also been linked to shrinkage of dendritic spines (Stein et al., 2015). Stein et al. used 2-photon laser scanning microscopy (TPLSM) to monitor structural changes in the dendritic spines of GFP-expressing hippocampal neurons. Low-frequency uncaging of glutamate produced a ∼20% decrease in spine size that was independent of ion-flow through the NMDAR (**Figure 1C**). While high-frequency glutamate uncaging produced an increase in spine volume, the same stimulus in the presence of either 7CK or MK-801 led to spine shrinkage. This result is consistent with the finding that HFS (delivered electrically) in the presence of MK-801 produces LTD instead of LTP (Nabavi et al., 2013). Spine shrinkage was also abolished when p38 MAPK activity was blocked (Stein et al., 2015), which is again consistent with the observation that levels of phosphorylated p38 (which is the active form) were increased during ion-flow independent LTD (Nabavi et al., 2013). In the future, it will

be important to elucidate how the initial movement in the NMDAR cytoplasmic domain subsequently affects signaling molecules, such as cofilin, calcineurin and p38, implicated in LTD.

An ion-flux-independent mechanism for NMDAR-dependent LTD has been challenged by some recent studies (Babiec et al., 2014; Volianskis et al., 2015; Sanderson et al., 2016) but confirmed by others (Kim et al., 2015; Stein et al., 2015; Carter and Jahr, 2016). It is notable that the experimental conditions used in these recent studies that failed to detect ion-flux-independent LTD were not identical to those supporting this form of LTD. For instance, NMDAR antagonists were typically acutely washed in and then out of the preparation during LTD induction (Volianskis et al., 2015), instead of being present throughout the experimental duration. Furthermore, control pathways, which monitor transmission onto the same neurons but do not receive the conditioning stimulus, were generally not included (Babiec et al., 2014; Volianskis et al., 2015; Sanderson et al., 2016). These differences in methodology are significant and can make an impact in the outcome and interpretation of results (Nabavi et al., 2014). Therefore, it will be important to compare carefully the experimental conditions employed by different studies. Nevertheless, it remains possible that two different, independent

TOOLBOX | FRET measurements using fluorescence lifetime imaging microscopy.

FRET is a non-radiative energy transfer mechanism between two fluorescent molecules. There are two main requirements for successful FRET. First the fluorescence emission of the FRET donor must overlap with the FRET acceptor absorption spectrum; and second, these fluorescent molecules must be no more than ~10 nm apart from each other (Lakowicz, 2006). This spatial requirement of FRET is very sensitive; it can thus be used as a "molecular ruler" to assess protein structure (Gustiananda et al., 2004) or to monitor subtle conformational changes (Dore et al., 2015).

FRET can be measured by acquiring a series of images in different combinations of excitation and emission channels or by photobleaching of the FRET acceptor. However, these methods are prone to errors and are generally not well suited for measurements in living cells expressing fluorescent proteins (Selvin, 2000; Yasuda, 2006; Piston and Kremers, 2007). Fluorescence lifetime is defined as the average time a molecule stays in its excited state before emitting a photon (**A**). Because lifetime is an intrinsic property of fluorophores, it is independent of experimental conditions such as concentration, excitation intensity and photobleaching (Lakowicz, 2006; Yasuda, 2006). Importantly, by adding an additional route for the donor fluorophore to return to ground state, the degree of FRET makes the fluorescence lifetime of the donor proportionally shorter (**A,B**). To measure fluorescence lifetimes, the most common approach is time correlated single photon counting (TCSPC; Becker et al., 2004) which calculates the time delay between the detection of fluorescence photons and laser excitation pulses (**B**). When TCSPC is combined with laser scanning microscopy, it is possible to obtain fluorescence lifetimes, and hence detect changes in donor-acceptor distances, at every pixel of an image (**B,C**).

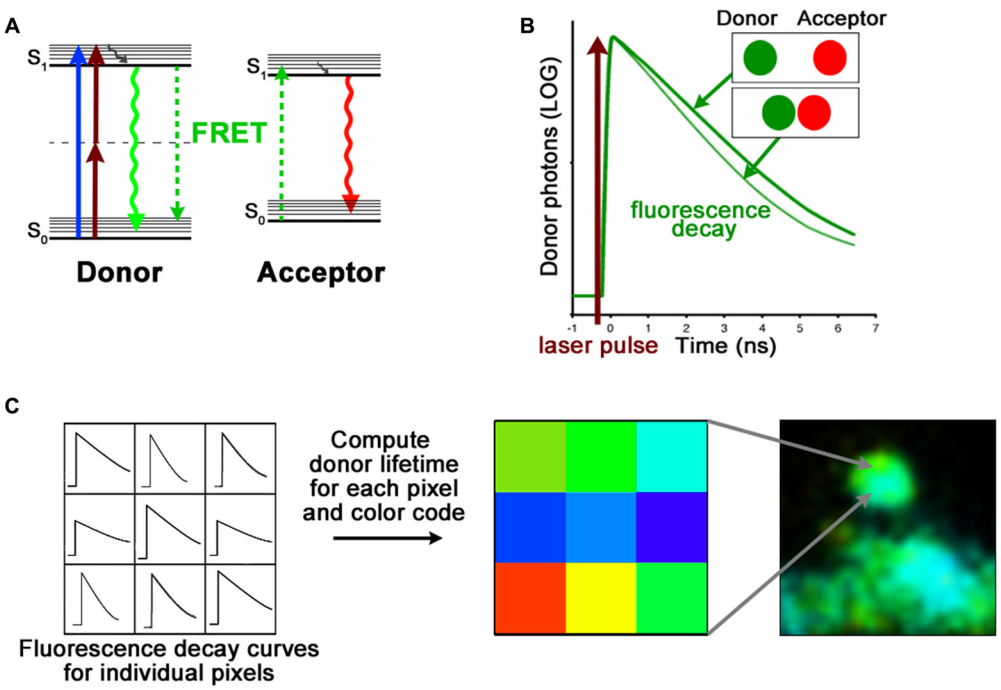

FRET-FLIM. (A) Jablonski diagram of FRET donor and acceptor energy levels. After excitation by a 1-photon (blue arrow) or 2-photon (brown arrows) laser, the FRET donor can return to ground state by emitting a photon (green arrow) or by transferring its energy to a nearby acceptor (dashed green arrows). **(B)** The fluorescence lifetime of the FRET donor, which becomes shorter with increased proximity of the FRET acceptor, is calculated with the fluorescence decay curve. **(C)** Time-correlated single photon counting (TCSPC) records fluorescence decay curves for each pixel of an image. By fitting these curves, the fluorescence lifetime of the FRET donor can be assessed. The FLIM image is then color coded according to the FRET donor lifetime at each pixel.

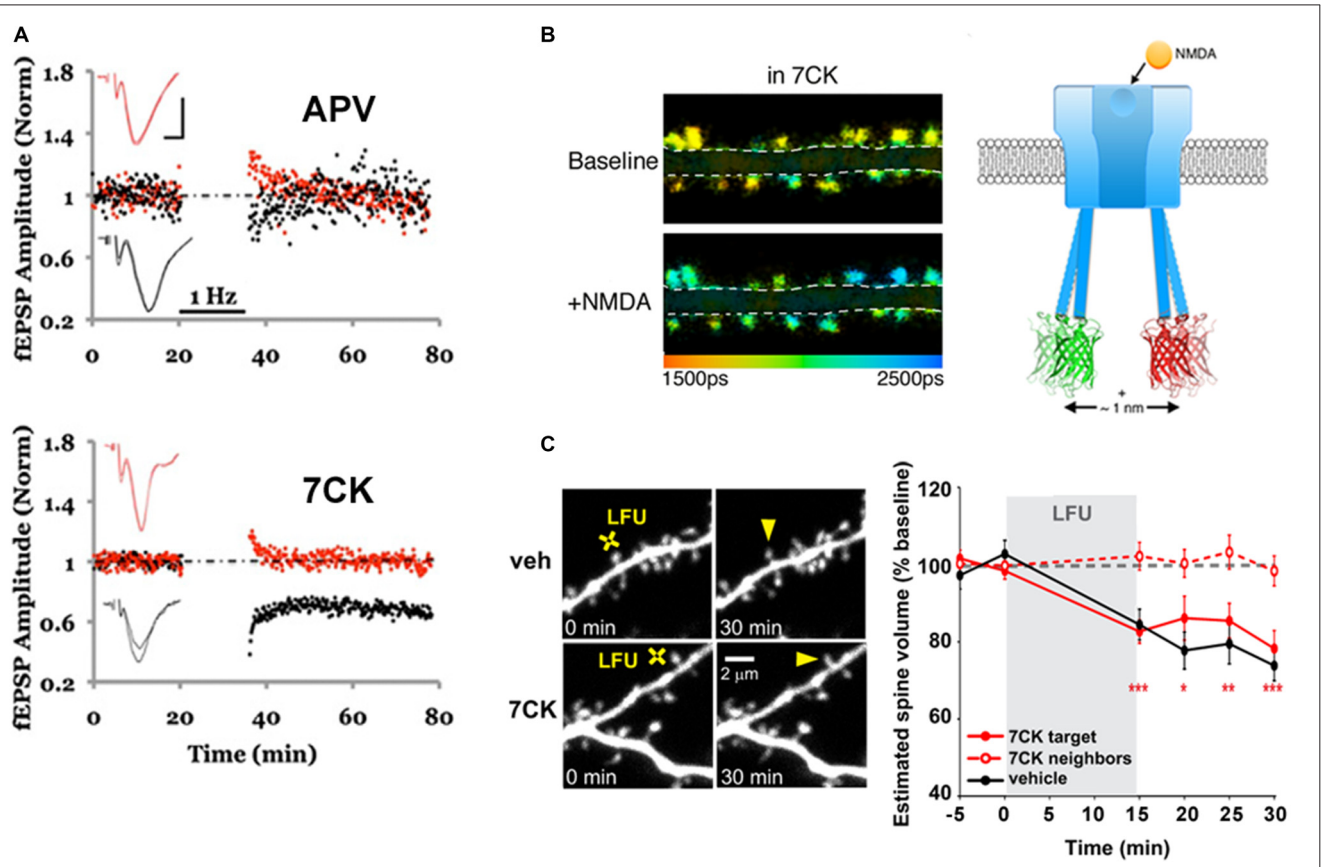

FIGURE 1 | Ion-flux independent long-term depression (LTD). (A) APV, but not 7-chloro-kynurenate (7CK), blocks LTD. LTD (1 Hz, black bar) was delivered to the test pathway (black symbols), while the control pathway (red symbols) received no stimulus; the slice was incubated in APV (top) or 7CK (bottom) throughout the experiment. Note that there was no change to the control or test pathway in APV, as expected, whereas the test pathway was significantly depressed after LTD induction in 7CK; representative of $N = 15$, APV, $p > 0.05$ LTD; $N = 15$, 7CK, $p < 0.01$ LTD. Insets: superimposed traces obtained before and after LTD in the test (black line) and control (red line) pathways. Scale bars 0.3 mV, 5 ms. Modified from Nabavi et al. (2013). **(B)** Chemical LTD induction (+NMDA) resulted in spines that exhibit less Förster Resonance Energy Transfer (FRET; and higher GFP fluorescence lifetimes; ps = picoseconds) between the GFP- and mCherry-tagged GluN1 subunits (see **Toolbox**), indicating movement of the NMDAR cytoplasmic domain. Modified from Dore et al. (2015). **(C)** A low frequency glutamate uncaging protocol (LFU), similar to the 1 Hz electrical stimulation in **(A)**, induced spine shrinkage both in vehicle or 7CK-incubated GFP-expressing neurons, indicating that ion-flux through the NMDAR is not required for spine shrinkage. Modified from Stein et al. (2015).

forms of NMDAR-dependent LTD exist: one that requires ion-flow through NMDARs and one that does not. Different experimental conditions could selectively recruit either of these two forms.

TRAFFICKING OF NMDAR IS REGULATED BY SYNAPTIC ACTIVITY BUT NOT ION-FLUX

In addition to its more recently described role in LTD, a few older studies have indicated that ligand binding to the NMDAR, in the absence of ion-flux, could control NMDAR trafficking (Vissel et al., 2001; Barria and Malinow, 2002; Nong et al., 2003). The Westbrook lab showed that even with its pore blocked, ligand binding to the NMDAR drove tyrosine dephosphorylation of GluN2A subunits, resulting in NMDAR endocytosis and decreased NMDA currents. Another group separately observed that an initial application of glycine was sufficient to prime NMDARs for subsequent use-dependent endocytosis, again leading to a decline in NMDA currents (Nong et al., 2003). Moreover, synaptic replacement of GluN2B- with GluN2A-containing NMDARs, an important developmentally controlled process (Hestrin, 1992; Monyer et al., 1994; Sheng et al., 1994; Stocca and Vicini, 1998; Tovar and Westbrook, 1999), required ligand binding without ion flux (Barria and Malinow, 2002). Interestingly, the replacement of synaptic GluN2B-containing NMDARs by newly synthetized GluN2B-containing NMDARs did not require ligand binding. It is important to note that these effects on NMDAR trafficking required both agonist and co-agonist binding to NMDARs as they were blocked by antagonists to the glutamate binding site on GluN2 subunits or to the glycine binding site on GluN1 subunits (Vissel et al., 2001; Barria and Malinow, 2002; Nong et al., 2003); in contrast, LTD only requires ligand binding to GluN2 subunits (Nabavi et al., 2013).

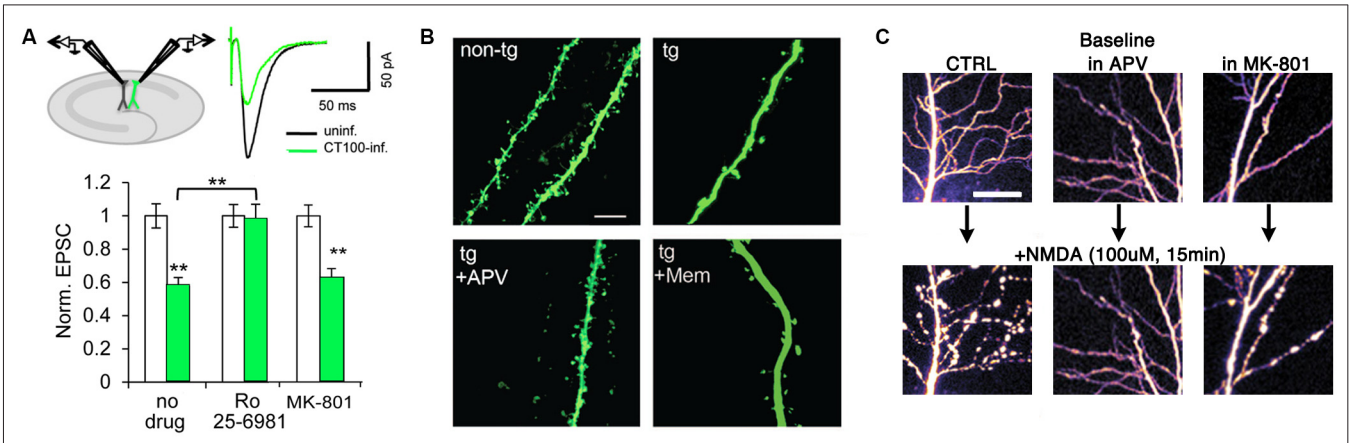

FIGURE 2 | Metabotropic NMDAR activity can induce synaptic dysfunction. (A) APP-CT100 overexpression depresses synaptic transmission without ion-flux. Model figure for a dual whole-cell recording of an infected and a neighboring uninfected CA1 neuron (top left) and an example trace of evoked AMPA receptor (AMPAR) currents of such a recording (top right). Bottom, results from paired-recordings performed in ACSF containing no drug ($N = 41$), Ro 25-6981 ($N = 37$) or MK-801 ($N = 25$); **indicates $p < 0.001$. Modified from Kessels et al. (2013). **(B)** Spine density is reduced in a transgenic mouse model of Alzheimer's disease (AD), APV blocks the effect but not memantine. Scale bar, 5 μm. Modified from Birnbaum et al. (2015). **(C)** Sustained NMDA application causes excito-toxic insults to CA1 neurons in the form of blebbing of dendrites (left panels). This effect is blocked by APV and CGP-78608 (middle panels) but not MK-801 (right panels). Scale bar, 25 μm. Modified from Weilinger et al. (2016).

METABOTROPIC NMDAR ACTIVITY CAN INDUCE SYNAPTIC DYSFUNCTION

Recent results have suggested a role for metabotropic NMDAR activity in amyloid-beta mediated synaptic dysfunction, which may contribute to hippocampal deficits in Alzheimer's disease (AD) and precede neurological symptoms by a decade or more (Terry et al., 1991; Reiman et al., 1996). A number of studies using electrophysiology and imaging have reported that amyloid-beta impairs LTP, depresses synaptic transmission and induces synapse loss in various hippocampal preparations (Chapman et al., 1999; Larson et al., 1999; Walsh et al., 2002; Wang et al., 2002; Kamenetz et al., 2003; Snyder et al., 2005; Hsieh et al., 2006; Shankar et al., 2007; Wei et al., 2010; Birnbaum et al., 2015). The effect of intracellularly delivered amyloid-beta is not clear, as one report indicated synaptic depression (Ripoli et al., 2014) while another indicated synaptic potentiation (Whitcomb et al., 2015). In many of these studies the electrophysiological results could be corroborated using imaging. For instance, Wei et al. (2010) used TPLSM to show that GFP-filled dendritic spines close to axons or dendrites overexpressing amyloid-beta displayed a smaller increase in spine volume following a chemically-induced LTP protocol as compared to more distant spines, suggesting that secreted amyloid-beta impaired LTP. Hsieh et al. (2006) used TPLSM of AMPARs tagged with the pH-sensitive GFP-variant SEP (Super-Ecliptic-Phluorin) to measure surface AMPARs and found that amyloid-beta reduced surface GluA1 and GluA2. Likewise, immunostaining and imaging primary cultures treated with amyloid-beta revealed a reduction in surface NMDARs (Snyder et al., 2005) and AMPARs (Almeida et al., 2005; Alfonso et al., 2014). The decrease in synaptic AMPAR and NMDAR currents correlates, therefore, with a decrease in surface receptors as determined with optical techniques. Finally, several groups have shown using TPLSM or confocal microscopy that endogenously expressed or exogenously applied amyloid-beta reduces spine density in GFP-expressing neurons (Hsieh et al., 2006; Shrestha et al., 2006; Calabrese et al., 2007; Shankar et al., 2007; Wei et al., 2010; Zempel et al., 2010), which may explain the electrophysiologically observed decreased frequency of miniature excitatory postsynaptic currents (Kamenetz et al., 2003; Hsieh et al., 2006). Therefore, amyloid-beta induces synaptic insults that can be directly observed through imaging.

A mechanism proposed to account for synaptic impairment by amyloid-beta is enhanced ionotropic glutamate receptor endocytosis. Indeed, there is evidence that inhibiting endocytic signaling pathways or overexpressing mutant endocytic-resistant receptors can ameliorate the reduction in AMPAR and/or NMDAR currents (Snyder et al., 2005; Hsieh et al., 2006; Knafo et al., 2016). Notably, Kessels et al. (2013) reported that despite block of ion flux, not all NMDAR antagonists prevented amyloid-beta-induced depression of AMPAR-mediated transmission. The GluN2 antagonists (R)-CPP, Ro25-6981, and ifenprodil afforded a complete block; whereas the GluN1 antagonist 7CK and the NMDAR pore blocker MK-801 had no effect (**Figure 2A**; Kessels et al., 2013). Thus, the block of depression correlated with actions on different NMDAR subunits rather than block of ion-flux. In another model, amyloid-beta oligomers exogenously applied to organotypic hippocampal slices acutely depressed AMPAR-mediated transmission in a manner that was dependent on synaptic stimulation and NMDAR activation but not NMDAR ion-flux (Tamburri et al., 2013). Both studies therefore suggest that amyloid-beta activates a metabotropic NMDAR signaling pathway that depresses synaptic transmission. The evidence that this pathway could then be involved in eventual spine loss comes from three other studies using imaging techniques. Two studies (Shankar et al., 2007, 2008) showed using TPLSM that (R)-CPP

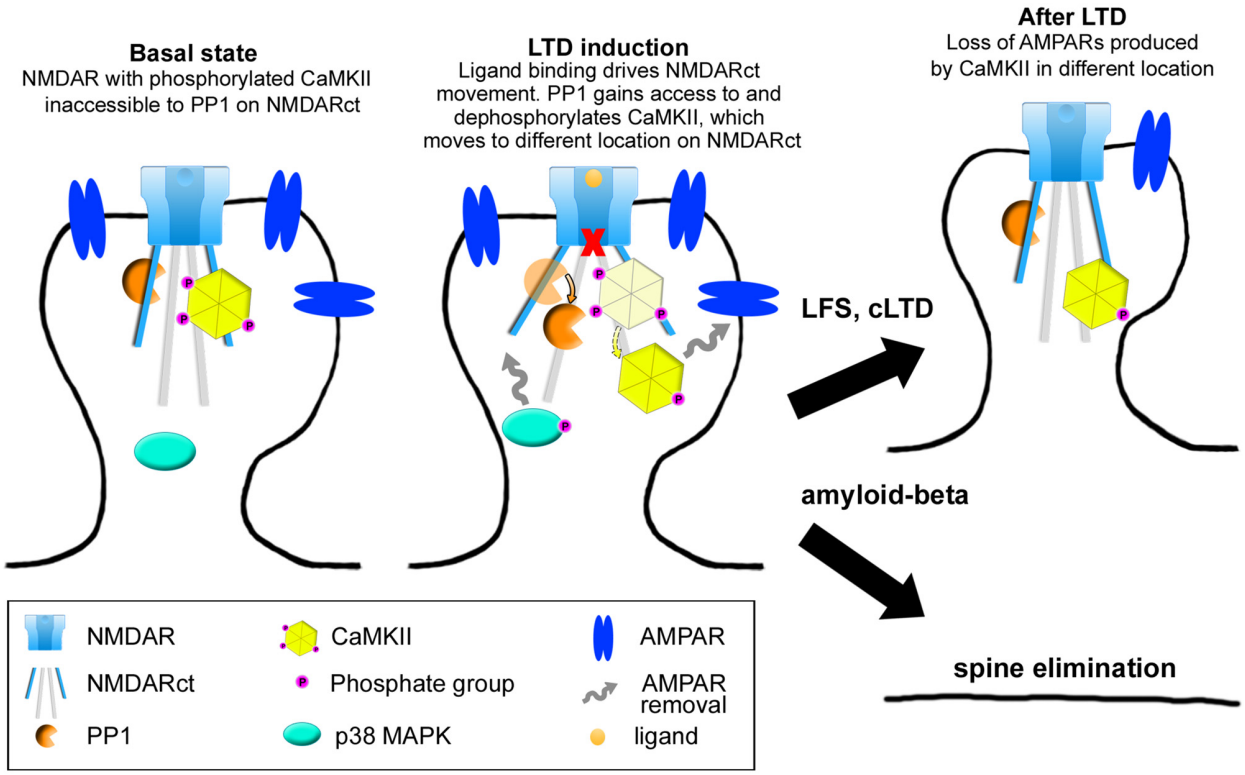

FIGURE 3 | Model of NMDAR metabotropic functions. In baseline conditions, the NMDAR interacts with both protein-phosphatase 1 (PP1) and calcium-calmodulin dependent protein kinase II (CaMKII) which is phosphorylated at Thr286. Upon ligand binding, movement in the NMDAR cytoplasmic domain permits PP1 catalytic access to phospho-CaMKII-T286, this movement also inducing activation and phosphorylation of p38 MAPK. These signaling molecules (along with others) will eventually lead to AMPAR removal. In the context of LTD, these events will produce spine shrinkage whereas in the case of sustained amyloid-beta presence, spine elimination will occur.

prevented amyloid-beta-induced spine loss in GFP-expressing organotypic slice neurons. Birnbaum et al. (2015) subsequently demonstrated that the competitive GluN2 antagonist APV also blocked spine loss in transgenic AD mice (as well as in hippocampal slices incubated in amyloid-beta oligomers), whilst MK-801, memantine, another NMDAR pore blocker, and buffering postsynaptic calcium ions with BAPTA had no effect (**Figure 2B**). That study (Birnbaum et al., 2015) also showed an amyloid-beta-induced reduction in PSD-95 and synaptophysin levels that was blocked by APV but not by MK-801 or memantine. Moreover, they demonstrated that p38 MAPK phosphorylation was increased by amyloid-beta in a NMDAR ion-flux independent manner and that spine loss depended on p38 MAPK activity (Birnbaum et al., 2015), supporting a link, previously examined (Hsieh et al., 2006), between LTD and amyloid-beta-induced depression. Taken together, these imaging results are in agreement with electrophysiological experiments and support the hypothesis that amyloid-beta toxicity depresses synaptic transmission via metabotropic NMDAR signaling that results in eventual spine loss.

The role of NMDARs in mediating excitotoxicity has been extensively described (reviewed in Choi, 1992), and it has been widely suggested that excessive Ca^{2+} influx through the receptor is responsible for inducing cell death (Choi, 1995; Tu et al., 2010). Interestingly, recent findings suggest that a metabotropic NMDAR "signalsome"—involving the NMDAR, the pannexin-1 channel (Panx1) and src kinase—is capable of inducing cellular dysfunction in response to excessive NMDAR stimulation (Weilinger et al., 2016). TPLSM was used to image fluorescently labeled CA1 neurons in acute rat hippocampal slices treated with a high dose of NMDA. This protocol induced blebbing in the dendrites of CA1 neurons as well as mitochondrial dysfunction, an effect that was blocked by co-application of the GluN1 antagonist CGP-78608 and APV, but not by MK-801, indicating that ligand binding to the NMDAR was capable of damaging neuronal morphology independently of ion flux through the receptor (**Figure 2C**). Interestingly, Panx1 channels appear to be located almost exclusively at the PSD (Zoidl et al., 2007), which suggests that this metabotropic NMDAR "signalsome" is synaptic. Additional experiments demonstrated that ligand binding, but not NMDAR ion flux, was necessary for downstream activation of Panx1 (Thompson et al., 2006, 2008; Weilinger et al., 2012). Metabotropic NMDAR activity did not change the degree of interaction between GluN1 and Panx1, but it did increase Src kinase binding to GluN1, Src activation, as well as Src-dependent phosphorylation

of Panx1. Peptides that either disrupted the GluN1-Src interaction (Src_{48}) or interfered with Panx1 phosphorylation (Tat-$Panx_{308}$) were neuroprotective *in vitro*, and injection of Tat-$Panx_{308}$ reduced brain lesion volume in an *in vivo* model of stroke. Indeed, as ischemia in the brain is believed to drive subsequent excitotoxicity, these results suggest that targeting Src or Panx1 in a clinical setting could be therapeutically effective.

CONCLUDING REMARKS

A number of studies have provided evidence that physiological and pathological processes can be triggered by ligand binding to the NMDAR, without requiring flow of ions through its pore. It will be important to determine conditions that control whether an ionotropic or metabotropic NMDAR mechanism is engaged during LTD. Ion-flux independent LTD appears to be mediated by a movement in the NMDAR cytoplasmic domain that affects its interactions with at least two signaling proteins, PP1 and CaMKII. Subsequent signaling, with increased p38 MAPK phosphorylation likely, leads to AMPAR removal, shrinkage of dendritic spines and depressed synaptic transmission (**Figure 3**). Interestingly, it seems that if the stimulus recruiting metabotropic NMDAR function is sustained, as in the contexts of amyloid-beta overproduction or excitotoxic conditions following ischemia, metabotropic NMDAR activity can also lead to synaptic and neuronal dysfunction.

AUTHOR CONTRIBUTIONS

KD, JA and RM wrote the manuscript. KD designed figures.

REFERENCES

Alfonso, S., Kessels, H. W., Banos, C. C., Chan, T. R., Lin, E. T., Kumaravel, G., et al. (2014). Synapto-depressive effects of amyloid beta require PICK1. *Eur. J. Neurosci.* 39, 1225–1233. doi: 10.1111/ejn.12499

Almeida, C. G., Tampellini, D., Takahashi, R. H., Greengard, P., Lin, M. T., Snyder, E. M., et al. (2005). Beta-amyloid accumulation in APP mutant neurons reduces PSD-95 and GluR1 in synapses. *Neurobiol. Dis.* 20, 187–198. doi: 10.1016/j.nbd.2005.02.008

Aow, J., Dore, K., and Malinow, R. (2015). Conformational signaling required for synaptic plasticity by the NMDA receptor complex. *Proc. Natl. Acad. Sci. U S A* 112, 14711–14716. doi: 10.1073/pnas.1520029112

Babiec, W. E., Guglietta, R., Jami, S. A., Morishita, W., Malenka, R. C., and O'Dell, T. J. (2014). Ionotropic NMDA receptor signaling is required for the induction of long-term depression in the mouse hippocampal CA1 region. *J. Neurosci.* 34, 5285–5290. doi: 10.1523/JNEUROSCI.5419-13.2014

Barria, A., and Malinow, R. (2002). Subunit-specific NMDA receptor trafficking to synapses. *Neuron* 35, 345–353. doi: 10.1016/s0896-6273(02)00776-6

Becker, W., Bergmann, A., Hink, M. A., König, K., Benndorf, K., and Biskup, C. (2004). Fluorescence lifetime imaging by time-correlated single-photon counting. *Microsc. Res. Tech.* 63, 58–66. doi: 10.1002/jemt.10421

Birnbaum, J. H., Bali, J., Rajendran, L., Nitsch, R. M., and Tackenberg, C. (2015). Calcium flux-independent NMDA receptor activity is required for A β oligomer-induced synaptic loss. *Cell Death Dis.* 6:e1791. doi: 10.1038/cddis.2015.160

Bliss, T. V., and Collingridge, G. L. (1993). A synaptic model of memory: long-term potentiation in the hippocampus. *Nature* 361, 31–39. doi: 10.1038/361031a0

Calabrese, B., Shaked, G. M., Tabarean, I. V., Braga, J., Koo, E. H., and Halpain, S. (2007). Rapid, concurrent alterations in pre- and postsynaptic structure induced by naturally-secreted amyloid-β protein. *Mol. Cell. Neurosci.* 35, 183–193. doi: 10.1016/j.mcn.2007.02.006

Carter, B. C., and Jahr, C. E. (2016). Postsynaptic, not presynaptic NMDA receptors are required for spike-timing-dependent LTD induction. *Nature Neuroscience.* doi: 10.1038/nn.4343 [Epub ahead of print]

Chapman, P. F., White, G. L., Jones, M. W., Cooper-Blacketer, D., Marshall, V. J., Irizarry, M., et al. (1999). Impaired synaptic plasticity and learning in aged amyloid precursor protein transgenic mice. *Nat. Neurosci.* 2, 271–276.

Choi, D. W. (1992). Excitotoxic cell death. *J. Neurobiol.* 23, 1261–1276. doi: 10.1002/neu.480230915

Choi, D. W. (1995). Calcium: still center-stage in hypoxic-ischemic neuronal death. *Trends Neurosci.* 18, 58–60. doi: 10.1016/0166-2236(95)80018-w

Coultrap, S. J., Freund, R. K., O'Leary, H., Sanderson, J. L., Roche, K. W., Dell'Acqua, M. L., et al. (2014). Autonomous CaMKII mediates both LTP and LTD using a mechanism for differential substrate site selection. *Cell Rep.* 6, 431–437. doi: 10.1016/j.celrep.2014.01.005

Dore, K., Aow, J., and Malinow, R. (2015). Agonist binding to the NMDA receptor drives movement of its cytoplasmic domain without ion flow. *Proc. Natl. Acad. Sci. U S A* 112, 14705–14710. doi: 10.1073/pnas.1520023112

Gustiananda, M., Liggins, J. R., Cummins, P. L., and Gready, J. E. (2004). Conformation of prion protein repeat peptides probed by FRET measurements and molecular dynamics simulations. *Biophys. J.* 86, 2467–2483. doi: 10.1016/s0006-3495(04)74303-9

Hestrin, S. (1992). Developmental regulation of NMDA receptor-mediated synaptic currents at a central synapse. *Nature* 357, 686–689. doi: 10.1038/357686a0

Hsieh, H., Boehm, J., Sato, C., Iwatsubo, T., Tomita, T., Sisodia, S., et al. (2006). AMPAR removal underlies Aβ-induced synaptic depression and dendritic spine loss. *Neuron* 52, 831–843. doi: 10.1016/j.neuron.2006.10.035

Husi, H., Ward, M. A., Choudhary, J. S., Blackstock, W. P., and Grant, S. G. (2000). Proteomic analysis of NMDA receptor-adhesion protein signaling complexes. *Nat. Neurosci.* 3, 661–669. doi: 10.1038/76615

Kamenetz, F., Tomita, T., Hsieh, H., Seabrook, G., Borchelt, D., Iwatsubo, T., et al. (2003). APP processing and synaptic function. *Neuron* 37, 925–937. doi: 10.1016/s0896-6273(03)00124-7

Kessels, H. W., Nabavi, S., and Malinow, R. (2013). Metabotropic NMDA receptor function is required for β-amyloid-induced synaptic depression. *Proc. Natl. Acad. Sci. U S A* 110, 4033–4038. doi: 10.1073/pnas.1219605110

Kim, C. H., Chung, H. J., Lee, H. K., and Huganir, R. L. (2001). Interaction of the AMPA receptor subunit GluR2/3 with PDZ domains regulates hippocampal long-term depression. *Proc. Natl. Acad. Sci. U S A* 98, 11725–11730. doi: 10.1073/pnas.211132798

Kim, Y., Hsu, C. L., Cembrowski, M. S., Mensh, B. D., and Spruston, N. (2015). Dendritic sodium spikes are required for long-term potentiation at distal synapses on hippocampal pyramidal neurons. *Elife* 4:e06414. doi: 10.7554/eLife.06414

Knafo, S., Sánchez-Puelles, C., Palomer, E., Delgado, I., Draffin, J. E., Mingo, J., et al. (2016). PTEN recruitment controls synaptic and cognitive function in Alzheimer's models. *Nat. Neurosci.* 19, 443–453. doi: 10.1038/nn.4225

Lakowicz, J. R. (2006). *Principles of Fluorescence Spectroscopy*. 3rd Edn. USA: Spinger.

Larson, J., Lynch, G., Games, D., and Seubert, P. (1999). Alterations in synaptic transmission and long-term potentiation in hippocampal slices from young and aged PDAPP mice. *Brain Res.* 840, 23–35. doi: 10.1016/s0006-8993(99)01698-4

Lin, J. W., Ju, W., Foster, K., Lee, S. H., Ahmadian, G., Wyszynski, M., et al. (2000). Distinct molecular mechanisms and divergent endocytotic pathways of AMPA receptor internalization. *Nat. Neurosci.* 3, 1282–1290. doi: 10.1038/81814

Lisman, J. (1989). A mechanism for the Hebb and the anti-Hebb processes underlying learning and memory. *Proc. Natl. Acad. Sci. U S A* 86, 9574–9578. doi: 10.1073/pnas.86.23.9574

Lüscher, C., Xia, H., Beattie, E. C., Carroll, R. C., von Zastrow, M., Malenka, R. C., et al. (1999). Role of AMPA receptor cycling in synaptic transmission and plasticity. *Neuron* 24, 649–658. doi: 10.1016/s0896-6273(00)81119-8

Malenka, R. C. (1994). Synaptic plasticity in the hippocampus: LTP and LTD. *Cell* 78, 535–538. doi: 10.1016/0092-8674(94)90517-7

Malenka, R. C., Kauer, J. A., Perkel, D. J., Mauk, M. D., Kelly, P. T., Nicoll, R. A., et al. (1989). An essential role for postsynaptic calmodulin and protein kinase activity in long-term potentiation. *Nature* 340, 554–557. doi: 10.1038/340554a0

Malinow, R., Schulman, H., and Tsien, R. W. (1989). Inhibition of postsynaptic PKC or CaMKII blocks induction but not expression of LTP. *Science* 245, 862–866. doi: 10.1126/science.2549638

Mayford, M., Wang, J., Kandel, E. R., and O'Dell, T. J. (1995). CaMKII regulates the frequency-response function of hippocampal synapses for the production of both LTD and LTP. *Cell* 81, 891–904. doi: 10.1016/0092-8674(95)90009-8

Monyer, H., Burnashev, N., Laurie, D. J., Sakmann, B., and Seeburg, P. H. (1994). Developmental and regional expression in the rat brain and functional properties of four NMDA receptors. *Neuron* 12, 529–540. doi: 10.1016/0896-6273(94)90210-0

Mulkey, R. M., Herron, C. E., and Malenka, R. C. (1993). An essential role for protein phosphatases in hippocampal long-term depression. *Science* 261, 1051–1055. doi: 10.1126/science.8394601

Nabavi, S., Fox, R., Alfonso, S., Aow, J., and Malinow, R. (2014). GluA1 trafficking and metabotropic NMDA: addressing results from other laboratories inconsistent with ours. *Philos. Trans. R. Soc. Lond. B Biol. Sci.* 369:20130145. doi: 10.1098/rstb.2013.0145

Nabavi, S., Kessels, H. W., Alfonso, S., Aow, J., Fox, R., and Malinow, R. (2013). Metabotropic NMDA receptor function is required for NMDA receptor-dependent long-term depression. *Proc. Natl. Acad. Sci. U S A* 110, 4027–4032. doi: 10.1073/pnas.1219454110

Nong, Y., Huang, Y. Q., Ju, W., Kalia, L. V., Ahmadian, G., Wang, Y. T., et al. (2003). Glycine binding primes NMDA receptor internalization. *Nature* 422, 302–307. doi: 10.1038/nature01497

Otmakhov, N., Tao-Cheng, J. H., Carpenter, S., Asrican, B., Dosemeci, A., Reese, T. S., et al. (2004). Persistent accumulation of calcium/calmodulin-dependent protein kinase II in dendritic spines after induction of NMDA receptor-dependent chemical long-term potentiation. *J. Neurosci.* 24, 9324–9331. doi: 10.1523/JNEUROSCI.2350-04.2004

Passafaro, M., Nakagawa, T., Sala, C., and Sheng, M. (2003). Induction of dendritic spines by an extracellular domain of AMPA receptor subunit GluR2. *Nature* 424, 677–681. doi: 10.1038/nature01781

Piston, D. W., and Kremers, G. J. (2007). Fluorescent protein FRET: the good, the bad and the ugly. *Trends Biochem. Sci.* 32, 407–414. doi: 10.1016/j.tibs.2007.08.003

Reiman, E. M., Caselli, R. J., Yun, L. S., Chen, K., Bandy, D., Minoshima, S., et al. (1996). Preclinical evidence of Alzheimer's disease in persons homozygous for the epsilon 4 allele for apolipoprotein E. *N. Engl. J. Med.* 334, 752–758. doi: 10.1056/nejm199603213341202

Ripoli, C., Cocco, S., Li Puma, D. D., Piacentini, R., Mastrodonato, A., Scala, F., et al. (2014). Intracellular accumulation of amyloid-β (Aβ) protein plays a major role in Aβ-induced alterations of glutamatergic synaptic transmission and plasticity. *J. Neurosci.* 34, 12893–12903. doi: 10.1523/JNEUROSCI.1201-14.2014

Rodríguez-Moreno, A., and Lerma, J. (1998). Kainate receptor modulation of GABA release involves a metabotropic function. *Neuron* 20, 1211–1218. doi: 10.1016/s0896-6273(00)80501-2

Sanderson, J. L., Gorski, J. A., and Dell'Acqua, M. L. (2016). NMDA receptor-dependent LTD requires transient synaptic incorporation of Ca^{2+}-permeable AMPARs mediated by AKAP150-anchored PKA and calcineurin. *Neuron* 89, 1000–1015. doi: 10.1016/j.neuron.2016.01.043

Scanziani, M., Malenka, R. C., and Nicoll, R. A. (1996). Role of intercellular interactions in heterosynaptic long-term depression. *Nature* 380, 446–450. doi: 10.1038/380446a0

Selvin, P. R. (2000). The renaissance of fluorescence resonance energy transfer. *Nat. Struct. Biol.* 7, 730–734. doi: 10.1038/78948

Shankar, G. M., Bloodgood, B. L., Townsend, M., Walsh, D. M., Selkoe, D. J., and Sabatini, B. L. (2007). Natural oligomers of the Alzheimer amyloid-β protein induce reversible synapse loss by modulating an NMDA-type glutamate receptor-dependent signaling pathway. *J. Neurosci.* 27, 2866–2875. doi: 10.1523/JNEUROSCI.4970-06.2007

Shankar, G. M., Li, S., Mehta, T. H., Garcia-Munoz, A., Shepardson, N. E., Smith, I., et al. (2008). Amyloid-β protein dimers isolated directly from Alzheimer's brains impair synaptic plasticity and memory. *Nat. Med.* 14, 837–842. doi: 10.1038/nm1782

Sheng, M., Cummings, J., Roldan, L. A., Jan, Y. N., and Jan, L. Y. (1994). Changing subunit composition of heteromeric NMDA receptors during development of rat cortex. *Nature* 368, 144–147. doi: 10.1038/368144a0

Shi, S., Hayashi, Y., Esteban, J. A., and Malinow, R. (2001). Subunit-specific rules governing AMPA receptor trafficking to synapses in hippocampal pyramidal neurons. *Cell* 105, 331–343. doi: 10.1016/s0092-8674(01)00321-x

Shrestha, B. R., Vitolo, O. V., Joshi, P., Lordkipanidze, T., Shelanski, M., and Dunaevsky, A. (2006). Amyloid β peptide adversely affects spine number and motility in hippocampal neurons. *Mol. Cell. Neurosci.* 33, 274–282. doi: 10.1016/j.mcn.2006.07.011

Silva, A. J., Stevens, C. F., Tonegawa, S., and Wang, Y. (1992). Deficient hippocampal long-term potentiation in alpha-calcium-calmodulin kinase II mutant mice. *Science* 257, 201–206. doi: 10.1126/science.1378648

Snyder, E. M., Nong, Y., Almeida, C. G., Paul, S., Moran, T., Choi, E. Y., et al. (2005). Regulation of NMDA receptor trafficking by amyloid-β. *Nat. Neurosci.* 8, 1051–1058. doi: 10.1038/nn1503

Stein, I. S., Gray, J. A., and Zito, K. (2015). Non-ionotropic NMDA receptor signaling drives activity-induced dendritic spine shrinkage. *J. Neurosci.* 35, 12303–12308. doi: 10.1523/JNEUROSCI.4289-14.2015

Stocca, G., and Vicini, S. (1998). Increased contribution of NR2A subunit to synaptic NMDA receptors in developing rat cortical neurons. *J. Physiol.* 507, 13–24. doi: 10.1111/j.1469-7793.1998.013bu.x

Strack, S., Barban, M. A., Wadzinski, B. E., and Colbran, R. J. (1997). Differential inactivation of postsynaptic density-associated and soluble Ca^{2+}/calmodulin-dependent protein kinase II by protein phosphatases 1 and 2A. *J. Neurochem.* 68, 2119–2128. doi: 10.1046/j.1471-4159.1997.68052119.x

Tamburri, A., Dudilot, A., Licea, S., Bourgeois, C., and Boehm, J. (2013). NMDA-receptor activation but not ion flux is required for amyloid-β induced synaptic depression. *PloS One* 8:e65350. doi: 10.1371/journal.pone.0065350

Terry, R. D., Masliah, E., Salmon, D. P., Butters, N., DeTeresa, R., Hill, R., et al. (1991). Physical basis of cognitive alterations in Alzheimer's disease: synapse loss is the major correlate of cognitive impairment. *Ann. Neurol.* 30, 572–580. doi: 10.1002/ana.410300410

Thompson, R. J., Jackson, M. F., Olah, M. E., Rungta, R. L., Hines, D. J., Beazely, M. A., et al. (2008). Activation of pannexin-1 hemichannels augments aberrant bursting in the hippocampus. *Science* 322, 1555–1559. doi: 10.1126/science.1165209

Thompson, R. J., Zhou, N., and MacVicar, B. A. (2006). Ischemia opens neuronal gap junction hemichannels. *Science* 312, 924–927. doi: 10.1126/science.1126241

Tovar, K. R., and Westbrook, G. L. (1999). The incorporation of NMDA receptors with a distinct subunit composition at nascent hippocampal synapses *in vitro*. *J. Neurosci.* 19, 4180–4188.

Traynelis, S. F., Wollmuth, L. P., McBain, C. J., Menniti, F. S., Vance, K. M., Ogden, K. K., et al. (2010). Glutamate receptor ion channels: structure, regulation and function. *Pharmacol. Rev.* 62, 405–496. doi: 10.1124/pr.109.002451

Tu, W., Xu, X., Peng, L., Zhong, X., Zhang, W., Soundarapandian, M. M., et al. (2010). DAPK1 interaction with NMDA receptor NR2B subunits mediates brain damage in stroke. *Cell* 140, 222–234. doi: 10.1016/j.cell.2009.12.055

Vissel, B., Krupp, J. J., Heinemann, S. F., and Westbrook, G. L. (2001). A use-dependent tyrosine dephosphorylation of NMDA receptors is independent of ion flux. *Nat. Neurosci.* 4, 587–596. doi: 10.1038/88404

Volianskis, A., France, G., Jensen, M. S., Bortolotto, Z. A., Jane, D. E., and Collingridge, G. L. (2015). Long-term potentiation and the role of N-methyl-D-aspartate receptors. *Brain Res.* 1621, 5–16. doi: 10.1016/j.brainres.2015.01.016

Wallrabe, H., and Periasamy, A. (2005). Imaging protein molecules using FRET and FLIM microscopy. *Curr. Opin. Biotechnol.* 16, 19–27. doi: 10.1016/j.copbio.2004.12.002

Walsh, D. M., Klyubin, I., Fadeeva, J. V., Cullen, W. K., Anwyl, R., Wolfe, M. S., et al. (2002). Naturally secreted oligomers of amyloid β protein potently inhibit hippocampal long-term potentiation *in vivo*. *Nature* 416, 535–539. doi: 10.1038/416535a

Wang, H. W., Pasternak, J. F., Kuo, H., Ristic, H., Lambert, M. P., Chromy, B., et al. (2002). Soluble oligomers of β amyloid (1–42) inhibit long-term potentiation but not long-term depression in rat dentate gyrus. *Brain Res.* 924, 133–140. doi: 10.1016/s0006-8993(01)03058-x

Wei, W., Nguyen, L. N., Kessels, H. W., Hagiwara, H., Sisodia, S., and Malinow, R. (2010). Amyloid β from axons and dendrites reduces local spine number and plasticity. *Nat. Neurosci.* 13, 190–196. doi: 10.1038/nn.2476

Weilinger, N. L., Lohman, A. W., Rakai, B. D., Ma, E. M., Bialecki, J., Maslieieva, V., et al. (2016). Metabotropic NMDA receptor signaling couples Src family kinases to pannexin-1 during excitotoxicity. *Nat. Neurosci.* 19, 432–442. doi: 10.1038/nn.4236

Weilinger, N. L., Tang, P. L., and Thompson, R. J. (2012). Anoxia-induced NMDA receptor activation opens pannexin channels via Src family kinases. *J. Neurosci.* 32, 12579–12588. doi: 10.1523/jneurosci.1267-12.2012

Whitcomb, D. J., Hogg, E. L., Regan, P., Piers, T., Narayan, P., Whitehead, G., et al. (2015). Intracellular oligomeric amyloid-β rapidly regulates GluA1 subunit of AMPA receptor in the hippocampus. *Sci. Rep.* 5:10934. doi: 10.1038/srep10934

Yasuda, R. (2006). Imaging spatiotemporal dynamics of neuronal signaling using fluorescence resonance energy transfer and fluorescence lifetime imaging microscopy. *Curr. Opin. Neurobiol.* 16, 551–561. doi: 10.1016/j.conb.2006.08.012

Zempel, H., Thies, E., Mandelkow, E., and Mandelkow, E. M. (2010). Aβ oligomers cause localized Ca^{2+} elevation, missorting of endogenous Tau into dendrites, Tau phosphorylation and destruction of microtubules and spines. *J. Neurosci.* 30, 11938–11950. doi: 10.1523/JNEUROSCI.2357-10.2010

Zoidl, G., Petrasch-Parwez, E., Ray, A., Meier, C., Bunse, S., Habbes, H. W., et al. (2007). Localization of the pannexin1 protein at postsynaptic sites in the cerebral cortex and hippocampus. *Neuroscience* 146, 9–16. doi: 10.1016/j.neuroscience.2007.01.061

Conflict of Interest Statement: The authors declare that the research was conducted in the absence of any commercial or financial relationships that could be construed as a potential conflict of interest.

frontiers in Synaptic Neuroscience

REVIEW
published: 23 August 2016
doi: 10.3389/fnsyn.2016.00028

Correlative Light Electron Microscopy: Connecting Synaptic Structure and Function

Isabell Begemann[1,2] *and Milos Galic*[1,2]*

[1] DFG Cluster of Excellence 'Cells in Motion', (EXC 1003), University of Muenster, Muenster, Germany, [2] Institute of Medical Physics and Biophysics, University Hospital Münster, University of Muenster, Muenster, Germany

Many core paradigms of contemporary neuroscience are based on information obtained by electron or light microscopy. Intriguingly, these two imaging techniques are often viewed as complementary, yet separate entities. Recent technological advancements in microscopy techniques, labeling tools, and fixation or preparation procedures have fueled the development of a series of hybrid approaches that allow correlating functional fluorescence microscopy data and ultrastructural information from electron micrographs from a singular biological event. As correlative light electron microscopy (CLEM) approaches become increasingly accessible, long-standing neurobiological questions regarding structure-function relation are being revisited. In this review, we will survey what developments in electron and light microscopy have spurred the advent of correlative approaches, highlight the most relevant CLEM techniques that are currently available, and discuss its potential and limitations with respect to neuronal and synapse-specific applications.

Keywords: correlative light electron microscopy, CLEM, synapse, neuron, fluorescence microscopy, electron microscopy, TEM, SEM

OPEN ACCESS

Edited by:
Marc Fivaz,
Duke NUS Graduate Medical School, Singapore

Reviewed by:
Jeff Lichtman,
Harvard University, USA
Christian Wilms,
Scientifica Ltd., UK

***Correspondence:**
Milos Galic
galic@uni-muenster.de

Received: *23 March 2016*
Accepted: *12 August 2016*
Published: *23 August 2016*

Citation:
Begemann I and Galic M (2016) Correlative Light Electron Microscopy: Connecting Synaptic Structure and Function. Front. Synaptic Neurosci. 8:28. doi: 10.3389/fnsyn.2016.00028

INTRODUCTION

Neurons transmit the majority of trans-cellular signals via synaptic contacts. To correctly and reliably respond to various stimuli (e.g., different input frequencies), each synapse hosts an elaborate machinery to regulate signal transmission in a context-dependent manner. On the molecular level, synaptic transmission in its most simple form relies on fusion of ~40 nm large vesicles at the presynaptic site, diffusion of released neuro-transmitters across the 30 nm wide synaptic cleft, and subsequent ligand-specific activation of receptors at the postsynaptic site. Considering the small size of this signaling unit, it is not surprising that major advancements in understanding synaptic function have been closely correlated with progress in imaging technology. For instance, the notion that communication across synaptic clefts relies on chemical signals would not have been possible without detailed information from electron micrographs on synapse ultrastructure (Derobertis and Bennett, 1955; Pappas and Bennett, 1966) and vesicle dynamics (Heuser and Reese, 1973). Likewise, our understanding about the function of individual synaptic proteins has substantially advanced with the introduction of ion and protein markers (Shimomura et al., 1962; Tsien, 1981; Heim et al., 1994) for fluorescence light microscopy. Intriguingly, and despite the fact that today's neuroscience is building up on information obtained with electron and light microscopy, strategies to combine these two approaches only recently have started gaining traction.

The emergence of such dual approaches, termed correlative light electron microscopy (CLEM), from a sparsely known branch of imaging to center stage can be linked to a series of landmark papers from the nineties (Deerinck et al., 1994; Svitkina et al., 1995). Since then, fueled by advances in imaging and labeling techniques, publications using CLEM approaches have steadily been rising. In this review, we will revisit what developments have incited the advent of correlative imaging approaches, and highlight the most relevant dual microscopy techniques that are currently available. We begin by giving an overview of electron and light-based imaging methods that can be used for CLEM, followed by a section describing how individual approaches can be successfully combined to create correlative approaches. Next, we will reflect on technical concerns that need to be taken care of when designing dual imaging experiments, before closing with a discussion on current limitations and future challenges associated with CLEM.

ELECTRON AND LIGHT-BASED TECHNIQUES USED FOR CLEM

CLEM describes a continuously growing number of procedures that allow merging electron and light-based images from the same object. Thus, at least in theory, each existing electron and light microscopy technique where ultrastructure remains intact could be paired to generate a CLEM image. To illustrate this combinatorial potential, and to expound existing limitations, we begin this section by discussing electron and light microscopy techniques suitable for correlative approaches, before proceeding to examples where CLEM was successful applied to study neuronal and synaptic function.

Electron Microscopy–Visualizing the Ultrastructure

Electron micrographs in CLEM rely to a large extent on transmission electron microscopy (TEM) and scanning electron microscopy (SEM). TEM, which enables visualization of 50–100 nm thick cross-sections of samples with a resolution of down to a few Angstrom (Pierce and Buseck, 1974; Ruska, 1987; Erni et al., 2009), was critically involved in the detailed characterization of synaptic structures (Gray, 1959; Pappas and Bennett, 1966; Fifkova and Delay, 1982; Landis and Reese, 1983; Watanabe et al., 2013, 2014), and has helped to advance our understanding on age and disease-dependent changes in synaptic properties (DeKosky and Scheff, 1990; Navlakha et al., 2013).

Contrary to TEM, where electron shadows are used to create the image, SEM-based strategies utilizes the interaction of electrons with molecules in the sample to recreate the image. One commonly applied SEM strategy, where secondary electrons are used to determine the surface topography of objects with a precision of ∼1 nm (Vernon-Parry, 2000), was central for investigating surface features such as the morphology of neuromuscular junctions (Desaki and Uehara, 1981) as well as structural reorganization during exploratory dendritic filopodia formation in hippocampal neurons (Galic et al., 2014). In addition, back-scattered electrons created by interaction with heavy elements (i.e., high atomic number) in the uncoated sample can also be used to render images comparable to transmission electron micrographs of ultrathin sections, an approach that is of particular relevance for embedded sections on an electron-opaque surface or samples that are investigated '*en block*' (Briggman et al., 2011).

A single cross-section, or the surface of the sample, is lacking information on the three-dimensional organization within the biological specimen. Here, cryo-fracture, where frozen samples are broken to expose cell structures along the fracture line (Castejon and Caraballo, 1980; Castejon, 1996), or unroofing, where intracellular structures are uncovered by brief bursts of ultrasound (Lang, 2003), can be used together with deep-etching (Heuser and Salpeter, 1979) to gain insights into subcellular organization. While useful, these strategies lack the capability for systematic three-dimensional sample reconstruction that can be achieved with serial sectioning, where successive ultrathin slices are imaged. Early attempts of serial sectioning reach back to the late 60s (De Rosier and Klug, 1968), and have since then continuously been used to investigate neuronal networks (White et al., 1986) and synaptic connection (Mishchenko et al., 2010). In modern serial section TEM (ssTEM), sections of 60 ± 20 nm are cut with an ultra-microtome and placed manually on a metal support grid (Harris et al., 2006). More recently, automated tape-collecting ultra-microtome SEM (ATUM-SEM) has emerged as a powerful alternative (Hayworth et al., 2006; Kasthuri et al., 2007, 2015; Terasaki et al., 2013; Morgan et al., 2016). Here, sections of 30 nm are cut by an ultra-microtome and collected from the water bath using a conveyor-belt like support tape. As the support tape is electron-opaque, a finely focused SEM beam is applied to raster the surface of the sample and backscattered electrons are used to reconstruct the image. Thus, compared to ssTEM, ATUM-based strategies not only allow thinner sectioning and rapid imaging of larger areas but also substantially reduce errors associated with manual sample handling (Hayworth et al., 2014). Alternatively, an embedded tissue block can also be sectioned directly within the SEM vacuum chamber, either using a diamond knife (serial block-face SEM, SBEM; Leighton, 1981; Denk and Horstmann, 2004) or by milling with a focused ion-beam (FIB-SEM; Watkins et al., 1986; Knott et al., 2008). In the latter, a scanning electron microscope is used to image the surface of the embedded sample, while a high current focused ion beam continuously slices off sections perpendicular to the SEM axis, thus allowing 3D reconstruction of the sample. Compared to diamond-based sectioning, FIB-SEM is thus not only faster but also permits sectioning samples with a step size in the single nm range (Knott et al., 2008; Merchan-Perez et al., 2009; Lehmann et al., 2014).

Another strategy for detailed three-dimensional reconstructions relies on electron tomography (ET). In this approach, a tilt series (usually ranging from −60° to +60°) of two-dimensional images is generated to reconstruct the three-dimensional shape of an object within the single slice (Crowther et al., 1970; Hoppe et al., 1974; Penczek, 2010; Ercius et al., 2015). ET was successfully used to resolve ultrastructural features of the presynapse (Perkins et al., 2015) and synaptic vesicle populations in saccular hair cells (Lenzi et al., 1999). Yet,

while ET is suitable for atomic-resolution, radiation damage, and limitations in interpretability for thicker sections need to be considered when preparing the sample (Tocheva et al., 2010).

Finally, we would like to note that further electron-based imaging strategies exist (e.g., STEM (Crewe et al., 1970; Engel, 1978), tSEM (Kuwajima et al., 2013)). While not commonly used in CLEM studies, it is plausible to envision that some of these additional types of electron microscopy may be beneficial for a particular question. For readers interested in learning more on electron microscopy techniques, we recommend reading one of the many excellent reviews available on this exciting topic (Briggman and Bock, 2012; Knott and Genoud, 2013; Miranda et al., 2015; Perkins et al., 2015).

Light Microscopy–Monitoring and Manipulating Cell Function

While the electron microscopy techniques described above are well suited to investigate ultrastructural features with high axial resolution, they lack spatio-temporal information available with light microscopy. To increase penetration depth and reduce background compared to whole field illumination (Epi), CLEM studies frequently rely on confocal microscopy, where a pinhole is used to reduce out-of-focus light (Minsky, 1988), light sheet microscopy, where a light beam perpendicular to the objective illuminates only the focal plane (Engelbrecht and Stelzer, 2006; Keller et al., 2008), or two-photon microscopy, where simultaneous absorption of two photons is used for spatially controlled illumination (Denk et al., 1990). Resolution in light and electron microscopy is based on numerical aperture and wavelength. However, unlike in electron microscopy, where resolution is limited by the spot size (SEM) or the grain of the detector (TEM), the limiting factors in light microscopy is the wavelength (Rayleigh, 1879; Abbe, 1883). To reach beyond the diffraction limit, several approaches have been introduced over the last decade. Among the most prominent super-resolution microscopy techniques used in CLEM studies are stimulated emission depletion microscopy (STED), where a depletion laser limits the width of the emitting light source (Hell and Wichmann, 1994; Klar et al., 2001), and stochastic techniques, such as fluorescent photo-activation localization microscopy (PALM; Betzig and Chichester, 1993; Betzig et al., 2006) or stochastic optical reconstruction microscopy (STORM; Rust et al., 2006), where light emitted from sequentially activated fluorophores is fitted to determine its precise localization. As before, we would like to note that additional light-based approaches [e.g., total internal reflection fluorescence microscopy (Axelrod, 1981) or structured illumination microscopy (Neil et al., 1997)] can be used in CLEM approaches. Readers interested to learn more about fluorescence microscopy techniques, we refer to one of the many excellent reviews focused on these topics (Lichtman and Conchello, 2005; Combs, 2010; Huang et al., 2010).

Fluorescence light microscopy not only allows to visualize cells within neuronal circuits (Livet et al., 2007), but a continuously growing number of molecular probes and genetically encoded markers also provide tools to study a variety of neuronal and synaptic properties. Parameters that can be analyzed include among others subcellular protein localization (Chalfie et al., 1994; Heim et al., 1994; Kilgore et al., 2013), protein activity (Adams et al., 1991), ion dynamics (Tsien, 1980, 1981; Tsien et al., 1982; Minta and Tsien, 1989; Nakai et al., 2001), pH (Tanasugarn et al., 1984; Miesenbock et al., 1998), membrane potential or voltage (Davila et al., 1973; Siegel and Isacoff, 1997; Zochowski et al., 2000), or lipid species (Stauffer et al., 1998). Intriguingly, light is also suitable to actively manipulate the biological sample in a precise spatio-temporal manner. One commonly used approach relies on light-activation of caged substrates. Relevant for neurobiology, strategies for uncaging calcium (Ellisdavies and Kaplan, 1994), IP3 (Wang and Augustine, 1995), and various neurotransmitters (Ellis-Davies, 2011) have been realized. More recently, light has also been used to regulate protein function (Cao et al., 2008; Tischer and Weiner, 2014). This approach, coined optogenetics, has provided among others tools for controlling neuronal and synaptic activity with unprecedented spatio-temporal precision (Boyden et al., 2005; Fenno et al., 2011; Rost et al., 2015). Finally, it is worth mentioning that even physical cell parameters, such as shape or membrane tension, can be altered by light in living samples, using for instance optical tweezers (Ashkin, 1970; Zhang and Liu, 2008). In summary, when combined with electron microscopy, these light-based approaches allow precisely altering a specific parameter while monitoring the cellular responses followed by analysis of the corresponding ultrastructural features.

Correlative Light and Electron Microscopy in Neuroscience

Although the potential of combining ultrastructural information with functional studies was early noticed, first attempts to combine these microscopy techniques were limited to depicting separately prepared and imaged biological samples (Porter et al., 1945). Experiments where fluorescence and EM images of subcellular structures from the same cell were aligned started appearing in the 1970s (Hollander, 1970; Nakai and Iwashita, 1976), and have since then been applied to investigate a variety of neurobiological questions.

To fully understand neuronal or synaptic function, the cellular context needs to be considered. It is thus not surprising, that large efforts have been put into elucidating ultrastructural information within the intact tissue. *In situ* CLEM, where data from life-cell fluorescence imaging is combined with EM micrographs, has advanced our understanding of neuronal circuits (Bock et al., 2011; Briggman et al., 2011; Lee et al., 2016), and has also shed light on subcellular behaviors such as axosome shedding (**Figure 1A**) (Bishop et al., 2004). An alternative strategy, frequently applied to gain information of individual neurons *in situ*, relies on array tomography (AT), where plastic-embedded tissue samples are sliced with an ultra-microtome, bonded array-wise onto a glass coverslip, stained, and finally imaged by fluorescence and electron microscopy (**Figure 1B**) (Micheva and Smith, 2007; Rah et al., 2013; Collman et al., 2015). By combining super-resolution techniques and serial sectioning, it was even possible to detect presynaptic dense projection proteins at a lateral resolution of 35–65 nm (Watanabe

et al., 2011). While serial sectioning-based CLEM approaches allow studying biological samples with high axial and lateral resolution, sample preparation, and 3D image alignment can be challenging (Micheva and Smith, 2007; Collman et al., 2015). Here, SBEM and FIB-SEM based approaches, where *en-block* EM imaging and fluorescence approaches are merged to obtain CLEM images, have helped to streamline *in situ* studies focused on the complexity of the nervous system (Briggman et al., 2011; Blazquez-Llorca et al., 2015), or to reconstruct whole cortical neurons (Maco et al., 2013) and single synapses (Bosch et al., 2015).

Orthogonal to *in situ* approaches described above, CLEM can also be applied to neurons isolated from brain tissues and cultured *in vitro* (Banker and Cowan, 1977). As such, cultured neurons are compatible with each CLEM technique described above (**Figure 1C**) (Al Jord et al., 2014; Paez-Segala et al., 2015; Fares et al., 2016). Although these cells lack the physiological context usually encountered by neurons within a tissue, cultured neurons may still yield advantages compared to *in situ* samples depending on the biological question. One such example, and complementing the section-based CLEM assays described so far, is the analysis of processes at the cellular surface, such as curvature-dependent protein recruitment to deforming plasma membranes (**Figure 1D**) (Galic et al., 2014).

TECHNICAL CONSIDERATIONS

In this section, we will focus on technical possibilities and limitations that need to be taken into consideration when designing a CLEM experiment. We start by discussing challenges arising from sample preparation. Next, we will survey what markers are suitable for which technique, and discuss strategies for alignment of corresponding fluorescence images and electron micrographs with respect to their potential and drawbacks.

Sample Preparation for CLEM Images

The quality of correlative image alignment critically relies on the ability to maintain the native organization of the cell during fixation and subsequent sample preparation. Thus, CLEM techniques not only need to be optimized for signal strength, but also for shape preservation. Formaldehyde, glutaraldehyde, and osmium tetroxide (OsO_4), have been the standard fixatives for decades, including for brain tissues that are due to their softness easily damaged during fixation and subsequent processing. Classical fixation protocols include whole animal perfusion via the vascular system for larger specimens (e.g., whole brain) as well as immersion of tissue slice and cultured cells. Once the biological sample is fixed, the actual preparation for the respective EM technique is rendered. For slice-based assays, two different approaches exist: the pre-embedding method and the post-embedding method. For both methods, correlative approaches have been reported (Watanabe et al., 2011; Kopek et al., 2012). In the pre-embedding method, the antigen–antibody reaction is performed before (i.e., pre) plastic embedding and subsequent ultrathin sectioning. While better for preserving ultra-structures, this approach is often hindered by poor penetration of the antibody. In the post-embedding method, the antigen–antibody reaction is performed after (i.e., post) plastic embedding. As labeling takes place on thin tissue slices, antigens are more easily accessible. However, OsO_4, which is often used as fixative and stain for membrane structures, can quench the fluorescence signal, and epoxy-based resins used due to its good preservation and ultra-sectioning properties partially inhibit photo-switching of fluorophores (Kim et al., 2015). Here, a number of modifications, such as using acrylic resins as embedding material or replacing OsO_4 with uranyl acetate, tannic acid or *p*-phenylenediamine, have helped to enhance compatibility and immunoreactivity (Phend et al., 1995; Osamura et al., 2000; Akagi et al., 2006; Kim et al., 2015). Complementing these slice-based assays, cells can also be prepared for analysis of surface features. As before, samples are fixed. However, rather than embedding the sample, a platinum replica of the surface is generated (Heuser et al., 1976), or the sample is subjected to critical point drying and surface staining, prior to image acquisition via SEM. Finally, one last concern is that chemical fixation is not instantaneous (Szczesny et al., 1996). To circumvent this issue, quick-freezing, where samples are 'slammed' on a super-cold block of metal sprayed with liquid helium (Heuser et al., 1976) or high-pressure freezing, where samples are frozen in milli seconds while pressure is increased to avoid water crystallization (Hunziker et al., 1984; Dahl and Staehelin, 1989), have improved preservation quality.

Picking the Right Markers for CLEM

Unfortunately, not all markers are equally well suited for individual CLEM approaches. To account for these limitations, a series of labeling techniques has emerged. Considering its widespread availability, the most commonly used markers for CLEM are genetically encoded fluorescence tags, such as GFP, that can be detected in electron micrographs via immuno-gold labeling (**Figure 2A**) (Kukulski et al., 2011; Galic et al., 2012). In order to distinguish several proteins in the same sample, immuno-gold particles of variable sizes directed against different fluorescence tags can be used. However, since sample fixation may interfere with genetically encoded fluorescence markers (Muller-Reichert and Verkade, 2014) and gold particles may quench the fluorophore in parallel fluorescence/electron imaging (Kandela and Albrecht, 2007), additional markers are desirable. One such alternative relies on quantum dots (QDs; **Figure 2B**), which were shown to have a 10 times higher labeling efficiency than immuno-gold (Giepmans et al., 2005; Kuipers et al., 2015). These semiconductor nanocrystals consist of a cadmium selenide core surrounded by a zinc sulfide shell coated with affinity ligands (e.g., antibodies) for targeting the desired biomolecules (Alivisatos, 1996). Intriguingly, as the fluorescence wavelength of these photo-stable nanocrystals depends on their core size, it is possible to label samples with fluorescently different QDs, and then to distinguish individual QDs in electron micrographs by size (Giepmans et al., 2005; Kuipers et al., 2015). A minor disadvantage of QDs, however, lies in the difficulty to precisely measure sizes of small QDs due to its low contrast in EM (Brown and Verkade, 2010). While widely used, both

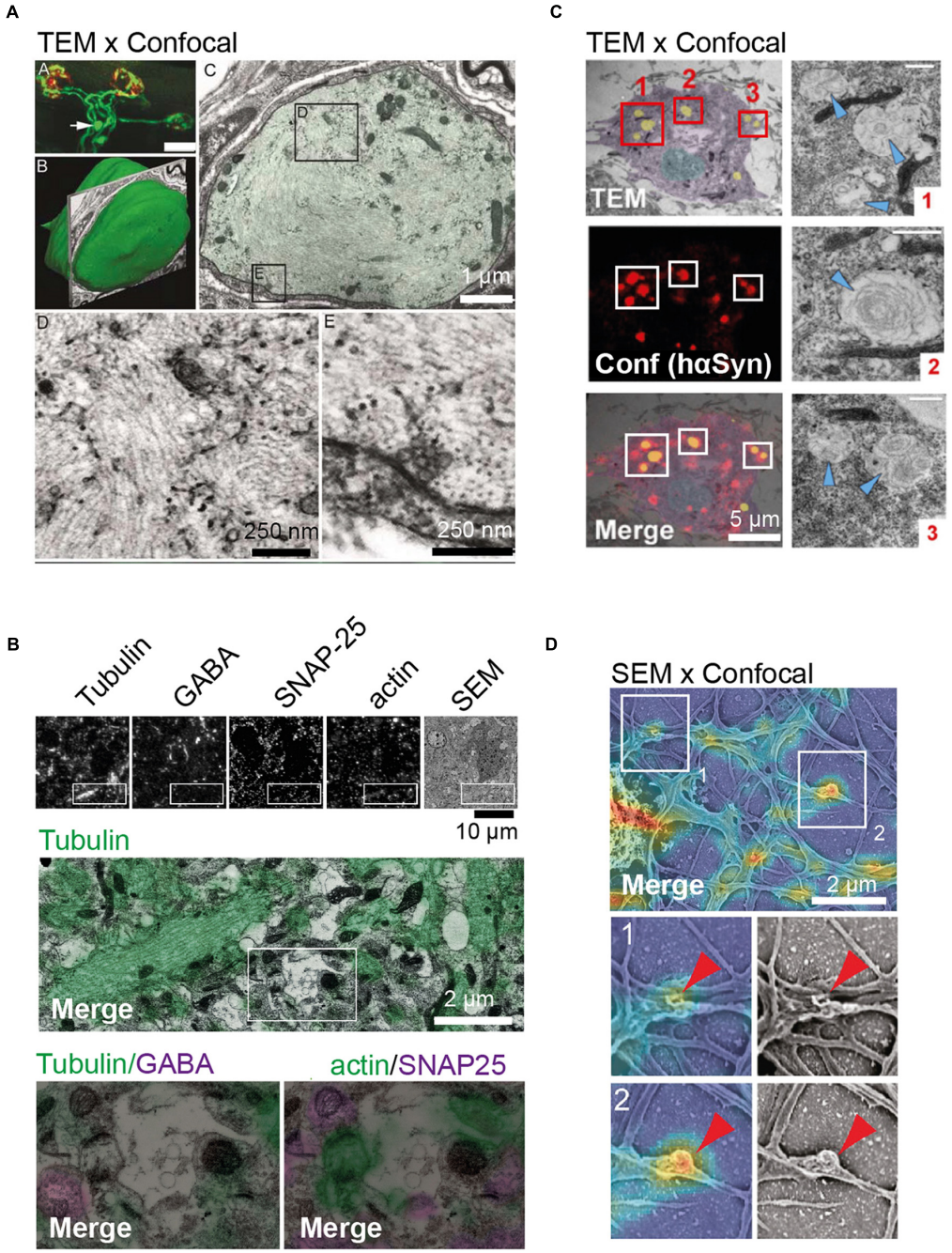

FIGURE 1 | Examples of *in situ* and *in vitro* correlative light electron microscopy (CLEM) approaches. (A) *In situ* CLEM of confocal and transmission electron microscopy (TEM) images showing axonal retreat from neuromuscular junctions. Top left image shows confocal image depicting axonal bulb (arrow) present 25 um from the neuromuscular junction site (in red). Middle left image illustrating surface rendering of the bulb indicated above. Top right image shows TEM, shows that the bulb is sheathed by Schwann cells. TEM images at the bottom depict neurofilament disorganization in axonal bulb. **(B)** *In situ* CLEM of confocal and scanning electron microscopy (SEM) images of 70 nm section from the mouse cerebral cortex. From left to right: immunostaining of ultrathin sections for tubulin, GABA, SNAP-25, β-actin, and SEM image. Below, the boxed region is shown at a higher magnification. **(C)** *In vitro* CLEM of confocal and TEM images of hippocampal neurons. Ultrastructure of hα-Syn inclusions in cultured neurons from $SNCA^{+/-}$ mice shown in TEM (top), confocal image (middle), and as merged CLEM image (bottom). For illustration, the nucleus is rendered in blue, the cytosol in purple, and inclusions in yellow. To the right, high-resolution images of inclusions (red boxes 1–3), with arrowheads indicating filamentous structures, are shown. **(D)** *In vitro* CLEM of confocal and SEM images of cultured hippocampal neurons. Alignment of SEM and fluorescence signal for actin in cultured hippocampal neurons (top) and magnified sections of actin-rich convoluted nodes that form along dendritic arbors (bottom) are shown. Scale bars: **(A)** 25 μm at the top left, 1 μm at the top right, 0.25 μm at the bottom; **(B)** 10 μm at the top and 2 μm at the bottom; **(C)** 5 μm; **(D)** 2 μm. Pictures reprinted with permission from: **(A)** (Bishop et al., 2004); **(B)** (Micheva and Smith, 2007); **(C)** (Fares et al., 2016); **(D)** (Galic et al., 2014).

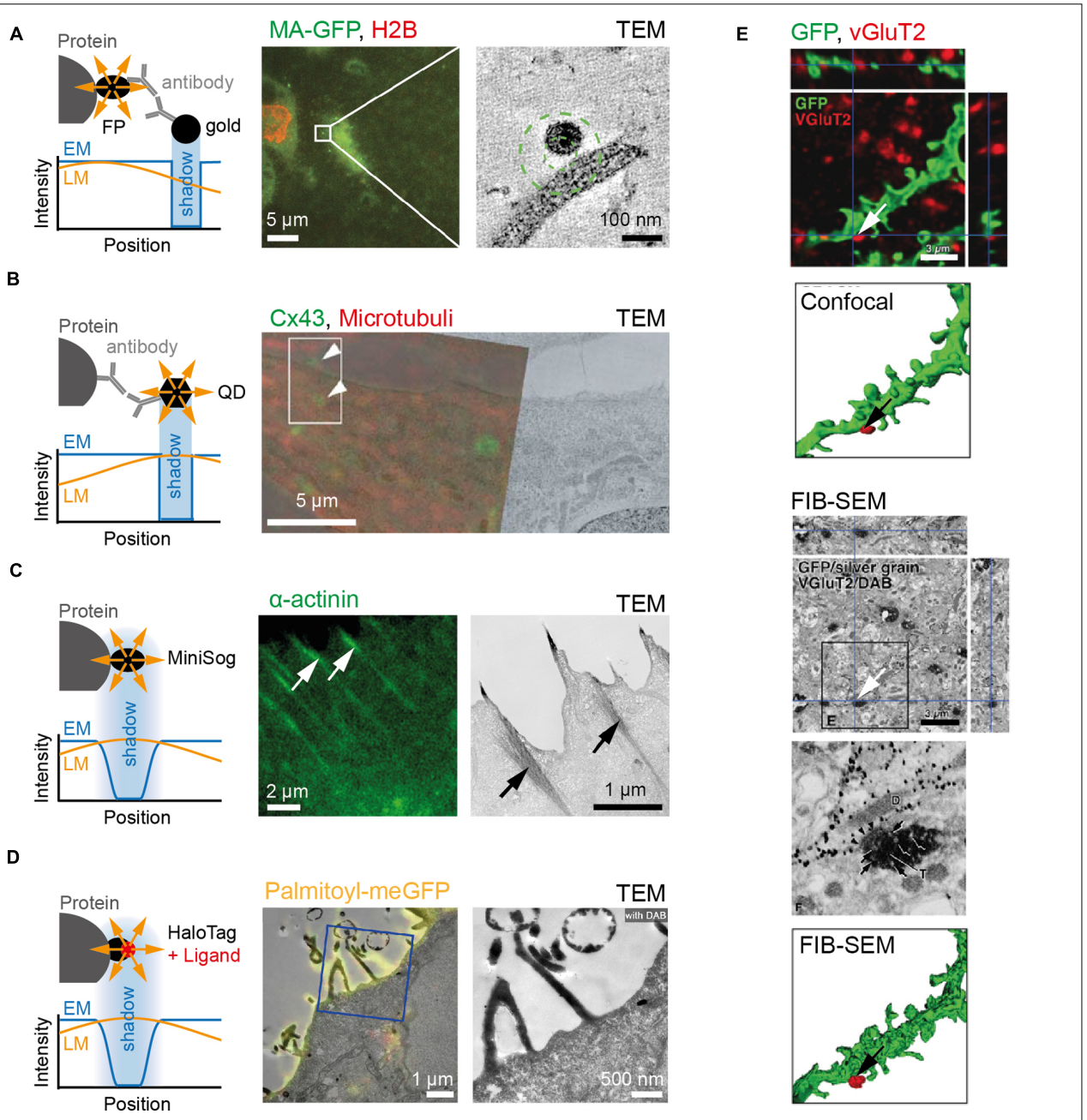

FIGURE 2 | Examples of markers commonly used for CLEM. (A) To the left, cartoon depicting immune-gold labeling of genetically encoded fluorescent protein. Note difference between the relative position of signal in fluorescence (yellow) and electron microscope (blue) images caused by antibodies. To the right, an example showing fluorescence and electron micrographs of HIV particle labeled with MA-EGFP on MDCK cells expressing RFP-tagged Histone 2B. **(B)** To the left, cartoon depicting protein and signal from QD in fluorescence (yellow) and electron microscope (blue) images. Note difference between protein epitope recognized by antibody and QD signal position. To the right, example depicting RFL6 fibroblasts fixed and stained with primary antibodies followed by secondary antibodies linked to QDs. QDs identify Cx43 at gap junctions and trafficking intermediates (green) and α-tubulin in microtubules (red). **(C)** To the left, cartoon depicting genetically encoded MiniSOG, as well as the relative position and signal shape for fluorescence (yellow) and electron microscope (blue) images. To the right, an example showing fluorescence and electron micrographs of HeLa cells expressing miniSOG labeled α-actinin. **(D)** To the left, cartoon depicting HaloTag labeling of protein as well as position and signal shape for fluorescence (yellow) and electron microscope (blue) images. To the right, an example showing fluorescence and electron micrographs of Hela cell transfected with Palmitoyl-HaloTag-meGFP. **(E)** Dendrites of medium-size spiny neurons in the rat neostriatum labeled with membrane-targeted GFP and immunolabeled with Cy5 against vesicular glutamate transporter2 (VGluT2; top). After detection by fluorescence microscopy, GFP and VGluT2 immunoreactivities were further developed for focused ion-beam SEM (FIB-SEM) via immunogold/silver enhancement and immunoperoxidase/DAB methods, respectively (bottom). Scale bars: **(A)** 5 µm to the left and 100 nm to the right; **(B)** 5 µm; **(C)** 2 µm to the left and 1 µm to the right; **(D)** 1 µm to the left and 500 nm to the right; **(E)** 3 µm. Pictures reprinted with permission from: **(A)** (Kukulski et al., 2011); **(B)** (Giepmans et al., 2005); **(C)** (Shu et al., 2011); **(D)** (Liss et al., 2015); **(E)** (Sonomura et al., 2013).

methods are hampered by a localization error due to spatial separation between the protein epitope and the electro-dense particle that is visualized in light and electron micrographs (Kandela et al., 2007; van Donselaar et al., 2007). To bypass this imprecision, Aptamers directed against the fluorescence tag (Shui et al., 2012) linked to gold (Javier et al., 2008; Chang et al., 2013), or nano-bodies directed against fluorescent proteins that can be conjugated to gold nanoparticles (Van de Broek et al., 2011; Ries et al., 2012) may provide promising alternatives.

Orthogonal to these approaches, several strategies have emerged that take advantage of singlet oxygen generators. Genetically encoded singlet oxygen generators are of particular relevance for samples that are investigated '*en block*' (i.e., SBEM and FIB-SEM) and thus preclude post-staining of individual sections. One such example is the genetically encoded miniSOG (**Figure 2C**), which not only fluoresces when illuminated by blue light, but also yields an osmophilic reaction product by catalyzing the polymerization of 3,3′-Diaminobenzidine (DAB) into electron-dense polymers that are detectable in electron micrographs (Shu et al., 2011). The same strategy is also applicable using the Halo-Tag system, where a modified haloalkene dehalogenase (Los et al., 2008) is used to covalently bind to specific ligands such as tetramethylrhodamine (TMR; **Figure 2D**). Like miniSOG, TMR fluoresces upon illumination and is visible in EM due to DAB oxidation (Liss et al., 2015). Other self-labeling systems are provided by SNAP/CLIP-tags, in which the enzyme domain is bound to the protein of interest and labeled with a cell–permeable fluorescent ligand (Liss et al., 2015). Finally, cells can also be transfected with APEX, a non-fluorescent peroxidase that withstands strong fixation to yield light-independently EM contrast (Martell et al., 2012). However, considering that the reaction product can diffuse, these approaches may yield best results when staining enclosed structures. Notably, multiple procedures can be combined within a sample for visualization (**Figure 2E**).

Strategies of Aligning Fluorescence Image and Electron Micrograph in CLEM

Correlation of fluorescence images and electron micrographs can be challenging for a number of reasons. For one, the region of interest can cover less than 0.0004% of the total sample area (Begemann et al., 2015), thus offering only on a limited number of reference points for navigation. And even after the region of interest acquired at the light microscope is found again on the electron microscope, rotation, magnification, and tilting angle still need to be adjusted for image alignment. This is of particular relevance in pre-embedding approaches, where, unlike to post-embedding strategies, the angle of the respective acquisition planes may differ. To tackle these obstacles, several strategies for navigation and image alignment have emerged for *in situ* and *in vitro* approaches.

For *in situ* CLEM, various fiduciary markers have been described that are equally suitable for pre-embedding and post-embedding strategies. In both approaches, the region of interest in the embedded sample is identified using a previously determined set of reference points. Here both, biological (e.g., blood vessels and dirt) and artificial (e.g., silica beads and gold markers) landmarks have proven to be useful for navigation. Once identified, individual EM sections are made and, if desired, 3D reconstruction of individual slices can be prepared by manual or automatic alignment using fiduciary landmarks present in adjacent sections (Bishop et al., 2004; Bock et al., 2011; Lee et al., 2016). Finally, electron micrographs (2D or 3D) are merged with the corresponding fluorescence images either manually or automatically using large features visible in both images (e.g., blood vessels and silica beads) for coarse alignment. For subsequent fine-adjustment, subcellular structures (e.g., gold fiduciary markers, nucleus, and filopodia) can be used. To estimate how accurate the alignment is, cross-correlation analysis between light and electron micrographs can be performed.

In vitro CLEM approaches permit the generation of additional reference systems for image alignment on the plating substrate (i.e., glass and plastic). For example, a unique reference point can be created at the position where the fluorescence image is acquired, using for instance laser etching (Colombelli et al., 2008; Bishop et al., 2011; Urwyler et al., 2015) or a scratching device such as diamond objective markers (Sochacki et al., 2014). Upon processing, this reference point can then be used for navigation on the electron microscope and for subsequent image alignment. Another popular reference system relies on pre-formed structured (Svitkina, 2009; Benedetti et al., 2014) and stochastic (Begemann et al., 2015) micro-patterns or fiducial landmarks (Kukulski et al., 2011) for re-finding the region of interest on the EM as well as subsequent image alignment. Intriguingly, such reference points are not only suitable for manual alignment, but also for software-assisted solutions (Begemann et al., 2015), rendering these approaches an attractive entry point compared to more sophisticated CLEM strategies.

Finally, simultaneous fluorescence and electron imaging may provide an alternative strategy. Here, a number of custom-made (Liv et al., 2013; Nishiyama et al., 2014; Peddie et al., 2014; de Boer et al., 2015) and commercial (e.g., from Fei and Zeiss) instruments have been presented. These instruments, which are equally suitable for *in situ* and *in vitro* samples, integrate light- and electron imaging in one apparatus (iCLEM), thus ensuring dual imaging of the region of interest without need of later image alignment. However, as sample preparation for iCLEM is restricted to techniques suitable for parallel LM and EM (Agronskaia et al., 2008), and due to the limited availability of such instruments, iCLEM has not yet reached the optional users.

CLEM–POTENTIAL AND LIMITATIONS

In this review, we have discussed possible combinations for correlating optical and electron microscopy approaches. We mentioned how improvements in imaging techniques, sample preparation, markers, and image alignment have facilitated

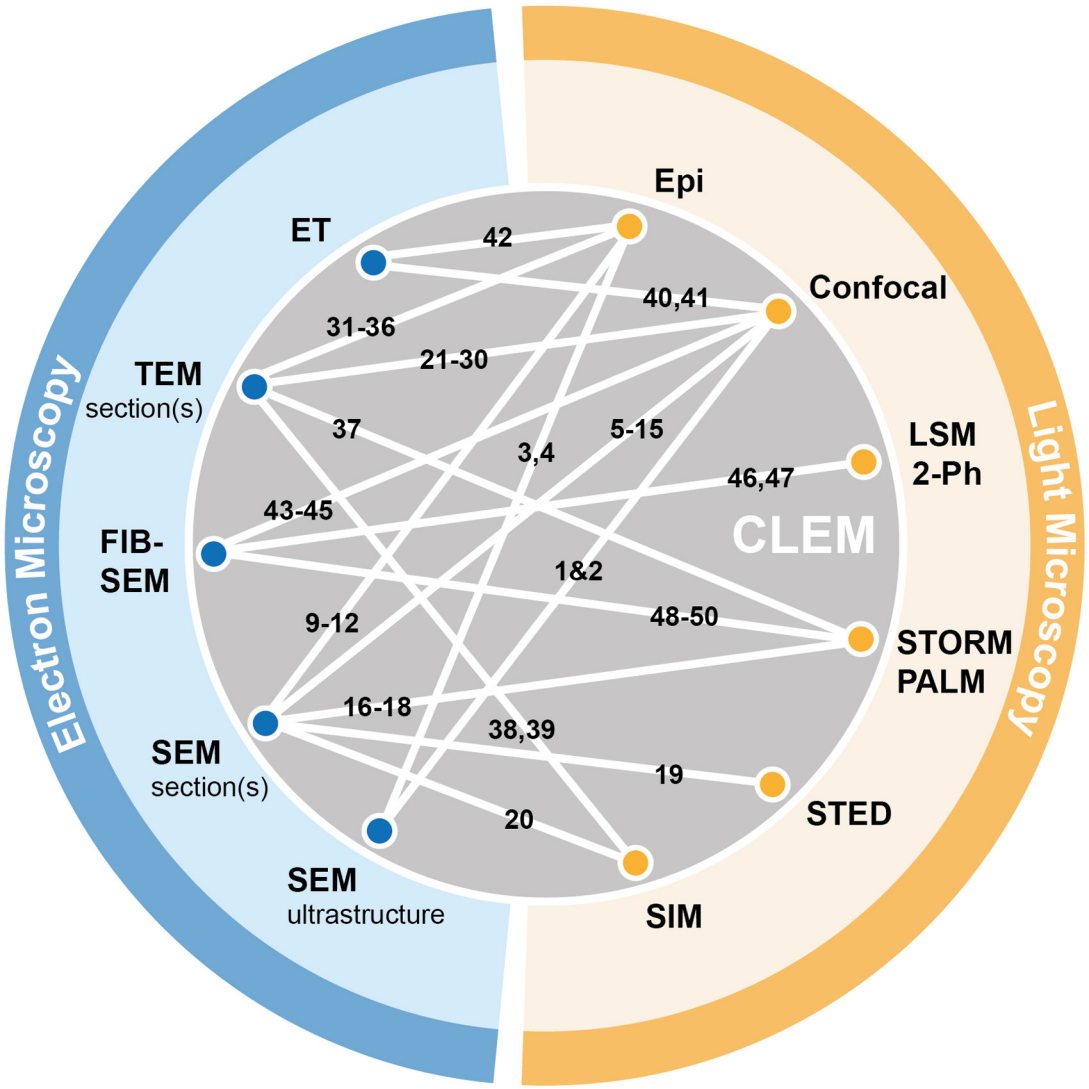

FIGURE 3 | Graphical summary of existing CLEM approaches. Electron microscopy (blue) and light-based techniques (yellow) that were successfully combined in correlative approaches are depicted by white lines connecting the respective methods. References corresponding to individual publications using specific CLEM approaches (numbered 1–50) can be found in the Supplementary Materials (Supplementary Table S1).

development of novel CLEM approaches, and showed examples where these strategies were successfully used for structure-function analysis in neurons and synapses. In order to visualize the combinatorial potential, we provide a chart summarizing published CLEM pairings (**Figure 3**).

While correlative approaches have revealed aspects of neuronal and synaptic function that would not have been possible without it, challenges still remain due to the limited temporal and spatial resolution of CLEM. From this perspective, recent work on liquid cell electron microscopy (Ross, 2015), where electron-permeable membranes are used to host aqueous solutions under atmospheric pressure conditions for TEM and SEM imaging (Danilatos et al., 2011; Ominami et al., 2015), cryo-ET to study the supramolecular architecture of cellular structures (Medalia et al., 2002; Beck et al., 2007), and the continuous increase in sophistication and computational power used for image analysis have captured the imagination of people. While it remains elusive whether these and other emerging techniques will merge or replace CLEM-based studies, they are exemplary for an ongoing push toward visualization and comprehensive analysis of biological function on the structural level.

Taken together, the possibilities of applying correlative approaches to study neuronal and synapse function are growing thanks to the continuous progress in techniques, tools and protocols for combining these two types of microscopy. Alas, while correlative approaches in neurobiology have substantially increased in quality and availability, truly artifact-free preparation techniques for precise molecule-localization are yet to be achieved.

AUTHOR CONTRIBUTIONS

IB and MG conceived the idea, prepared illustrations for publication and wrote the manuscript.

FUNDING

The authors acknowledge funding from the Cluster of Excellence 'Cells in Motion' (DFG, EXC-1003) to IB (PP-2014-04) and MG (FF-2016-03).

ACKNOWLEDGMENT

The authors thank members of the Galic and Matis labs for critical reading of the manuscript.

SUPPLEMENTARY MATERIAL

The Supplementary Material for this article can be found online at: http://journal.frontiersin.org/article/10.3389/fnsyn.2016.00028

REFERENCES

Abbe (1883). The relation of aperture and power in the microscope. *J. R. Microsc. Soc.* 3, 790–812. doi: 10.1111/j.1365-2818.1883.tb05956.x

Adams, S. R., Harootunian, A. T., Buechler, Y. J., Taylor, S. S., and Tsien, R. Y. (1991). Fluorescence ratio imaging of cyclic AMP in single cells. *Nature* 349, 694–697. doi: 10.1038/349694a0

Agronskaia, A. V., Valentijn, J. A., van Driel, L. F., Schneijdenberg, C. T., Humbel, B. M., van Bergen en Henegouwen, P. M., et al. (2008). Integrated fluorescence and transmission electron microscopy. *J. Struct. Biol.* 164, 183–189. doi: 10.1016/j.jsb.2008.07.003

Akagi, T., Ishida, K., Hanasaka, T., Hayashi, S., Watanabe, M., Hashikawa, T., et al. (2006). Improved methods for ultracryotomy of CNS tissue for ultrastructural and immunogold analyses. *J. Neurosci. Methods* 153, 276–282. doi: 10.1016/j.jneumeth.2005.11.007

Al Jord, A., Lemaitre, A. I., Delgehyr, N., Faucourt, M., Spassky, N., and Meunier, A. (2014). Centriole amplification by mother and daughter centrioles differs in multiciliated cells. *Nature* 516, 104–107. doi: 10.1038/nature13770

Alivisatos, A. P. (1996). Semiconductor clusters, nanocrystals, and quantum dots. *Science* 271, 933–937. doi: 10.1126/science.271.5251.933

Ashkin, A. (1970). Acceleration and trapping of particles by radiation pressure. *Phys. Rev. Lett.* 24, 156–159. doi: 10.1103/PhysRevLett.24.156

Axelrod, D. (1981). Cell-substrate contacts illuminated by total internal reflection fluorescence. *J. Cell Biol.* 89, 141–145. doi: 10.1083/jcb.89.1.141

Banker, G. A., and Cowan, W. M. (1977). Rat hippocampal neurons in dispersed cell culture. *Brain Res.* 126, 297–342. doi: 10.1016/0006-8993(77)90594-7

Beck, M., Lucic, V., Forster, F., Baumeister, W., and Medalia, O. (2007). Snapshots of nuclear pore complexes in action captured by cryo-electron tomography. *Nature* 449, 611–615. doi: 10.1038/nature06170

Begemann, I., Viplav, A., Rasch, C., and Galic, M. (2015). Stochastic micro-pattern for automated correlative fluorescence – scanning electron microscopy. *Sci. Rep.* 5, 17973. doi: 10.1038/srep17973

Benedetti, L., Sogne, E., Rodighiero, S., Marchesi, D., Milani, P., and Francolini, M. (2014). Customized patterned substrates for highly versatile correlative light-scanning electron microscopy. *Sci. Rep.* 4, 7033. doi: 10.1038/srep07033

Betzig, E., and Chichester, R. J. (1993). Single molecules observed by near-field scanning optical microscopy. *Science* 262, 1422–1425. doi: 10.1126/science.262.5138.1422

Betzig, E., Patterson, G. H., Sougrat, R., Lindwasser, O. W., Olenych, S., Bonifacino, J. S., et al. (2006). Imaging intracellular fluorescent proteins at nanometer resolution. *Science* 313, 1642–1645. doi: 10.1126/science.1127344

Bishop, D., Nikic, I., Brinkoetter, M., Knecht, S., Potz, S., Kerschensteiner, M., et al. (2011). Near-infrared branding efficiently correlates light and electron microscopy. *Nat. Methods* 8, 568–570. doi: 10.1038/nmeth.1622

Bishop, D. L., Misgeld, T., Walsh, M. K., Gan, W. B., and Lichtman, J. W. (2004). Axon branch removal at developing synapses by axosome shedding. *Neuron* 44, 651–661. doi: 10.1016/j.neuron.2004.10.026

Blazquez-Llorca, L., Hummel, E., Zimmerman, H., Zou, C., Burgold, S., Rietdorf, J., et al. (2015). Correlation of two-photon in vivo imaging and FIB/SEM microscopy. *J. Microsc.* 259, 129–136. doi: 10.1111/jmi.12231

Bock, D. D., Lee, W. C., Kerlin, A. M., Andermann, M. L., Hood, G., Wetzel, A. W., et al. (2011). Network anatomy and in vivo physiology of visual cortical neurons. *Nature* 471, 177–182. doi: 10.1038/nature09802

Bosch, C., Martinez, A., Masachs, N., Teixeira, C. M., Fernaud, I., Ulloa, F., et al. (2015). FIB/SEM technology and high-throughput 3D reconstruction of dendritic spines and synapses in GFP-labeled adult-generated neurons. *Front. Neuroanat.* 9:60. doi: 10.3389/fnana.2015.00060

Boyden, E. S., Zhang, F., Bamberg, E., Nagel, G., and Deisseroth, K. (2005). Millisecond-timescale, genetically targeted optical control of neural activity. *Nat. Neurosci.* 8, 1263–1268. doi: 10.1038/nn1525

Briggman, K. L., and Bock, D. D. (2012). Volume electron microscopy for neuronal circuit reconstruction. *Curr. Opin. Neurobiol.* 22, 154–161. doi: 10.1016/j.conb.2011.10.022

Briggman, K. L., Helmstaedter, M., and Denk, W. (2011). Wiring specificity in the direction-selectivity circuit of the retina. *Nature* 471, 183–188. doi: 10.1038/nature09818

Brown, E., and Verkade, P. (2010). The use of markers for correlative light electron microscopy. *Protoplasma* 244, 91–97. doi: 10.1007/s00709-010-0165-1

Cao, C., Lu, S., Kivlin, R., Wallin, B., Card, E., Bagdasarian, A., et al. (2008). AMP-activated protein kinase contributes to UV- and H2O2-induced apoptosis in human skin keratinocytes. *J. Biol. Chem.* 283, 28897–28908. doi: 10.1074/jbc.M804144200

Castejon, O. J. (1996). Contribution of conventional and high resolution scanning electron microscopy and cryofracture technique to the study of cerebellar synaptic junctions. *Scanning Microsc.* 10, 177–186.

Castejon, O. J., and Caraballo, A. J. (1980). Application of cryofracture and SEM to the study of human cerebellar cortex. *Scan. Electron Microsc.* 4, 197–207.

Chalfie, M., Tu, Y., Euskirchen, G., Ward, W. W., and Prasher, D. C. (1994). Green fluorescent protein as a marker for gene expression. *Science* 263, 802–805. doi: 10.1126/science.8303295

Chang, Y. C., Yang, C. Y., Sun, R. L., Cheng, Y. F., Kao, W. C., and Yang, P. C. (2013). Rapid single cell detection of *Staphylococcus aureus* by aptamer-conjugated gold nanoparticles. *Sci. Rep.* 3, 1863. doi: 10.1038/srep01863

Collman, F., Buchanan, J., Phend, K. D., Micheva, K. D., Weinberg, R. J., and Smith, S. J. (2015). Mapping synapses by conjugate light-electron array tomography. *J. Neurosci.* 35, 5792–5807. doi: 10.1523/JNEUROSCI.4274-14.2015

Colombelli, J., Tangemo, C., Haselman, U., Antony, C., Stelzer, E. H., Pepperkok, R., et al. (2008). A correlative light and electron microscopy method based on laser micropatterning and etching. *Methods Mol. Biol.* 457, 203–213. doi: 10.1007/978-1-59745-261-8_15

Combs, C. A. (2010). Fluorescence microscopy: a concise guide to current imaging methods. *Curr. Protoc. Neurosci.* Chapter 2, Unit2.1. doi: 10.1002/0471142301.ns0201s50

Crewe, A. V., Wall, J., and Langmore, J. (1970). Visibility of single atoms. *Science* 168, 1338–1340. doi: 10.1126/science.168.3937.1338

Crowther, R. A., Derosier, D. J., and Klug, A. (1970). Reconstruction of 3 dimensional structure from projections and its application to electron microscopy. *Proc. R. Soc. Lond. A* 317, 319–340. doi: 10.1098/rspa.1970.0119

Dahl, R., and Staehelin, L. A. (1989). High-pressure freezing for the preservation of biological structure – theory and practice. *J. Electron Microsc. Tech.* 13, 165–174. doi: 10.1002/jemt.1060130305

Danilatos, G., Rattenberger, J., and Dracopoulos, V. (2011). Beam transfer characteristics of a commercial environmental SEM and a low vacuum SEM. *J. Microsc.* 242, 166–180. doi: 10.1111/j.1365-2818.2010.03455.x

Davila, H. V., Salzberg, B. M., Cohen, L. B., and Waggoner, A. S. (1973). A large change in axon fluorescence that provides a promising method

for measuring membrane potential. *Nat. New Biol.* 241, 159–160. doi: 10.1038/newbio241159a0

de Boer, P., Hoogenboom, J. P., and Giepmans, B. N. (2015). Correlated light and electron microscopy: ultrastructure lights up! *Nat. Methods* 12, 503–513. doi: 10.1038/nmeth.3400

De Rosier, D. J., and Klug, A. (1968). Reconstruction of three dimensional structures from electron micrographs. *Nature* 217, 130–134. doi: 10.1038/217130a0

Deerinck, T. J., Martone, M. E., Lev-Ram, V., Green, D. P., Tsien, R. Y., Spector, D. L., et al. (1994). Fluorescence photooxidation with eosin: a method for high resolution immunolocalization and in situ hybridization detection for light and electron microscopy. *J. Cell Biol.* 126, 901–910. doi: 10.1083/jcb.126.4.901

DeKosky, S. T., and Scheff, S. W. (1990). Synapse loss in frontal cortex biopsies in Alzheimer's disease: correlation with cognitive severity. *Ann. Neurol.* 27, 457–464. doi: 10.1002/ana.410270502

Denk, W., and Horstmann, H. (2004). Serial block-face scanning electron microscopy to reconstruct three-dimensional tissue nanostructure. *PLoS Biol.* 2:e329. doi: 10.1371/journal.pbio.0020329

Denk, W., Strickler, J. H., and Webb, W. W. (1990). Two-photon laser scanning fluorescence microscopy. *Science* 248, 73–76. doi: 10.1126/science.2321027

Derobertis, E. D. P., and Bennett, H. S. (1955). Some features of the submicroscopic morphology of synapses in frog and earthworm. *J. Biophys. Biochem. Cytol.* 1, 47–58. doi: 10.1083/jcb.1.1.47

Desaki, J., and Uehara, Y. (1981). The overall morphology of neuromuscular junctions as revealed by scanning electron microscopy. *J. Neurocytol.* 10, 101–110. doi: 10.1007/BF01181747

Ellis-Davies, G. C. (2011). A practical guide to the synthesis of dinitroindolinyl-caged neurotransmitters. *Nat. Protoc.* 6, 314–326. doi: 10.1038/nprot.2010.193

Ellisdavies, G. C. R., and Kaplan, J. H. (1994). Nitrophenyl-Egta, a photolabile chelator that selectively binds Ca2+ with high-affinity and releases it rapidly upon photolysis. *Proc. Natl. Acad. Sci. U.S.A.* 91, 187–191. doi: 10.1073/pnas.91.1.187

Engel, A. (1978). The STEM: an attractive tool for the biologist. *Ultramicroscopy* 3, 355–357. doi: 10.1016/S0304-3991(78)80052-7

Engelbrecht, C. J., and Stelzer, E. H. (2006). Resolution enhancement in a light-sheet-based microscope (SPIM). *Opt. Lett.* 31, 1477–1479. doi: 10.1364/OL.31.001477

Ercius, P., Alaidi, O., Rames, M. J., and Ren, G. (2015). Electron tomography: a three-dimensional analytic tool for hard and soft materials research. *Adv. Mater.* 27, 5638–5663. doi: 10.1002/adma.201501015

Erni, R., Rossell, M. D., Kisielowski, C., and Dahmen, U. (2009). Atomic-resolution imaging with a sub-50-pm electron probe. *Phys. Rev. Lett.* 102, 096101. doi: 10.1103/PhysRevLett.102.096101

Fares, M. B., Maco, B., Oueslati, A., Rockenstein, E., Ninkina, N., Buchman, V. L., et al. (2016). Induction of de novo alpha-synuclein fibrillization in a neuronal model for Parkinson's disease. *Proc. Natl. Acad. Sci. U.S.A.* 113, E912–E921. doi: 10.1073/pnas.1512876113

Fenno, L., Yizhar, O., and Deisseroth, K. (2011). The development and application of optogenetics. *Annu. Rev. Neurosci.* 34, 389–412. doi: 10.1146/annurev-neuro-061010-113817

Fifkova, E., and Delay, R. J. (1982). Cytoplasmic actin in neuronal processes as a possible mediator of synaptic plasticity. *J. Cell Biol.* 95, 345–350. doi: 10.1083/jcb.95.1.345

Galic, M., Jeong, S., Tsai, F. C., Joubert, L. M., Wu, Y. I., Hahn, K. M., et al. (2012). External push and internal pull forces recruit curvature-sensing N-BAR domain proteins to the plasma membrane. *Nat. Cell Biol.* 14, 874–881. doi: 10.1038/ncb2533

Galic, M., Tsai, F. C., Collins, S. R., Matis, M., Bandara, S., and Meyer, T. (2014). Dynamic recruitment of the curvature-sensitive protein ArhGAP44 to nanoscale membrane deformations limits exploratory filopodia initiation in neurons. *Elife* 3, e03116. doi: 10.7554/eLife.03116

Giepmans, B. N., Deerinck, T. J., Smarr, B. L., Jones, Y. Z., and Ellisman, M. H. (2005). Correlated light and electron microscopic imaging of multiple endogenous proteins using Quantum dots. *Nat. Methods* 2, 743–749. doi: 10.1038/nmeth791

Gray, E. G. (1959). Axo-somatic and axo-dendritic synapses of the cerebral cortex: an electron microscope study. *J. Anat.* 93, 420–433.

Harris, K. M., Perry, E., Bourne, J., Feinberg, M., Ostroff, L., and Hurlburt, J. (2006). Uniform serial sectioning for transmission electron microscopy. *J. Neurosci.* 26, 12101–12103. doi: 10.1523/JNEUROSCI.3994-06.2006

Hayworth, K. J., Kasthuri, N., Schalek, R., and Lichtman, J. (2006). Automating the collection of ultrathin serial sections for large volume TEM reconstructions. *Microsc. Microanal.* 12, 86–87. doi: 10.1017/S1431927606066268

Hayworth, K. J., Morgan, J. L., Schalek, R., Berger, D. R., Hildebrand, D. G., and Lichtman, J. W. (2014). Imaging ATUM ultrathin section libraries with WaferMapper: a multi-scale approach to EM reconstruction of neural circuits. *Front. Neural Circuits* 8:68. doi: 10.3389/fncir.2014.00068

Heim, R., Prasher, D. C., and Tsien, R. Y. (1994). Wavelength mutations and posttranslational autoxidation of green fluorescent protein. *Proc. Natl. Acad. Sci. U.S.A.* 91, 12501–12504. doi: 10.1073/pnas.91.26.12501

Hell, S. W., and Wichmann, J. (1994). Breaking the diffraction resolution limit by stimulated emission: stimulated-emission-depletion fluorescence microscopy. *Opt. Lett.* 19, 780–782. doi: 10.1364/OL.19.000780

Heuser, J. E., and Reese, T. S. (1973). Evidence for recycling of synaptic vesicle membrane during transmitter release at the frog neuromuscular junction. *J. Cell Biol.* 57, 315–344. doi: 10.1083/jcb.57.2.315

Heuser, J. E., Reese, T. S., and Landis, D. M. (1976). Preservation of synaptic structure by rapid freezing. *Cold Spring Harb. Symp. Quant. Biol.* 40, 17–24. doi: 10.1101/SQB.1976.040.01.004

Heuser, J. E., and Salpeter, S. R. (1979). Organization of acetylcholine receptors in quick-frozen, deep-etched, and rotary-replicated Torpedo postsynaptic membrane. *J. Cell Biol.* 82, 150–173. doi: 10.1083/jcb.82.1.150

Hollander, H. (1970). The section embedding (SE) technique. A new method for the combined light microscopic and electron microscopic examination of central nervous tissue. *Brain Res.* 20, 39–47.

Hoppe, W., Gassmann, J., Hunsmann, N., Schramm, H. J., and Sturm, M. (1974). 3-dimensional reconstruction of individual negatively stained yeast fatty-acid synthetase molecules from tilt series in electron-microscope. *Hoppe Seylers Z. Physiol. Chem.* 355, 1483–1487.

Huang, B., Babcock, H., and Zhuang, X. (2010). Breaking the diffraction barrier: super-resolution imaging of cells. *Cell* 143, 1047–1058. doi: 10.1016/j.cell.2010.12.002

Hunziker, E. B., Herrmann, W., Schenk, R. K., Mueller, M., and Moor, H. (1984). Cartilage ultrastructure after high pressure freezing, freeze substitution, and low temperature embedding. I. Chondrocyte ultrastructure–implications for the theories of mineralization and vascular invasion. *J. Cell Biol.* 98, 267–276.

Javier, D. J., Nitin, N., Levy, M., Ellington, A., and Richards-Kortum, R. (2008). Aptamer-targeted gold nanoparticles as molecular-specific contrast agents for reflectance imaging. *Bioconjug. Chem.* 19, 1309–1312. doi: 10.1021/bc8001248

Kandela, I. K., and Albrecht, R. M. (2007). Fluorescence quenching by colloidal heavy metals nanoparticles: implications for correlative fluorescence and electron microscopy studies. *Scanning* 29, 152–161. doi: 10.1002/sca.20055

Kandela, I. K., Bleher, R., and Albrecht, R. M. (2007). Multiple correlative immunolabeling for light and electron microscopy using fluorophores and colloidal metal particles. *J. Histochem. Cytochem.* 55, 983–990. doi: 10.1369/jhc.6A7124.2007

Kasthuri, N., Hayworth, K., Lichtman, J., Erdman, N., and Ackerley, C. A. (2007). New technique for ultra-thin serial brain section imaging using scanning electron microscopy. *Microsc. Microanal.* 13, 26–27. doi: 10.1017/S1431927607078002

Kasthuri, N., Hayworth, K. J., Berger, D. R., Schalek, R. L., Conchello, J. A., Knowles-Barley, S., et al. (2015). Saturated reconstruction of a volume of neocortex. *Cell* 162, 648–661. doi: 10.1016/j.cell.2015.06.054

Keller, P. J., Schmidt, A. D., Wittbrodt, J., and Stelzer, E. H. (2008). Reconstruction of zebrafish early embryonic development by scanned light sheet microscopy. *Science* 322, 1065–1069. doi: 10.1126/science.1162493

Kilgore, J. A., Dolman, N. J., and Davidson, M. W. (2013). A review of reagents for fluorescence microscopy of cellular compartments and structures, Part II: reagents for non-vesicular organelles. *Curr. Protoc. Cytom.* 66, Unit 12.31. doi: 10.1002/0471142956.cy1231s66

Kim, D., Deerinck, T. J., Sigal, Y. M., Babcock, H. P., Ellisman, M. H., and Zhuang, X. (2015). Correlative stochastic optical reconstruction microscopy and electron microscopy. *PLoS ONE* 10:e0124581. doi: 10.1371/journal.pone.0124581

Klar, T. A., Engel, E., and Hell, S. W. (2001). Breaking Abbe's diffraction resolution limit in fluorescence microscopy with stimulated emission depletion beams of various shapes. *Phys. Rev. E Stat. Nonlin. Soft. Matter. Phys.* 64, 066613. doi: 10.1103/PhysRevE.64.066613

Knott, G., and Genoud, C. (2013). Is EM dead? *J. Cell Sci.* 126, 4545–4552. doi: 10.1242/jcs.124123

Knott, G., Marchman, H., Wall, D., and Lich, B. (2008). Serial section scanning electron microscopy of adult brain tissue using focused ion beam milling. *J. Neurosci.* 28(Pt. 20), 2959–2964. doi: 10.1523/JNEUROSCI.3189-07.2008

Kopek, B. G., Shtengel, G., Xu, C. S., Clayton, D. A., and Hess, H. F. (2012). Correlative 3D superresolution fluorescence and electron microscopy reveal the relationship of mitochondrial nucleoids to membranes. *Proc. Natl. Acad. Sci. U.S.A.* 109, 6136–6141. doi: 10.1073/pnas.1121558109

Kuipers, J., de Boer, P., and Giepmans, B. N. (2015). Scanning EM of non-heavy metal stained biosamples: large-field of view, high contrast and highly efficient immunolabeling. *Exp. Cell Res.* 337, 202–207. doi: 10.1016/j.yexcr.2015.07.012

Kukulski, W., Schorb, M., Welsch, S., Picco, A., Kaksonen, M., and Briggs, J. A. (2011). Correlated fluorescence and 3D electron microscopy with high sensitivity and spatial precision. *J. Cell Biol.* 192, 111–119. doi: 10.1083/jcb.201009037

Kuwajima, M., Mendenhall, J. M., Lindsey, L. F., and Harris, K. M. (2013). Automated transmission-mode scanning electron microscopy (tSEM) for large volume analysis at nanoscale resolution. *PLoS ONE* 8:e59573. doi: 10.1371/journal.pone.0059573

Landis, D. M. D., and Reese, T. S. (1983). Cytoplasmic organization in cerebellar dendritic spines. *J. Cell Biol.* 97, 1169–1178. doi: 10.1083/jcb.97.4.1169

Lang, T. (2003). Imaging SNAREs at work in 'unroofed' cells–approaches that may be of general interest for functional studies on membrane proteins. *Biochem. Soc. Trans.* 31, 861–864. doi: 10.1042/bst0310861

Lee, W. C., Bonin, V., Reed, M., Graham, B. J., Hood, G., Glattfelder, K., et al. (2016). Anatomy and function of an excitatory network in the visual cortex. *Nature* 532, 370–374. doi: 10.1038/nature17192

Lehmann, T., Hess, M., Wanner, G., and Melzer, R. R. (2014). Dissecting a neuron network: FIB-SEM-based 3D-reconstruction of the visual neuropils in the sea spider *Achelia langi* (Dohrn, 1881) (Pycnogonida). *BMC Biol.* 12:59. doi: 10.1186/s12915-014-0059-3

Leighton, S. B. (1981). SEM images of block faces, cut by a miniature microtome within the SEM – a technical note. *Scan. Electron Microsc.* 233, 73–76.

Lenzi, D., Runyeon, J. W., Crum, J., Ellisman, M. H., and Roberts, W. M. (1999). Synaptic vesicle populations in saccular hair cells reconstructed by electron tomography. *J. Neurosci.* 19, 119–132.

Lichtman, J. W., and Conchello, J. A. (2005). Fluorescence microscopy. *Nat. Methods* 2, 910–919. doi: 10.1038/nmeth817

Liss, V., Barlag, B., Nietschke, M., and Hensel, M. (2015). Self-labelling enzymes as universal tags for fluorescence microscopy, super-resolution microscopy and electron microscopy. *Sci. Rep.* 5, 17740. doi: 10.1038/srep17740

Liv, N., Zonnevylle, A. C., Narvaez, A. C., Effting, A. P., Voorneveld, P. W., Lucas, M. S., et al. (2013). Simultaneous correlative scanning electron and high-NA fluorescence microscopy. *PLoS ONE* 8:e55707. doi: 10.1371/journal.pone.0055707

Livet, J., Weissman, T. A., Kang, H., Draft, R. W., Lu, J., Bennis, R. A., et al. (2007). Transgenic strategies for combinatorial expression of fluorescent proteins in the nervous system. *Nature* 450, 56–62. doi: 10.1038/nature06293

Los, G. V., Encell, L. P., McDougall, M. G., Hartzell, D. D., Karassina, N., Zimprich, C., et al. (2008). HaloTag: a novel protein labeling technology for cell imaging and protein analysis. *ACS Chem. Biol.* 3, 373–382. doi: 10.1021/cb800025k

Maco, B., Holtmaat, A., Cantoni, M., Kreshuk, A., Straehle, C. N., Hamprecht, F. A., et al. (2013). Correlative in vivo 2 photon and focused ion beam scanning electron microscopy of cortical neurons. *PLoS ONE* 8:e57405. doi: 10.1371/journal.pone.0057405

Martell, J. D., Deerinck, T. J., Sancak, Y., Poulos, T. L., Mootha, V. K., Sosinsky, G. E., et al. (2012). Engineered ascorbate peroxidase as a genetically encoded reporter for electron microscopy. *Nat. Biotechnol.* 30, 1143–1148. doi: 10.1038/nbt.2375

Medalia, O., Weber, I., Frangakis, A. S., Nicastro, D., Gerisch, G., and Baumeister, W. (2002). Macromolecular architecture in eukaryotic cells visualized by cryoelectron tomography. *Science* 298, 1209–1213. doi: 10.1126/science.1076184

Merchan-Perez, A., Rodriguez, J. R., Alonso-Nanclares, L., Schertel, A., and Defelipe, J. (2009). Counting Synapses Using FIB/SEM microscopy: a true revolution for ultrastructural volume reconstruction. *Front. Neuroanat.* 3:18. doi: 10.3389/neuro.05.018.2009

Micheva, K. D., and Smith, S. J. (2007). Array tomography: a new tool for imaging the molecular architecture and ultrastructure of neural circuits. *Neuron* 55, 25–36. doi: 10.1016/j.neuron.2007.06.014

Miesenbock, G., De Angelis, D. A., and Rothman, J. E. (1998). Visualizing secretion and synaptic transmission with pH-sensitive green fluorescent proteins. *Nature* 394, 192–195. doi: 10.1038/28190

Minsky, M. (1988). Memoir on inventing the confocal scanning microscope. *Scanning* 10, 128–138. doi: 10.1002/sca.4950100403

Minta, A., and Tsien, R. Y. (1989). Fluorescent indicators for cytosolic sodium. *J. Biol. Chem.* 264, 19449–19457.

Miranda, K., Girard-Dias, W., Attias, M., de Souza, W., and Ramos, I. (2015). Three dimensional reconstruction by electron microscopy in the life sciences: an introduction for cell and tissue biologists. *Mol. Reprod. Dev.* 82, 530–547. doi: 10.1002/mrd.22455

Mishchenko, Y., Hu, T., Spacek, J., Mendenhall, J., Harris, K. M., and Chklovskii, D. B. (2010). Ultrastructural analysis of hippocampal neuropil from the connectomics perspective. *Neuron* 67, 1009–1020. doi: 10.1016/j.neuron.2010.08.014

Morgan, J. L., Berger, D. R., Wetzel, A. W., and Lichtman, J. W. (2016). The fuzzy logic of network connectivity in mouse visual Thalamus. *Cell* 165, 192–206. doi: 10.1016/j.cell.2016.02.033

Muller-Reichert, T., and Verkade, P. (2014). Preface. Correlative light and electron microscopy II. *Methods Cell Biol.* 124, xvii–xviii. doi: 10.1016/B978-0-12-801075-4.09983-3

Nakai, J., Ohkura, M., and Imoto, K. (2001). A high signal-to-noise Ca(2+) probe composed of a single green fluorescent protein. *Nat. Biotechnol.* 19, 137–141. doi: 10.1038/84397

Nakai, Y., and Iwashita, T. (1976). Correlative light and electron microscopy of the frog adrenal gland cells using adjacent epon-embedded sections. *Arch. Histol. Jpn.* 39, 183–191. doi: 10.1679/aohc1950.39.183

Navlakha, S., Suhan, J., Barth, A. L., and Bar-Joseph, Z. (2013). A high-throughput framework to detect synapses in electron microscopy images. *Bioinformatics* 29, i9–i17. doi: 10.1093/bioinformatics/btt222

Neil, M. A., Juskaitis, R., and Wilson, T. (1997). Method of obtaining optical sectioning by using structured light in a conventional microscope. *Opt. Lett.* 22, 1905–1907. doi: 10.1364/OL.22.001905

Nishiyama, H., Koizumi, M., Ogawa, K., Kitamura, S., Konyuba, Y., Watanabe, Y., et al. (2014). Atmospheric scanning electron microscope system with an open sample chamber: configuration and applications. *Ultramicroscopy* 147, 86–97. doi: 10.1016/j.ultramic.2014.06.001

Ominami, Y., Kawanishi, S., Ushiki, T., and Ito, S. (2015). A novel approach to scanning electron microscopy at ambient atmospheric pressure. *Microscopy* 64, 97–104. doi: 10.1093/jmicro/dfu107

Osamura, R. Y., Itoh, Y., and Matsuno, A. (2000). Applications of plastic embedding to electron microscopic immunocytochemistry and in situ hybridization in observations of production and secretion of peptide hormones. *J. Histochem. Cytochem.* 48, 885–891. doi: 10.1177/002215540004800701

Paez-Segala, M. G., Sun, M. G., Shtengel, G., Viswanathan, S., Baird, M. A., Macklin, J. J., et al. (2015). Fixation-resistant photoactivatable fluorescent proteins for CLEM. *Nat. Methods* 12, 215–218. doi: 10.1038/nmeth.3225

Pappas, G. D., and Bennett, M. V. L. (1966). Specialized junctions involved in electrical transmission between neurons. *Ann. N. Y. Acad. Sci.* 137, 495–508. doi: 10.1111/j.1749-6632.1966.tb50177.x

Peddie, C. J., Blight, K., Wilson, E., Melia, C., Marrison, J., Carzaniga, R., et al. (2014). Correlative and integrated light and electron microscopy of in-resin GFP fluorescence, used to localise diacylglycerol in mammalian cells. *Ultramicroscopy* 143, 3–14. doi: 10.1016/j.ultramic.2014.02.001

Penczek, P. A. (2010). Fundamentals of three-dimensional reconstruction from projections. *Methods Enzymol.* 482, 1–33. doi: 10.1016/S0076-6879(10)82001-4

Perkins, G. A., Jackson, D. R., and Spirou, G. A. (2015). Resolving presynaptic structure by electron tomography. *Synapse* 69, 268–282. doi: 10.1002/syn.21813

Phend, K. D., Rustioni, A., and Weinberg, R. J. (1995). An osmium-free method of epon embedment that preserves both ultrastructure and antigenicity for post-embedding immunocytochemistry. *J. Histochem. Cytochem.* 43, 283–292. doi: 10.1177/43.3.7532656

Pierce, L., and Buseck, P. R. (1974). Electron imaging of pyrrhotite superstructures. *Science* 186, 1209–1212. doi: 10.1126/science.186.4170.1209

Porter, K. R., Claude, A., and Fullam, E. F. (1945). A study of tissue culture cells by electron microscopy: methods and preliminary observations. *J. Exp. Med.* 81, 233–246. doi: 10.1084/jem.81.3.233

Rah, J. C., Bas, E., Colonell, J., Mishchenko, Y., Karsh, B., Fetter, R. D., et al. (2013). Thalamocortical input onto layer 5 pyramidal neurons measured using quantitative large-scale array tomography. *Front. Neural Circuits* 7:177. doi: 10.3389/fncir.2013.00177

Rayleigh (1879). Investigations in optics, with special reference to the spectroscope. *Phil. Mag.* 8, 261–274. doi: 10.1080/14786447908639715

Ries, J., Kaplan, C., Platonova, E., Eghlidi, H., and Ewers, H. (2012). A simple, versatile method for GFP-based super-resolution microscopy via nanobodies. *Nat. Methods* 9, 582–584. doi: 10.1038/nmeth.1991

Ross, F. M. (2015). Opportunities and challenges in liquid cell electron microscopy. *Science* 350, aaa9886. doi: 10.1126/science.aaa9886

Rost, B. R., Schneider, F., Grauel, M. K., Wozny, C., Bentz, C. G., Blessing, A., et al. (2015). Optogenetic acidification of synaptic vesicles and lysosomes. *Nat. Neurosci.* 18, 1845–1852. doi: 10.1038/nn.4161

Ruska, E. (1987). Nobel lecture. The development of the electron microscope and of electron microscopy. *Biosci. Rep.* 7, 607–629.

Rust, M. J., Bates, M., and Zhuang, X. W. (2006). Sub-diffraction-limit imaging by stochastic optical reconstruction microscopy (STORM). *Nat. Methods* 3, 793–795. doi: 10.1038/nmeth929

Shimomura, O., Johnson, F. H., and Saiga, Y. (1962). Extraction, purification and properties of aequorin, a bioluminescent protein from the luminous hydromedusan, *Aequorea*. *J. Cell Comp. Physiol.* 59, 223–239. doi: 10.1002/jcp.1030590302

Shu, X., Lev-Ram, V., Deerinck, T. J., Qi, Y., Ramko, E. B., Davidson, M. W., et al. (2011). A genetically encoded tag for correlated light and electron microscopy of intact cells, tissues, and organisms. *PLoS Biol.* 9:e1001041. doi: 10.1371/journal.pbio.1001041

Shui, B., Ozer, A., Zipfel, W., Sahu, N., Singh, A., Lis, J. T., et al. (2012). RNA aptamers that functionally interact with green fluorescent protein and its derivatives. *Nucleic Acids Res.* 40, e39. doi: 10.1093/nar/gkr1264

Siegel, M. S., and Isacoff, E. Y. (1997). A genetically encoded optical probe of membrane voltage. *Neuron* 19, 735–741. doi: 10.1016/S0896-6273(00)80955-1

Sochacki, K. A., Shtengel, G., van Engelenburg, S. B., Hess, H. F., and Taraska, J. W. (2014). Correlative super-resolution fluorescence and metal-replica transmission electron microscopy. *Nat. Methods* 11, 305–308. doi: 10.1038/nmeth.2816

Sonomura, T., Furuta, T., Nakatani, I., Yamamoto, Y., Unzai, T., Matsuda, W., et al. (2013). Correlative analysis of immunoreactivity in confocal laser-scanning microscopy and scanning electron microscopy with focused ion beam milling. *Front. Neural Circuits* 7:26. doi: 10.3389/fncir.2013.00026

Stauffer, T. P., Ahn, S., and Meyer, T. (1998). Receptor-induced transient reduction in plasma membrane PtdIns(4,5)P2 concentration monitored in living cells. *Curr. Biol.* 8, 343–346. doi: 10.1016/S0960-9822(98)70135-6

Svitkina, T. (2009). Imaging cytoskeleton components by electron microscopy. *Methods Mol. Biol.* 586, 187–206. doi: 10.1007/978-1-60761-376-3_10

Svitkina, T. M., Verkhovsky, A. B., and Borisy, G. G. (1995). Improved procedures for electron microscopic visualization of the cytoskeleton of cultured cells. *J. Struct. Biol.* 115, 290–303. doi: 10.1006/jsbi.1995.1054

Szczesny, P. J., Walther, P., and Muller, M. (1996). Light damage in rod outer segments: the effects of fixation on ultrastructural alterations. *Curr. Eye. Res.* 15, 807–814. doi: 10.3109/02713689609017621

Tanasugarn, L., McNeil, P., Reynolds, G. T., and Taylor, D. L. (1984). Microspectrofluorometry by digital image processing: measurement of cytoplasmic pH. *J. Cell Biol.* 98, 717–724. doi: 10.1083/jcb.98.2.717

Terasaki, M., Shemesh, T., Kasthuri, N., Klemm, R. W., Schalek, R., Hayworth, K. J., et al. (2013). Stacked endoplasmic reticulum sheets are connected by helicoidal membrane motifs. *Cell* 154, 285–296. doi: 10.1016/j.cell.2013.06.031

Tischer, D., and Weiner, O. D. (2014). Illuminating cell signalling with optogenetic tools. *Nat. Rev. Mol. Cell Biol.* 15, 551–558. doi: 10.1038/nrm3837

Tocheva, E. I., Li, Z., and Jensen, G. J. (2010). Electron cryotomography. *Cold Spring Harb. Perspect. Biol.* 2, a003442. doi: 10.1101/cshperspect.a003442

Tsien, R. Y. (1980). New calcium indicators and buffers with high selectivity against magnesium and protons: design, synthesis, and properties of prototype structures. *Biochemistry* 19, 2396–2404. doi: 10.1021/bi00552a018

Tsien, R. Y. (1981). A non-disruptive technique for loading calcium buffers and indicators into cells. *Nature* 290, 527–528. doi: 10.1038/290527a0

Tsien, R. Y., Pozzan, T., and Rink, T. J. (1982). Calcium homeostasis in intact lymphocytes: cytoplasmic free calcium monitored with a new, intracellularly trapped fluorescent indicator. *J. Cell Biol.* 94, 325–334. doi: 10.1083/jcb.94.2.325

Urwyler, O., Izadifar, A., Dascenco, D., Petrovic, M., He, H. H., Ayaz, D., et al. (2015). Investigating CNS synaptogenesis at single-synapse resolution by combining reverse genetics with correlative light and electron microscopy. *Development* 142, 394–405. doi: 10.1242/dev.115071

Van de Broek, B., Devoogdt, N., D'Hollander, A., Gijs, H. L., Jans, K., Lagae, L., et al. (2011). Specific cell targeting with nanobody conjugated branched gold nanoparticles for photothermal therapy. *ACS Nano* 5, 4319–4328. doi: 10.1021/nn1023363

van Donselaar, E., Posthuma, G., Zeuschner, D., Humbel, B. M., and Slot, J. W. (2007). Immunogold labeling of cryosections from high-pressure frozen cells. *Traffic* 8, 471–485. doi: 10.1111/j.1600-0854.2007.00552.x

Vernon-Parry, K. D. (2000). Scanning electron microscopy: an Introduction. *III-Vs Rev.* 13, 40–44. doi: 10.1016/S0961-1290(00)80006-X

Wang, S. S. H., and Augustine, G. J. (1995). Confocal imaging and local photolysis of caged compounds – dual probes of synaptic function. *Neuron* 15, 755–760. doi: 10.1016/0896-6273(95)90167-1

Watanabe, S., Liu, Q., Davis, M. W., Hollopeter, G., Thomas, N., Jorgensen, N. B., et al. (2013). Ultrafast endocytosis at *Caenorhabditis elegans* neuromuscular junctions. *Elife* 2, e00723. doi: 10.7554/eLife.00723

Watanabe, S., Punge, A., Hollopeter, G., Willig, K. I., Hobson, R. J., Davis, M. W., et al. (2011). Protein localization in electron micrographs using fluorescence nanoscopy. *Nat. Methods* 8, 80–84. doi: 10.1038/nmeth.1537

Watanabe, S., Trimbuch, T., Camacho-Perez, M., Rost, B. R., Brokowski, B., Sohl-Kielczynski, B., et al. (2014). Clathrin regenerates synaptic vesicles from endosomes. *Nature* 515, 228–233. doi: 10.1038/nature13846

Watkins, R. E. J., Rockett, P., Thoms, S., Clampitt, R., and Syms, R. (1986). Focused ion-beam milling. *Vacuum* 36, 961–967. doi: 10.1016/0042-207x(86)90148-X

White, J. G., Southgate, E., Thomson, J. N., and Brenner, S. (1986). The structure of the nervous system of the nematode *Caenorhabditis elegans*. *Philos. Trans. R. Soc. Lond. B Biol. Sci.* 314, 1–340. doi: 10.1098/rstb.1986.0056

Zhang, H., and Liu, K. K. (2008). Optical tweezers for single cells. *J. R. Soc. Interface* 5, 671–690. doi: 10.1098/rsif.2008.0052

Zochowski, M., Wachowiak, M., Falk, C. X., Cohen, L. B., Lam, Y. W., Antic, S., et al. (2000). Imaging membrane potential with voltage-sensitive dyes. *Biol. Bull.* 198, 1–21. doi: 10.2307/1542798

Conflict of Interest Statement: The authors declare that the research was conducted in the absence of any commercial or financial relationships that could be construed as a potential conflict of interest.

frontiers in Synaptic Neuroscience

REVIEW
published: 30 June 2016
doi: 10.3389/fnsyn.2016.00016

Advanced Fluorescence Protein-Based Synapse-Detectors

Hojin Lee[1,2†], *Won Chan Oh*[1†], *Jihye Seong*[2,3*] *and Jinhyun Kim*[1,2*]

[1] Center for Functional Connectomics, Korea Institute of Science and Technology, Seoul, South Korea, [2] Neuroscience Program, Korea University of Science and Technology, Daejeon, South Korea, [3] Center for Diagnosis Treatment Care of Dementia, Korea Institute of Science and Technology, Seoul, South Korea

The complex information-processing capabilities of the central nervous system emerge from intricate patterns of synaptic input-output relationships among various neuronal circuit components. Understanding these capabilities thus requires a precise description of the individual synapses that comprise neural networks. Recent advances in fluorescent protein engineering, along with developments in light-favoring tissue clearing and optical imaging techniques, have rendered light microscopy (LM) a potent candidate for large-scale analyses of synapses, their properties, and their connectivity. Optically imaging newly engineered fluorescent proteins (FPs) tagged to synaptic proteins or microstructures enables the efficient, fine-resolution illumination of synaptic anatomy and function in large neural circuits. Here we review the latest progress in fluorescent protein-based molecular tools for imaging individual synapses and synaptic connectivity. We also identify associated technologies in gene delivery, tissue processing, and computational image analysis that will play a crucial role in bridging the gap between synapse- and system-level neuroscience.

OPEN ACCESS

Edited by:
George Augustine,
National Technical University,
Singapore

Reviewed by:
Lucas Pozzo-Miller,
The University of Alabama at Birmingham, USA
Maurizio Giustetto,
University of Torino, Italy

***Correspondence:**
Jihye Seong
jseong@kist.re.kr
Jinhyun Kim
jinnykim@me.com

†Co-first author.

Received: 09 May 2016
Accepted: 13 June 2016
Published: 30 June 2016

Citation:
Lee H, Oh WC, Seong J and Kim J (2016) Advanced Fluorescence Protein-Based Synapse-Detectors. Front. Synaptic Neurosci. 8:16. doi: 10.3389/fnsyn.2016.00016

Keywords: fluorescent protein sensors, synaptic connectivity, synapses, gene delivery, mapping and localization, light microscopy

INTRODUCTION

The synapse is the primary site for neurons to make functional contacts for exchanging information. The term "synapse", meaning conjunction in Greek (synapsis = together + to fasten), was coined in 1897 by the eminent physiologist Charles Scott Sherrington (Nobel Laureate 1932). But the idea that synapses play critical roles as dynamically polarized, communication contacts was proposed

Abbreviations: 3′UTR, 3′ untranslated region; AMPAR, α-amino-hydroxy-5-methyl-4-isoxazolepropionic acid receptor; CA3, Cornu Ammonis 3; CALI, chromophore-assisted light inactivation; CaMKII, calcium/calmodulin-dependent kinase II; CFP, Cyan fluorescent protein; CD4, cluster of differentiation 4; ChR, Channelrhodopsin; CRISPR, clustered regularly-interspaced short palindromic repeats; ENABLED, endogenous labeling via exon duplication; EM, electron microscopy; FMN, flavin mononucleotide; FP, fluorescent protein; fSPIM, fluorescent selective plane illumination microscopy; GFP, green fluorescent protein; HA, hemagglutinin; HSV-1, Herpes simplex virus-1; iDISCO, immunolabeling-enabled three-dimensional imaging of solvent-cleared organs; ID-PRIME, Interaction-Dependent Probe Incorporation Mediated by Enzymes; InSynC, Inhibition of Synaptic Release with CALI; KI, knock-in; LAP, lipoic acid acceptor peptide; LM, light microscopy; LOV2, light, oxygen, and voltage 2; LpIA, lipoic acid ligase; mGluR, metabotropic glutamate receptors; mGRASP, Mammalian GFP Reconstitution Across Synaptic Partners; miniSOG, mini small singlet oxygen generator; NCBI, National Center for Biotechnology Information; NS3, Nonstructural protein 3; OFP, Orange fluorescent protein; PDZ, PSD-95, Drosophila disc large tumor suppressor (Dlg1), and zonula occludens-1 protein (zo-1); PSD-95, postsynaptic density protein-95; rAAV, recombinant adeno-associated virus; SM protein, Sec1/Munc18-like protein; SNARE, SNAP (Soluble N-ethylmaleimide-sensitive factor attachment protein) Receptor; syb, synaptobrevin; spGFP, split-GFP; sypHTomato, Synaptophysin-fused pHTomato; TimeSTAMP, Time-Specific Tagging for the Age Measurement of Proteins; VAMP2, vesicle-associated membrane protein 2; VenusNT, Venus N-terminal; VenusCT, Venus C-terminal; VGluT, vesicular glutamate transporter; YFP, Yellow fluorescent protein.

by Santiago Ramon y Cajal (Nobel Laureate 1906). Since then, the synapse as a structural and functional communication unit has been in the spotlight of neuroscientific inquiry (Cowan et al., 2001). In fact, many studies have demonstrated that synaptic events, such as changes in molecular composition, structure, efficacy, and potentiation, play important roles in brain functions including memory formation, perception, and other complex behaviors (Tsien et al., 1996; Markram et al., 1997; Malinow and Malenka, 2002; Russo et al., 2010; Caroni et al., 2014). An important focus has been to visualize the synapse and to measure its activity. In 1954, DeRobertis and Palay first observed synapses independently by electron microscopy (EM) and George Gray suggested there may be different types of synapses, i.e., excitatory and inhibitory (De Robertis and Bennett, 1955; Palay and Palade, 1955; Palay, 1956; Gray, 1959). EM provides enough resolution for nanometer-scale imaging of the synaptic ultrastructure, something that cannot be achieved by light microscopy (LM) because of its diffraction limit. However, despite recent advances that have reduced the time needed for image acquisition and reconstruction, EM remains inherently time-consuming, labor-intensive, and volume-limited for large neural circuits.

With the recent engineering of fluorescent proteins (FPs) and new developments in light-favoring tissue clearing and advanced optical methods, LM is rising as a potent alternative tool for investigating individual synapses in the context of neural networks (Gray, 1959; Keller et al., 2008; Kim et al., 2012; Tomer et al., 2012; Chung et al., 2013; Richardson and Lichtman, 2015). Imaging the synapse with LM by using newly engineered FPs tagged to synaptic proteins or targeted to synaptic structures enables fine-resolution illumination of synaptic anatomy and function in large neural circuits, possibly in real-time. In this review, we describe recent FP-based molecular tools for imaging individual synapses and synaptic connectivity in the contexts of single- and dual component synaptic detection. We also identify crucial technologies: gene delivery of molecular synapse detector; tissue clearing for whole-brain imaging; and computational analysis, whose parallel development has potential to bridge synaptic sensor engineering and systems neuroscience. We end by proposing a scheme of technological integration for synaptic neuroscience at the systems level.

SINGLE COMPONENT SYNAPTIC DETECTION

The discovery of green fluorescent protein (GFP) and its derivatives revolutionized the visualization of biological phenomena, including the individual synapse and its functions. GFP and other FPs are relatively inert and small (27 kDa) and can be used to tag synaptic proteins while minimally interfering with their normal functions. In fact, the distribution, trafficking, and physiological changes of synaptic proteins caused by neural activity became evident in the last two decades, largely through observations of synaptic proteins, such as synaptophysin (Li and Murthy, 2001) vesicle-associated membrane protein 2 (VAMP2; Ahmari et al., 2000), postsynaptic density protein-95 (PSD-95; Nelson et al., 2013) calcium/calmodulin-dependent kinase II (CaMKII; Shen et al., 2000), α-amino-hydroxy-5-methyl-4-isoxazolepropionic acid receptor (AMPAR; Zamanillo et al., 1999) and so forth, that had been tagged with FPs. Recently, sophisticated molecular engineering has allowed even more precise and detailed visualization of synaptic structure, composition, and physiology (Chen et al., 2014; Fortin et al., 2014; **Figure 1**, **Table 1**).

pH-Sensitive FPs for Visualizing Vesicle Release: pHluorin, pHTomato, and pHuji

Although previous, straightforward, FP-based detection of synaptic distribution revealed many important details of synaptic physiology, synaptic vesicle release/recycling and neural activity-driven changes in membrane-bound synaptic proteins are difficult to be detected by regular FP-tagging. Special sensors of vesicle secretion and neurotransmission have been developed by linking vesicle membrane proteins with pH-sensitive mutants of GFP called pHlourin (Miesenböck et al., 1998). The fluorescence intensity of pHluorin largely depends on the pH of its biochemical environment: in acidic environments with pH below 6.5, pHluorin is mostly nonfluorescent in 480 nm of light illumination, but becomes highly fluorescent in neutral environments with pH around 7.4. This special feature of pHluorin was achieved by several mutations on residues important for the proton-relay of tyrosine 66 in the chromophore (S147D, N149Q, T161I, S202F, and Q204T). These amino acid substitutions, which set the pKa of pHluorin to around 7.0, can facilitate the pH-dependent switching of the electrostatic environment of the chromophore, allowing the pH-dependent changes in fluorescent intensity (Sankaranarayanan and Ryan, 2000). When pHluorin is fused to presynaptic vesicle proteins such as VAMP2 (Miesenböck et al., 1998), synaptophysin (Zhu et al., 2009), and vesicular glutamate transporter (vGluT; Voglmaier et al., 2006), the release and recycle of synaptic vesicles can be monitored as the pH inside the synaptic vesicles (∼5.5) transitions to the pH of the extracellular environment (∼7.4). Thus, by tracking changes in pHluorin fluorescence intensity, one can detect real-time presynaptic exocytosis in living, active neurons. Similarly, postsynaptic endo-/exo-cytosis and related receptor dynamics can be visualized by pHluorin-fused mGluRs, for instance (Pelkey et al., 2007).

More recently, red pH-sensitive FPs such as pHTomato (Li and Tsien, 2012) and pHuji (Shen et al., 2014) have been developed, allowing for the simultaneous monitoring of multiple synaptic activities when combined with the green GFP-based sensors (e.g., GCaMP). pHTomato (pKa ∼ 7.8) was derived from mStrawberry by introducing six mutations (F41T, F83L, S182K, I194K, V195T, and G196D). Synaptophysin-fused pHTomato (sypHTomato) has been shown to be suitable for simultaneously monitoring the fusion of synaptic vesicles and, when paired with GCaMP3, postsynaptic Ca^{2+} changes in living neurons. In addition, multiple synaptic events have been successfully measured by using sophisticated combinations of these pH-sensitive FP-fused synaptic proteins and spectrally distinct variants of optogentic stimulators (ChR2-T2A-vGluT-pHlourin

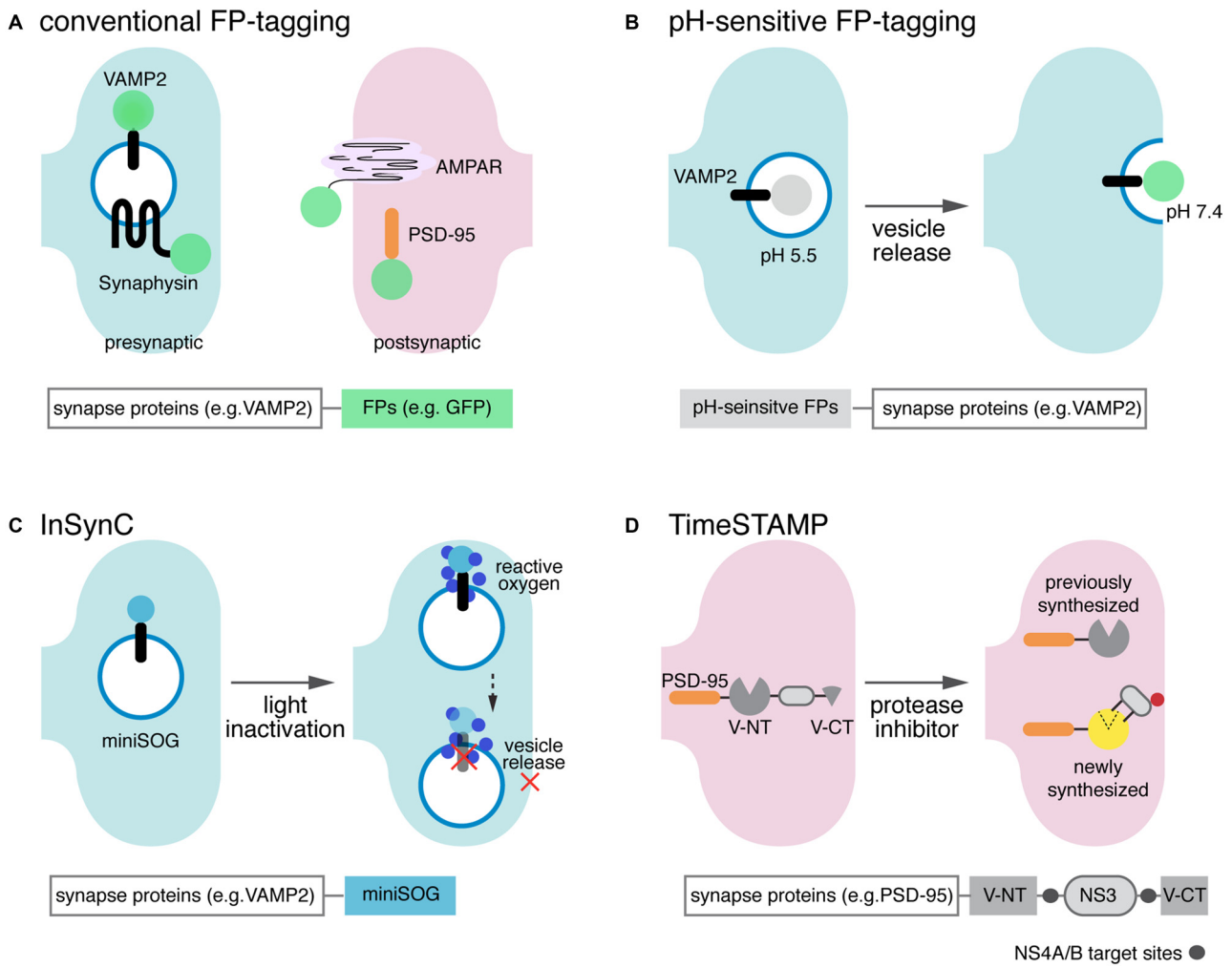

FIGURE 1 | Scheme of single component synapse detectors. (A) Graphical depiction of the conventional green fluorescent protein (GFP) tagging scheme and summary of the expressed carrier-sensor construct. GFP (green circle) and other fluorescent proteins (FPs) are directly tagged to synaptic proteins in the presynaptic terminal or postsynaptic spines. Major targets for tagging include presynaptic vesicle proteins (e.g., vesicle-associated membrane protein 2 (VAMP2) and synaptophysin), postsynaptic receptors (e.g., α-amino-hydroxy-5-methyl-4-isoxazolepropionic acid receptor, AMPAR) and postsynaptic density protein-95 (PSD-95). **(B)** pH-sensitive FP mutants are fused to synaptic vesicle membrane proteins, such as VAMP2, to visualize vesicle secretion/recycling and neurotransmission. A pH-sensitive GFP variant, pHluorin does not fluoresce (gray circle) when inside the acidic chemical environment of the synaptic vesicle, but becomes highly fluorescent (green circle) when the vesicle is released and exposed to the neutral extracellular environment. **(C)** Inhibition of Synaptic Release with CALI (InSynC): attached to target SNARE proteins, molecular actuators such as mini small singlet oxygen generator (miniSOG; light blue filled-in circle) selectively inactivate specific synaptic proteins that regulate vesicle release and other synaptic events. When illuminated with blue light, miniSOG stimulates generation of reactive oxygen species (small, dark blue filled-in circles), which then oxidizes susceptible amino acid residues in target vesicle proteins and deactivates protein functions. **(D)** TimeSTAMP effectively tracks spatiotemporally controlled protein synthesis and trafficking in living neurons. In the presence of a membrane-permeable protease inhibitor, NS3 protease (gray oval) activity is inhibited, and Venus C-terminus (Venus CT) and Venus N-terminus (Venus NT) reconstitute as fluorescent Venus (yellow circle). Reconstituted Venus accumulates in the postsynaptic spine, the trafficking destination of the fused PSD-95. When the protease inhibitor is present, however, NS3 protease cleaves the protease target sites (gray circles flanking NS3), preventing Venus reconstitution.

and VChR1-T2A-synpHTomato). However, the pH-sensitivity of pHTomato is relatively low (3-fold change in pH 5.5–7.5). Thus, a new red pH-sensitive FP, named pHuji, has been more recently derived from mApple (Shaner et al., 2008) by including a K163Y mutation, resulting in high pH sensitivity (20-fold change in pH 5.5–7.5). The use of different colored pH-sensitive FPs together with a Ca^{2+} indicator and/or a spectrally distinct optogenetic modulator offers a new promising readout system for complex, coordinated synaptic events.

Inhibition of Synaptic Release with CALI (InSynC)

Beyond merely visualizing the distributions and endo-/exocytosis of synaptic proteins by tagging them with FPs and their pH-sensitive variants, genetically encoded chromophore-assisted light inactivation (CALI) has been developed to selectively inactivate specific synaptic protein functions that regulate synaptic events such as synaptic release (Lin et al., 2013). CALI is based on light-induced generation of reactive oxygen and the

consequent inactivation of nearby attached synaptic proteins. Its original agents were synthetic chromophores for example malachite green (Jay, 1988), fluorescein (Beck et al., 2002), FlAsH (Marek and Davis, 2002), ReAsH (Tour et al., 2003), and eosin (Takemoto et al., 2011) and FPs such as KillerRed (Bulina et al., 2006). To precisely inhibit synaptic release with improved target specificity and inactivation efficiency compared to these CALI agents, inhibition of synaptic release with CALI (InSynC) has been recently developed using a newly engineered flavoprotein called mini small singlet oxygen generator (miniSOG), fused with the SNARE proteins VAMP2 and synaptophysin (Lin et al., 2013). miniSOG was originally derived from the light, oxygen, and voltage 2 (LOV2) domain of phototropin, a blue light photoreceptor (Shu et al., 2011). Under blue light illumination, this photoreceptor binds to and excites flavin mononucleotide (FMN), which then functions as an oxygen generator in cells. miniSOG contains the single amino acid substitution of FMN-binding residue Cys426 to Gly on the LOV2 domain, allowing for more efficient energy transfer to FMN, and contains further mutations for enhanced brightness. When illuminated by blue light, synaptic proteins can be selectively inactivated by miniSOG-mediated oxidization of susceptible residues such as tryptophan, tyrosine, histidine, cysteine, and methionine. InSynC by miniSOG can selectively inhibit vesicle release at individual synapses *in vitro* and *in vivo* thanks to the high efficiency of its light-induced oxygen generation, independence of exogenous cofactors, and small size (106 residues, 14 kDa; Lin et al., 2013). However, further engineering is required for investigating the functional dynamics of synaptic circuits with physiologically relevant temporal resolutions, as inactivation by InSynC persists relatively long (∼1 h) after light stimulation.

Time-Specific Tagging for the Age Measurement of Proteins (TimeSTAMP)

Another new strategy beyond merely visualizing synaptic proteins by tagging with FPs is time-specific tagging for the age measurement of proteins (TimeSTAMP; Lin et al., 2008). As spatiotemporally controlled protein synthesis and trafficking are critical for synaptogenesis, synaptic connectivity, and long-lasting changes in synapses, TimeSTAMP is beneficial for tracking important, newly synthesized synaptic proteins such as PSD-95 and CaMKII in living neurons. TimeSTAMP is a drug-controllable, time-specific tagging strategy based on the hepatitis C virus NS3 protease and its cell-permeable inhibitor BILN-2061. PSD-95-GFP, for example, was fused to NS3 protease flanked by NS4A/B target sites and the C-terminal HA tag (PSD-95-GFP-TS-HA). In the absence of the specific inhibitor BILN-2061, NS3 protease cleaves the NS4A/B target sites allowing the C-terminal HA-tag to be cleaved from PSD-95-GFP and degraded; but drug application will allow the HA-tag to be accumulated. This allows distinguishing between newly and previously synthesized PSD-95 by measuring HA/GFP signals at a time defined by the drug application. For the TimeSTAMP strategy, the NS3 protease domain was chosen because it is small (19 kDa) and monomeric, specific to its substrate, and not cytotoxic, and most of all, NS3 shows high selectivity and efficiency of its cell-permeable inhibitor.

Although the first version of TimeSTAMP has worked successfully in primary hippocampal neurons to track PSD-95 accumulation during synaptic growth, and in *Drosophila* for whole-brain mapping of newly synthesized CaMKII, it required *post hoc* immunostaining against epitope tags, limiting the benefits of pulse-chase labeling through time. Thus, TimeSTAMP2 has been introduced, replacing HA-tag with split-fluorescence proteins (e.g., Yellow fluorescent protein, YFP; Orange fluorescent protein, OFP). In fluorescent TimeSTAMP2, for instance, Venus yellow fluorescent protein is separated by an NS3 domain flanked by NS4A/B target sites into VenusNT (1-158 aa) and VenusCT (159-238 aa) for drug-dependent fluorescence. In the absence of BILN-2061, VenusCT is cleaved and degraded by the active NS domain resulting in no yellow fluorescence, while VenusNT and CT are reconstituted as fluorescent forms after drug application. This allows optical pulse labeling of synaptic proteins such as PSD-95 and Neuroligin with a drug-defined temporal resolution. Additionally, photo-oxidizing TimeSTAMP using miniSOG inserted into TS:YFP can be used to visualize new proteins at an EM-based ultrastructural level (Butko et al., 2012).

DUAL COMPONENT SYNAPTIC DETECTION

Thus far, we have described methods for detecting synapses by labeling single components, either pre- or post-synaptic. Although these single-component tools allow for detecting, measuring, and manipulating synaptic structures and activities, they do not address the critical fact that synapses are bilateral microstructures involving *both* presynaptic terminal and postsynaptic density. For reliable synapse detection, therefore, several recent studies introduced new methods for labeling synaptic interactions between pre- and post-synaptic components, such as using split-FPs or enzymes to label neurexin-neuroligin interactions. Here we review dual-component methods using handshaking-like transmembrane molecular interaction across the synaptic cleft, with particular attention to GFP Reconstitution Across Synaptic Partners (GRASP; **Figure 2**, **Table 1**).

Mammalian GFP Reconstitution Across Synaptic Partners (mGRASP)

To detect particular synaptic connections with LM, the Mammalian GFP Reconstitution Across Synaptic Partners (mGRASP) technique takes advantage of the complementarity of two non-fluorescent split-GFP fragments, each of which is tethered specifically to the pre- and postsynaptic membrane, respectively (Kim et al., 2012). When two neurons, each expressing one of the fragments, are closely opposed across a

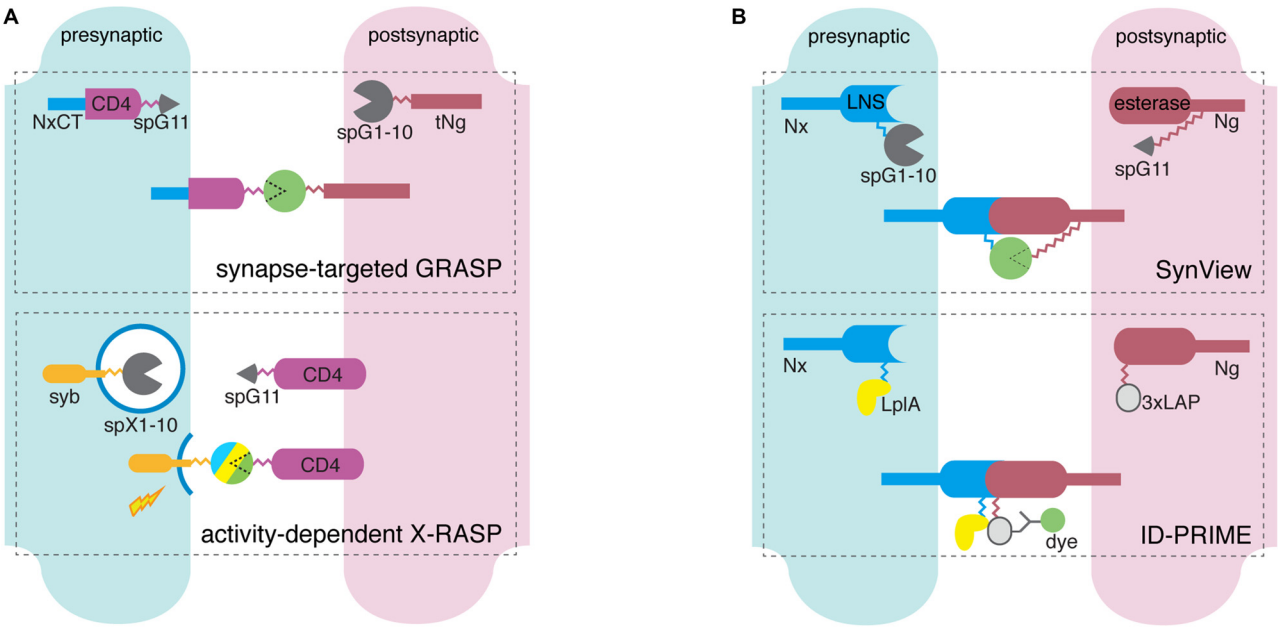

FIGURE 2 | Scheme of dual component synapse detectors. (A) GFP reconstitution-dependent molecular tools detect pre- and postsynaptic membrane apposition through the reconstitution of spGFP fragments each attached to the extracellular ends of membrane protein carriers. Synapse-targeted GFP Reconstitution Across Synaptic Partners (GRASP) utilizes a presynaptic component of spGFP11 (spG11, circular wedge) linked to a CD4-neurexin-1β C-terminus (NxCT) fusion through flexible peptide linkers (gray zigzag), and a postsynaptic component of spGFP1-10 (spG1-10) and truncated neuroligin-1 (tNg) connected with a linker. SpG11 and spG1-10 unite at synapses, not random membrane contacts. In activity-dependent X-RASP the presynaptic split-XFP1-10 (spX1-10) is fused to SNARE proteins such as synaptobrevin (syb), and unites with CD4-bound spG11 when presynaptic activity triggers vesicle release. **(B)** Neurexin (Nx)-neuroligin (Ng) interaction-dependent molecular tools detect individual synapses through fluorescent protein (FP)-based (SynView) and enzymatic reaction-based (Interaction-Dependent Probe Incorporation Mediated by Enzymes, ID-PRIME) direct visualization of Nx-Ng interaction. In SynView, spG11 is inserted between the esterase and proximal extracellular domain of Ng, and spG1-10 in the middle of the LNS domain of Nx. GFP reconstitutes when Nx and Ng unites. ID-PRIME uses the identical set of synaptic protein carriers, but tandem LAP tags (3xLAP) and lipoic acid ligase A (LplA) are attached to C-terminus of Ng esterase domain and Nx LNS domain, respectively. Nx-Ng interaction initiates LplA-mediated lipoic acid tagging to 3xLAP, and signals useful for imaging originate from antibody-fluorophore conjugates.

synaptic cleft, the split fragments are reconstituted as fluorescent GFP in that location. This dual component synapse detection bypasses the Abbe's diffraction limit and allows relatively rapid and accurate synapse mapping with LM. This method takes advantage of the fast folding kinetics and stability after maturation of superfolder GFP (Pédelacq et al., 2006), split into two fragments, namely spGFP1-10 (first 214 residues comprising ten β barrels) and spGFP11 (16 residues, 11th β-barrel strand). The GRASP technique was initially implemented in *C. elegans* (Feinberg et al., 2008; Park et al., 2011) and later in *Drosophila* (Gordon and Scott, 2009; Fan et al., 2013; Gorostiza et al., 2014). In the original GRASP constructs, membrane carriers (human CD4) for split-GFP fragments were not synapse-specific—fluorescence could arise wherever any membranes expressing fragment pairs were closely apposed. This became a critical issue for mammalian synapse detection because the mammalian nervous system contains much more compactly intermingled neurites than the invertebrate nervous system.

In a previous study, we engineered and successfully applied mGRASP for mapping fine-scale synaptic connectivity in the mouse brain (Kim et al., 2012). The primary features of mGRASP include targeting specific synapses, and matching the approximately 20 nm-wide synaptic cleft without gross changes in endogenous synaptic organization and physiology. Based on published sequences from NCBI, we generated synapse-specific chimeric carriers. Both the pre- and postsynaptic mGRASP components share a common six-subcomponent framework: (1) a signal peptide; (2) a split-GFP fragment; (3) an extracellular domain; (4) a transmembrane domain; (5) an intracellular domain; and (6) a fluorescent protein for neurite and soma visualization. The presynaptic mGRASP component consists of the signal peptide of nematode β-integrin (PAT-3, residues 1–29), GFP β-strand 11 (spGFP11, 16 residues), two flexible GGGGS linkers, the extracellular and transmembrane domains of human CD4-2 (residues 25–242). Rat neurexin-1β (residues 414–468) containing the PDZ-binding motif constitutes the intracellular domain for maintenance of correct localization at the presynaptic site. mCerulean is fused to the intracellular end of the presynaptic mGRASP to visualize axonal expression. The postsynaptic mGRASP component is based primarily on mouse neuroligin-1, which interacts with presynaptic adhesion proteins including β-neurexins, and mediates the formation and maintenance of synapses between neurons. To prevent nonspecific synaptogenesis through interactions with its

TABLE 1 | Summarized methods of single and dual component synapse detection.

	Single component			Dual component				
	Synaptic release-detecting FPs	**InSynC**	**TimeSTAMP**	**GRASP**	**mGRASP**	**Syb:GRASP XRASP**	**SynView**	**ID-PRIME**
Detection/working module	pH-sensitive FPs: pHluorin, pHTomato	miniSOG-generated reactive oxygen	Reconstitution of VenusNT and VenusCT	Reconstitution of spGFP1-10 and spGFP11	Reconstitution of spGFP1-10 and spGFP11	Reconstitution of spXFP1-10 and spXFP11	Reconstitution of spGFP1-10 and spGFP11	Enzymatic interaction of LplA and LAP
Synaptic targeting module	Synaptophysin, VAMP2, PSD-95, CaMKII, vGLUT1, mGluRs	Synaptophysin, VAMP2	PSD-95, CaMKII, Neuroligin	Human CD4, PTP-3A, nlg-1	Rat neurexin1-β, mouse neuroligin-1	Synaptobrevin, human CD4	Rat neurexin-1β, rat neuroligin-1, 2	Human neurexin-3β, mouse neurexin-1β, rat neuroligin-1
Model Systems								
In vitro	HEK, primary cultured neurons, organotypic slices	Primary cultured neurons, organotypic slices	HEK, primary cultured neurons	N/A	N/A	HEK	HEK, COS-7, primary cultured neurons	HEK, primary cultured neurons
In vivo	N/A	N/A	N/A	*C.elegans, Drosophila*	Mouse	*Drosophila*	N/A	N/A
Remarks	Tracking of presynaptic vesicle release, postsynaptic receptor trafficking	Optically inhibiting synaptic release with good spatial resolution	Optical pulse-chase labeling of synaptic proteins with high spatiotemporal resolution	*in vivo* synaptic detection in invertebrate circuits	*in vivo* synaptic detection in vertebrate circuits	Activity-dependent labeling of multiple synaptic inputs	Synapse labeling by direct interaction of neurexin-neuroligin	Enzyme-based visualization of direct interaction of neurexin-neuroligin
	Lacks *in vivo* application with quantitative analysis	Lacks physiologically relevant temporal resolutions due to slow recovery	Awaits mammalian *in vivo* application	Limited to apply mammalian system	Limited to detect functional synaptic connections	Limited to apply mammalian system, limited temporal resolutions	Lacks *in vivo* verification and application	Requires separate introduction of exogenous ligase and antibody-fluorophore conjugates
References	Miesenböck et al. (1998), Sankaranarayanan and Ryan (2000), Kopec et al. (2006), Voglmaier et al. (2006) and Li and Tsien (2012)	Lin et al. (2013)	Lin et al. (2008) and Butko et al. (2012)	Feinberg et al. (2008), Gordon and Scott (2009), Gong et al. (2010), Park et al. (2011), Yuan et al. (2011), Fan et al. (2013), Pech et al. (2013) and Gorostiza et al. (2014)	Feng et al. (2012), Kim et al. (2012) and Druckmann et al. (2014)	Karuppudurai et al. (2014), Frank et al. (2015), Macpherson et al. (2015) and Li et al. (2016)	Tsetsenis et al. (2014)	Liu et al. (2013)

endogenous partner, neurexin, the extracellular esterase domain of neuroligin is deleted in the main skeleton of the postsynaptic mGRASP. Similar to presynaptic mGRASP, post-mGRASP is composed a signal peptide from the esterase-truncated neuroligin-1 (residues 1–49), GFP β-strand 1-10 (spGFP1-10, 648 residues), the extracellular, transmembrane, and intracellular regions of neuroligin (71, 19, and 127 residues, respectively), followed by the self-cleavable 2A peptide-fused dTomato for visualizing postsynaptic neuronal morphology. This optimized mGRASP enabled the comprehensive synaptic connectivity mapping of hippocampal CA3-CA1 and identified spatially structured patterns of synaptic connectivity (Druckmann et al., 2014). It is important to note that brain-wide synapse detection for comprehensive fine-scale mapping becomes achievable not only by advanced molecular engineering to label the synapse such as mGRASP, but also by appropriately engineered computational analysis (Feng et al., 2012, 2015).

Current GRASP technology has proved to be a tool suitable for rapid and accurate mapping of synaptic connectivity in nematode (Feinberg et al., 2008), fruit fly (Gordon and Scott, 2009), and mouse (Kim et al., 2012; Druckmann et al., 2014). Yet, further improvements to GRASP such as multi-colored FPs for analyzing convergent synaptic inputs, various carriers for neural activities, and tailored computational analyses will provide a clear overview of complex synaptic connectivity and its operation. We next discuss recent efforts in these directions.

Engineering FPs for Multi-Color GRASP

A neuron oftentimes receives multiple inputs from different presynaptic neurons of distinct cell types and/or various brain areas. For comprehensive mapping of complex synaptic circuits, multiple synaptic detection is beneficial, as described earlier in the section describing pH-sensitive FPs. The current version of GRASP restricts convergent synaptic mapping because it relies on only a single pair of spGFP fragments such that spectral overlap of its signals hinders simultaneous imaging with previously well-established GFP-based tools such as GCaMP. Therefore, the multi-color GRASP (XRASP) components have been developed recently (Macpherson et al., 2015; Li et al., 2016). Given that Cyan fluorescent protein (CFP), GFP, and YFP have identical structures except for several residues in the chromophore located in beta barrels of 1-10, C-RASP and Y-RASP were generated by color-shifting mutations in spGFP1-10 (Y66W, S72A, F145A*, N146I, and H148D for C-RASP, *additional mutation in Li et al., 2016, T65G, V68L, S72A and T203Y for Y-RASP) paired with the unaltered spGFP11 (Li et al., 2016). Multi-color GRASP (XRASP) was tested *in vivo* in several circuits, including the Kenyon cells of the mushroom body, and projection neurons of the thermosensory and olfactory systems in the fruit fly. Reconstructed CFP and YFP signals showed minimal spectral overlap with the GRASP emission and excitation spectra. Extended choices of multi-color GRASP (XRASP) will allow simultaneous imaging of multiple, convergent connectivity and functional activity. However, more red-shifted XRASP is required for *in vivo* 2-photon imaging together with Ca^{2+} indicators and for fine-scale synapse labeling from multiple inputs within the single neuron, because it has proved difficult to separate CFP/GFP/YFP signals in the complex mammalian nerve system.

Engineering Carriers for Activity-Dependent GRASP

To understand functional organizations underlying complex brain functions that go beyond structural connectivity patterns, it will be essential to identify active synaptic connectivity at defined times and conditions. For the activity-dependent GRASP system, synaptobrevin (syb), a key constituent of synaptic vesicle membrane, was used as a synaptic carrier instead of constantly membrane-targeted carriers in the previous GRASP systems. The straightforward fusion of syb and spGFP1-10 (syb:spGFP1-10) with the original CD4:spGFP11 can together form activity-dependent GRASP, called the syb:GRASP system. Given activity-dependent interactions of syb with SNARE-SM protein complex triggering synaptic vesicle release, syb:GRASP showed preferential labeling of active synapses as a boost of GRASP fluorescence signals in well-studied thermosensory and olfactory circuits in the fruit fly (Macpherson et al., 2015). This new strategy for mapping active synaptic connectivity might expedite the mapping of functional connectivity at the synapse level in a way previously achieved only by difficult combinations of Ca^{2+} imaging and exhaustive EM reconstruction (Bock et al., 2011; Briggman et al., 2011). Yet, these new techniques raise basic concerns about possible side effects caused by the overexpression of key synaptic vesicle proteins, and need further optimization before they can be applied to mammalian networks.

FP- and Enzyme-Based Visualization of Neuroligin-Neurexin Interaction

An alternative way to detect synapses has been suggested by imaging neurexin-neuroligin interactions. Presynaptic neurexin and postsynaptic neurolign are transmembrane adhesion proteins and their interaction at the synaptic cleft has been believed to be a key process for synaptic formation, maintenance, and connectivity (Li and Sheng, 2003; Graf et al., 2004; Chen et al., 2010; Krueger et al., 2012). Therefore, it is thought that identifying sites of neurexin-neuroligin interactions could provide selective visualization of synapses. Similar to the GRASP approaches, this method, based on neuroligin-neurexin interactions using splitGFP, is called SynView. It is composed of spGFP1-10-inserted neurexin-1β between residues N275-D276 or A200-G201 for the presynaptic component, and the split-GFP11-inserted neuroligin-1 in the C-terminal end of the extracellular esterase (between Q641-Y642) for the postsynaptic component (Tsetsenis et al., 2014). Another method for visualizing neuroligin-neurexin interactions is based on mutated bacterial lipoic acid ligase (LpIA) and lipoic acid acceptor peptide (LAP) tags (Uttamapinant et al., 2010, 2012), and is called Interaction-Dependent Probe Incorporation

Mediated by Enzymes (ID-PRIME; Liu et al., 2013). Using the same principle of SynView, ID-PRIME was designed to detect trans-synaptic contacts of neurexin and neuroligin enzymatically using lipoic acid. These two methods successfully imaged the direct interactions of neurexin-neuroligin synaptic adhesive molecules. However, these methods seem restricted to particular investigations of the dynamics of neurexin-neuroligin, rather general synaptic mapping. In addition, it is known that overexpressing these synaptic adhesion molecules causes substantial structural and physiological perturbations of normal synaptic compartments and cleft structures.

BRIDGING TOOLS BETWEEN MOLECULAR SYNAPSE DETECTORS AND BRAIN-WIDE SYNAPSE MAPPING

Thus far, we have described methods for detecting synapses focusing on molecular engineering. To exert these genetically encoded synapse detectors to brain-wide synaptic mapping at the system level, there need to be critically partnered technologies such as gene delivery, advanced imaging, and digital representation platform that are appropriate for neural system (**Figure 3**).

Gene Delivery System for Synapse Detectors in the Mouse Brain

Improving the targeting specificity for types of cells and scaling up the scope of synaptic sensor delivery are among the crucial initial steps needed to expand single-synapse level analysis to systems level neuroscience. Gene delivery technologies, particularly for the nervous system, have developed at a breathtaking pace over the past decades, establishing methodologies that can be classified into two main categories: germ line manipulation and viral injection.

Genetic Manipulation-Based Gene Delivery

To avoid side effects that can sometimes be caused by the overexpression of FP-tagged synaptic proteins, and to mimic expression patterns of endogenous proteins, gene knock-in (KI) technology has been used to substitute wild-type genes with FP-tagged copies. For synaptic detectors based on universal synaptic proteins such as PSD-95, however, this standard KI method leads to expression of FP-tagged synapse detectors globally, throughout the brain, which makes it difficult to acquire high resolution images of a particular cell type. Therefore, a recent study introduced a conditional KI strategy called endogenous labeling via exon duplication (ENABLED; Fortin et al., 2014). In the ENABLED strategy, a knocked-in gene cassette is composed of the floxed last exon and 3'UTR of PSD-95 followed by its mVenus-tagged duplicated last exon and 3'UTR. The FP-tagged duplicated gene will be selectively expressed only in Cre-expressing neurons because its translation is designed to be blocked by translation stop signals in the endogenous copy in the absence of Cre recombinase. When this PSD-95-ENABLED mouse line is crossed with a dopaminergic cell-type specific DAT-Cre line, for instance, PSD-95^{mVenus} is expressed specifically in dopaminergic neurons. PSD-95-ENABLED was shown to functionally replace wild-type PSD-95 and to sparsely label a particular cell-type, allowing insights into the detailed distribution and dynamics of synapses. In applying this strategy to a wide variety of synaptic proteins, one concern with using the ENABLED strategy is that it is limited to synaptic proteins that are compatible with C-terminal FP-tagging.

Thanks to incredibly fast developments and improvements in genetic manipulation technologies such as clustered regularly-interspaced short palindromic repeats (CRISPR) and effector nucleases Cas system (Cong et al., 2013; Wang et al., 2013; Fujii et al., 2014; Aida et al., 2015), the generation of synapse detector KI mouse lines is becoming time- and cost-efficient, and is dramatically facilitating synapse mapping.

Viral System-Based Gene Delivery

Spatially targeted gene delivery into the mature brain can be achieved through stereotactic microinjection of viral vectors expressing FP-tagged proteins. Diverse virus families have been recruited into this effort: Retroviridae (e.g., lentivirus), Parvoviridae (e.g., rAAV), Adenoviridae (e.g., canine adenovirus), and Alphaviridae (e.g., sindbis virus), including some that cross the synapse, such as Rhabdoviridae (e.g., rabies virus) and Herpesviridae (e.g., HSV-1 and pseudorabies virus; Nassi et al., 2015). Because of their low cytotoxicity and stable expression, lentiviruses and rAAVs are the most widely used viral vectors in neuroanatomical tracing studies and human clinical trials testing gene therapy. In fact, spatially restricted injection of Cre-(in)dependent rAAV vectors have been used for mGRASP-assisted synaptic mapping.

In parallel, ongoing efforts include searching for and engineering new types of virus to allow transduction efficiency/specificity and retrograde infection. Canine adenovirus has drawn attention because of its strong retrograde transport capability and relatively large payload size (~30 kb); further, several successful applications of Canine adenovirus in the mouse brain suggest a powerful complement to the lentivirus and rAAV (Bru et al., 2010; Ekstrand et al., 2014; Junyent and Kremer, 2015; Schwarz et al., 2015). Additionally, systemic delivery of viral vectors in animal models has proved to be effective and safe for various serotypes of AAV (Foust et al., 2009; Bevan et al., 2011; Gray et al., 2011; Yang et al., 2014; Deverman et al., 2016).

Advanced Brain-Wide Imaging and Digital Representation of Synaptic Detectors

Once FP-based synaptic detectors are introduced into the brain as described above, appropriate brain-wide imaging and digital representation technologies are necessary to map synaptic connectivity. Happily, there has been remarkable progress in tissue clearing methodology such as BABB (Dodt et al.,

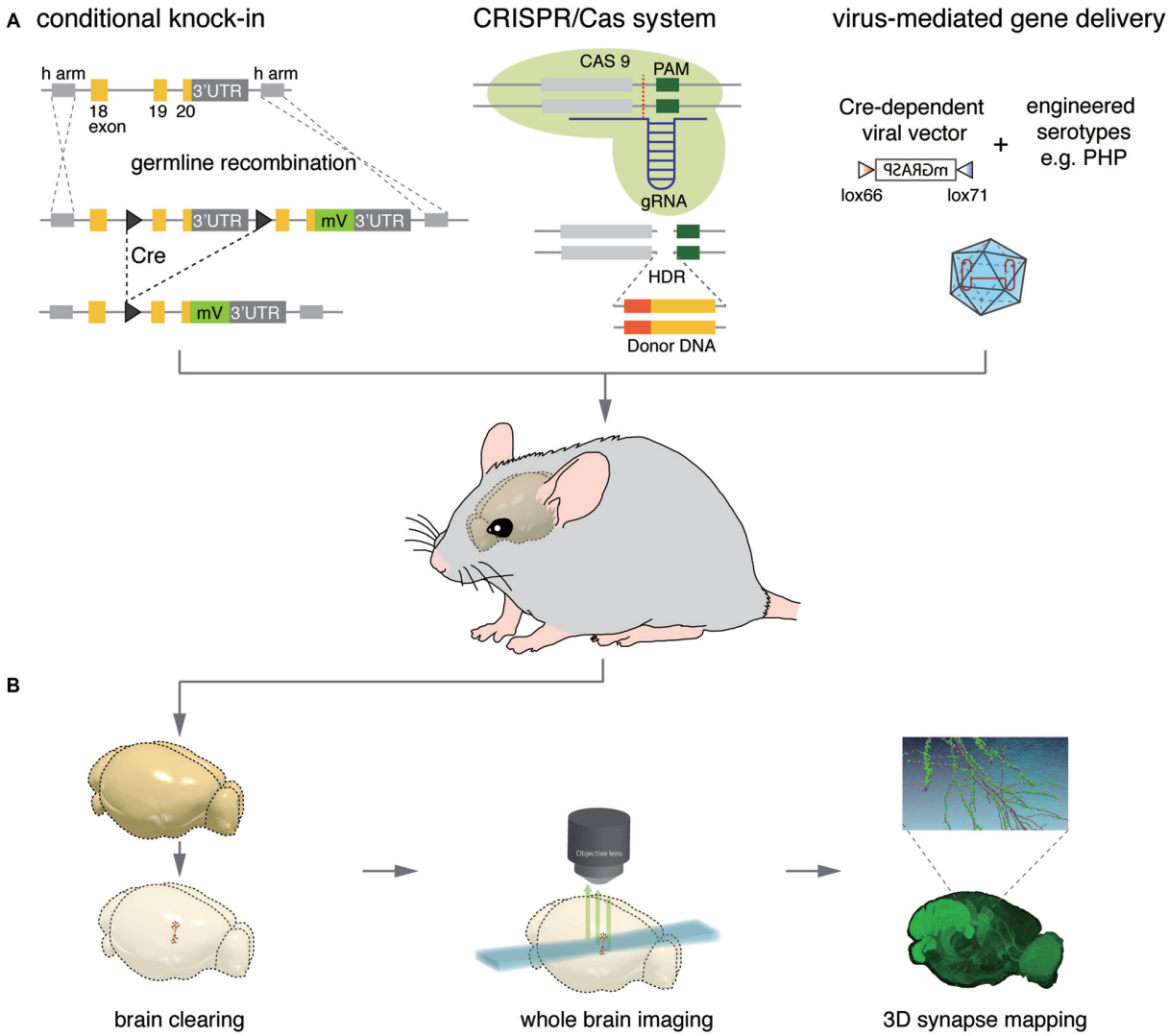

FIGURE 3 | Convergence of technologies for synaptic neuroscience at the systems level. (A) Synapse-detector genes can be delivered to target neural components through germline manipulation-based and viral system-based methods. Exogenous genetic materials can be effectively introduced to the germline with high expression specificity via Cre-mediated conditional knock-in (KI) strategies and the homology directed repair (HDR) pathway of the clustered regularly-interspaced short palindromic repeats (CRISPR)/Cas system. In a Cre-mediated conditional KI strategy called endogenous labeling via exon duplication (ENABLED), a KI cassette including duplicates of exons 19 and 20 and the 3'UTR of PSD-95 is generated. The first duplicate is flanked by head-to-tail oriented loxP sites (black arrows), while the second duplicate has monovalent Venus (mV) inserted between exon 20 and the 3'UTR. The two duplicate sequences, along with exon 18, are flanked by a set of homology arms (h arm), which mediates KI cassette insertion through homologous recombination. Cre-lox recombination excises the first duplicate containing translation stop signals and polyadenylation sequences, and activates mV expression only in Cre-expressing neurons. Transient expression of sensor genes using viral vectors benefits from efforts to engineer expression through Cre-dependent expression cassettes e.g., Cre-dependent Mammalian GRASP (mGRASP) constructs and newly engineered serotypes that have more selective tropism and transduction efficiency (e.g., AAV-PHP.B). Local tissue or systemic injection of such viral systems can lead to flexible, versatile gene delivery in mature organisms. **(B)** Combination of light-favoring brain clearing, whole-brain imaging, and computational techniques for three-dimensional synapse mapping enables single-synapse level analysis of synaptic profiles across the whole brain. Further improvements in lipid extraction, refractive index matching, advanced light-sheet microscopy, and large-scale data processing and 3D reference space generation will accelerate systems neuroscience at the synaptic scale.

2007), CUBIC (Susaki et al., 2014) 3DISCO (Ertürk et al., 2012), immunolabeling-enabled three-dimensional imaging of solvent-cleared organs (iDISCO; Renier et al., 2014), SeeDB (Ke et al., 2013) and CLARITY (Chung et al., 2013; Tomer et al., 2014) that are needed to prepare the intact brain for imaging while avoiding distortions caused by physical sectioning. These new clearing techniques, together with advanced optical methods such as fluorescent selective plane illumination microscopy (fSPIM; Huisken et al., 2004), will allow high-throughput whole brain imaging. Also, once images are acquired, digital representation programs are necessary to reliably extract synaptic wiring information from the

images, and to bring data from different sections and animals into register with one another (Johnson et al., 2010; Oh et al., 2014). Improvements in this software will be greatly beneficial.

In our view, new clearing methods, optics, and tailored computational analysis platforms together with advanced synaptic detectors such as mGRASP are very promising developments for the complete mapping of mammalian synaptic connectivity.

CONCLUSION AND PERSPECTIVE

Here we reviewed new FP-based synapse detection techniques, which are useful for rapidly imaging individual synapses and synaptic connectivity in the whole brain with LM. Recent technical developments have allowed a focus of neuroscience to move from individual synapses to ensemble interactions among neurons of various cell types through multiple synaptic pathways. Comprehensively mapping individual synapses in the whole brain will provide firm grounds for further anatomical and functional studies and such mapping is essential for analyzing large-scale information processing phenomena. We believe that rapid, scalable synaptic cartography with the triad of single-synapse resolution, brain-wide scope, and cell-type-specific connectivity requires a synergistic combination of advanced technologies, and that FP-based neurosensors are the key to this grand integrative project.

AUTHOR CONTRIBUTIONS

HL, WCO, JS, and JK wrote this manuscript.

ACKNOWLEDGMENTS

HL, WCO, JK, and JS are supported by the Korea Institute of Science and Technology (KIST) Institutional Program (2E26190 and 2N41660, respectively) and the Samsung Science and Technology Foundation.

REFERENCES

Ahmari, S. E., Buchanan, J., and Smith, S. J. (2000). Assembly of presynaptic active zones from cytoplasmic transport packets. *Nat. Neurosci.* 3, 445–451. doi: 10.1038/74814

Aida, T., Chiyo, K., Usami, T., Ishikubo, H., Imahashi, R., Wada, Y., et al. (2015). Cloning-free CRISPR/Cas system facilitates functional cassette knock-in in mice. *Genome Biol.* 16:87. doi: 10.1186/s13059-015-0653-x

Beck, S., Sakurai, T., Eustace, B. K., Beste, G., Schier, R., Rudert, F., et al. (2002). Fluorophore-assisted light inactivation: a high-throughput tool for direct target validation of proteins. *Proteomics* 2, 247–255. doi: 10.1002/1615-9861(200203)2:3<247::aid-prot247 >3.0.co;2-k

Bevan, A. K., Duque, S., Foust, K. D., Morales, P. R., Braun, L., Schmelzer, L., et al. (2011). Systemic gene delivery in large species for targeting spinal cord, brain and peripheral tissues for pediatric disorders. *Mol. Ther.* 19, 1971–1980. doi: 10.1038/mt.2011.157

Bock, D. D., Lee, W.-C. A., Kerlin, A. M., Andermann, M. L., Hood, G., Wetzel, A. W., et al. (2011). Network anatomy and *in vivo* physiology of visual cortical neurons. *Nature* 471, 177–182. doi: 10.1038/nature09802

Briggman, K. L., Helmstaedter, M., and Denk, W. (2011). Wiring specificity in the direction-selectivity circuit of the retina. *Nature* 471, 183–188. doi: 10.1038/nature09818

Bru, T., Salinas, S., and Kremer, E. J. (2010). An update on canine adenovirus type 2 and its vectors. *Viruses* 2, 2134–2153. doi: 10.3390/v2092134

Bulina, M. E., Chudakov, D. M., Britanova, O. V., Yanushevich, Y. G., Staroverov, D. B., Chepurnykh, T. V., et al. (2006). A genetically encoded photosensitizer. *Nat. Biotechnol.* 24, 95–99. doi: 10.1038/nbt1175

Butko, M. T., Yang, J., Geng, Y., Kim, H. J., Jeon, N. L., Shu, X., et al. (2012). Fluorescent and photo-oxidizing TimeSTAMP tags track protein fates in light and electron microscopy. *Nat. Neurosci.* 15, 1742–1751. doi: 10.1038/nn.3246

Caroni, P., Chowdhury, A., and Lahr, M. (2014). Synapse rearrangements upon learning: from divergent-sparse connectivity to dedicated sub-circuits. *Trends Neurosci.* 37, 604–614. doi: 10.1016/j.tins.2014.08.011

Chen, Y., Akin, O., Nern, A., Tsui, C. Y. K., Pecot, M. Y., and Zipursky, S. L. (2014). Cell-type-specific labeling of synapses *in vivo* through synaptic tagging with recombination. *Neuron* 81, 280–293. doi: 10.1016/j.neuron.2013.12.021

Chen, S. X., Tari, P. K., She, K., and Haas, K. (2010). Neurexin-neuroligin cell adhesion complexes contribute to synaptotropic dendritogenesis via growth stabilization mechanisms in and *in vivo*. *Neuron* 67, 967–983. doi: 10.1016/j.neuron.2010.08.016

Chung, K., Wallace, J., Kim, S.-Y., Kalyanasundaram, S., Andalman, A. S., Davidson, T. J., et al. (2013). Structural and molecular interrogation of intact biological systems. *Nature* 497, 332–337. doi: 10.1038/nature12107

Cong, L., Ran, F. A., Cox, D., Lin, S., Barretto, R., Habib, N., et al. (2013). Multiplex genome engineering using CRISPR/Cas systems. *Science* 339, 819–823. doi: 10.1126/science.1231143

Cowan, W. M., Südhof, T. C., and Stevens, C. F. (2001). *Synapses*. Baltimore: JHU Press.

De Robertis, E. D., and Bennett, H. S. (1955). Some features of the submicroscopic morphology of synapses in frog and earthworm. *J. Biophys. Biochem. Cytol.* 1, 47–58. doi: 10.1083/jcb.1.1.47

Deverman, B. E., Pravdo, P. L., Simpson, B. P., Kumar, S. R., Chan, K. Y., Banerjee, A., et al. (2016). Cre-dependent selection yields AAV variants for widespread gene transfer to the adult brain. *Nat. Biotechnol.* 34, 204–209. doi: 10.1038/nbt.3440

Dodt, H.-U., Leischner, U., Schierloh, A., Jährling, N., Mauch, C. P., Deininger, K., et al. (2007). Ultramicroscopy: three-dimensional visualization of neuronal networks in the whole mouse brain. *Nat. Methods* 4, 331–336. doi: 10.1038/nmeth1036

Druckmann, S., Feng, L., Lee, B., Yook, C., Zhao, T., Magee, J. C., et al. (2014). Structured synaptic connectivity between hippocampal regions. *Neuron* 81, 629–640. doi: 10.1016/j.neuron.2013.11.026

Ekstrand, M. I., Nectow, A. R., Knight, Z. A., Latcha, K. N., Pomeranz, L. E., and Friedman, J. M. (2014). Molecular profiling of neurons based on connectivity. *Cell* 157, 1230–1242. doi: 10.1016/j.cell.2014.03.059

Ertürk, A., Becker, K., Jährling, N. J. A., Mauch, C. P., Hojer, C. D., Egen, J. G., et al. (2012). Three-dimensional imaging of solvent-cleared organs using 3DISCO. *Nat. Protoc.* 7, 1983–1995. doi: 10.1038/nprot.2012.119

Fan, P., Manoli, D. S., Ahmed, O. M., Chen, Y., Agarwal, N., Kwong, S., et al. (2013). Genetic and neural mechanisms that inhibit Drosophila from mating with other species. *Cell* 154, 89–102. doi: 10.1016/j.cell.2013.06.008

Feinberg, E. H., VanHoven, M. K., Bendesky, A., Wang, G., Fetter, R. D., Shen, K., et al. (2008). GFP reconstitution across synaptic partners (GRASP) defines cell contacts and synapses in living nervous systems. *Neuron* 57, 353–363. doi: 10.1016/j.neuron.2007.11.030

Feng, L., Zhao, T., and Kim, J. (2012). Improved synapse detection for mGRASP-assisted brain connectivity mapping. *Bioinformatics* 28, i25–i31. doi: 10.1093/bioinformatics/bts221

Feng, L., Zhao, T., and Kim, J. (2015). neuTube 1.0: a new design for efficient neuron reconstruction software based on the SWC format. *eNeuro* 2, 1–10. doi: 10.1523/ENEURO.0049-14.2014

Fortin, D. A., Tillo, S. E., Yang, G., Rah, J. C., Melander, J. B., Bai, S., et al. (2014). Live imaging of endogenous PSD-95 using ENABLED: a conditional strategy to fluorescently label endogenous proteins. *J. Neurosci.* 34, 16698–16712. doi: 10.1523/JNEUROSCI.3888-14.2014

Foust, K. D., Nurre, E., Montgomery, C. L., Hernandez, A., Chan, C. M., and Kaspar, B. K. (2009). Intravascular AAV9 preferentially targets neonatal neurons and adult astrocytes. *Nat. Biotechnol.* 27, 59–65. doi: 10.1038/nbt.1515

Fujii, W., Onuma, A., Sugiura, K., and Naito, K. (2014). Efficient generation of genome-modified mice via offset-nicking by CRISPR/Cas system. *Biochem. Biophys. Res. Commun.* 445, 791–794. doi: 10.1016/j.bbrc.2014.01.141

Frank, D. D., Jouandet, G. C., Kearney, P. J., Macpherson, L. J., and Gallio, M. (2015). Temperature representation in the *Drosophila* brain. *Nature* 519, 358–361. doi: 10.1038/nature14284

Gong, Z., Liu, J., Guo, C., Zhou, Y., Teng, Y., and Liu, L. (2010). Two pairs of neurons in the central brain control *Drosophila* innate light preference. *Science* 330, 499–502. doi: 10.1126/science.1195993

Gordon, M. D., and Scott, K. (2009). Motor control in a Drosophila taste circuit. *Neuron* 61, 373–384. doi: 10.1016/j.neuron.2008.12.033

Gorostiza, E. A., Depetris-Chauvin, A., Frenkel, L., Pírez, N., and Ceriani, M. F. (2014). Circadian pacemaker neurons change synaptic contacts across the day. *Curr. Biol.* 24, 2161–2167. doi: 10.1016/j.cub.2014.07.063

Graf, E. R., Zhang, X., Jin, S.-X., Linhoff, M. W., and Craig, A. M. (2004). Neurexins induce differentiation of GABA and glutamate postsynaptic specializations via neuroligins. *Cell* 119, 1013–1026. doi: 10.1016/j.cell.2004.11.035

Gray, E. G. (1959). Axo-somatic and axo-dendritic synapses of the cerebral cortex: an electron microscope study. *J. Anat.* 93, 420–433.

Gray, S. J., Matagne, V., Bachaboina, L., Yadav, S., Ojeda, S. R., and Samulski, R. J. (2011). Preclinical differences of intravascular AAV9 delivery to neurons and glia: a comparative study of adult mice and nonhuman primates. *Mol. Ther.* 19, 1058–1069. doi: 10.1038/mt.2011.72

Huisken, J., Swoger, J., Del Bene, F., Wittbrodt, J., and Stelzer, E. H. K. (2004). Optical sectioning deep inside live embryos by selective plane illumination microscopy. *Science* 305, 1007–1009. doi: 10.1126/science.1100035

Jay, D. G. (1988). Selective destruction of protein function by chromophore-assisted laser inactivation. *Proc. Natl. Acad. Sci. U S A* 85, 5454–5458. doi: 10.1073/pnas.85.15.5454

Johnson, G. A., Badea, A., Brandenburg, J., Cofer, G., Fubara, B., Liu, S., et al. (2010). Waxholm space: an image-based reference for coordinating mouse brain research. *Neuroimage* 53, 365–372. doi: 10.1016/j.neuroimage.2010.06.067

Junyent, F., and Kremer, E. J. (2015). CAV-2–why a canine virus is a neurobiologist's best friend. *Curr. Opin. Pharmacol.* 24, 86–93. doi: 10.1016/j.coph.2015.08.004

Karuppudurai, T., Lin, T.-Y., Ting, C.-Y., Pursley, R., Melnattur, K. V., Diao, F., et al. (2014). A hard-wired glutamatergic circuit pools and relays uv signals to mediate spectral preference in *Drosophila*. *Neuron* 81, 603–615. doi: 10.1016/j.neuron.2013.12.010

Ke, M.-T., Fujimoto, S., and Imai, T. (2013). SeeDB: a simple and morphology-preserving optical clearing agent for neuronal circuit reconstruction. *Nat. Neurosci.* 16, 1154–1161. doi: 10.1038/nn.3447

Keller, P. J., Schmidt, A. D., Wittbrodt, J., and Stelzer, E. H. K. (2008). Reconstruction of zebrafish early embryonic development by scanned light sheet microscopy. *Science* 322, 1065–1069. doi: 10.1126/science.1162493

Kim, J., Zhao, T., Petralia, R. S., Yu, Y., Peng, H., Myers, E., et al. (2012). mGRASP enables mapping mammalian synaptic connectivity with light microscopy. *Nat. Methods* 9, 96–102. doi: 10.1038/nmeth.1784

Kopec, C. D., Li, B., Wei, W., Boehm, J., and Malinow, R. (2006). Glutamate receptor exocytosis and spine enlargement during chemically induced long-term potentiation. *J. Neurosci.* 26, 2000–2009. doi: 10.1523/JNEUROSCI.3918-05.2006

Krueger, D. D., Tuffy, L. P., Papadopoulos, T., and Brose, N. (2012). The role of neurexins and neuroligins in the formation, maturation and function of vertebrate synapses. *Curr. Opin. Neurobiol.* 22, 412–422. doi: 10.1016/j.conb.2012.02.012

Li, Y., Guo, A., and Li, H. (2016). CRASP: CFP reconstitution across synaptic partners. *Biochem. Biophys. Res. Commun.* 469, 352–356. doi: 10.1016/j.bbrc.2015.12.011

Li, Z., and Murthy, V. N. (2001). Visualizing postendocytic traffic of synaptic vesicles at hippocampal synapses. *Neuron* 31, 593–605. doi: 10.1016/s0896-6273(01)00398-1

Li, Z., and Sheng, M. (2003). Some assembly required: the development of neuronal synapses. *Nat. Rev. Mol. Cell Biol.* 4, 833–841. doi: 10.1038/nrm1242

Li, Y., and Tsien, R. W. (2012). pHTomato, a red, genetically encoded indicator that enables multiplex interrogation of synaptic activity. *Nat. Neurosci.* 15, 1047–1053. doi: 10.1038/nn.3126

Lin, M. Z., Glenn, J. S., and Tsien, R. Y. (2008). A drug-controllable tag for visualizing newly synthesized proteins in cells and whole animals. *Proc. Natl. Acad. Sci. U S A* 105, 7744–7749. doi: 10.1073/pnas.0803060105

Lin, J. Y., Sann, S. B., Zhou, K., Nabavi, S., Proulx, C. D., Malinow, R., et al. (2013). Optogenetic inhibition of synaptic release with chromophore-assisted light inactivation (CALI). *Neuron* 79, 241–253. doi: 10.1016/j.neuron.2013.05.022

Liu, D. S., Loh, K. H., Lam, S. S., White, K. A., and Ting, A. Y. (2013). Imaging trans-cellular neurexin-neuroligin interactions by enzymatic probe ligation. *PLoS One* 8:e52823. doi: 10.1371/journal.pone.0052823

Macpherson, L. J., Zaharieva, E. E., Kearney, P. J., Alpert, M. H., Lin, T.-Y., Turan, Z., et al. (2015). Dynamic labelling of neural connections in multiple colours by trans-synaptic fluorescence complementation. *Nat. Commun.* 6:10024. doi: 10.1038/ncomms10024

Malinow, R., and Malenka, R. C. (2002). AMPA receptor trafficking and synaptic plasticity. *Annu. Rev. Neurosci.* 25, 103–126. doi: 10.1146/annurev.neuro.25.112701.142758

Marek, K. W., and Davis, G. W. (2002). Transgenically encoded protein photoinactivation (FlAsH-FALI): acute inactivation of synaptotagmin I. *Neuron* 36, 805–813. doi: 10.1016/S0896-6273(02)01068-1

Markram, H., Lübke, J., Frotscher, M., and Sakmann, B. (1997). Regulation of synaptic efficacy by coincidence of postsynaptic APs and EPSPs. *Science* 275, 213–215. doi: 10.1126/science.275.5297.213

Miesenböck, G., De Angelis, D. A., and Rothman, J. E. (1998). Visualizing secretion and synaptic transmission with pH-sensitive green fluorescent proteins. *Nature* 394, 192–195. doi: 10.1038/28190

Nassi, J. J., Cepko, C. L., Born, R. T., and Beier, K. T. (2015). Neuroanatomy goes viral!. *Front. Neuroanat.* 9:80. doi: 10.3389/fnana.2015.00080

Nelson, C. D., Kim, M. J., Hsin, H., Chen, Y., and Sheng, M. (2013). Phosphorylation of threonine-19 of PSD-95 by GSK-3β is required for PSD-95 mobilization and long-term depression. *J. Neurosci.* 33, 12122–12135. doi: 10.1523/JNEUROSCI.0131-13.2013

Oh, S. W., Harris, J. A., Ng, L., Winslow, B., Cain, N., Mihalas, S., et al. (2014). A mesoscale connectome of the mouse brain. *Nature* 508, 207–214. doi: 10.1038/nature13186

Palay, S. L. (1956). Synapses in the central nervous system. *J. Biophys. Biochem. Cytol.* 2, 193–202. doi: 10.1083/jcb.2.4.193

Palay, S. L., and Palade, G. E. (1955). The fine structure of neurons. *J. Biophys. Biochem. Cytol.* 1, 69–88. doi: 10.1083/jcb.1.1.69

Park, J., Knezevich, P. L., Wung, W., O'Hanlon, S. N., Goyal, A., Benedetti, K. L., et al. (2011). A conserved juxtacrine signal regulates synaptic partner recognition in Caenorhabditis elegans. *Neural Dev.* 6:28. doi: 10.1186/1749-8104-6-28

Pech, U., Pooryasin, A., Birman, S., and Fiala, A. (2013). Localization of the contacts between Kenyon cells and aminergic neurons in the *Drosophila* melanogaster brain using SplitGFP reconstitution. *J. Comp. Neurol.* 521, 3992–4026. doi: 10.1002/cne.23388

Pédelacq, J.-D., Cabantous, S., Tran, T., Terwilliger, T. C., and Waldo, G. S. (2006). Engineering and characterization of a superfolder green fluorescent protein. *Nat. Biotechnol.* 24, 79–88. doi: 10.1038/nbt1172

Pelkey, K. A., Yuan, X., Lavezzari, G., Roche, K. W., and McBain, C. J. (2007). mGluR7 undergoes rapid internalization in response to activation by the allosteric agonist AMN082. *Neuropharmacology* 52, 108–117. doi: 10.1016/j.neuropharm.2006.07.020

Renier, N., Wu, Z., Simon, D. J., Yang, J., Ariel, P., and Tessier-Lavigne, M. (2014). iDISCO: a simple, rapid method to immunolabel large tissue samples for volume imaging. *Cell* 159, 896–910. doi: 10.1016/j.cell.2014.10.010

Richardson, D. S., and Lichtman, J. W. (2015). Clarifying tissue clearing. *Cell* 162, 246–257. doi: 10.1016/j.cell.2015.06.067

Russo, S. J., Dietz, D. M., Dumitriu, D., Morrison, J. H., Malenka, R. C., and Nestler, E. J. (2010). The addicted synapse: mechanisms of synaptic and

structural plasticity in nucleus accumbens. *Trends Neurosci.* 33, 267–276. doi: 10.1016/j.tins.2010.02.002

Sankaranarayanan, S., and Ryan, T. A. (2000). Real-time measurements of vesicle-SNARE recycling in synapses of the central nervous system. *Nat. Cell Biol.* 2, 197–204. doi: 10.1038/35008615

Schwarz, L. A., Miyamichi, K., Gao, X. J., Beier, K. T., Weissbourd, B., DeLoach, K. E., et al. (2015). Viral-genetic tracing of the input-output organization of a central noradrenaline circuit. *Nature* 524, 88–92. doi: 10.1038/nature14600

Shaner, N. C., Lin, M. Z., McKeown, M. R., Steinbach, P. A., Hazelwood, K. L., Davidson, M. W., et al. (2008). Improving the photostability of bright monomeric orange and red fluorescent proteins. *Nat. Methods* 5, 545–551. doi: 10.1038/nmeth.1209

Shen, Y., Rosendale, M., Campbell, R. E., and Perrais, D. (2014). pHuji, a pH-sensitive red fluorescent protein for imaging of exo- and endocytosis. *J. Cell Biol.* 207, 419–432. doi: 10.1083/jcb.201404107

Shen, K., Teruel, M. N., Connor, J. H., Shenolikar, S., and Meyer, T. (2000). Molecular memory by reversible translocation of calcium/calmodulin-dependent protein kinase II. *Nat. Neurosci.* 3, 881–886. doi: 10.1038/78783

Shu, X., Lev-Ram, V., Deerinck, T. J., Qi, Y., Ramko, E. B., Davidson, M. W., et al. (2011). A genetically encoded tag for correlated light and electron microscopy of intact cells, tissues and organisms. *PLoS Biol.* 9:e1001041. doi: 10.1371/journal.pbio.1001041

Susaki, E. A., Tainaka, K., Perrin, D., Kishino, F., Tawara, T., Watanabe, T. M., et al. (2014). Whole-brain imaging with single-cell resolution using chemical cocktails and computational analysis. *Cell* 157, 726–739. doi: 10.1016/j.cell.2014.03.042

Takemoto, K., Matsuda, T., McDougall, M., Klaubert, D. H., Hasegawa, A., Los, G. V., et al. (2011). Chromophore-assisted light inactivation of HaloTag fusion proteins labeled with eosin in living cells. *ACS Chem. Biol.* 6, 401–406. doi: 10.1021/cb100431e

Tomer, R., Khairy, K., Amat, F., and Keller, P. J. (2012). Quantitative high-speed imaging of entire developing embryos with simultaneous multiview light-sheet microscopy. *Nat. Methods* 9, 755–763. doi: 10.1038/nmeth.2062

Tomer, R., Ye, L., Hsueh, B., and Deisseroth, K. (2014). Advanced CLARITY for rapid and high-resolution imaging of intact tissues. *Nat. Protoc.* 9, 1682–1697. doi: 10.1038/nprot.2014.123

Tour, O., Meijer, R. M., Zacharias, D. A., Adams, S. R., and Tsien, R. Y. (2003). Genetically targeted chromophore-assisted light inactivation. *Nat. Biotechnol.* 21, 1505–1508. doi: 10.1038/nbt914

Tsetsenis, T., Boucard, A. A., Araç, D., Brunger, A. T., and Südhof, T. C. (2014). Direct visualization of trans-synaptic neurexin-neuroligin interactions during synapse formation. *J. Neurosci.* 34, 15083–15096. doi: 10.1523/JNEUROSCI.0348-14.2014

Tsien, J. Z., Huerta, P. T., and Tonegawa, S. (1996). The essential role of hippocampal CA1 NMDA receptor-dependent synaptic plasticity in spatial memory. *Cell* 87, 1327–1338. doi: 10.1016/s0092-8674(00)81827-9

Uttamapinant, C., Tangpeerachaikul, A., Grecian, S., Clarke, S., Singh, U., Slade, P., et al. (2012). Fast, cell-compatible click chemistry with copper-chelating azides for biomolecular labeling. *Angew. Chem. Int. Ed Engl.* 51, 5852–5856. doi: 10.1002/anie.201108181

Uttamapinant, C., White, K. A., Baruah, H., Thompson, S., Fernández-Suárez, M., Puthenveetil, S., et al. (2010). A fluorophore ligase for site-specific protein labeling inside living cells. *Proc. Natl. Acad. Sci. U S A* 107, 10914–10919. doi: 10.1073/pnas.0914067107

Voglmaier, S. M., Kam, K., Yang, H., Fortin, D. L., Hua, Z., Nicoll, R. A., et al. (2006). Distinct endocytic pathways control the rate and extent of synaptic vesicle protein recycling. *Neuron* 51, 71–84. doi: 10.1016/j.neuron.2006.05.027

Wang, H., Yang, H., Shivalila, C. S., Dawlaty, M. M., Cheng, A. W., Zhang, F., et al. (2013). One-step generation of mice carrying mutations in multiple genes by CRISPR/Cas-mediated genome engineering. *Cell* 153, 910–918. doi: 10.1016/j.cell.2013.04.025

Yang, B., Treweek, J. B., Kulkarni, R. P., Deverman, B. E., Chen, C.-K., Lubeck, E., et al. (2014). Single-cell phenotyping within transparent intact tissue through whole-body clearing. *Cell* 158, 945–958. doi: 10.1016/j.cell.2014.07.017

Yuan, Q., Xiang, Y., Yan, Z., Han, C., Jan, L. Y., and Jan, Y. N. (2011). Light-induced structural and functional plasticity in Drosophila larval visual system. *Science* 333, 1458–1462. doi: 10.1126/science.1207121

Zamanillo, D., Sprengel, R., Hvalby, O., Jensen, V., Burnashev, N., Rozov, A., et al. (1999). Importance of AMPA receptors for hippocampal synaptic plasticity but not for spatial learning. *Science* 284, 1805–1811. doi: 10.1126/science.284.5421.1805

Zhu, Y., Xu, J., and Heinemann, S. F. (2009). Two pathways of synaptic vesicle retrieval revealed by single-vesicle imaging. *Neuron* 61, 397–411. doi: 10.1016/j.neuron.2008.12.024

Conflict of Interest Statement: The authors declare that the research was conducted in the absence of any commercial or financial relationships that could be construed as a potential conflict of interest.

frontiers in Synaptic Neuroscience

MINI REVIEW
published: 16 September 2016
doi: 10.3389/fnsyn.2016.00029

Organelle-Specific Sensors for Monitoring Ca^{2+} Dynamics in Neurons

*Seok-Kyu Kwon, Yusuke Hirabayashi and Franck Polleux**

Department of Neuroscience, Mortimer B. Zuckerman Mind Brain Behavior Institute, Kavli Institute for Brain Science, Columbia University Medical Center, New York, NY, USA

Calcium (Ca^{2+}) plays innumerable critical functions in neurons ranging from regulation of neurotransmitter release and synaptic plasticity to activity-dependent transcription. Therefore, more than any other cell types, neurons are critically dependent on spatially and temporally controlled Ca^{2+} dynamics. This is achieved through an exquisite level of compartmentalization of Ca^{2+} storage and release from various organelles. The function of these organelles in the regulation of Ca^{2+} dynamics has been studied for decades using electrophysiological and optical methods combined with pharmacological and genetic alterations. Mitochondria and the endoplasmic reticulum (ER) are among the organelles playing the most critical roles in Ca^{2+} dynamics in neurons. At presynaptic boutons, Ca^{2+} triggers neurotransmitter release and synaptic plasticity, and postsynaptically, Ca^{2+} mobilization mediates long-term synaptic plasticity. To explore Ca^{2+} dynamics in live cells and intact animals, various synthetic and genetically encoded fluorescent Ca^{2+} sensors were developed, and recently, many groups actively increased the sensitivity and diversity of genetically encoded Ca^{2+} indicators (GECIs). Following conjugation with various signal peptides, these improved GECIs can be targeted to specific subcellular compartments, allowing monitoring of organelle-specific Ca^{2+} dynamics. Here, we review recent findings unraveling novel roles for mitochondria- and ER-dependent Ca^{2+} dynamics in neurons and at synapses.

Keywords: synapse, mitochondria, endoplasmic reticulum, circuit function, calcium dynamics

OPEN ACCESS

Edited by:
Marc Fivaz, Duke NUS Graduate Medical School, Singapore

Reviewed by:
Lucas Pozzo-Miller, University of Alabama at Birmingham, USA
William N. Green, University of Chicago, USA

****Correspondence:***
Franck Polleux
fp2304@cumc.columbia.edu

Received: *13 June 2016*
Accepted: *30 August 2016*
Published: *16 September 2016*

Citation:
Kwon S-K, Hirabayashi Y and Polleux F (2016) Organelle-Specific Sensors for Monitoring Ca^{2+} Dynamics in Neurons. Front. Synaptic Neurosci. 8:29. doi: 10.3389/fnsyn.2016.00029

INTRODUCTION

Calcium (Ca^{2+}) ions govern prevalent physiological processes in various cell types (Rizzuto and Pozzan, 2006; Clapham, 2007). This is especially prominent in excitable cells like neurons where Ca^{2+} influx through the plasma membrane and release of Ca^{2+} from internal stores transduce the effects of changes in membrane polarization and therefore mediate faithful transfer or storage of information over various timescales (milliseconds to minutes/hours). Therefore, regulation of intracellular Ca^{2+} homeostasis is central to the proper function of neuronal circuits. The maintenance of baseline levels of intracellular Ca^{2+} levels is regulated in part through exchangers and pumps such as the plasma membrane Ca^{2+}-ATPase (PMCA pump), the Na^{+}/Ca^{2+} exchanger (NCX), and the Na^{+}/Ca^{2+}-K^{+} exchanger (NCKX) which extrude Ca^{2+} through the plasma membrane into the extracellular space. In addition to these mechanisms, intracellular organelles, such as mitochondria and endoplasmic reticulum

(ER), are able to regulate cytoplasmic Ca^{2+} ($[Ca^{2+}]_c$) through mitochondrial calcium uniporter (MCU) and smooth endoplasmic reticulum Ca^{2+}-ATPase (SERCA), respectively.

In neurons, mitochondria and ER play important physiological roles via $[Ca^{2+}]_c$ regulation, thereby diverse synaptic functions including basal synaptic transmission, presynaptic short-term plasticity, and long-term plasticity can be regulated by these organelles (Verkhratsky, 2005; Bardo et al., 2006; Mattson et al., 2008; Vos et al., 2010). In addition, impaired Ca^{2+} homeostasis in the nervous system has been proposed to play an important function in the physio-pathological mechanisms underlying Alzheimer's disease, Parkinson's disease, and spinocerebellar ataxia (Verkhratsky, 2005; Mattson et al., 2008; Schon and Przedborski, 2011).

To monitor Ca^{2+} dynamics, various fluorescent Ca^{2+} dyes and genetically encoded Ca^{2+} indicators (GECIs) were developed and applied both *in vitro* and *in vivo*. Also, GECIs tagged with target peptide sequences have allowed imaging of Ca^{2+} dynamics in specific organelles (Rizzuto et al., 1992; Palmer et al., 2004; Palmer and Tsien, 2006).

Previously published reviews have already summarized the usefulness and limitations of various Ca^{2+} sensors and GECIs applied to neuronal and non-neuronal cells (Palmer and Tsien, 2006; Knopfel, 2012; Tian et al., 2012; Rose et al., 2014). In this review, we only describe recently uncovered insights about Ca^{2+} dynamics and its regulation by mitochondria and ER, and we discuss how these organelle-specific Ca^{2+} sensors have been used for the exploration of the role of these subcellular compartments in the regulation of Ca^{2+} homeostasis and synaptic function in neurons.

UNVEILED SYNAPTIC FUNCTIONS OF MITOCHONDRIA-DEPENDENT Ca^{2+} HOMEOSTASIS

Mitochondrial Ca^{2+} uptake has been studied since the 1950s from studies of rat heart muscle and kidney (Slater and Cleland, 1953; Deluca and Engstrom, 1961). In the nervous system, mitochondria were described at presynaptic terminals and dendrites of various neuronal subtypes using the light and electron microscope (EM) several decades ago (Bartelmez and Hoerr, 1933; Palay, 1956; Gray, 1963; Shepherd and Harris, 1998; Rowland et al., 2000). In axons, mitochondria are short and sparsely distributed, and interestingly, several studies showed that half of presynaptic boutons are occupied by mitochondria (Shepherd and Harris, 1998; Kang et al., 2008). In contrast, dendritic mitochondria have tubular shapes and they are rarely observed in postsynaptic spines in the excitatory neurons (Sheng and Hoogenraad, 2007; Kasthuri et al., 2015).

At presynaptic boutons and terminals, synaptic vesicle (SV) fusion with the plasma membrane occurs following increase of $[Ca^{2+}]_c$ following opening of voltage-sensitive Ca^{2+} channels (VSCC) followed by Ca^{2+} binding to sensors like synaptotagmins (Schneggenburger and Neher, 2005; Neher and Sakaba, 2008; Jahn and Fasshauer, 2012; Südhof, 2012). The ability of mitochondria to import Ca^{2+} into the mitochondrial matrix ($[Ca^{2+}]_m$) plays a role in regulating presynaptic $[Ca^{2+}]_c$. This has been characterized in various species, neuronal cell types and circuits (**Figure 1A**). At the *Drosophila* neuromuscular junction (NMJ), the GTPase dMiro mutant lacks presynaptic mitochondria through impaired axonal transport (Guo et al., 2005; Wang and Schwarz, 2009). During prolonged stimulation, these mutants lacking presynaptic mitochondria displayed subtle, but significantly increased presynaptic Ca^{2+} accumulation and display decrease forms of sustained synaptic transmission or synaptic "fatigue" (Guo et al., 2005). *Drosophila* Drp1 mutants also deplete presynaptic mitochondria at NMJ and exhibit elevated presynaptic Ca^{2+} levels in resting and evoked states. However, spontaneous release (mini Excitatory junctional potential, mEJP) was not altered, but the evoked synaptic transmission was impaired during high frequency stimulation, and this defect was partially rescued by ATP (Verstreken et al., 2005) suggesting that mitochondria plays a role in synaptic transmission through their ability to generate ATP through oxidative phosphorylation. Although mitochondrial Ca^{2+} uptake has limited effects on *Drosophila* NMJ neurons, in mammalian NMJ terminals, acute inhibition of mitochondrial Ca^{2+} uptake causes rapid depression of the endplate potential (EPP) and increased asynchronous release (David and Barrett, 2003). Furthermore, in synapses of the mammalian central nervous system (CNS), mitochondria-dependent Ca^{2+} uptake accelerates the recovery from synaptic depression in the calyx of Held (Billups and Forsythe, 2002). Other studies in mammalian hippocampal neurons claimed that impaired mitochondrial anchoring at presynaptic sites increases presynaptic Ca^{2+} during repetitive stimulation and produces short-term facilitation (STF), and insulin-like growth factor-1 receptor (IGF-1R) signaling regulates resting mitochondrial Ca^{2+} level and spontaneous transmission (Kang et al., 2008; Gazit et al., 2016). Although most pharmacological studies employed uncoupling agents as mitochondrial Ca^{2+} influx blocker, which may affect ATP production, these reports support presynaptic control via mitochondrial Ca^{2+} import (Ly and Verstreken, 2006). A recent study demonstrates that presynaptic boutons associated with mitochondria display lower levels of $[Ca^{2+}]_c$ accumulation than presynaptic boutons not associated with mitochondria (Kwon et al., 2016). Furthermore, acute inhibition of mitochondria calcium import increased $[Ca^{2+}]_c$ accumulation at presynaptic boutons occupied by mitochondria. In the same study, we demonstrate that this mitochondria-dependent regulation of $[Ca^{2+}]_c$ plays an important role in regulating presynaptic release properties including spontaneous release, asynchronous release and short-term synaptic plasticity.

In addition to regulation of $[Ca^{2+}]_c$ clearance, Ca^{2+} release from mitochondria plays important roles at presynaptic sites (**Figure 1A**). Following the sustained high frequency stimulation, an enhancement of synaptic transmission lasting tens of seconds to minutes is observed and which is called post-tetanic potentiation (PTP; Zucker, 1989). Mitochondrial Ca^{2+} release is suggested as one of the underlying mechanisms for this prolonged enhancement of synaptic transmission. Pharmacological inhibition of mitochondrial Ca^{2+} uptake and release at the crayfish NMJ impaired PTP (Tang and Zucker, 1997; Zhong et al., 2001). Furthermore,

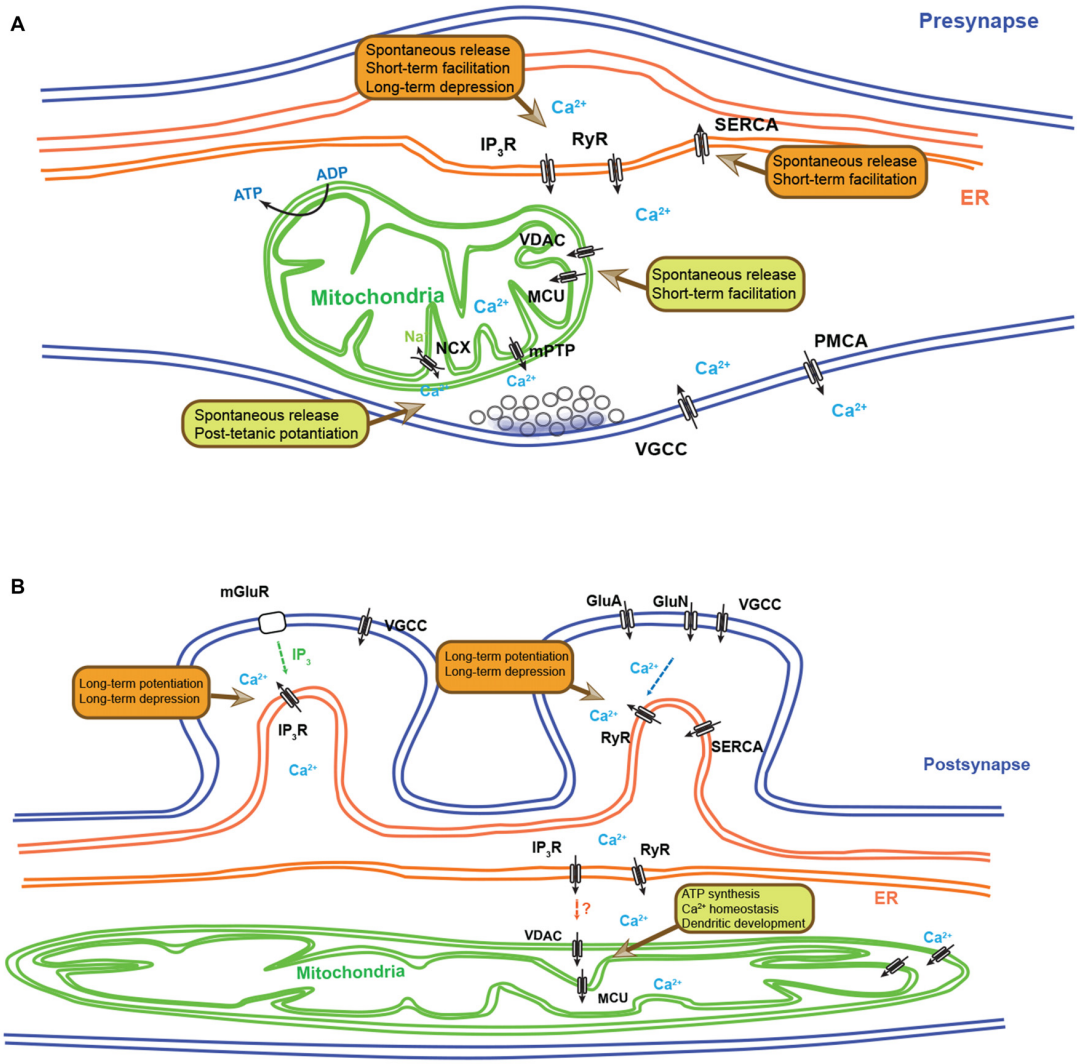

FIGURE 1 | Synaptic functions regulated by endoplasmic reticulum (ER) and mitochondria-dependent Ca^{2+} homeostasis. (A) Schematic diagram depicting the presynaptic functions regulated by ER- and mitochondria-dependent Ca^{2+} dynamics. Ca^{2+} release from ER can modulate spontaneous neurotransmitter release, short-term facilitation (STF) and long-term depression (LTD). Ca^{2+} re-uptake by the ER controls the spontaneous release and STF. Presynaptic mitochondria also play important roles in regulating spontaneous neurotransmitter release, STF and post-tetanic potentiation (PTP) through their ability to regulate Ca^{2+} clearance. **(B)** A simplified schematic diagram depicting the postsynaptic functions regulated by ER- and mitochondria-dependent Ca^{2+} dynamics. Ca^{2+} release from ER via IP_3-induced Ca^{2+} release (IICR) and Ca^{2+}-induced Ca^{2+} release (CICR) controls long-term potentiation (LTP) and LTD. In fact, depending on neuronal and synaptic subtypes, IP_3R and RyR show differential distribution and distinct synaptic functions. Dendritic mitochondrial Ca^{2+} influx can regulate ATP synthesis, Ca^{2+} homeostasis and dendritic development. In non-neuronal cell types, direct Ca^{2+} exchange between ER and mitochondria have been described, but their role in neurons has not yet been documented. IP_3R, IP_3 receptor; RyR, ryanodine receptor; SERCA, smooth endoplasmic reticulum Ca^{2+}-ATPase; VGCC, voltage-gated Ca^{2+} channel; PMCA, plasma membrane Ca^{2+}-ATPase; NCX: the Na^+/Ca^{2+} exchanger; mPTP, mitochondrial permeability transition pore; MCU, mitochondrial calcium uniporter; VDAC, voltage-dependent anion channel; mGluR, metabotropic glutamate receptor; GluN, NMDA receptor.

similar phenotypes were observed at mouse NMJ and hippocampal mossy fiber synapses with blocking the mitochondrial NCX, which mediates mitochondrial Ca^{2+} release (García-Chacón et al., 2006; Lee et al., 2007).

In contrast to presynaptic boutons and terminals, the postsynaptic function of mitochondrial Ca^{2+} regulation is less well-documented. In mouse hippocampal pyramidal neurons (Li et al., 2004), a minority (<5%) of dendritic spines contains mitochondria. Also, large branched spines in hippocampal CA3 contain mitochondria (Chicurel and Harris, 1992). However, a physiological role of these postsynaptic mitochondria is largely unknown. In general, mitochondria are distributed primarily in dendrite shaft and therefore localized microns away from the postsynaptic density, but might still be able to buffer $[Ca^{2+}]_c$ mobilized through Ca^{2+}-channels and glutamate receptors (Thayer and Miller, 1990; White and Reynolds, 1995; Wang and Thayer, 2002). This mitochondrial calcium import can stimulate tricarboxylic acid (TCA) cycle and might

increase ATP production (Kann and Kovács, 2007) and may also regulate other ATP-dependent Ca^{2+} pumps like PMCA and SERCA. While it is still unclear whether or not mitochondria play significant roles in regulating postsynaptic $[Ca^{2+}]_c$ under physiological conditions of neurotransmission, they might play a role in pathophysiological contexts. For example, neurons lacking LRRK2, a protein associated with Parkinson's disease, show impaired dendritic Ca^{2+} homeostasis through mitochondrial defects and thought to cause defective mitochondrial depolarization and reduction in dendritic complexity (**Figure 1B**; Cherra et al., 2013).

Overall, mitochondria-dependent Ca^{2+} clearance and release in neurons plays important physiological and developmental roles pre- and post-synaptically but their functional importance seems to depend on the neuronal subtypes and the structure/size of the pre- and postsynaptic compartments.

MITOCHONDRIAL Ca^{2+}-IMAGING IN NEURONS AND AT SYNAPSES

To investigate organelle-specific Ca^{2+} dynamics, various Ca^{2+} sensors are developed (**Table 1**). One of the first method developed to monitor mitochondrial Ca^{2+} dynamics was established using rhod-2, a cationic chemical Ca^{2+}-binding fluorophore preferentially accumulating in the mitochondrial matrix presumably because of the highly negative membrane potential across the mitochondrial inner membrane (Minta et al., 1989). Then, in the calyx of Held, rhod-2 and rhod-FF (low affinity version) were used to visualize presynaptic mitochondrial Ca^{2+} transient (Billups and Forsythe, 2002). However, these dyes cannot be precisely targeted to these organelles. Therefore, GECIs have recently become the preferred method to image Ca^{2+} in specific organelles including mitochondria. For mitochondrial matrix localization, the targeting presequence of subunit VIII of human cytochrome c oxidase (COXVIII) was tagged to GECIs (Rizzuto et al., 1992). Mitochondria-targeted aequorin (mt-AEQ), a luminescent Ca^{2+} indicator, was first employed to monitor the neuronal mitochondrial Ca^{2+}, and this probe showed NMDA-induced mitochondrial Ca^{2+} increase in hippocampal neurons (Baron et al., 2003). However, this probe needs a chemical reaction characterized by a modest turnover rate and has very limited dynamic range (Palmer and Tsien, 2006). Other GECIs have been developed and tested in various neuronal subtypes with the same targeting sequence. Mitochondrial-targeted ratiometric pericam (2mtRP) consists of circularly permutated Enhanced yellow fluorescent protein (cpEFYP) conjugated with Ca^{2+}-responsive calmodulin (CaM) and its binding peptide (Nagai et al., 2001; Robert et al., 2001). This probe has a bimodal excitation spectrum and the relative emission intensity is dependent on Ca^{2+}-binding. In hippocampal neurons, the use of 2mtRP described mitochondrial Ca^{2+} uptake and also determined cytosolic Ca^{2+} rise upon synaptic activation via dual imaging with cytosolic Ca^{2+} dye (fura-red AM; Young et al., 2008). Other CaM conjugated cpEGFPs called GCaMPs (mito-GCaMP2, 2mtGCaMP6m, and mito-GCaMP5G) were used to monitor axonal mitochondrial Ca^{2+} (Gazit et al., 2016; Kwon et al., 2016; Marland et al., 2016). Both sensors displayed action potential (AP)-dependent mitochondrial Ca^{2+} import. In addition, red fluorescent GECIs by replacing cpEGFP with cpmApple or cpmRuby (mtRCaMP1e and LAR-GECO1.2) revealed mitochondrial Ca^{2+} import simultaneously with cytosolic Ca^{2+} (Akerboom et al., 2013; Wu et al., 2014).

However, these fluorescent proteins have some limitations, for example, they are affected by pH and mitochondrial matrix pH (pH_m) can be changed by Ca^{2+} influx (Abad et al., 2004; Poburko et al., 2011; Chouhan et al., 2012; Marland et al., 2016). In addition to this point, $[Ca^{2+}]_m$ can span broad ranges (0.05–300 μM) depending on cell types and stimulation protocol (Arnaudeau et al., 2001; Palmer and Tsien, 2006). Thus, K_d value for Ca^{2+} of mitochondrial GECI should be considered for experimental purposes because high affinity (low K_d) sensors can be easily saturated by high $[Ca^{2+}]_m$ and low affinity (high K_d) sensors may not be sensitive enough to detect small $[Ca^{2+}]_m$ changes. Several studies reported low affinity mitochondrial Ca^{2+} probes for avoiding saturation (Arnaudeau et al., 2001; Suzuki et al., 2014).

In conclusion, these mitochondria-targeted GECIs allow imaging of mitochondria Ca^{2+} dynamics in neurons and have revealed interesting, synapse-specific properties of mitochondria in the regulation of $[Ca^{2+}]_c$ and neurotransmitter release properties.

REGULATION OF SYNAPTIC Ca^{2+} DYNAMICS BY THE ENDOPLASMIC RETICULUM

Neurons are among the most polarized cell types in our body and consists of a soma, relatively short dendrites and long axons. ER is found throughout the entire length of neuronal processes, and usually rough ER is prominent in the cell body and proximal dendrites, whereas smooth ER is dominant in distal dendrites, spines and axons (Spacek and Harris, 1997; Verkhratsky, 2005). ER imports and sequesters large amount of Ca^{2+} ($[Ca^{2+}]_{er}$ ~500 μM) through SERCA and store-operated Ca^{2+} entry (SOCE) mechanism (Verkhratsky, 2005; Bardo et al., 2006). Ca^{2+} release from ER is mediated by two major mechanisms, called Ca^{2+}-induced Ca^{2+} release (CICR) and IP_3-induced Ca^{2+} release (IICR; Verkhratsky, 2005; Bardo et al., 2006). CICR is caused by the cytosolic Ca^{2+} increase through N-Methyl-D-Aspartate receptors (NMDAR, GluN receptors) and voltage-gated Ca^{2+} channels (VGCCs), whereas IICR is triggered by IP_3, which is generated via activation of phospholipase C (PLC) depending on metabotropic glutamate receptors (mGluRs) or other receptors like receptor tyrosine kinases (**Figure 1**).

Ryanodine receptors (RyRs) are involved in CICR, and they have three major subtypes; RyR1, RyR2, and RyR3. All of these isoforms are detected in the brain, and show region-specific expression (Sharp et al., 1993; Furuichi et al., 1994; Giannini et al., 1995; Verkhratsky, 2005; Bardo et al., 2006; Baker et al., 2013). Similar to RyRs, IP_3 receptor (IP_3R), which mediate IICR,

TABLE 1 | Organelle-specific Ca^{2+} sensors in neurobiology.

Organelle	Sensors	Neuron type	K_d for Ca^{2+} (μM)	Excitation used (nm)	Emission filter (nm)	Dynamic Range (F_{max}/F_{min}, R_{max}/R_{min})	Reference
Mitochondria	**Dye** Rhod-2, Rhod-FF	The calyx of Held	0.57, 19	575	590	3.4	Billups and Forsythe (2002)
	GECI						
	mito-aequorin	Hippocampal (Hp) neuron	1–2	Luminescence			Baron et al. (2003)
	2mtRP (ratioPericam)	Hp neuron	1.7	Ratiometric, 405/485	535/20	10	Young et al. (2008)
	mito-GCaMP2	Hp neuron	0.195	488	507	5	Marland et al. (2016)
	2mtGCaMP6m	Hp neuron	0.167	488	510	38	Patron et al. (2014), Gazit et al. (2016)
	mtRCaMP1e	Cortical neuron	1.6	572	592.5	6.5	Akerboom et al. (2013)
	LAR-GECO1.2	DRG and Hp neurons	12	561	589		Wu et al. (2014)
ER	**Dye**						
	Mag-Fura-2	Sensory neuron	53	Ratiometric, 340/380	510	25	Solovyova et al. (2002)
	GECI						
	D1ER	Hp neuron	0.8, 60	FRET, 450	475/40, 535/25	1.6	Zhang et al. (2010)
	erGAP1	DRG neuron, Hp slice	12	Luminescence, 403/470	510	3∼4	Rodriguez-Garcia et al. (2014)
	G-CEPIA1er	Cerebellar Purkinje cell	672	488	511	4.7 ± 0.3	Suzuki et al. (2014)
	GCaMPer (10.19)	Cortical neurons	400	490	540/50	14	Henderson et al. (2015)

consist of three isoforms, IP_3R1, IP_3R2, and IP_3R3, but IP_3R1 is the dominant form in the brain (Sharp et al., 1993, 1999; Verkhratsky, 2005; Bardo et al., 2006; Baker et al., 2013).

Long-term synaptic plasticity is regulated by Ca^{2+}-dependent signaling mechanisms such as Ca^{2+}/calmodulin-dependent kinase II (CaMKII), calcineurin (a Ca^{2+}-dependent phosphatase), protein phosphatase 1 (PP1) and protein kinase C (PKC; Malenka and Nicoll, 1999; Yang et al., 1999; Lüscher and Malenka, 2012). Therefore, Ca^{2+} release from intracellular stores like the ER regulates long-term synaptic plasticity in specific circuits.

In cerebellar Purkinje cell dendrites, mGluR-IP_3-dependent Ca^{2+} increase is observed during parallel fiber (PF) stimulation and this mediates long-term depression (LTD) of PF-Purkinje cell pathway (Finch and Augustine, 1998; Takechi et al., 1998; Miyata et al., 2000; Wang et al., 2000). At synapses made by hippocampal Schaffer collateral (SC) onto CA1 pyramidal neurons, both long-term potentiation (LTP) and LTD are linked to IP_3-dependent signaling (Oliet et al., 1997; Nishiyama et al., 2000; Raymond and Redman, 2002; Nagase et al., 2003). In addition, CICR is also observed in CA1 pyramidal neuronal spines, and LTD is abolished in RyR3-deficient mice and following application of RyR inhibitor (ryanodine) although the connection between CICR and LTP is controversial in SC-CA1 pathway (Reyes and Stanton, 1996; Emptage et al., 1999; Futatsugi et al., 1999; Sandler and Barbara, 1999; Kovalchuk et al., 2000; Nishiyama et al., 2000; Raymond and Redman, 2002). Hippocampal mossy fiber pathway (MF, dentate gyrus to CA3) shows IICR- and CICR-dependent LTP and LTD, however, there are conflicting results regarding the underlying mechanisms (**Figure 1B**; Yeckel et al., 1999; Itoh et al., 2001; Kapur et al., 2001; Mellor and Nicoll, 2001; Lauri et al., 2003; Lei et al., 2003).

Presynaptic ER-dependent Ca^{2+} release is also detected and contributes to changes in neurotransmitter release properties and short-term synaptic plasticity at various inhibitory and excitatory synapses including basket cell to Purkinje cell synapses, hippocampal MF pathway, SC-CA1 and CA3-CA3 pyramidal neuron synapses (**Figure 1A**; Llano et al., 2000; Emptage et al., 2001; Liang et al., 2002; Galante and Marty, 2003; Lauri et al., 2003; Sharma and Vijayaraghavan, 2003; Unni et al., 2004; Mathew and Hablitz, 2008).

In addition to Ca^{2+} efflux, Ca^{2+} uptake by ER via SERCA pump affects STF at SC-CA1 presynapses and NMJ (**Figure 1A**; Castonguay and Robitaille, 2001; Scullin and Partridge, 2010; Scullin et al., 2010). Stromal interaction molecules (STIMs) and Orai1, which allow SOCE, are localized to neuronal compartment including dendritic spines, and impaired SOCE alters α-amino-3-hydroxy-5-methyl-4-isoxazolepropionic acid receptor (AMPAR) trafficking, neuronal Ca^{2+} signaling and LTP in CA1 pyramidal neuron and cerebellar Purkinje neurons (Baba et al., 2003; Hartmann et al., 2014; Korkotian et al., 2014; Garcia-Alvarez et al., 2015; Segal and Korkotian, 2015).

IMAGING NEURONAL ER Ca^{2+} DYNAMICS

As mentioned above, ER contains high levels of Ca^{2+}, therefore, in order to monitor Ca^{2+} dynamics in the ER lumen, low affinity sensors were employed. Mag-Fura-2, a low affinity membrane-permeable dye (K_d = 53 μM), has been the first applied for neuronal ER Ca^{2+} measurement, and after loading this dye in the cytoplasm and organelles, cytosolic dye was removed by perfusion with dye-free pipette solution (Solovyova et al., 2002). This allowed for the first time the visualization of caffeine-induced Ca^{2+} release and reuptake in the ER of dorsal root ganglia (DRG) neurons (**Table 1**).

However, this method can non-specifically label internal compartments, therefore, genetically targeted sensors have been developed more recently for the visualization of ER-derived Ca^{2+} dynamics (**Table 1**). The signal sequence of calreticulin, a Ca^{2+}-binding protein in ER, and an ER retention sequence, KDEL, lead GECIs into the ER lumen, and to optimize for measuring a massive amount of $[Ca^{2+}]_{er}$, various mutations were applied to the CaM domain or EF-hand motif of existing GECIs for reducing their Ca^{2+} affinity. A fluorescence resonance energy transfer (FRET)-based Ca^{2+} sensor, D1ER, showed altered ER Ca^{2+} leak function in hippocampal neurons of presenilin double knockout and Alzheimer's disease model mice (Zhang et al., 2010). Also, bioluminescence-based sensor, GFP-Aequorin protein (GAP), was modified and targeted to ER of DRG and hippocampal neurons, and showed 3- to 4-fold larger ratio change than D1ER (Rodriguez-Garcia et al., 2014). In addition, recently established GCaMP variants for ER Ca^{2+} detection, calcium-measuring organelle-entrapped protein indicator one in the ER (CEPIA1er) and GCaMPer (10.19), characterized ER Ca^{2+} uptake and release in cortical neurons and cerebellar Purkinje cells (Suzuki et al., 2014; Henderson et al., 2015). Interestingly, cerebellar Purkinje cells displayed differential ER Ca^{2+} dynamics in postsynaptic compartment depending on the nature of synaptic inputs (Okubo et al., 2015). These lumenal ER Ca^{2+} indicators also revealed interesting dynamics in dendritic spines, which suggest that $[Ca^{2+}]_{er}$ and therefore $[Ca^{2+}]_c$ can undergo synapse-specific regulation (Suzuki et al., 2014; Henderson et al., 2015).

FUTURE PERSPECTIVES

Recent studies characterized the roles of presynaptic mitochondria and circuit-specific ER Ca^{2+} mobility in dendrites directly via live imaging (Okubo et al., 2015; Kwon et al., 2016), however, organelle-specific Ca^{2+} dynamics at local synapses is only beginning to be explored. Genetically-encoded Ca^{2+} sensors targeted to intracellular organelle and/or to specific synapses as well as functional indicators (like pHluorin-tagged synaptophysin or GluRs) will lead to the identification of synapse- and circuit-specific roles of mitochondria and ER Ca^{2+} in neurons.

MCU has been recently shown to be associated with multiple regulatory proteins, which seems to modify or gate its gating properties and can prevent or enhance mitochondrial Ca^{2+} uptake upon changes in cytosolic Ca^{2+} dynamics (Perocchi et al., 2010; Mallilankaraman et al., 2012; Csordás et al., 2013; Plovanich et al., 2013; Raffaello et al., 2013; Sancak et al., 2013; De Stefani et al., 2015). In addition, MCU activity can be differentially controlled in different tissues (Fieni et al., 2012). Therefore, future investigations should probe the function of this MCU-regulatory complex in neurons and test if MCU and/or MCU-associated proteins can act as neuronal subtype-specific and/or synapse-specific functional modifiers.

In non-neuronal cells, ER and mitochondria establish focal connections which play a key role in Ca^{2+} transfer from ER to mitochondria which has been characterized via intra- and inter-organelle Ca^{2+} imaging (Rizzuto et al., 1993, 2012; Csordás et al., 2010; Kornmann, 2013). This transfer modulates ATP production in mitochondria and may also affect lipid exchange between these two organelles (Voelker, 1990; Cárdenas et al., 2010; Fujimoto and Hayashi, 2011). At present, in neurons, the role of Ca^{2+} translocation between ER and mitochondria is largely unknown. Although immuno-EM images *in vivo* and Ca^{2+} imaging with dyes in respiratory motor neurons suggested ER-mitochondria Ca^{2+} crosstalk, future work will need to establish the context in which ER-mitochondria interface regulates Ca^{2+} dynamics and synaptic function (Takei et al., 1992; Shoshan-Barmatz et al., 2004; Mironov and Symonchuk, 2006).

AUTHOR CONTRIBUTIONS

All three authors co-wrote the manuscript.

FUNDING

This work was partially funded by support from the NIH-NINDS (R01NS067557, FP), Japan society for the promotion of science fellowship for research abroad and The Uehara Memorial Foundation (YH), and a grant from the Human Frontier Science Program long-term fellowship (S-KK).

REFERENCES

Abad, M. F., Di Benedetto, G., Magalhães, P. J., Filippin, L., and Pozzan, T. (2004). Mitochondrial pH monitored by a new engineered green fluorescent protein mutant. *J. Biol. Chem.* 279, 11521–11529. doi: 10.1074/jbc.m306766200

Akerboom, J., Carreras Calderón, N., Tian, L., Wabnig, S., Prigge, M., Tolö, J., et al. (2013). Genetically encoded calcium indicators for multi-color neural activity imaging and combination with optogenetics. *Front. Mol. Neurosci.* 6:2. doi: 10.3389/fnmol.2013.00002

Arnaudeau, S., Kelley, W. L., Walsh, J. V. Jr., and Demaurex, N. (2001). Mitochondria recycle Ca^{2+} to the endoplasmic reticulum and prevent the depletion of neighboring endoplasmic reticulum regions. *J. Biol. Chem.* 276, 29430–29439. doi: 10.1074/jbc.m103274200

Baba, A., Yasui, T., Fujisawa, S., Yamada, R. X., Yamada, M. K., Nishiyama, N., et al. (2003). Activity-evoked capacitative Ca^{2+} entry: implications in synaptic plasticity. *J. Neurosci.* 23, 7737–7741.

Baker, K. D., Edwards, T. M., and Rickard, N. S. (2013). The role of intracellular calcium stores in synaptic plasticity and memory consolidation.

Neurosci. Biobehav. Rev. 37, 1211–1239. doi: 10.1016/j.neubiorev.2013.04.011

Bardo, S., Cavazzini, M. G., and Emptage, N. (2006). The role of the endoplasmic reticulum Ca^{2+} store in the plasticity of central neurons. *Trends Pharmacol. Sci.* 27, 78–84. doi: 10.1016/j.tips.2005.12.008

Baron, K. T., Wang, G. J., Padua, R. A., Campbell, C., and Thayer, S. A. (2003). NMDA-evoked consumption and recovery of mitochondrially targeted aequorin suggests increased Ca^{2+} uptake by a subset of mitochondria in hippocampal neurons. *Brain Res.* 993, 124–132. doi: 10.1016/j.brainres.2003.09.022

Bartelmez, G. W., and Hoerr, N. L. (1933). The vestibular club endings in ameiurus. Further evidence on the morphology of the synapse. *J. Comp. Neurol.* 57, 401–428. doi: 10.1002/cne.900570303

Billups, B., and Forsythe, I. D. (2002). Presynaptic mitochondrial calcium sequestration influences transmission at mammalian central synapses. *J. Neurosci.* 22, 5840–5847.

Cárdenas, C., Miller, R. A., Smith, I., Bui, T., Molgo, J., Muller, M., et al. (2010). Essential regulation of cell bioenergetics by constitutive InsP3 receptor Ca^{2+} transfer to mitochondria. *Cell* 142, 270–283. doi: 10.1016/j.cell.2010.06.007

Castonguay, A., and Robitaille, R. (2001). Differential regulation of transmitter release by presynaptic and glial Ca^{2+} internal stores at the neuromuscular synapse. *J. Neurosci.* 21, 1911–1922.

Cherra, S. J. III, Steer, E., Gusdon, A. M., Kiselyov, K., and Chu, C. T. (2013). Mutant LRRK2 elicits calcium imbalance and depletion of dendritic mitochondria in neurons. *Am. J. Pathol.* 182, 474–484. doi: 10.1016/j.ajpath.2012.10.027

Chicurel, M. E., and Harris, K. M. (1992). Three-dimensional analysis of the structure and composition of CA3 branched dendritic spines and their synaptic relationships with mossy fiber boutons in the rat hippocampus. *J. Comp. Neurol.* 325, 169–182. doi: 10.1002/cne.903250204

Chouhan, A. K., Ivannikov, M. V., Lu, Z., Sugimori, M., Llinas, R. R., and Macleod, G. T. (2012). Cytosolic calcium coordinates mitochondrial energy metabolism with presynaptic activity. *J. Neurosci.* 32, 1233–1243. doi: 10.1523/jneurosci.1301-11.2012

Clapham, D. E. (2007). Calcium signaling. *Cell* 131, 1047–1058. doi: 10.1016/j.cell.2007.11.028

Csordás, G., Golenár, T., Seifert, E. L., Kamer, K. J., Sancak, Y., Perocchi, F., et al. (2013). MICU1 controls both the threshold and cooperative activation of the mitochondrial Ca^{2+} uniporter. *Cell Metab.* 17, 976–987. doi: 10.1016/j.cmet.2013.04.020

Csordás, G., Várnai, P., Golenár, T., Roy, S., Purkins, G., Schneider, T. G., et al. (2010). Imaging interorganelle contacts and local calcium dynamics at the ER-mitochondrial interface. *Mol. Cell* 39, 121–132. doi: 10.1016/j.molcel.2010.06.029

David, G., and Barrett, E. F. (2003). Mitochondrial Ca^{2+} uptake prevents desynchronization of quantal release and minimizes depletion during repetitive stimulation of mouse motor nerve terminals. *J. Physiol.* 548, 425–438. doi: 10.1113/jphysiol.2002.035196

De Stefani, D., Patron, M., and Rizzuto, R. (2015). Structure and function of the mitochondrial calcium uniporter complex. *Biochim. Biophys. Acta* 1853, 2006–2011. doi: 10.1016/j.bbamcr.2015.04.008

Deluca, H. F., and Engstrom, G. W. (1961). Calcium uptake by rat kidney mitochondria. *Proc. Natl. Acad. Sci. U S A* 47, 1744–1750. doi: 10.1073/pnas.47.11.1744

Emptage, N., Bliss, T. V., and Fine, A. (1999). Single synaptic events evoke NMDA receptor-mediated release of calcium from internal stores in hippocampal dendritic spines. *Neuron* 22, 115–124. doi: 10.1016/s0896-6273(00)80683-2

Emptage, N. J., Reid, C. A., and Fine, A. (2001). Calcium stores in hippocampal synaptic boutons mediate short-term plasticity, store-operated Ca^{2+} entry and spontaneous transmitter release. *Neuron* 29, 197–208. doi: 10.1016/s0896-6273(01)00190-8

Fieni, F., Lee, S. B., Jan, Y. N., and Kirichok, Y. (2012). Activity of the mitochondrial calcium uniporter varies greatly between tissues. *Nat. Commun.* 3:1317. doi: 10.1038/ncomms2325

Finch, E. A., and Augustine, G. J. (1998). Local calcium signalling by inositol-1,4,5-trisphosphate in Purkinje cell dendrites. *Nature* 396, 753–756. doi: 10.1038/25541

Fujimoto, M., and Hayashi, T. (2011). New insights into the role of mitochondria-associated endoplasmic reticulum membrane. *Int. Rev. Cell Mol. Biol.* 292, 73–117. doi: 10.1016/B978-0-12-386033-0.00002-5

Furuichi, T., Furutama, D., Hakamata, Y., Nakai, J., Takeshima, H., and Mikoshiba, K. (1994). Multiple types of ryanodine receptor/Ca^{2+} release channels are differentially expressed in rabbit brain. *J. Neurosci.* 14, 4794–4805.

Futatsugi, A., Kato, K., Ogura, H., Li, S. T., Nagata, E., Kuwajima, G., et al. (1999). Facilitation of NMDAR-independent LTP and spatial learning in mutant mice lacking ryanodine receptor type 3. *Neuron* 24, 701–713. doi: 10.1016/s0896-6273(00)81123-x

Galante, M., and Marty, A. (2003). Presynaptic ryanodine-sensitive calcium stores contribute to evoked neurotransmitter release at the basket cell-Purkinje cell synapse. *J. Neurosci.* 23, 11229–11234.

Garcia-Alvarez, G., Lu, B., Yap, K. A., Wong, L. C., Thevathasan, J. V., Lim, L., et al. (2015). STIM2 regulates PKA-dependent phosphorylation and trafficking of AMPARs. *Mol. Biol. Cell* 26, 1141–1159. doi: 10.1091/mbc.e14-07-1222

García-Chacón, L. E., Nguyen, K. T., David, G., and Barrett, E. F. (2006). Extrusion of Ca^{2+} from mouse motor terminal mitochondria via a Na^{+}-Ca^{2+} exchanger increases post-tetanic evoked release. *J. Physiol.* 574, 663–675. doi: 10.1113/jphysiol.2006.110841

Gazit, N., Vertkin, I., Shapira, I., Helm, M., Slomowitz, E., Sheiba, M., et al. (2016). IGF-1 receptor differentially regulates spontaneous and evoked transmission via mitochondria at hippocampal synapses. *Neuron* 89, 583–597. doi: 10.1016/j.neuron.2015.12.034

Giannini, G., Conti, A., Mammarella, S., Scrobogna, M., and Sorrentino, V. (1995). The ryanodine receptor/calcium channel genes are widely and differentially expressed in murine brain and peripheral tissues. *J. Cell Biol.* 128, 893–904. doi: 10.1083/jcb.128.5.893

Gray, E. G. (1963). Electron microscopy of presynaptic organelles of the spinal cord. *J. Anat.* 97, 101–106.

Guo, X., Macleod, G. T., Wellington, A., Hu, F., Panchumarthi, S., Schoenfield, M., et al. (2005). The GTPase dMiro is required for axonal transport of mitochondria to *Drosophila* synapses. *Neuron* 47, 379–393. doi: 10.1016/j.neuron.2005.06.027

Hartmann, J., Karl, R. M., Alexander, R. P., Adelsberger, H., Brill, M. S., Rühlmann, C., et al. (2014). STIM1 controls neuronal Ca^{2+} signaling, mGluR1-dependent synaptic transmission and cerebellar motor behavior. *Neuron* 82, 635–644. doi: 10.1016/j.neuron.2014.03.027

Henderson, M. J., Baldwin, H. A., Werley, C. A., Boccardo, S., Whitaker, L. R., Yan, X., et al. (2015). A low affinity GCaMP3 variant (GCaMPer) for imaging the endoplasmic reticulum calcium store. *PLoS One* 10:e0139273. doi: 10.1371/journal.pone.0139273

Itoh, S., Ito, K., Fujii, S., Kaneko, K., Kato, K., Mikoshiba, K., et al. (2001). Neuronal plasticity in hippocampal mossy fiber-CA3 synapses of mice lacking the inositol-1,4,5-trisphosphate type 1 receptor. *Brain Res.* 901, 237–246. doi: 10.1016/s0006-8993(01)02373-3

Jahn, R., and Fasshauer, D. (2012). Molecular machines governing exocytosis of synaptic vesicles. *Nature* 490, 201–207. doi: 10.1038/nature11320

Kang, J. S., Tian, J. H., Pan, P. Y., Zald, P., Li, C., Deng, C., et al. (2008). Docking of axonal mitochondria by syntaphilin controls their mobility and affects short-term facilitation. *Cell* 132, 137–148. doi: 10.1016/j.cell.2007.11.024

Kann, O., and Kovács, R. (2007). Mitochondria and neuronal activity. *Am. J. Physiol. Cell Physiol.* 292, C641–C657. doi: 10.1152/ajpcell.00222.2006

Kapur, A., Yeckel, M., and Johnston, D. (2001). Hippocampal mossy fiber activity evokes Ca^{2+} release in CA3 pyramidal neurons via a metabotropic glutamate receptor pathway. *Neuroscience* 107, 59–69. doi: 10.1016/s0306-4522(01)00293-7

Kasthuri, N., Hayworth, K. J., Berger, D. R., Schalek, R. L., Conchello, J. A., Knowles-Barley, S., et al. (2015). Saturated reconstruction of a volume of neocortex. *Cell* 162, 648–661. doi: 10.1016/j.cell.2015.06.054

Knopfel, T. (2012). Genetically encoded optical indicators for the analysis of neuronal circuits. *Nat. Rev. Neurosci.* 13, 687–700. doi: 10.1523/JNEUROSCI.0381-14.2014

Korkotian, E., Frotscher, M., and Segal, M. (2014). Synaptopodin regulates spine plasticity: mediation by calcium stores. *J. Neurosci.* 34, 11641–11651. doi: 10.1523/JNEUROSCI.0381-14.2014

Kornmann, B. (2013). The molecular hug between the ER and the mitochondria. *Curr. Opin. Cell Biol.* 25, 443–448. doi: 10.1016/j.ceb.2013.02.010

Kovalchuk, Y., Eilers, J., Lisman, J., and Konnerth, A. (2000). NMDA receptor-mediated subthreshold Ca^{2+} signals in spines of hippocampal neurons. *J. Neurosci.* 20, 1791–1799.

Kwon, S., Sando, R. III, Lewis, T. L., Hirabayashi, Y., Maximov, A., and Polleux, F. (2016). LKB1 regulates mitochondria-dependent presynaptic calcium clearance and neurotransmitter release properties at excitatory synapses along cortical axons. *PLoS Biol.* 14:e1002516. doi: 10.1371/journal.pbio.1002516

Lauri, S. E., Bortolotto, Z. A., Nistico, R., Bleakman, D., Ornstein, P. L., Lodge, D., et al. (2003). A role for Ca^{2+} stores in kainate receptor-dependent synaptic facilitation and LTP at mossy fiber synapses in the hippocampus. *Neuron* 39, 327–341. doi: 10.1016/s0896-6273(03)00369-6

Lee, D., Lee, K. H., Ho, W. K., and Lee, S. H. (2007). Target cell-specific involvement of presynaptic mitochondria in post-tetanic potentiation at hippocampal mossy fiber synapses. *J. Neurosci.* 27, 13603–13613. doi: 10.1523/JNEUROSCI.3985-07.2007

Lei, S., Pelkey, K. A., Topolnik, L., Congar, P., Lacaille, J. C., and McBain, C. J. (2003). Depolarization-induced long-term depression at hippocampal mossy fiber-CA3 pyramidal neuron synapses. *J. Neurosci.* 23, 9786–9795.

Li, Z., Okamoto, K., Hayashi, Y., and Sheng, M. (2004). The importance of dendritic mitochondria in the morphogenesis and plasticity of spines and synapses. *Cell* 119, 873–887. doi: 10.1016/j.cell.2004.11.003

Liang, Y., Yuan, L. L., Johnston, D., and Gray, R. (2002). Calcium signaling at single mossy fiber presynaptic terminals in the rat hippocampus. *J. Neurophysiol.* 87, 1132–1137.

Llano, I., Gonzalez, J., Caputo, C., Lai, F. A., Blayney, L. M., Tan, Y. P., et al. (2000). Presynaptic calcium stores underlie large-amplitude miniature IPSCs and spontaneous calcium transients. *Nat. Neurosci.* 3, 1256–1265. doi: 10.1038/81781

Lüscher, C., and Malenka, R. C. (2012). NMDA receptor-dependent long-term potentiation and long-term depression (LTP/LTD). *Cold Spring Harb Perspect. Biol.* 4:a005710. doi: 10.1101/cshperspect.a005710

Ly, C. V., and Verstreken, P. (2006). Mitochondria at the synapse. *Neuroscientist* 12, 291–299. doi: 10.1177/1073858406287661

Malenka, R. C., and Nicoll, R. A. (1999). Long-term potentiation–a decade of progress? *Science* 285, 1870–1874. doi: 10.1126/science.285.5435.1870

Mallilankaraman, K., Doonan, P., Cárdenas, C., Chandramoorthy, H. C., Müller, M., Miller, R., et al. (2012). MICU1 is an essential gatekeeper for MCU-mediated mitochondrial Ca^{2+} uptake that regulates cell survival. *Cell* 151, 630–644. doi: 10.1016/j.cell.2012.10.011

Marland, J. R., Hasel, P., Bonnycastle, K., and Cousin, M. A. (2016). Mitochondrial calcium uptake modulates synaptic vesicle endocytosis in central nerve terminals. *J. Biol. Chem.* 291, 2080–2086. doi: 10.1074/jbc.M115.686956

Mathew, S. S., and Hablitz, J. J. (2008). Calcium release via activation of presynaptic IP3 receptors contributes to kainate-induced IPSC facilitation in rat neocortex. *Neuropharmacology* 55, 106–116. doi: 10.1016/j.neuropharm.2008.05.005

Mattson, M. P., Gleichmann, M., and Cheng, A. (2008). Mitochondria in neuroplasticity and neurological disorders. *Neuron* 60, 748–766. doi: 10.1016/j.neuron.2008.10.010

Mellor, J., and Nicoll, R. A. (2001). Hippocampal mossy fiber LTP is independent of postsynaptic calcium. *Nat. Neurosci.* 4, 125–126. doi: 10.1038/83941

Minta, A., Kao, J. P., and Tsien, R. Y. (1989). Fluorescent indicators for cytosolic calcium based on rhodamine and fluorescein chromophores. *J. Biol. Chem.* 264, 8171–8178.

Mironov, S. L., and Symonchuk, N. (2006). ER vesicles and mitochondria move and communicate at synapses. *J. Cell Sci.* 119, 4926–4934. doi: 10.1242/jcs.03254

Miyata, M., Finch, E. A., Khiroug, L., Hashimoto, K., Hayasaka, S., Oda, S. I., et al. (2000). Local calcium release in dendritic spines required for long-term synaptic depression. *Neuron* 28, 233–244. doi: 10.1016/s0896-6273(00)00099-4

Nagai, T., Sawano, A., Park, E. S., and Miyawaki, A. (2001). Circularly permuted green fluorescent proteins engineered to sense Ca^{2+}. *Proc. Natl. Acad. Sci. U S A* 98, 3197–3202. doi: 10.1073/pnas.051636098

Nagase, T., Ito, K. I., Kato, K., Kaneko, K., Kohda, K., Matsumoto, M., et al. (2003). Long-term potentiation and long-term depression in hippocampal CA1 neurons of mice lacking the IP(3) type 1 receptor. *Neuroscience* 117, 821–830. doi: 10.1016/s0306-4522(02)00803-5

Neher, E., and Sakaba, T. (2008). Multiple roles of calcium ions in the regulation of neurotransmitter release. *Neuron* 59, 861–872. doi: 10.1016/j.neuron.2008.08.019

Nishiyama, M., Hong, K., Mikoshiba, K., Poo, M. M., and Kato, K. (2000). Calcium stores regulate the polarity and input specificity of synaptic modification. *Nature* 408, 584–588. doi: 10.1038/35046067

Okubo, Y., Suzuki, J., Kanemaru, K., Nakamura, N., Shibata, T., and Iino, M. (2015). Visualization of Ca^{2+} filling mechanisms upon synaptic inputs in the endoplasmic reticulum of cerebellar purkinje cells. *J. Neurosci.* 35, 15837–15846. doi: 10.1523/JNEUROSCI.3487-15.2015

Oliet, S. H., Malenka, R. C., and Nicoll, R. A. (1997). Two distinct forms of long-term depression coexist in CA1 hippocampal pyramidal cells. *Neuron* 18, 969–982. doi: 10.1016/s0896-6273(00)80336-0

Palay, S. L. (1956). Synapses in the central nervous system. *J. Biophys. Biochem. Cytol.* 2, 193–202. doi: 10.1083/jcb.2.4.193

Palmer, A. E., Jin, C., Reed, J. C., and Tsien, R. Y. (2004). Bcl-2-mediated alterations in endoplasmic reticulum Ca^{2+} analyzed with an improved genetically encoded fluorescent sensor. *Proc. Natl. Acad. Sci. U S A* 101, 17404–17409. doi: 10.1073/pnas.0408030101

Palmer, A. E., and Tsien, R. Y. (2006). Measuring calcium signaling using genetically targetable fluorescent indicators. *Nat. Protoc.* 1, 1057–1065. doi: 10.1038/nprot.2006.172

Patron, M., Checchetto, V., Raffaello, A., Teardo, E., Vecellio Reane, D., Mantoan, M., et al. (2014). MICU1 and MICU2 finely tune the mitochondrial Ca^{2+} uniporter by exerting opposite effects on MCU activity. *Mol. Cell* 53, 726–737. doi: 10.1016/j.molcel.2014.01.013

Perocchi, F., Gohil, V. M., Girgis, H. S., Bao, X. R., McCombs, J. E., Palmer, A. E., et al. (2010). MICU1 encodes a mitochondrial EF hand protein required for Ca^{2+} uptake. *Nature* 467, 291–296. doi: 10.1038/nature09358

Plovanich, M., Bogorad, R. L., Sancak, Y., Kamer, K. J., Strittmatter, L., Li, A. A., et al. (2013). MICU2, a paralog of MICU1, resides within the mitochondrial uniporter complex to regulate calcium handling. *PLoS One* 8:e55785. doi: 10.1371/journal.pone.0055785

Poburko, D., Santo-Domingo, J., and Demaurex, N. (2011). Dynamic regulation of the mitochondrial proton gradient during cytosolic calcium elevations. *J. Biol. Chem.* 286, 11672–11684. doi: 10.1074/jbc.M110.159962

Raffaello, A., De Stefani, D., Sabbadin, D., Teardo, E., Merli, G., Picard, A., et al. (2013). The mitochondrial calcium uniporter is a multimer that can include a dominant-negative pore-forming subunit. *EMBO J.* 32, 2362–2376. doi: 10.1038/emboj.2013.157

Raymond, C. R., and Redman, S. J. (2002). Different calcium sources are narrowly tuned to the induction of different forms of LTP. *J. Neurophysiol.* 88, 249–255.

Reyes, M., and Stanton, P. K. (1996). Induction of hippocampal long-term depression requires release of Ca^{2+} from separate presynaptic and postsynaptic intracellular stores. *J. Neurosci.* 16, 5951–5960.

Rizzuto, R., Brini, M., Murgia, M., and Pozzan, T. (1993). Microdomains with high Ca^{2+} close to IP3-sensitive channels that are sensed by neighboring mitochondria. *Science* 262, 744–747. doi: 10.1126/science.8235595

Rizzuto, R., De Stefani, D., Raffaello, A., and Mammucari, C. (2012). Mitochondria as sensors and regulators of calcium signalling. *Nat. Rev. Mol. Cell Biol.* 13, 566–578. doi: 10.1038/nrm3412

Rizzuto, R., and Pozzan, T. (2006). Microdomains of intracellular Ca^{2+}: molecular determinants and functional consequences. *Physiol. Rev.* 86, 369–408. doi: 10.1152/physrev.00004.2005

Rizzuto, R., Simpson, A. W., Brini, M., and Pozzan, T. (1992). Rapid changes of mitochondrial Ca^{2+} revealed by specifically targeted recombinant aequorin. *Nature* 358, 325–327. doi: 10.1038/358325a0

Robert, V., Gurlini, P., Tosello, V., Nagai, T., Miyawaki, A., Di Lisa, F., et al. (2001). Beat-to-beat oscillations of mitochondrial $[Ca^{2+}]$ in cardiac cells. *EMBO J.* 20, 4998–5007. doi: 10.1093/emboj/20.17.4998

Rodriguez-Garcia, A., Rojo-Ruiz, J., Navas-Navarro, P., Aulestia, F. J., Gallego-Sandin, S., Garcia-Sancho, J., et al. (2014). GAP, an aequorin-based fluorescent indicator for imaging Ca^{2+} in organelles. *Proc. Natl. Acad. Sci. U S A* 111, 2584–2589. doi: 10.1073/pnas.1316539111

Rose, T., Goltstein, P. M., Portugues, R., and Griesbeck, O. (2014). Putting a finishing touch on GECIs. *Front. Mol. Neurosci.* 7:88. doi: 10.3389/fnmol.2014.00088

Rowland, K. C., Irby, N. K., and Spirou, G. A. (2000). Specialized synapse-associated structures within the calyx of Held. *J. Neurosci.* 20, 9135–9144.

Sancak, Y., Markhard, A. L., Kitami, T., Kovács-Bogdán, E., Kamer, K. J., Udeshi, N. D., et al. (2013). EMRE is an essential component of the mitochondrial calcium uniporter complex. *Science* 342, 1379–1382. doi: 10.1126/science.1242993

Sandler, V. M., and Barbara, J. G. (1999). Calcium-induced calcium release contributes to action potential-evoked calcium transients in hippocampal CA1 pyramidal neurons. *J. Neurosci.* 19, 4325–4336.

Schneggenburger, R., and Neher, E. (2005). Presynaptic calcium and control of vesicle fusion. *Curr. Opin. Neurobiol.* 15, 266–274. doi: 10.1016/j.conb.2005.05.006

Schon, E. A., and Przedborski, S. (2011). Mitochondria: the next (neurode)generation. *Neuron* 70, 1033–1053. doi: 10.1016/j.neuron.2011.06.003

Scullin, C. S., and Partridge, L. D. (2010). Contributions of SERCA pump and ryanodine-sensitive stores to presynaptic residual Ca^{2+}. *Cell Calcium* 47, 326–338. doi: 10.1016/j.ceca.2010.01.004

Scullin, C. S., Wilson, M. C., and Partridge, L. D. (2010). Developmental changes in presynaptic Ca^{2+} clearance kinetics and synaptic plasticity in mouse Schaffer collateral terminals. *Eur. J. Neurosci.* 31, 817–826. doi: 10.1111/j.1460-9568.2010.07137.x

Segal, M., and Korkotian, E. (2015). Roles of calcium stores and store-operated channels in plasticity of dendritic spines. *Neuroscientist* doi: 10.1177/1073858415613277 [Epub ahead of print].

Sharma, G., and Vijayaraghavan, S. (2003). Modulation of presynaptic store calcium induces release of glutamate and postsynaptic firing. *Neuron* 38, 929–939. doi: 10.1016/s0896-6273(03)00322-2

Sharp, A. H., McPherson, P. S., Dawson, T. M., Aoki, C., Campbell, K. P., and Snyder, S. H. (1993). Differential immunohistochemical localization of inositol 1,4,5-trisphosphate- and ryanodine-sensitive Ca^{2+} release channels in rat brain. *J. Neurosci.* 13, 3051–3063.

Sharp, A. H., Nucifora, F. C. Jr., Blondel, O., Sheppard, C. A., Zhang, C., Snyder, S. H., et al. (1999). Differential cellular expression of isoforms of inositol 1,4,5-triphosphate receptors in neurons and glia in brain. *J. Comp. Neurol.* 406, 207–220. doi: 10.1002/(SICI)1096-9861(19990405)406:2<207::AID-CNE6>3.0.CO;2-7

Sheng, M., and Hoogenraad, C. C. (2007). The postsynaptic architecture of excitatory synapses: a more quantitative view. *Annu. Rev. Biochem.* 76, 823–847. doi: 10.1146/annurev.biochem.76.060805.160029

Shepherd, G. M., and Harris, K. M. (1998). Three-dimensional structure and composition of CA3→CA1 axons in rat hippocampal slices: implications for presynaptic connectivity and compartmentalization. *J. Neurosci.* 18, 8300–8310.

Shoshan-Barmatz, V., Zalk, R., Gincel, D., and Vardi, N. (2004). Subcellular localization of VDAC in mitochondria and ER in the cerebellum. *Biochim. Biophys. Acta* 1657, 105–114. doi: 10.1016/j.bbabio.2004.02.009

Slater, E. C., and Cleland, K. W. (1953). The effect of calcium on the respiratory and phosphorylative activities of heart-muscle sarcosomes. *Biochem. J.* 55, 566–590. doi: 10.1042/bj0550566

Solovyova, N., Veselovsky, N., Toescu, E. C., and Verkhratsky, A. (2002). Ca^{2+} dynamics in the lumen of the endoplasmic reticulum in sensory neurons: direct visualization of Ca^{2+}-induced Ca^{2+} release triggered by physiological Ca^{2+} entry. *EMBO J.* 21, 622–630. doi: 10.1093/emboj/21.4.622

Spacek, J., and Harris, K. M. (1997). Three-dimensional organization of smooth endoplasmic reticulum in hippocampal CA1 dendrites and dendritic spines of the immature and mature rat. *J. Neurosci.* 17, 190–203. doi: 10.1002/hipo.20238

Südhof, T. C. (2012). The presynaptic active zone. *Neuron* 75, 11–25. doi: 10.1016/j.neuron.2012.06.012

Suzuki, J., Kanemaru, K., Ishii, K., Ohkura, M., Okubo, Y., and Iino, M. (2014). Imaging intraorganellar Ca^{2+} at subcellular resolution using CEPIA. *Nat. Commun.* 5:4153. doi: 10.1038/ncomms5153

Takechi, H., Eilers, J., and Konnerth, A. (1998). A new class of synaptic response involving calcium release in dendritic spines. *Nature* 396, 757–760. doi: 10.1038/25547

Takei, K., Stukenbrok, H., Metcalf, A., Mignery, G. A., Südhof, T. C., Volpe, P., et al. (1992). Ca^{2+} stores in Purkinje neurons: endoplasmic reticulum subcompartments demonstrated by the heterogeneous distribution of the InsP3 receptor, Ca^{2+}-ATPase and calsequestrin. *J. Neurosci.* 12, 489–505.

Tang, Y., and Zucker, R. S. (1997). Mitochondrial involvement in post-tetanic potentiation of synaptic transmission. *Neuron* 18, 483–491. doi: 10.1016/s0896-6273(00)81248-9

Thayer, S. A., and Miller, R. J. (1990). Regulation of the intracellular free calcium concentration in single rat dorsal root ganglion neurones *in vitro*. *J. Physiol.* 425, 85–115. doi: 10.1113/jphysiol.1990.sp018094

Tian, L., Hires, S. A., and Looger, L. L. (2012). Imaging neuronal activity with genetically encoded calcium indicators. *Cold Spring Harb. Protoc.* 2012, 647–656. doi: 10.1101/pdb.top069609

Unni, V. K., Zakharenko, S. S., Zablow, L., DeCostanzo, A. J., and Siegelbaum, S. A. (2004). Calcium release from presynaptic ryanodine-sensitive stores is required for long-term depression at hippocampal CA3-CA3 pyramidal neuron synapses. *J. Neurosci.* 24, 9612–9622. doi: 10.1523/JNEUROSCI.5583-03.2004

Verkhratsky, A. (2005). Physiology and pathophysiology of the calcium store in the endoplasmic reticulum of neurons. *Physiol. Rev.* 85, 201–279. doi: 10.1152/physrev.00004.2004

Verstreken, P., Ly, C. V., Venken, K. J., Koh, T. W., Zhou, Y., and Bellen, H. J. (2005). Synaptic mitochondria are critical for mobilization of reserve pool vesicles at *Drosophila* neuromuscular junctions. *Neuron* 47, 365–378. doi: 10.1016/j.neuron.2005.06.018

Voelker, D. R. (1990). Characterization of phosphatidylserine synthesis and translocation in permeabilized animal cells. *J. Biol. Chem.* 265, 14340–14346.

Vos, M., Lauwers, E., and Verstreken, P. (2010). Synaptic mitochondria in synaptic transmission and organization of vesicle pools in health and disease. *Front. Synaptic Neurosci.* 2:139. doi: 10.3389/fnsyn.2010.00139

Wang, S. S., Denk, W., and Häusser, M. (2000). Coincidence detection in single dendritic spines mediated by calcium release. *Nat. Neurosci.* 3, 1266–1273. doi: 10.1038/81792

Wang, X., and Schwarz, T. L. (2009). The mechanism of Ca^{2+} -dependent regulation of kinesin-mediated mitochondrial motility. *Cell* 136, 163–174. doi: 10.1016/j.cell.2008.11.046

Wang, G. J., and Thayer, S. A. (2002). NMDA-induced calcium loads recycle across the mitochondrial inner membrane of hippocampal neurons in culture. *J. Neurophysiol.* 87, 740–749.

White, R. J., and Reynolds, I. J. (1995). Mitochondria and Na^+/Ca^{2+} exchange buffer glutamate-induced calcium loads in cultured cortical neurons. *J. Neurosci.* 15, 1318–1328.

Wu, J., Prole, D. L., Shen, Y., Lin, Z., Gnanasekaran, A., Liu, Y., et al. (2014). Red fluorescent genetically encoded Ca^{2+} indicators for use in mitochondria and endoplasmic reticulum. *Biochem. J.* 464, 13–22. doi: 10.1042/bj20140931

Yang, S. N., Tang, Y. G., and Zucker, R. S. (1999). Selective induction of LTP and LTD by postsynaptic $[Ca^{2+}]_i$ elevation. *J. Neurophysiol.* 81, 781–787.

Yeckel, M. F., Kapur, A., and Johnston, D. (1999). Multiple forms of LTP in hippocampal CA3 neurons use a common postsynaptic mechanism. *Nat. Neurosci.* 2, 625–633. doi: 10.1038/10180

Young, K. W., Bampton, E. T., Pinòn, L., Bano, D., and Nicotera, P. (2008). Mitochondrial Ca^{2+} signalling in hippocampal neurons. *Cell Calcium* 43, 296–306. doi: 10.1016/j.ceca.2007.06.007

Zhong, N., Beaumont, V., and Zucker, R. S. (2001). Roles for mitochondrial and reverse mode Na^+/Ca^{2+} exchange and the plasmalemma Ca^{2+} ATPase in post-tetanic potentiation at crayfish neuromuscular junctions. *J. Neurosci.* 21, 9598–9607.

Zhang, H., Sun, S., Herreman, A., De Strooper, B., and Bezprozvanny, I. (2010). Role of presenilins in neuronal calcium homeostasis. *J. Neurosci.* 30, 8566–8580. doi: 10.1523/JNEUROSCI.1554-10.2010

Zucker, R. S. (1989). Short-term synaptic plasticity. *Annu. Rev. Neurosci.* 12, 13–31. doi: 10.1146/annurev.neuro.12.1.13

Conflict of Interest Statement: The authors declare that the research was conducted in the absence of any commercial or financial relationships that could be construed as a potential conflict of interest.

frontiers in Synaptic Neuroscience

REVIEW
published: 29 June 2016
doi: 10.3389/fnsyn.2016.00018

Understanding Synaptogenesis and Functional Connectome in *C. elegans* by Imaging Technology

Jung-Hwa Hong[1,2] *and Mikyoung Park*[1,3]*

[1] Center for Functional Connectomics, Korea Institute of Science and Technology, Seoul, South Korea, [2] Department of Life Sciences, Korea University, Seoul, South Korea, [3] Department of Neuroscience, Korea University of Science and Technology, Daejeon, South Korea

Formation of functional synapses is a fundamental process for establishing neural circuits and ultimately for expressing complex behavior. Extensive research has interrogated how such functional synapses are formed and how synapse formation contributes to the generation of neural circuitry and behavior. The nervous system of *Caenorhabditis elegans*, due to its relatively simple structure, the transparent body, and tractable genetic system, has been adapted as an excellent model to investigate synapses and the functional connectome. Advances in imaging technology together with the improvement of genetically encoded molecular tools enabled us to visualize synapses and neural circuits of the animal model, which provide insights into our understanding of molecules and their signaling pathways that mediate synapse formation and neuronal network modulation. Here, we review synaptogenesis in active zones and the mapping of local connectome in *C. elegans* nervous system whose understandings have been extended by the advances in imaging technology along with the genetic molecular tools.

Keywords: presynaptic assembly, synaptic specificity, synaptogenesis, functional connectome, neural circuits, imaging, *C. elegans*

OPEN ACCESS

Edited by:
George Augustine,
Nanyang Technological University, Singapore

Reviewed by:
Fabrice Ango,
University of Montpellier, France
Antonio Malgaroli,
Università Vita-Salute San Raffaele, Italy

***Correspondence:**
Mikyoung Park
mikyoungpark7@gmail.com;
mpark@kist.re.kr

Received: *25 April 2016*
Accepted: *17 June 2016*
Published: *29 June 2016*

Citation:
Hong J-H and Park M (2016) Understanding Synaptogenesis and Functional Connectome in C. elegans by Imaging Technology. Front. Synaptic Neurosci. 8:18. doi: 10.3389/fnsyn.2016.00018

INTRODUCTION

One of the fundamental goals of neuroscience is to understand the generation of functional nervous system that underlies neural basis of behavior and cognition. Extensive research has attempted to interrogate the molecular and cellular mechanisms of synapse formation and functional neural circuit development. Ever since it was proposed by Sydney Brenner in the mid 1960's (Brenner, 1974), the nematodes *Caenorhabditis elegans* (*C. elegans*) has been considered as an ideal model organism to study synaptic development and neural circuitry. The organism has relatively simple nervous system, having 302 neurons and its neurochemistry and genetics are similar to those of mammals. Moreover, the complete structure and connectivity of *C. elegans* nervous system have been deciphered through genetic screens and reconstruction of electron micrographs (EM) of serial sections, which led to discovery of novel molecules important for development and maintenance of functional synaptic connectivity (White et al., 1986). *C. elegans* with its transparent body was the first animal in which the green fluorescent protein (GFP) was expressed (Chalfie et al., 1994). Combined with its stable expression of fluorescently tagged proteins (Mello et al., 1991; Frokjaer-Jensen et al., 2008), studies with *C. elegans* have made major contributions to our knowledge on neural development, axonal migration, and synapse formation. Recently, selective plane illumination microscopy (SPIM) techniques such as tiling light-sheet

SPIM (TLS-SPIM) (Fu et al., 2016) and inverted SPIM (iSPIM) (Wu et al., 2011) have been developed and utilized to achieve high spatiotemporal resolution 3-dimensional live imaging of *C. elegans* embyos with no detectable phototoxicity, which could enable studies on synaptogenesis and axon guidance during embryogenesis in *C. elegans*. Another recent work adopting complementation-activated light microscopy (CALM) in which proteins are conjugated with non-fluorescent split-fluorescent proteins, which become to be fluorescent when complemented with synthetic peptides enabled single-molecule imaging with a precision of 30 nm within synapses in live worms (Zhan et al., 2014).

Rapid developments of advanced imaging technologies have expanded our understanding of the molecular and cellular basis of synaptogenesis with great depth, taking a huge step closer to revealing functional neural connectome. Here, we discuss on the synaptogenesis in presynaptic active zones revealed by both conventional and advanced imaging set-ups and review recent work utilizing advanced imaging technology to unravel the functional connectome of neural circuits. Rather than dealing with the mechanistic aspects of synapse formation and neural circuits development, this review will mainly focus on how synaptic ultrastructure, synaptic formation, and functional neural connectome have been sophisticated by the advanced imaging technology. For more in-depth reviews on the mechanism of synaptogenesis, synaptic specificity, and neural circuits development, see Campbell et al. (2015), Cherra and Jin (2015), Jin (2015), Zhen and Samuel (2015), Yogev and Shen (2014), Chia et al. (2013), and Park and Shen (2012).

IMAGING SYNAPSE ASSEMBLY

Chemical synapses are specialized intercellular junctions with two apposed compartments, the pre-synaptic terminal and the postsynaptic target, and the synaptic cleft which is about 20 nm gap between the pre- and postsynapses (Cowan and Kandel, 2001). Proper organization of pre- and postsynaptic components with precise regulation underlies formation of functional synapses. For the past decades, tremendous details regarding the morphology and assembly of *C. elegans* synaptic structure have been revealed with development of genetic tools and imaging technology. This section focuses on presynaptic assembly and synaptic specificity revealed by genetically encoded molecular tools and imaging technologies.

Presynaptic Active Zone Imaging

The presynaptic compartment in *C. elegans* exhibits an overall structural organization similar to that in vertebrates, with synaptic vesicles clustered in and around the electron-dense membrane structure called active zone known to serve as a major site of neurotransmitter release. Ultrastructural analysis have shown that, despite the variations among the appearances, synapses of various organisms commonly display synaptic vesicle docking and fusion at active zone that can be identified by darkly stained membrane structures (Zhai and Bellen, 2004; Ackermann et al., 2015).

Many studies using *C. elegans* have investigated the role of various proteins localized at active zone in synapse formation (Yeh et al., 2005; Watanabe et al., 2011). Classical EM analysis has provided initial assessment of *C. elegans* synaptic components but its requirement for ultrathin sectioning of samples approximately 50 nm thickness (White et al., 1986) limits the resolution and impairs detailed visualization of fine structures. The multifunctional synaptic scaffolding protein SYD-2/liprin-α is one of the key proteins identified to regulate synaptic development in *C. elegans* and *Drosophila* (Zhen and Jin, 1999). The loss-of-function analysis on SYD-2/liprin-α and uncoordinated-10 (UNC-10)/Rab3-interacting molecule (RIM), which is another dense-projection components (Weimer et al., 2006) revealed reduced vesicle recruitment at active zone (Stigloher et al., 2011; Kittelmann et al., 2013), and smaller dense-projection due to loss of SYD-2/liprin-α function (Kittelmann et al., 2013) unlike the finding showing an expanded dense-projection (Zhen and Jin, 1999). One suggested explanation for variability in *syd-2* mutant synaptic ultrastructure is due to the differences in fixation procedure (Kittelmann et al., 2013). Nevertheless, it is certain that advanced and optimized imaging technique led to identification of regulatory proteins to retain synaptic vesicle at active zone.

A method which comprises of correlative fluorescence electron microscopy was developed and optimized to observe the nanoscopic localization of SYD-2/liprin-α in *C. elegans* active zone (Watanabe et al., 2011). The technique employed both stimulated emission depletion (STED) microscopy and photoactivated localization microscopy (PALM) on ultrathin sections for protein localization at super-resolution nanoscale level and subsequently correlate the protein localization with ultrastructures by electron microscope. The localization of SYD-2/liprin-α to the *C. elegans* presynaptic dense-projection observed by this technique (Watanabe et al., 2011) was consistent with the earlier finding from the immunoelectron micrograph (Yeh et al., 2005) but the result was more advanced to provide the precise localization of the proteins in small and dense structures likely within the synapse at the level of nanoscale super-resolution.

In addition, studies using advanced EM tomography of 250 nm thick sections combined with high-pressure freezing (HPF) and freeze substitution (Stigloher et al., 2011; Kittelmann et al., 2013) have resolved the highly complex structure of dense-projections at cholinergic neuromuscular junctions (NMJs) of *C. elegans*, revealing composition of building units forming bay-like structures in which synaptic vesicles are docked to the active zone membrane. Furthermore, serial reconstruction of HPF EM sections and EM tomography enabled the construction of a high-resolution 3D model of presynaptic ultrastructure, overcoming resolution limitation raised by the conventional EM and revealing a physical link between dense-projections and synaptic vesicles within *C. elegans* presynaptic active zone.

Presynaptic Assembly Imaging

Cell type-specific tagging of synaptic proteins with fluorescent reporter has been a key reagent to study synaptogenesis and its regulation in *C. elegans* (Nonet, 1999; Shen and Bargmann, 2003;

Sieburth et al., 2005; Yeh et al., 2005). Hierarchical assembly of presynaptic active zone was observed in *C. elegans* HSNL synapses by fluorescently labeling the multiple active zone proteins and expressing them in the various mutant animals (Patel et al., 2006). Fluorescent protein fused with a synaptic vesicle-associated protein RAB-3 visualized synaptic vesicle clusters and confirmed the presynaptic localization of various active zone components, including SYD-1, SYD-2/liprin-α, ELKS-1/ERC/CAZ-associated structural protein (CAST), GIT, and SAD-1 kinase in the HSNL synapses (Patel et al., 2006). Altering the location of SYG-1/Neph1 by ectopically expressing SYG-2/Nephrin in the secondary vulval epithelial cells, led to ectopic localizations of presynaptic components, including RAB-3, SYD-1, SYD-2/liprin-α, GIT, and ELKS-1/ERC/CAST in the HSNL regions where the secondary vulval epithelial cells made contacts (**Figure 1A**). This supported the idea that along with SYG-2/Nephrin as an upstream signal of SYG-1/Neph1, SYG-1/Neph1 defines the presynaptic localization and is sufficient to recruit presynaptic components, including the two key scaffold molecules SYD-1 and SYD-2/liprin-α (Zhen and Jin, 1999) to the regions defined by its localization (Patel et al., 2006; **Figure 1B**).

In *syd-1* and *syd-2* mutants, the presynaptic components, including RAB-3, ELKS-1/ERC/CAST, GIT, SAD-1,

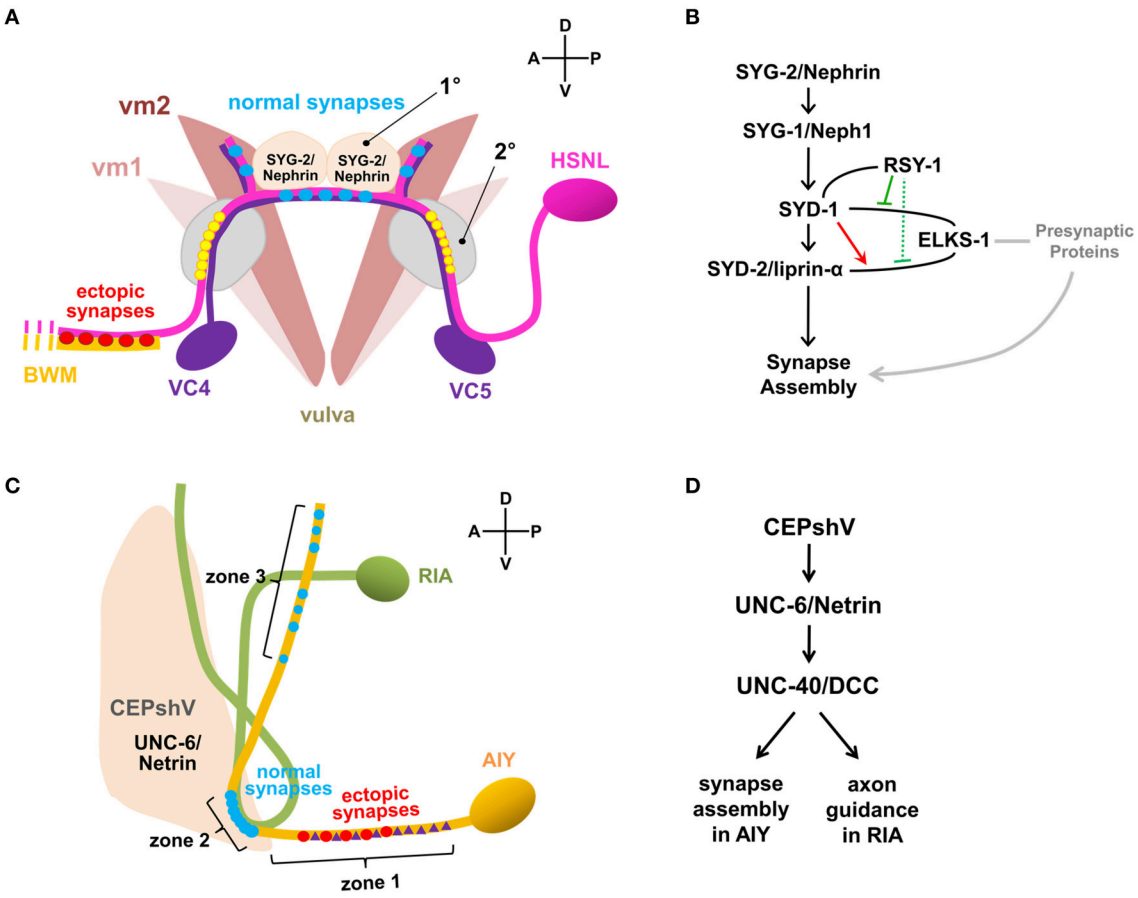

FIGURE 1 | Synaptic specificity regulated by non-neuronal factors. (A) Synaptic connectivity of neurons and muscles associated in the egg-laying circuit of *C. elegans*. HSNL forms synapses with vulval muscle 2 (vm2) and ventral cord (VC) motor neurons, VC4 and VC5 specifically to the regions immediately adjacent to the primary epithelial cells (1°) which secretes SYG-2/Nephrin. Mutations in SYG-1/Neph1 or SYG-2/Nephrin disrupt synaptic specificity of HSNL and cause ectopic synapse formation with select body wall muscle (BWM). Ectopic positioning of SYG-2/Nephrin to the secondary epithelial cells (2°) recruited SYG-1/Neph1 to HSNL near the secondary epithelial cells, which was shown to be sufficient to form synapses ectopically at the sites where SYG-1/Neph1 is recruited (yellow circles). **(B)** Pathway for HSNL synapse assembly. SYG-2/Nephrin ensures proper localization of SYG-1/Neph1 which defines presynaptic localization of the active zone proteins. ELKS-1/ERC/CAST could function redundantly with SYD-1 or other unidentified presynaptic proteins that positively regulate synapse assembly (gray lines). In the presence of SYD-1, the SYD-2/liprin-α and ELKS-1/ERC/CAST interaction was enhanced (red arrow). In the presence of RSY-1, SYD-1, and ELKS-1/ERC/CAST interaction is weakened (solid green), suggesting RSY-1 as a negative regulator in the HSNL presynaptic assembly process likely by weakening the SYD-2/liprin-α and ELKS-1/ERC/CAST interaction (dotted green) indirectly through the RSY-1 and SYD-1 interaction. Plain lines indicate biochemical interactions. **(C)** Synaptic connectivity of AIY and RIA interneurons regulated by ventral cephalic sheath cells (CEPshV) at *C. elegans* nerve ring. Synapses between AIY and RIA are formed *en passent* as they are ensheathed in zone 2 by CEPshV, which secretes UNC-6/Netrin that regulates UNC-40/DCC activity in AIY. Abnormal distend positioning of CEPshV toward zone 1 causes ectopic localizations of both presynapses (red circles) and UNC-40/DCC (purple triangles) in zone 1 of AIY. **(D)** Pathways for AIY and RIA connectivity. CEPshV secretes UNC-6/Netrin, which regulates both positioning of presynapses in AIY and axon guidance of postsynaptic RIA through UNC-40/DCC activity to the location specified by CEPshV.

UNC-57/endophilin, and SNN-1/synapsin-1 were failed to be assembled, identifying those presynaptic components as downstream molecules of SYD-1 and SYD-2/liprin-α in the active zone assembly process (Patel et al., 2006). Gain-of-function mutation (Dai et al., 2006) or overexpression of SYD-2/liprin-α (Patel et al., 2006) in *syd-1* mutants completely restored the synaptic accumulation of SNB-1/synaptobrevin, whereas the SYD-1 overexpression in *syd-2* mutants was not sufficient to induce the rescue effect (Patel et al., 2006), illustrating the SYD-1 and SYD-2/liprin-α mediated presynaptic assembly with the SYD-1 as an upstream of SYD-2/liprin-α (**Figure 1B**). Although the loss of ELKS-1 function by itself did not induce apparent defects in synapse assembly in *C. elegans* HSNL synapses (Dai et al., 2006; Patel et al., 2006), synapse formation in the *syd-2* gain-of-function and *syd-1* double mutants exhibited a high dependency on ELKS-1 expression (Dai et al., 2006), suggesting that ELKS-1 functions redundantly with SYD-1 or other presynaptic proteins that positively regulate synapse assembly (**Figure 1B**).

Regulator of synaptogenesis-1 (RSY-1) was cloned as a negative regulator of synapse formation for its deletion mutants to lead to extra synapse formation and exhibit increased accumulation of SNB-1/synaptobrevin at presynaptic sites in the HSNL (Patel and Shen, 2009). A single-cell *in situ* protein-protein interaction assay revealed enhanced interaction between SYD-2/liprin-α and ELKS-1/ERC/CAST in presence of SYD-1 while direct interaction between SYD-1 and ELKS-1/ERC/CAST is weakened in presence of RSY-1, suggesting RSY-1 as a negative regulator of *C. elegans* HSNL synapse assembly likely by weakening the SYD-2/liprin-α and ELKS-1/ERC/CAST interaction indirectly through its interaction with SYD-1 (**Figure 1B**). Together, presynaptic differentiation at *C. elegans* HSNL synapses was initiated by SYG-1/Neph1, a synaptic specificity molecule that defines the location of presynaptic sites along the HSNL axon, leading to activate the presynaptic assembly process by recruiting the two key scaffolding proteins SYD-1 and SYD-2/liprin-α. SYD-2/liprin-α-centered assembly of presynaptic components was achieved through the inter-communications among positive (SYD-1 and ELKS-1/ERC/CAST) and negative (RSY-1) regulators (**Figure 1B**).

IMAGING SYNAPTIC SPECIFICITY

During the event of synapse formation, a precise apposition between the presynaptic release sites and postsynaptic receptors must be accomplished to ensure a rapid neurotransmitter release and reliable synaptic response. Neurons can select subpopulations of neurons they form synapses onto and can also select the defined specific subcellular sites to establish synapses (Akins and Biederer, 2006; White, 2007; Margeta and Shen, 2010). Such synaptic specificity is achieved by trans-synaptic adhesion between pre- and postsynaptic neurons (Yamagata et al., 2002; Graf et al., 2004; Choe et al., 2006), adhesion between the presynaptic neuron and a guidepost cell (Shen and Bargmann, 2003; Shen et al., 2004), molecules secreted from pre- or postsynaptic neurons (Umemori et al., 2004; Inaki et al., 2007) or from a guidepost cell (Christopherson et al., 2005; Colon-Ramos et al., 2007). In *C. elegans*, synaptic contacts are usually formed *en passant*, in which synapses are formed along the adjacent processes but not its terminus (White et al., 1986). Synaptic specificity studies in *C. elegans* have been accelerated upon the development of the expression tool of fluorescently tagged proteins in specific cell types driven by cell type-specific promoters, which enabled researchers to specifically label pre-, postsynapses, and neighboring guidepost cells (Nonet, 1999; Shen and Bargmann, 2003; Grunwald et al., 2004; Francis et al., 2005; Sieburth et al., 2005; Yeh et al., 2005; Hoerndli et al., 2013).

A specific synaptic connectivity between amphid interneuron Y (AIY) and ring interneuron A (RIA) in *C. elegans* nerve ring, considered as brain of the animal, was fluorescently visualized by expressing presynaptic RAB-3 in AIY and postsynaptic glutamate receptors GLR-1 in RIA (Colon-Ramos et al., 2007; Shao et al., 2013) (**Figure 1C**). The localization of synaptic connectivity between AIY and RIA has shown to be restricted in the zone 2 of AIY axon (**Figure 1C**) and such specificity is achieved by activation of both UNC-6/Netrin, a well-known axon guidance molecule that is exclusively expressed by glia-like ventral cephalic sheath cells (CEPshV) (Wadsworth et al., 1996) and the netrin receptor UNC-40/Deleted in Colorectal Cancer (DCC) (Colon-Ramos et al., 2007), supporting the idea that secreted molecules from glia govern synaptic specificity. Confocal microscopy revealed the projection of the CEPshV processes with respect to the region of innervation between AIY and RIA (**Figure 1C**). Loss-of-function in either UNC-34/enabled, a regulator of the actin cytoskeleton (Colon-Ramos et al., 2007) or circuit maintenance abnormal protein (CIMA-1), a regulator of synaptic maintenance in *C. elegans* (Shao et al., 2013), caused morphological alterations in CEPshV which migrated toward further posteriorly to ensheath AIY axon in zone 1 (**Figure 1C**). Morphological alterations in CEPshV led to ectopic localization of both UNC-40/DCC and presynaptic components in zone 1 (**Figure 1C**) due to the existence of UNC-6/Netrin secreted from CEPshV in zone 1 (Colon-Ramos et al., 2007). The process of RIA in *unc-34* mutants also abnormally migrated toward zone 1 where the ectopic synapses were formed (**Figure 1C**). Together, UNC-40/DCC plays two independent roles in each neuron, which are positioning of presynapses in AIY and axon guidance of postsynaptic RIA to the location specified by CEPshV (**Figure 1D**). These findings further support the model of non-neuronal contribution to the regulation of precise localization of synaptogenesis.

Earlier than the AIY-RIA synaptic specificity study, the *C. elegans* egg-laying circuit, which is predominantly innervated by the two hermaphrodite-specific motor neurons (HSNs), HSNL and HSNR, and the two ventral cord (VC) motor neurons, VC4 and VC5 has been reported to be regulated by non-neuronal factor. HSNL and HSNR synapse onto vulval muscle cells and onto the VC4 and VC5 neurons, while VC4 and VC5 neurons also synapse onto the vulval muscle cells. Despite the direct contact between HSN and VC processes, synapses formed between these cells are only restricted to the regions adjacent to the vulva (White et al., 1986) (**Figure 1A**). The specific positioning of synapses and the recognition between HSNL and its target

were determined by adjacent vulva epithelial guidepost cells that express SYG-2/Nephrin. SYG-2/Nephrin interacts with SYG-1/Neph1 expressed in the HSNL, to recruit SYG-1/Neph1 to the site along the HSNL axon where presynaptic sites are developed (Shen and Bargmann, 2003; Shen et al., 2004) (**Figure 1A**).

More recently, introduction of the GFP reconstitution across synaptic partners (GRASP) developed in *C. elegans* has overcome the challenges addressed by labor-intensive conventional EM analysis and increased the spatial resolution to visualize the pre- and postsynaptic contacts. GRASP is based on functional complementation between two non-fluorescent split-GFP fragments separately expressed in the pre- and postsynaptic neurons, which label synapses between two cells of close proximity in living animals (Feinberg et al., 2008). Using GRASP, specific visualization of synaptic contacts between AIY and RIA was observed with high spatial resolution (Shao et al., 2013). In addition, GRASP revealed restricted synaptic localization between AIY and CEPshV (Shao et al., 2013), which is consistent with the published EM data (White et al., 1986). Formation of ectopic synapses between AIY and CEPshV due to morphological alteration in CEPshV was confirmed as well (Shao et al., 2013) (**Figure 1C**). GRASP application has also confirmed the SYG-1/Neph1 and SYG-2/Nephrin as synaptic specificity regulators of HSN synapses with vulval muscles and VC neurons. Analyzing GRASP fluorescence in wild-type and *syg-1* or *syg-2* mutants recapitulated the synaptic connectivity of HSN neurons (Feinberg et al., 2008) (**Figure 1A**). Besides the *C. elegans* nervous system, the GRASP has also been widely adapted by other model systems, such as *Drosophila* (Gordon and Scott, 2009; Gong et al., 2010) mouse (Kim et al., 2012; Yamagata and Sanes, 2012) and the cultured hippocampal neuronal system (Tsetsenis et al., 2014). Lately, newly modified GRASP strategies, involving activity-dependent synaptic GRASP and multi-color fluorescence reconstitution across synapses (X-RASP) have been validated in *Drosophila*, allowing preferential labeling of active synapses and multi-color labeling of active synapses in one animal (Macpherson et al., 2015; Li et al., 2016). Continuous development of GRASP shows the potential to expand the utility of GRASP to identify and map synaptic connectivity of neural circuits in the living animal with high resolution.

IMAGING FUNCTIONAL NEURAL CIRCUITS

An underlying goal of neuroscience is to understand the neural connectome that are responsible for synaptic function and neuronal basis of behavior. Anatomical structural connectome of the whole nervous system of *C. elegans*, which has been fully mapped by EM of serial sections (White et al., 1986), has served as a useful resource for researchers to study circuit function, thus making the *C. elegans* nervous system as an excellent model to investigate functional connectome of neural circuits. For the past decade, optogenetics has been widely adapted to manipulate neural circuits and examine the corresponding changes in synaptic function and behavior (Fang-Yen et al., 2012; Husson et al., 2013). Optogenetics uses genetically encoded light-sensitive proteins such as channelrhodopsins (Nagel et al., 2003, 2005), halorhodopsins (Han and Boyden, 2007; Zhang et al., 2007; Husson et al., 2012b), and archaerhodopsins (Ihara et al., 1999) as optogenetic actuators to either activate or inhibit neuronal activity via light and genetically encoded sensors such as GCaMP calcium indicator (Tian et al., 2009) and Clomeleon chloride indicator (Kuner and Augustine, 2000; Berglund et al., 2006) as optogenetic sensors to monitor responses to the synaptic inputs. This section will discuss various experimental imaging approaches to interrogate the neural connection using the *C. elegans* nervous system.

The initial optogenetics was applied to manipulate the behavior of *C. elegans* (Nagel et al., 2005). Expression of Channelrhodopsin-2 (ChR2), a blue light-gated depolarizing cation channel used to activate neural activity in *C. elegans* body muscles caused blue light-evoked contractions (Nagel et al., 2003, 2005), whereas expression of NpHR, a yellow light-gated hyperpolarizing chloride ion pump applied to inhibit neural activity in *C. elegans* muscle cells caused an extension of the worm's body length and locomotion defects by whole-field illumination of yellow-green light (Zhang et al., 2007; Husson et al., 2012b). Aside from NpHR, a yellow-green light-sensitive archaerhodopsin-3 (Arch) (Ihara et al., 1999) and a green-blue light-sensitive Mac (Waschuk et al., 2005) have also been expressed in *C. elegans* and induced a stronger optical silencing effect than NpHR likely due to efficient protein trafficking to the plasma membrane (Chow et al., 2010; Husson et al., 2012b). The simultaneous use of Arch and Mac enabled inhibition of two different neuronal subpopulations, depending on the illuminating lights used.

Light-sensitive probes expressed in *C. elegans in vivo* are mostly under the control of a promoter sequence. However, promoter-driven single cell expression of optogenetic protein is challenging to achieve due to the lack of single cell-specific promoter and instead proteins are diversely expressed, eliciting robust behavioral responses upon whole-field illumination (Husson et al., 2013). Although it may be useful for inspecting a novel optogenetic protein, optical manipulation of individual neurons needs to be accomplished in order to obtain insights into individual contribution by single neurons in functional connectivity. To this aim, new methods have been adapted in *C. elegans* to drive selective optical manipulation, either by genetically modulated single cell-specific expression of optogenetic protein (Ezcurra et al., 2011; Schmitt et al., 2012; Cho and Sternberg, 2014; Guo et al., 2015) or selective illumination of target neurons with a high spatial and temporal resolution (Guo et al., 2009; Leifer et al., 2011; Stirman et al., 2011; Husson et al., 2012a,b; Kocabas et al., 2012; Cohen et al., 2014; Luo et al., 2014; Shipley et al., 2014; Trojanowski et al., 2014) in order to dissect functional connections within the neural circuits (**Table 1**).

Mainly adapted approach to specifically deliver light-sensitive opsins to individual neurons of *C. elegans* restricts the opsin expression by genetic application using Cre or FLP recombinases (Ezcurra et al., 2011; Schmitt et al., 2012; Cho and Sternberg, 2014; Guo et al., 2015) (**Figure 2**). The recombinase-dependent gene expression is driven by a set of two promoters, a first promoter driving the expression of opsin conjugated with a

TABLE 1 | Cell-specific optogenetic applications in *C. elegans*

Single-cell stimulation approach	Circuit	Cells manipulated	References
Cre or FLP recombinase application	Avoidance	ASH, AVA	Ezcurra et al., 2011
	Locomotion	ASH, AVA, PVC	Schmitt et al., 2012
	Avoidance circuit during sleep behavior	ASH, AVA, RIM, RIG	Cho and Sternberg, 2014
	Nociception and avoidance	ASH, ASI*, ADF*	Guo et al., 2015
Selective illumination	Locomotion	DB, VB	Leifer et al., 2011
	Avoidance	ASH, RIM	Guo et al., 2009
		ALM, AVM, PLM	Stirman et al., 2011 Leifer et al., 2011 Shipley et al., 2014
	Nociception	AQR, FLP, PVD	Husson et al., 2012a
		ASH, ALM, AVM	Husson et al., 2012b
		PVD	Cohen et al., 2014
	Chemotaxis	AIB, AIY, AIZ, RME, SMB	Kocabas et al., 2012
		ASER	Luo et al., 2014
	Feeding	MC, M1, M2, M4	Trojanowski et al., 2014

**Optogenetic manipulation driven by neuronal type-specific promoters rather than Cre/FLP recombinase application.*

fluorophore along with or without a bicistronic fluorescent reporter and a second promoter driving the expression of Cre or FLP recombinase. In the first promoter-containing construct, a transcription termination sequence flanked by recombinase recognition sequences, loxP or FRT that are recognized by Cre or FLP recombinase is enclosed in front of opsin. The Cre or FLP recombinase-mediated recombination of loxP or FRT sites excised the stop sequence and allows conditional expression of opsin only in the target cell where both promoters are active (Husson et al., 2013) (**Figure 2**). Using Cre and FLP system, ChR2 were specifically expressed in PVC interneurons which evoked forward locomotion and in AVA interneuron and ASH sensory neurons which evoked backward-movement upon photostimulation (Ezcurra et al., 2011; Schmitt et al., 2012) (**Table 1**). Further effort to isolate exclusive expression of the light-sensitive proteins in a single cell (Ezcurra et al., 2011) would need to define the role of individual single neurons in functional neural circuits.

Instead of using genetically generated system and whole-field illumination, spatiotemporally patterned illumination of neurons expressing light-sensitive optogenetic proteins in immobilized *C. elegans* was used by for the first time *in vivo* using a digital micromirror device (DMD) whose individual mirrors can be controlled independently to precisely determine the location and size of the regions to be illuminated while simultaneously recording the calcium levels using a genetically encoded calcium sensor, GCaMP to analyze the functional connections among neurons. Combining the optogenetic actuator ChR2 and the sensor GCaMP with the patterned illumination via a DMD technology, the functional connections from the sensory neuron ASH to the interneurons AVA and AVD and the connections between the interneurons RIM and AVA have been monitored (Guo et al., 2009; **Table 1**).

Improvement in microscopic analysis and optogenetic illumination system allowed manipulation of neural activity in a freely behaving *C. elegans* with a high spatiotemporal resolution, providing an in-depth analysis on functional neural circuits underlying behavior at a single-cell level. A modified three-panel liquid crystal display (3-LCD) projector for simultaneous multicolor illumination and a motorized X-Y stage for keeping the unrestrained worm centered in the camera's field of view with a standard inverted epifluorescence microscope were systemized (Stirman et al., 2011; Husson et al., 2012b) and the Colbert system was equipped to control locomotion and behavior in real time (Leifer et al., 2011; Luo et al., 2014; Shipley et al., 2014). Spatial regulation of optical illumination is controlled either by estimating the coordinates of targeted cells using the machine-vision algorithms (Leifer et al., 2011; Trojanowski et al., 2014) or by calculating the anterior-posterior (A-P) axis (Stirman et al., 2011). Both systems have been instrumental in defining neural coding of several behaviors in *C. elegans* linked to the motor circuit, avoidance circuit, nociceptive circuit, chemotaxis circuit, and feeding circuits of freely moving worms (**Table 1**). Using AIY expressing ChR2 and targeted illumination by the DMD technology, it was shown that optogenetic manipulation of AIY activity alone was sufficient to evoke chemotactic behavior in freely moving *C. elegans*, and was suggested that AIY is plausible to act as a control node for coordinating other taxis behaviors as well (Kocabas et al., 2012). Another report using the Colbert system equipped with

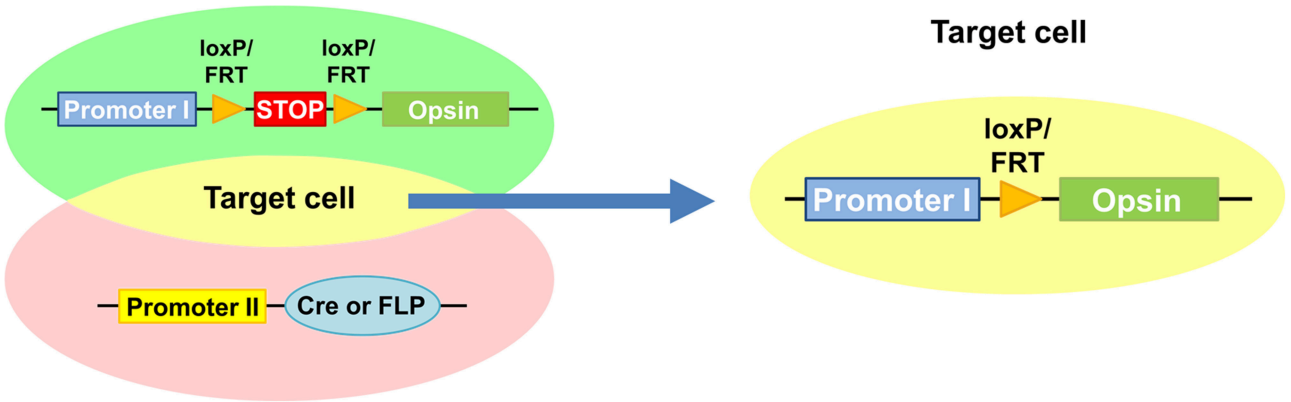

FIGURE 2 | Restricted expression of light-sensitive opsin mediated by Cre or FLP recombinases. Promoter 1-containing construct is designed to drive expression of opsin with a fluorescent reporter. Promoter 2 drives expression of Cre or FLP recombinase. Conditional expression of opsin is mediated by the Cre or FLP recombinases by removing a transcription termination sequence flanked by loxP or FRT only in target cell where the both promoters are active.

the DMD investigated an experience-dependent salt chemotaxis circuit. Optogenetic manipulation of neuronal activity of the ASER sensory neuron expressing ChR2 was shown to be connected to positive and negative chemotaxis in response to salt concentrations, indicating that ASER sensory neuron encodes the perception of salt concentration and the memory of the chemotactic set point in a chemotaxis circuit of *C. elegans* (Luo et al., 2014). In addition, optogenetic manipulations of specific pharyngeal neurons MC, M2, M4, and I1 in freely behaving worms by adopting ChR2 for optical stimulation and Mac for optical silencing along with the DMD for targeted illumination revealed a pharyngeal pumping/feeding circuit and identified the regulation of feeding rate by nicotinic and muscarinic receptors through the pharyngeal neuronal network (Trojanowski et al., 2014). Furthermore, multispectral illumination (Stirman et al., 2011) enables simultaneous application of optical stimulation and inhibition to an individual animal. Emerging studies have successfully facilitated multimodal optogenetic manipulation on *C. elegans* to independently excite different neurons in a single worm (Erbguth et al., 2012; Husson et al., 2012b; Schild and Glauser, 2015).

PERSPECTIVES

C. elegans is currently the best organism to study synapses and neuronal circuits because the connectivity of its 302 neurons has been well-defined by serial reconstruction of EM (White et al., 1986), the body is transparent, and it is a genetically tractable animal model. *C. elegans* was one of the first organisms that GFP was expressed to label protein (Chalfie et al., 1994), GRASP was utilized to visualize specific synaptic contacts (Feinberg et al., 2008), optogenetics was applied to manipulate behavior of live animals (Nagel et al., 2005), and more recently, sonogenetics using low-pressure ultrasound was challenged to activate specific ultrasonically sensitized neurons and modify locomotory behavior (Ibsen et al., 2015).

As genetically encoded fluorescent proteins have been rapidly developed for the past decades since the GFP was introduced in the field, it is also expected that the number of optogenetic tools will rapidly increase to likely provide optogenetic proteins with different spectral properties (Zhang et al., 2008; Gradinaru et al., 2010) and ionic specificities (Han and Boyden, 2007; Zhang et al., 2007) and help expand the understanding of synaptic function and neural circuits. During such processes, it is confidently predicted that *C. elegans* will provide a systematic *in vivo* platform to test the optogenetic tools newly developed and to ultimately apply to the synaptic function and functional connectome studies. Together with the improvement of fluorescent and optogenetic tools, continuous development in *C. elegans* imaging technology will promise a breakthrough in deciphering functional neural connectome.

In addition to the monitoring and controlling of existing neuronal circuits via optogenetic applications and advanced microscopy systems as described in this review, it is very plausible to develop the ways to actively manipulate neural circuits for instance by inserting new connections or removing existing connections, resulting in the reprogramming of neural circuits. Indeed, a recent study on artificial modifications of neural circuits was reported in *C. elegans* by expressing transgenically targeted heterologous connexin to insert a new electrical synapse between normally unconnected neurons in intact animals, which resulted in altered salt taste and olfactory chemotaxis behavior (Rabinowitch et al., 2014). Conversely, laser ablation method can be used to remove existing connection (Sulston and White, 1980; Bargmann et al., 1993; McIntire et al., 1993; Fang-Yen et al., 2012; Rabinowitch et al., 2013). Such artificial modification of neural circuits not only help understand fundamental functions of neuronal connectivity underlying complex behavior but could also be applied to disease brain circuits with the purpose of therapeutics at the circuit level.

AUTHOR CONTRIBUTIONS

All authors listed, have made substantial, direct and intellectual contribution to the work, and approved it for publication.

ACKNOWLEDGMENTS

The work in M. Park laboratory was supported by the KIST Institutional Programs (Project No. 2E26190 and 2E26170).

REFERENCES

Ackermann, F., Waites, C. L., and Garner, C. C. (2015). Presynaptic active zones in invertebrates and vertebrates. *EMBO Rep.* 16, 923–938. doi: 10.15252/embr.201540434

Akins, M. R., and Biederer, T. (2006). Cell-cell interactions in synaptogenesis. *Curr. Opin. Neurobiol.* 16, 83–89. doi: 10.1016/j.conb.2006.01.009

Bargmann, C. I., Hartwieg, E., and Horvitz, H. R. (1993). Odorant-selective genes and neurons mediate olfaction in *C. elegans*. *Cell* 74, 515–527. doi: 10.1016/0092-8674(93)80053-H

Berglund, K., Schleich, W., Krieger, P., Loo, L. S., Wang, D., Cant, N. B., et al. (2006). Imaging synaptic inhibition in transgenic mice expressing the chloride indicator, Clomeleon. *Brain Cell Biol.* 35, 207–228. doi: 10.1007/s11068-008-9019-6

Brenner, S. (1974). The genetics of *Caenorhabditis elegans*. *Genetics* 77, 71–94.

Campbell, J. C., Chin-Sang, I. D., and Bendena, W. G. (2015). Mechanosensation circuitry in *Caenorhabditis elegans*: a focus on gentle touch. *Peptides* 68, 164–174. doi: 10.1016/j.peptides.2014.12.004

Chalfie, M., Tu, Y., Euskirchen, G., Ward, W. W., and Prasher, D. C. (1994). Green fluorescent protein as a marker for gene expression. *Science* 263, 802–805. doi: 10.1126/science.8303295

Cherra, S. J. III, and Jin, Y. (2015). Advances in synapse formation: forging connections in the worm. *Wiley Interdiscip. Rev. Dev. Biol.* 4, 85–97. doi: 10.1002/wdev.165

Chia, P. H., Li, P., and Shen, K. (2013). Cell biology in neuroscience: cellular and molecular mechanisms underlying presynapse formation. *J. Cell Biol.* 203, 11–22. doi: 10.1083/jcb.201307020

Cho, J. Y., and Sternberg, P. W. (2014). Multilevel modulation of a sensory motor circuit during *C. elegans* sleep and arousal. *Cell* 156, 249–260. doi: 10.1016/j.cell.2013.11.036

Choe, K. M., Prakash, S., Bright, A., and Clandinin, T. R. (2006). Liprin-alpha is required for photoreceptor target selection in Drosophila. *Proc. Natl. Acad. Sci. U.S.A.* 103, 11601–11606. doi: 10.1073/pnas.0601185103

Chow, B. Y., Han, X., Dobry, A. S., Qian, X., Chuong, A. S., Li, M., et al. (2010). High-performance genetically targetable optical neural silencing by light-driven proton pumps. *Nature* 463, 98–102. doi: 10.1038/nature08652

Christopherson, K. S., Ullian, E. M., Stokes, C. C., Mullowney, C. E., Hell, J. W., Agah, A., et al. (2005). Thrombospondins are astrocyte-secreted proteins that promote CNS synaptogenesis. *Cell* 120, 421–433. doi: 10.1016/j.cell.2004.12.020

Cohen, E., Chatzigeorgiou, M., Husson, S. J., Steuer-Costa, W., Gottschalk, A., Schafer, W. R., et al. (2014). *Caenorhabditis elegans* nicotinic acetylcholine receptors are required for nociception. *Mol. Cell. Neurosci.* 59, 85–96. doi: 10.1016/j.mcn.2014.02.001

Colon-Ramos, D. A., Margeta, M. A., and Shen, K. (2007). Glia promote local synaptogenesis through UNC-6 (netrin) signaling in *C. elegans*. *Science* 318, 103–106. doi: 10.1126/science.1143762

Cowan, W. M., and Kandel, E. R. (2001). "A brief history of synapses and synaptic transmission," in *Synapses*,eds T. C. Sudhof, W. M. Cowan, and C. F. Stevens (Baltimore: The Johns Hopkins University Press), 1–88.

Dai, Y., Taru, H., Deken, S. L., Grill, B., Ackley, B., Nonet, M. L., et al. (2006). SYD-2 Liprin-alpha organizes presynaptic active zone formation through ELKS. *Nat. Neurosci.* 9, 1479–1487. doi: 10.1038/nn1808

Erbguth, K., Prigge, M., Schneider, F., Hegemann, P., and Gottschalk, A. (2012). Bimodal activation of different neuron classes with the spectrally red-shifted channelrhodopsin chimera C1V1 in *Caenorhabditis elegans*. *PLoS ONE* 7:e46827. doi: 10.1371/journal.pone.0046827

Ezcurra, M., Tanizawa, Y., Swoboda, P., and Schafer, W. R. (2011). Food sensitizes *C. elegans* avoidance behaviours through acute dopamine signalling. *EMBO J.* 30, 1110–1122. doi: 10.1038/emboj.2011.22

Fang-Yen, C., Gabel, C. V., Samuel, A. D., Bargmann, C. I., and Avery, L. (2012). Laser microsurgery in *Caenorhabditis elegans*. *Methods Cell Biol.* 107, 177–206. doi: 10.1016/B978-0-12-394620-1.00006-0

Feinberg, E. H., Vanhoven, M. K., Bendesky, A., Wang, G., Fetter, R. D., Shen, K., et al. (2008). GFP Reconstitution Across Synaptic Partners (GRASP) defines cell contacts and synapses in living nervous systems. *Neuron* 57, 353–363. doi: 10.1016/j.neuron.2007.11.030

Francis, M. M., Evans, S. P., Jensen, M., Madsen, D. M., Mancuso, J., Norman, K. R., et al. (2005). The Ror receptor tyrosine kinase CAM-1 is required for ACR-16-mediated synaptic transmission at the *C. elegans* neuromuscular junction. *Neuron* 46, 581–594. doi: 10.1016/j.neuron.2005.04.010

Frokjaer-Jensen, C., Davis, M. W., Hopkins, C. E., Newman, B. J., Thummel, J. M., Olesen, S. P., et al. (2008). Single-copy insertion of transgenes in *Caenorhabditis elegans*. *Nat. Genet.* 40, 1375–1383. doi: 10.1038/ng.248

Fu, Q., Martin, B. L., Matus, D. Q., and Gao, L. (2016). Imaging multicellular specimens with real-time optimized tiling light-sheet selective plane illumination microscopy. *Nat. Commun.* 7:11088. doi: 10.1038/ncomms11088

Gong, Z., Liu, J., Guo, C., Zhou, Y., Teng, Y., and Liu, L. (2010). Two pairs of neurons in the central brain control *Drosophila* innate light preference. *Science* 330, 499–502. doi: 10.1126/science.1195993

Gordon, M. D., and Scott, K. (2009). Motor control in a *Drosophila* taste circuit. *Neuron* 61, 373–384. doi: 10.1016/j.neuron.2008.12.033

Gradinaru, V., Zhang, F., Ramakrishnan, C., Mattis, J., Prakash, R., Diester, I., et al. (2010). Molecular and cellular approaches for diversifying and extending optogenetics. *Cell* 141, 154–165. doi: 10.1016/j.cell.2010.02.037

Graf, E. R., Zhang, X., Jin, S. X., Linhoff, M. W., and Craig, A. M. (2004). Neurexins induce differentiation of GABA and glutamate postsynaptic specializations via neuroligins. *Cell* 119, 1013–1026. doi: 10.1016/j.cell.2004.11.035

Grunwald, M. E., Mellem, J. E., Strutz, N., Maricq, A. V., and Kaplan, J. M. (2004). Clathrin-mediated endocytosis is required for compensatory regulation of GLR-1 glutamate receptors after activity blockade. *Proc. Natl. Acad. Sci. U.S.A.* 101, 3190–3195. doi: 10.1073/pnas.0306156101

Guo, M., Wu, T. H., Song, Y. X., Ge, M. H., Su, C. M., Niu, W. P., et al. (2015). Reciprocal inhibition between sensory ASH and ASI neurons modulates nociception and avoidance in *Caenorhabditis elegans*. *Nat. Commun.* 6, 5655. doi: 10.1038/ncomms6655

Guo, Z. V., Hart, A. C., and Ramanathan, S. (2009). Optical interrogation of neural circuits in *Caenorhabditis elegans*. *Nat. Methods* 6, 891–896. doi: 10.1038/nmeth.1397

Han, X., and Boyden, E. S. (2007). Multiple-color optical activation, silencing, and desynchronization of neural activity, with single-spike temporal resolution. *PLoS ONE* 2:e299. doi: 10.1371/journal.pone.0000299

Hoerndli, F. J., Maxfield, D. A., Brockie, P. J., Mellem, J. E., Jensen, E., Wang, R., et al. (2013). Kinesin-1 regulates synaptic strength by mediating the delivery, removal, and redistribution of AMPA receptors. *Neuron* 80, 1421–1437. doi: 10.1016/j.neuron.2013.10.050

Husson, S. J., Costa, W. S., Wabnig, S., Stirman, J. N., Watson, J. D., Spencer, W. C., et al. (2012a). Optogenetic analysis of a nociceptor neuron and network reveals ion channels acting downstream of primary sensors. *Curr. Biol.* 22, 743–752. doi: 10.1016/j.cub.2012.02.066

Husson, S. J., Gottschalk, A., and Leifer, A. M. (2013). Optogenetic manipulation of neural activity in *C. elegans*: from synapse to circuits and behaviour. *Biol. Cell* 105, 235–250. doi: 10.1111/boc.201200069

Husson, S. J., Liewald, J. F., Schultheis, C., Stirman, J. N., Lu, H., and Gottschalk, A. (2012b). Microbial light-activatable proton pumps as neuronal inhibitors to functionally dissect neuronal networks in *C. elegans*. *PLoS One* 7:e40937. doi: 10.1371/journal.pone.0040937

Ibsen, S., Tong, A., Schutt, C., Esener, S., and Chalasani, S. H. (2015). Sonogenetics is a non-invasive approach to activating neurons in *Caenorhabditis elegans*. *Nat. Commun.* 6, 8264. doi: 10.1038/ncomms9264

Ihara, K., Umemura, T., Katagiri, I., Kitajima-Ihara, T., Sugiyama, Y., Kimura, Y., et al. (1999). Evolution of the archaeal rhodopsins: evolution rate changes by gene duplication and functional differentiation. *J. Mol. Biol.* 285, 163–174. doi: 10.1006/jmbi.1998.2286

Inaki, M., Yoshikawa, S., Thomas, J. B., Aburatani, H., and Nose, A. (2007). Wnt4 is a local repulsive cue that determines synaptic target specificity. *Curr. Biol.* 17, 1574–1579. doi: 10.1016/j.cub.2007.08.013

Jin, Y. (2015). Unraveling the mechanisms of synapse formation and axon regeneration: the awesome power of *C. elegans* genetics. *Sci. China Life Sci.* 58, 1084–1088. doi: 10.1007/s11427-015-4962-9

Kim, J., Zhao, T., Petralia, R. S., Yu, Y., Peng, H., Myers, E., et al. (2012). mGRASP enables mapping mammalian synaptic connectivity with light microscopy. *Nat. Methods* 9, 96–102. doi: 10.1038/nmeth.1784

Kittelmann, M., Hegermann, J., Goncharov, A., Taru, H., Ellisman, M. H., Richmond, J. E., et al. (2013). Liprin-alpha/SYD-2 determines the size of dense projections in presynaptic active zones in *C. elegans*. *J. Cell Biol.* 203, 849–863. doi: 10.1083/jcb.201302022

Kocabas, A., Shen, C. H., Guo, Z. V., and Ramanathan, S. (2012). Controlling interneuron activity in *Caenorhabditis elegans* to evoke chemotactic behaviour. *Nature* 490, 273–277. doi: 10.1038/nature11431

Kuner, T., and Augustine, G. J. (2000). A genetically encoded ratiometric indicator for chloride: capturing chloride transients in cultured hippocampal neurons. *Neuron* 27, 447–459. doi: 10.1016/S0896-6273(00)00056-8

Leifer, A. M., Fang-Yen, C., Gershow, M., Alkema, M. J., and Samuel, A. D. (2011). Optogenetic manipulation of neural activity in freely moving *Caenorhabditis elegans*. *Nat. Methods* 8, 147–152. doi: 10.1038/nmeth.1554

Li, Y., Guo, A., and Li, H. (2016). CRASP: CFP reconstitution across synaptic partners. *Biochem. Biophys. Res. Commun.* 469, 352–356. doi: 10.1016/j.bbrc.2015.12.011

Luo, L., Wen, Q., Ren, J., Hendricks, M., Gershow, M., Qin, Y., et al. (2014). Dynamic encoding of perception, memory, and movement in a *C. elegans* chemotaxis circuit. *Neuron* 82, 1115–1128. doi: 10.1016/j.neuron.2014.05.010

Macpherson, L. J., Zaharieva, E. E., Kearney, P. J., Alpert, M. H., Lin, T. Y., Turan, Z., et al. (2015). Dynamic labelling of neural connections in multiple colours by trans-synaptic fluorescence complementation. *Nat. Commun.* 6:10024. doi: 10.1038/ncomms10024

Margeta, M. A., and Shen, K. (2010). Molecular mechanisms of synaptic specificity. *Mol. Cell. Neurosci.* 43, 261–267. doi: 10.1016/j.mcn.2009.11.009

McIntire, S. L., Jorgensen, E., Kaplan, J., and Horvitz, H. R. (1993). The GABAergic nervous system of *Caenorhabditis elegans*. *Nature* 364, 337–341. doi: 10.1038/364337a0

Mello, C. C., Kramer, J. M., Stinchcomb, D., and Ambros, V. (1991). Efficient gene transfer in *C.elegans*: extrachromosomal maintenance and integration of transforming sequences. *EMBO J.* 10, 3959–3970.

Nagel, G., Brauner, M., Liewald, J. F., Adeishvili, N., Bamberg, E., and Gottschalk, A. (2005). Light activation of channelrhodopsin-2 in excitable cells of *Caenorhabditis elegans* triggers rapid behavioral responses. *Curr. Biol.* 15, 2279–2284. doi: 10.1016/j.cub.2005.11.032

Nagel, G., Szellas, T., Huhn, W., Kateriya, S., Adeishvili, N., Berthold, P., et al. (2003). Channelrhodopsin-2, a directly light-gated cation-selective membrane channel. *Proc. Natl. Acad. Sci. U.S.A.* 100, 13940–13945. doi: 10.1073/pnas.1936192100

Nonet, M. L. (1999). Visualization of synaptic specializations in live *C. elegans* with synaptic vesicle protein-GFP fusions. *J. Neurosci. Methods* 89, 33–40. doi: 10.1016/S0165-0270(99)00031-X

Park, M., and Shen, K. (2012). WNTs in synapse formation and neuronal circuitry. *EMBO J.* 31, 2697–2704. doi: 10.1038/emboj.2012.145

Patel, M. R., Lehrman, E. K., Poon, V. Y., Crump, J. G., Zhen, M., Bargmann, C. I., et al. (2006). Hierarchical assembly of presynaptic components in defined *C. elegans* synapses. *Nat. Neurosci.* 9, 1488–1498. doi: 10.1038/nn1806

Patel, M. R., and Shen, K. (2009). RSY-1 is a local inhibitor of presynaptic assembly in *C. elegans*. *Science* 323, 1500–1503. doi: 10.1126/science.1169025

Rabinowitch, I., Chatzigeorgiou, M., and Schafer, W. R. (2013). A gap junction circuit enhances processing of coincident mechanosensory inputs. *Curr. Biol.* 23, 963–967. doi: 10.1016/j.cub.2013.04.030

Rabinowitch, I., Chatzigeorgiou, M., Zhao, B., Treinin, M., and Schafer, W. R. (2014). Rewiring neural circuits by the insertion of ectopic electrical synapses in transgenic *C. elegans*. *Nat. Commun.* 5:4442. doi: 10.1038/ncomms5442

Schild, L. C., and Glauser, D. A. (2015). Dual Color Neural Activation and Behavior Control with Chrimson and CoChR in *Caenorhabditis elegans*. *Genetics* 200, 1029–1034. doi: 10.1534/genetics.115.177956

Schmitt, C., Schultheis, C., Pokala, N., Husson, S. J., Liewald, J. F., Bargmann, C. I., et al. (2012). Specific expression of channelrhodopsin-2 in single neurons of *Caenorhabditis elegans*. *PLoS ONE* 7:e43164. doi: 10.1371/journal.pone.0043164

Shao, Z., Watanabe, S., Christensen, R., Jorgensen, E. M., and Colon-Ramos, D. A. (2013). Synapse location during growth depends on glia location. *Cell* 154, 337–350. doi: 10.1016/j.cell.2013.06.028

Shen, K., and Bargmann, C. I. (2003). The immunoglobulin superfamily protein SYG-1 determines the location of specific synapses in *C. elegans*. *Cell* 112, 619–630. doi: 10.1016/S0092-8674(03)00113-2

Shen, K., Fetter, R. D., and Bargmann, C. I. (2004). Synaptic specificity is generated by the synaptic guidepost protein SYG-2 and its receptor, SYG-1. *Cell* 116, 869–881. doi: 10.1016/S0092-8674(04)00251-X

Shipley, F. B., Clark, C. M., Alkema, M. J., and Leifer, A. M. (2014). Simultaneous optogenetic manipulation and calcium imaging in freely moving *C. elegans*. *Front. Neural Circuits* 8:28. doi: 10.3389/fncir.2014.00028

Sieburth, D., Ch'ng, Q., Dybbs, M., Tavazoie, M., Kennedy, S., Wang, D., et al. (2005). Systematic analysis of genes required for synapse structure and function. *Nature* 436, 510–517. doi: 10.1038/nature03809

Stigloher, C., Zhan, H., Zhen, M., Richmond, J., and Bessereau, J. L. (2011). The presynaptic dense projection of the *Caenorhabditis elegans* cholinergic neuromuscular junction localizes synaptic vesicles at the active zone through SYD-2/liprin and UNC-10/RIM-dependent interactions. *J. Neurosci.* 31, 4388–4396. doi: 10.1523/JNEUROSCI.6164-10.2011

Stirman, J. N., Crane, M. M., Husson, S. J., Wabnig, S., Schultheis, C., Gottschalk, A., et al. (2011). Real-time multimodal optical control of neurons and muscles in freely behaving *Caenorhabditis elegans*. *Nat. Methods* 8, 153–158. doi: 10.1038/nmeth.1555

Sulston, J. E., and White, J. G. (1980). Regulation and cell autonomy during postembryonic development of *Caenorhabditis elegans*. *Dev. Biol.* 78, 577–597. doi: 10.1016/0012-1606(80)90353-X

Tian, L., Hires, S. A., Mao, T., Huber, D., Chiappe, M. E., Chalasani, S. H., et al. (2009). Imaging neural activity in worms, flies and mice with improved GCaMP calcium indicators. *Nat. Methods* 6, 875–881. doi: 10.1038/nmeth.1398

Trojanowski, N. F., Padovan-Merhar, O., Raizen, D. M., and Fang-Yen, C. (2014). Neural and genetic degeneracy underlies *Caenorhabditis elegans* feeding behavior. *J. Neurophysiol.* 112, 951–961. doi: 10.1152/jn.00150.2014

Tsetsenis, T., Boucard, A. A., Arac, D., Brunger, A. T., and Sudhof, T. C. (2014). Direct visualization of trans-synaptic neurexin-neuroligin interactions during synapse formation. *J. Neurosci.* 34, 15083–15096. doi: 10.1523/JNEUROSCI.0348-14.2014

Umemori, H., Linhoff, M. W., Ornitz, D. M., and Sanes, J. R. (2004). FGF22 and its close relatives are presynaptic organizing molecules in the mammalian brain. *Cell* 118, 257–270. doi: 10.1016/j.cell.2004.06.025

Wadsworth, W. G., Bhatt, H., and Hedgecock, E. M. (1996). Neuroglia and pioneer neurons express UNC-6 to provide global and local netrin cues for guiding migrations in *C. elegans*. *Neuron* 16, 35–46. doi: 10.1016/S0896-6273(00)80021-5

Waschuk, S. A., Bezerra, A. G. Jr., Shi, L., and Brown, L. S. (2005). Leptosphaeria rhodopsin: bacteriorhodopsin-like proton pump from a eukaryote. *Proc. Natl. Acad. Sci. U.S.A.* 102, 6879–6883. doi: 10.1073/pnas.0409659102

Watanabe, S., Punge, A., Hollopeter, G., Willig, K. I., Hobson, R. J., Davis, M. W., et al. (2011). Protein localization in electron micrographs using fluorescence nanoscopy. *Nat. Methods* 8, 80–84. doi: 10.1038/nmeth.1537

Weimer, R. M., Gracheva, E. O., Meyrignac, O., Miller, K. G., Richmond, J. E., and Bessereau, J. L. (2006). UNC-13 and UNC-10/rim localize synaptic vesicles to specific membrane domains. *J. Neurosci.* 26, 8040–8047. doi: 10.1523/JNEUROSCI.2350-06.2006

White, E. L. (2007). Reflections on the specificity of synaptic connections. *Brain Res. Rev.* 55, 422–429. doi: 10.1016/j.brainresrev.2006.12.004

White, J. G., Southgate, E., Thomson, J. N., and Brenner, S. (1986). The structure of the nervous system of the nematode *Caenorhabditis elegans*. *Philos. Trans. R. Soc. Lond. B. Biol. Sci.* 314, 1–340. doi: 10.1098/rstb.1986.0056

Wu, Y., Ghitani, A., Christensen, R., Santella, A., Du, Z., Rondeau, G., et al. (2011). Inverted selective plane illumination microscopy (iSPIM) enables coupled cell

identity lineaging and neurodevelopmental imaging in *Caenorhabditis elegans*. *Proc. Natl. Acad. Sci. U.S.A.* 108, 17708–17713. doi: 10.1073/pnas.1108494108

Yamagata, M., and Sanes, J. R. (2012). Transgenic strategy for identifying synaptic connections in mice by fluorescence complementation (GRASP). *Front. Mol. Neurosci.* 5:18. doi: 10.3389/fnmol.2012.00018

Yamagata, M., Weiner, J. A., and Sanes, J. R. (2002). Sidekicks: synaptic adhesion molecules that promote lamina-specific connectivity in the retina. *Cell* 110, 649–660. doi: 10.1016/S0092-8674(02)00910-8

Yeh, E., Kawano, T., Weimer, R. M., Bessereau, J. L., and Zhen, M. (2005). Identification of genes involved in synaptogenesis using a fluorescent active zone marker in *Caenorhabditis elegans*. *J. Neurosci.* 25, 3833–3841. doi: 10.1523/JNEUROSCI.4978-04.2005

Yogev, S., and Shen, K. (2014). Cellular and molecular mechanisms of synaptic specificity. *Annu. Rev. Cell Dev. Biol.* 30, 417–437. doi: 10.1146/annurev-cellbio-100913-012953

Zhai, R. G., and Bellen, H. J. (2004). The architecture of the active zone in the presynaptic nerve terminal. *Physiology (Bethesda)* 19, 262–270. doi: 10.1152/physiol.00014.2004

Zhan, H., Stanciauskas, R., Stigloher, C., Dizon, K. K., Jospin, M., Bessereau, J. L., et al. (2014). *In vivo* single-molecule imaging identifies altered dynamics of calcium channels in dystrophin-mutant *C. elegans*. *Nat. Commun.* 5, 4974. doi: 10.1038/ncomms5974

Zhang, F., Prigge, M., Beyriere, F., Tsunoda, S. P., Mattis, J., Yizhar, O., et al. (2008). Red-shifted optogenetic excitation: a tool for fast neural control derived from *Volvox carteri*. *Nat. Neurosci.* 11, 631–633. doi: 10.1038/nn.2120

Zhang, F., Wang, L. P., Brauner, M., Liewald, J. F., Kay, K., Watzke, N., et al. (2007). Multimodal fast optical interrogation of neural circuitry. *Nature* 446, 633–639. doi: 10.1038/nature05744

Zhen, M., and Jin, Y. (1999). The liprin protein SYD-2 regulates the differentiation of presynaptic termini in *C. elegans*. *Nature* 401, 371–375. doi: 10.1038/43886

Zhen, M., and Samuel, A. D. (2015). *C. elegans* locomotion: small circuits, complex functions. *Curr. Opin. Neurobiol.* 33, 117–126. doi: 10.1016/j.conb.2015.03.009

Conflict of Interest Statement: The authors declare that the research was conducted in the absence of any commercial or financial relationships that could be construed as a potential conflict of interest.

Advantages of publishing in Frontiers

OPEN ACCESS
Articles are free to read, for greatest visibility

COLLABORATIVE PEER-REVIEW
Designed to be rigorous – yet also collaborative, fair and constructive

FAST PUBLICATION
Average 85 days from submission to publication (across all journals)

COPYRIGHT TO AUTHORS
No limit to article distribution and re-use

TRANSPARENT
Editors and reviewers acknowledged by name on published articles

SUPPORT
By our Swiss-based editorial team

IMPACT METRICS
Advanced metrics track your article's impact

GLOBAL SPREAD
5'100'000+ monthly article views and downloads

LOOP RESEARCH NETWORK
Our network increases readership for your article

Frontiers
EPFL Innovation Park, Building I • 1015 Lausanne • Switzerland
Tel +41 21 510 17 00 • Fax +41 21 510 17 01 • info@frontiersin.org
www.frontiersin.org

Find us on